Adaptive multiscale methods for fracture

Adaptive Multiskalen-Methoden zur Modellierung von Materialversagen

DISSERTATION

Zur Erlangung des akademischen Grades eines
Doktor-Ingenieur (Dr.-Ing.)
an der Fakultät Bauingenieurwesen
der Bauhaus Universität Weimar

vorgelegt von
M.E., Budarapu Pattabhi Ramaiah
geboren am 01. Juni 1979
in Andhra Pradesh, Indien

Mentor:
Prof. Dr.-Ing. Timon Rabczuk

Weimar, Juni 2014

To my family ...

Acknowledgements

The process of carrying out this research and writing thesis has been a wonderful adventure and very exciting. Nevertheless, it has not been without its share of pain and I could not have achieved this work without the help, support and encouragement of many around me.

First of all my deepest gratitude goes to my supervisor, Prof. Dr.-Ing Timon Rabczuk, for introducing me to the exciting nano world. His commitment, guidance and encouragement throughout my research certainly helped me to groom as a quality researcher. The freedom given by him to think on my own, helped me to create lot of ideas and work independently. His great enthusiasm as a teacher is inspiring. His suggestions regarding my thesis work were always useful in building my career.

My first work started in collaboration with Prof. Robert Gracie, University of Waterloo, Canada. Innumerable skype discussions between us helped me to dig into the field of multi-scale methods. His suggestions and guidance is useful in thinking out of the box.

Furthermore, special thanks to Prof. Tom Lahmer and Prof. Marco Paggi for their comments during the review and the defense of my thesis.

During my research, I spent one year at the Dept. of Aerospace Engg., in collaboration with Prof. D. Roy Mahaptra, Indian Institute of Science (IISc), Bangalore, India. The research collaboration helped in applying my multiscale techniques to practical problems. Many thanks to him for the nice cooperation. The support extended by my colleagues at IISc, in particular Phani, Brahma, Ramakrishna and Mytri is appreciated.

I would also like to thank Prof. Stéphane Bordas, Prof. Goangseup Zi, Prof. Xiaoying Zhuang, Prof. Qian Dong and Dr. Cosmin Anitescu for their assistance in insightful suggestions and collaboration in research.

I am grateful to thank all my colleagues at the ISM, especially Daniel, Schwendler, Ingmar, Kai, Heiko, Torsten, Mike, Hossein, Silani, Navid, Ehsan, Mohammad, Sofyan, Zarina, Fatemeh, Ilyani, Nam, Nhon, Luu, Michael, Nantha, Junhua, Jin-Wu, Yancheng, Shih-Wei, Chao and Yue Jia, for their friendly support. I am thankful for the help from the secretaries Frau Terber and Frau Rosemarie. It was fantastic time with the Indian community in Weimar, particularly with Venkatesan and his family and the master's students Navneet, Abhilash, Harsha, Vipin and Jhansi. Thanks to all for making my life in Weimar memorable.

Finally, a precious thanks to my family especially to my parents and wife for their emotional support and encouragement during my studies. Simple thanks are not enough for my wife (Sivalakshmi), who was actively involved in taking care of my kids (Harini and Vishnu) while I was deeply involved in my research. You will be remembered forever.

Pattabhi Ramaiah Budarapu
Weimar, June 2014

Abstract

Defects like cracks and dislocations evolve at nano scales and influence the macroscopic properties such as strength, toughness and ductility of a material. Molecular dynamics simulations promise to reveal the fundamental mechanics of material failure. The computational expense of molecular dynamics simulations limits its application to engineering problems involving macroscopic cracks and shear bands, which occur at larger length and time scales. Therefore, multiscale methods have been developed bridging different time and length scales.

Many multiscale methods for fracture are developed for “fictitious” materials based on “simple” potentials such as the Lennard-Jones potential. Moreover, multiscale methods for evolving cracks are rare. Sufficient methods to coarse grain the fine scale defects are missing. However, the existing multiscale methods for fracture do not adaptively adjust the fine scale domain as the crack propagates. Most methods, therefore only “enlarge” the fine scale domain and therefore drastically increase computational cost. Adaptive adjustment requires the fine scale domain to be refined and coarsened. One of the major difficulties in multiscale methods for fracture is to up-scale fracture related material information from the fine scale to the coarse scale, in particular for complex crack problems. Most of the existing approaches therefore were applied to examples with comparatively few macroscopic cracks.

The presented thesis contributes to concurrent multiscale strategy for simulation of fracture. The bridging scale method is enhanced using the phantom node method so that cracks can be modeled at the coarse scale. To ensure self-consistency in the bulk, a virtual atom cluster is devised providing the response of the intact material at the coarse scale. A molecular statics model is employed in the fine scale where crack propagation is modeled by naturally breaking the bonds. The fine scale and coarse scale models are coupled by enforcing the displacement boundary conditions on the ghost atoms. An energy criterion is used to detect the crack tip location. Adaptive refinement and coarsening schemes are developed and implemented during the crack propagation. The results were observed to be in excellent agreement with the pure atomistic simulations. The developed multiscale method is one of the first adaptive multiscale method for fracture.

A robust and simple three dimensional coarse graining technique to convert a given atomistic region into an equivalent coarse region, in the context of multiscale fracture has been developed. The present method is the first of its kind. The developed coarse graining technique can be applied to identify and upscale the defects like: cracks, dislocations and shear bands. The current method has been applied to estimate the equivalent coarse scale models of several complex fracture patterns arrived from the pure atomistic simulations. The upscaled fracture pattern agree well with the actual fracture pattern. The error in the potential energy of the pure atomistic and the coarse grained model was observed to be acceptable.

A first novel meshless adaptive multiscale method for fracture has been developed. The phantom node method is replaced by a meshless differential reproducing kernel particle method. The differential reproducing kernel particle method is comparatively more expensive but allows for a more “natural” coupling between the two scales due to the meshless interpolation functions. The higher order continuity is also beneficial. The centro symmetry parameter is used to detect the crack tip location. The developed multiscale method is employed to study the complex crack propagation. Results based on the meshless adaptive multiscale method were observed to be in excellent agreement with the pure atomistic simulations.

The developed multiscale methods are applied to study the fracture in practical materials like Graphene and Graphene on Silicon surface. The bond stretching and the bond reorientation were observed to be the net mechanisms of the crack growth in Graphene. The influence of time step on the crack propagation was studied using two different time steps. Pure atomistic simulations of fracture in Graphene on Silicon surface are presented. Details of the three dimensional multiscale method to study the fracture in Graphene on Silicon surface are discussed.

Contents

Contents v

List of Figures ix

List of Tables xvii

1 Introduction 1

1.1 Overview of multiscale methods 2

1.2 Motivation 4

1.3 Objectives and the outline 4

2 An Adaptive Multiscale Method for quasi-static crack growth 7

2.1 The Adaptive Multiscale Method 8

2.1.1 Fine scale model 10

2.1.2 Coarse scale model 11

2.1.3 The Phantom node method 15

2.1.4 Coupling the coarse and fine scales 17

2.2 Adaptivity 18

2.2.1 Preliminaries 18

2.2.2 Detection of the crack tip 19

2.2.3 Adaptive refinement 19

2.2.4 Adaptive coarsening 21

2.3 Numerical Examples 22

2.3.1 Example 1: Edge crack simulations 24

2.3.2 Example 2: Edge crack propagation studies 25

2.3.3 Example 3: Kinked crack propagation 30

2.4 Discussion 33

3 Efficient Coarse Graining in Multiscale Modeling of Fracture 37

3.1 Coarse grained model 37
  3.1.1 Crack surface approximation 38
  3.1.2 Centro symmetry parameter 39
  3.1.3 Crack surface orientation 41
  3.1.4 Validation 43
3.2 Numerical examples 45
  3.2.1 Example 1: Angular crack propagation 45
  3.2.2 Example 2: Dynamic crack propagation in a double notched specimen 49
  3.2.3 Example 3: Crack branching and coalescence 56
  3.2.4 Example 4: Three dimensional crack growth 61
3.3 Discussion 61

4 A meshless adaptive multiscale method for fracture 63

4.1 Meshless Adaptive Multiscale Method for Fracture (MAMMF) 64
  4.1.1 Coarse scale model 65
  4.1.2 Fine scale model 69
  4.1.3 Coupling the coarse and fine scales 69
  4.1.4 Cracking criteria 70
4.2 Adaptivity 71
  4.2.1 Adaptive refinement 72
  4.2.2 Adaptive coarsening 73
4.3 Numerical examples 75
  4.3.1 Example 1: Angled edge crack propagation 75
  4.3.2 Example 2: Crack propagation in double-notched specimen 76
  4.3.3 Example 3: Mixed mode edge crack propagation 80
4.4 Discussion 81

5 Crack propagation in Graphene on Silicon surface 85

5.1 Introduction 85
5.2 Three dimensional Adaptive Multiscale Method 87
  5.2.1 Coarse scale model 87
5.3 Numerical examples 91
  5.3.1 Example 1: Crack propagation in the armchair Graphene with an initial edge crack 91

    5.3.2 Example 2: Crack propagation in zigzag Graphene with an initial edge crack . . . 103
    5.3.3 Example 3: Crack growth in Graphene on Silicon surface . . . 107
  5.4 Discussion . . . 108

6 Concluding remarks and future scope 113
  6.1 Conclusions . . . 113
  6.2 Future scope . . . 114

Appendix A Derivation of the internal forces: fine scale 115

Appendix B Bond potentials 117
  B.1 Lennard-Jones potential . . . 117
  B.2 Tersoff potential . . . 117
  B.3 First derivative of the Tersoff potential . . . 119

Appendix C Derivation of the internal forces: coarse scale 123

Appendix D Algorithms 125
  D.1 Energy based refinement algorithm . . . 125
  D.2 Energy based coarsening algorithm . . . 125
  D.3 CSP based refinement algorithm . . . 125
  D.4 CSP based coarsening algorithm . . . 125

List of Figures

1.1 Schematic of a (a) hierarchical, (b) semi-concurrent and (c) concurrent multiscale methods; reproduced from [98]. 2

2.1 (a) Multiscale partition of a cracked atomistic lattice. The solid circles represent the atoms from the cracked atomistic model. The coarse scale nodes are denoted by squares. (b) A zoom around the crack tip. 8

2.2 (a) Schematic diagram of a coupled continuum-atomistic model. (b) Coarse scale domain with the crack. (c) Fine scale region containing the crack tip. The crack in the coarse scale region is modeled using the VAC and the fine scale model is embedded at the crack tip. 9

2.3 Atomic arrangement in an fcc crystal; (a) in the unit cell (b) in the space lattice and (c) in the ABC layers. The atoms in the ABC layers when projected onto a two dimensional space; (d) and (e) onto the (111) plane and (f) onto the (100) plane. 12

2.4 A demonstration of VAC based coarse scale domain in two dimensions. (a) Atomistic model with triangular lattice as on the (111) plane of an fcc material. (b) Equivalent continuum model with the VAC being placed at a particular Gauss point. (c) Details of the VAC 12

2.5 The principle of the phantom node method where the hashed region is integrated to build the energy equation (2.11). (a) Crack opening and propagation after the phantom nodes are placed on the cracked elements. (b) Equivalence of a cracked element in the real domain to, two elements with phantom nodes. 16

2.6 Schematic of the AMM for two dimensional problems. (a) The coarse and fine scale discretization along with the ghost atoms and the coupling boundary. (b) A zoom around the coupling boundary. 17

2.7 Sketch of the adaptive refinement operation. (a) Flagged elements to be refined are hatched in red color. (b) Increased atomistic region after the refinement operation. 21

2.8 Sketch of the adaptive coarsening operation. (a) Flagged elements to be coarsened are hatched in red color. (b) Reduced atomistic region after the coarsening operation. 22

2.9 Flow chart indicating the computer implementation steps for solving the crack propagation problem in the MFC and AMM. 23

2.10 Schematic diagram of the edge crack model used in examples 1 and 2. A triangular displacement load is applied on the top and bottom boundaries. . . 24

2.11 Deformed configurations of the (a) MS (b) MFC (c) AMM after the final load step and (d) comparison of atom positions around the crack tip, from the MS, MFC and AMM. 26

2.12 (a) Comparison of the LJ potential energy from the MS, MFC and AMM for the atoms around the crack tip, see Fig. 2.11(d); after the final load step. The bottom picture shows the LJ potential energy in eV and the ratio $\frac{\text{PE}}{\text{PE0}}$ is plotted in the top picture. (b) A zoom around the crack tip. 27

2.13 Percentage errors in (a) displacement and (b) the potential energy, between the MS and AMM. 28

2.14 Atom positions at the end of the simulation, from the MS, MFC and AMM with ghost atoms in red color. The first row corresponds to deformed configurations of the MS, MFC and AMM at the end of the first load step. Figures (d–i) correspond to the deformed configuration at the end of the simulation. 29

2.15 Comparison of the atom positions around the crack tip from the MS, MFC and AMM. 30

2.16 (a) Comparison of the LJ potential energy from the MS, MFC and AMM for the atoms around the crack tip, see Fig. 2.15; after the final load step. The bottom picture shows the LJ potential energy in eV and the ratio $\frac{\text{PE}}{\text{PE0}}$ is plotted in the top picture. (b) A zoom around the crack tip. 31

2.17 Percentage errors in (a) displacement and (b) the potential energy, between the MS and AMM. 32

2.18 Change in average potential energy per atom with the load step. 32

2.19 Schematic of the cantilever beam with the pre-notch, considered for the third example. 33

2.20 Deformation plots of the MFC and AMM models with angular loading. (a) and (b) shows the initial configuration of the MFC and AMM models. (c) and (e) shows the deformed configuration of the AMM model after the 18th and 24th load steps. Atom positions around the crack tip, after the the 18th and 24th load steps from the MFC and AMM models are compared in figures (d) and (f), respectively. The percentage displacement errors for the atoms in (d) and (f) are shown in (g) and (h), respectively. 34

3.1 Schematic of mesh based equivalent coarse scale model. (a) Coarse mesh superimposed on the atomistic model (b) elements containing the atoms on the crack surface are highlighted along with the normals of the crack surface in each element (c) calculation of level sets and (d) approximation of crack surface by joining the crack path in the regions containing the crack. 39

3.2 Schematic of meshless equivalent coarse scale model. (a) Meshfree particles superimposed on the atomistic model (b) regions containing the atoms on the crack surface are highlighted along with the normals of the crack surface in each region (c) calculation of level sets and (d) approximation of crack surface by joining the crack path in the regions containing the crack. 40

3.3 Schematic of averaging the approximated individual crack surface orientation in each crack region, to generate a smooth continuous equivalent crack surface. 42

3.4 Schematic of domain and surface descriptions of a body in coarse region (a) displacements, tractions and the crack along with their surfaces (b) a closeup of the crack tip indicating the directions on the normals on the crack surfaces. 44

3.5 Schematic of fine scale model with initial crack used in example 1. 46

3.6 Development of a CG model of a given fine scale model, for a quasi-static crack propagation of an angular edge crack. (a) Initial configuration of the fine scale model. (b) Fine scale model at the 15th load step highlighting the ghost atoms and the atoms on the crack surface. (c) Fine scale model at the 15th load step, superimposed with the rectangular discretization. (d) Normals and neighbours of two particular atoms on the crack surface. (e) Normals of all the crack regions. (f) Rectangular discretization of the fine scale model at the 15th load step, highlighting the crack regions and their CoGs and normals. 47

3.7 Equivalent CG models, atoms on the crack surface and the approximated crack surface along with their normals. (a) Distribution of Gauss points on the CG model in (b), used to calculate the potential energy. (b) Equivalent CG model of the fine scale model in Fig. 3.6(b). Equivalent CG model of the fine scale model at the (c) 10th load step (d) 13th load step (e) 20th load step and (f) 25th load steps. 48

3.8 Schematic of double notched specimen used in example 2. 50

3.9 Development of an equivalent coarse scale model of a given fine scale model, for a dynamic crack propagation of double edge crack model. (a) Initial configuration of the fine model. Fine model at (b) 48 pico-seconds (c) 78 pico-seconds (d) 88 pico-seconds (e) 108 pico-seconds and (f) 180 pico-seconds, along with the highlighted atoms on the crack surface, crack regions and their normals. . 51

3.10 A closeup of the deformed configuration at 108 pico-seconds. (a) Upper right area of fine scale model in Fig. 3.9(e), displaying small cracks and dislocation cores. (b) Normals of two atoms on the crack surface on the crack surface along with their neighbours. (c) A closeup of Fig. 3.9(e) on the left half. (d) A closeup of Fig. 3.9(e) on the right half. 52

3.11 CG model with approximated equivalent crack surface at 48 pico-seconds. (a) Atoms on the crack surface along with the highlighted regions containing the atoms on the crack surface and the approximated equivalent crack. (b) Gauss point distribution used to calculate the system energy. 52

3.12 Approximated crack surface with different discretizations of (a) 7×5 (c) 14×8 and (d) 21×12 nodes, along the x and y directions, respectively. The corresponding approximated equivalent crack surfaces are shown in subplots (b), (d) and (f), respectively. 53

3.13 Approximated crack surface with different discretizations of (a) 28×16 nodes, along the x and y directions, respectively. (b) The corresponding approximated equivalent crack surface. 54

3.14 Atoms on the crack surface based on different values CSP (a) 1.5 (b) 2.0 (c) 2.5 (d) 3.1 (e) 3.25 and (f) 3.5. The number of atoms on the crack surface starts reducing the CSP values more than 2.0. 55

3.15 Equivalent CG model of the crack propagation through branching. (a) Deformed configuration of the fine model at the final load step, superimposed with CG model discretization of 12×9 nodes along the x and y directions, respectively. (b) Highlighted atoms on the crack surface, crack regions and their normals of the fine model in Fig. 3.15(a) (c) crack paths in each crack region (d) equivalent approximated crack surface. (e) Configuration in Fig. 3.15(a) discretized with 8×10 nodes in the x and y directions, respectively (f) equivalent approximated crack surface of Fig. 3.15(e). 57

3.16 Equivalent CG model of a 3D crack propagation with a discretization of 6×4×2. (a) Deformed configuration of the atomistic model at 18 pico-seconds. (b) Another view of Fig. 3.16(a) highlighting the atoms on the crack surface. (c) and (d) Two dimensional projection of Fig. 3.16(a). (e) Atoms on the crack surface and the normals of the crack regions in 3D. (f) Two dimensional projection of Fig. 3.16(e). 58

3.17 Equivalent CG model of a 3D crack propagation with a discretization of 6×4×2, showing crack surfaces and their normals. (a) Highlighted crack regions in 3D. (b), (c) and (d) The crack surfaces in each crack region and their normals in different views. 59

3.18 Equivalent CG model of a 3D crack propagation with a discretization of 6×4×3, showing crack surfaces and their normals. (a) The deformed configuration at 18 pico-seconds. (b) and (c) The crack surfaces in each crack region and their normals in different views. (d) Two dimensional projection of Fig. 3.18(a). 60

4.1 (a) Schematic of a coupled continuum-atomistic model. (b) Coarse scale domain with the crack. (c) Fine scale region containing the crack tip. 64

4.2 Shape functions in (a) the continuous domain and (b) the discontinuous domain. 66

4.3 (a) Schematic of a multiscale model with initial crack. Unfilled circles denote the nodes in the coarse scale and the filled circles are the fine scale atoms. (b) A closeup of the coupling region within the radius of influence and (c) a closeup of the coarse region within the domain of influence. 70

4.4 Sketch of the adaptive refinement operation. (a) Flagged particles to be refined are hashed. (b) Increased atomistic region after the refinement operation. . . 72

4.5 Schematic of the adaptive coarsening operation. (a) Flagged particles to be coarsened are hashed. (b) Reduced atomistic region after the coarsening operation. 74

4.6 Geometry of the initial angled edge crack specimen along with the prescribed displacements studied in example 1. 75

4.7 Development of the multiscale model, for the quasi-static propagation of an angled edge crack. Configuration of the atomistic model: (a) at the start of the simulation, (b) at the 16^{th} load step, as the crack in the fine scale model starts to open and propagate and (c) at the 42^{nd} load step, at the end of the simulation. Configuration of the multiscale model: (d) at the start of the simulation, (e) at the 16^{th} load step, crack after changing the direction of propagation and (f) at the end of the simulation. A closeup around the crack tip; (g) of the atomistic model in figure (c) and (h) of the multiscale model in figure (f). (i) Comparison of the positions of atoms around the crack tip in (g) and (h). 77

4.8 Initial nodes, atoms, crack orientation and the domain of influence of the multiscale model based on the DRKP method. 78

4.9 Geometry of the double-notched specimen with initial cracks and prescribed displacements studied in example 2. 78

4.10 Development of the multiscale model for quasi-static propagation of a double edge notched specimen. Configurations at the start of the simulation, at the 19th load step and the end of the simulation; of the MS and the coupled models are plotted in (a)-(c) and (d)-(f), respectively. A closeup around the crack tip; (g) of the atomistic model in figure (c) and (h) of the multiscale model in figure (f). (i) Comparison of the positions of atoms around the crack tip in (g) and (h). 79

4.11 Initial nodes, atoms, crack orientation and the domain of influence of the multiscale model based on the DRKP method. 80

4.12 Schematic of the specimen with edge crack in mixed mode propagation studied in example 3. 81

4.13 Development of the multiscale model for mixed mode propagation of a edge crack specimen. Configurations at the start of the simulation, at the 27th load step and at the 42nd load step of the MS model are plotted in (a)-(c), and the corresponding deformed configurations of the multiscale model are plotted in (d)-(f), respectively. A closeup (c) and (d) around the crack tip are plotted in (g) and (h), respectively. A comparison of the atom positions around the crack tip from the MS and the DRKP models are plotted in (i). 82

5.1 (a) Multiscale partition of a cracked atomistic lattice. The solid circles represent the atoms from the cracked atomistic model. The coarse scale nodes are denoted by squares. (b) A zoom around the crack tip. 88

5.2 Silicon unit lattice in (a) an isometric view and (b) front view, highlighting the quarter atoms. (c) The front view of the space lattice. 88

5.3 Silicon space lattice in (a) isometric view, (b) equivalent VAC based continuum model, showing the VAC placed at the Gauss points in the lowest left element. Due to the periodicity of the lattice structure (refer Fig. (5.2)), any single atom can be considered as VAC. (c) The considered single atom VAC (atom 1) along with its four nearest neighbors. 89

5.4 Lattice orientation of grahene in the (a) arm-chair and in the (b) zig-zag directions. 92

5.5 Schematic of the edge crack model used in examples 1 and 2. 93

5.6 Distribution of the (a) strain with time, (b) system potential energy with strain and (c) a closeup of (b) around the crack propagation zone. Variation of the (d) stress along the y direction with strain, (e) a closeup of (d) around the crack propagation zone and (f) distribution of the potential energy with time for the crack growth in the arm-chair Graphene. 94

5.7 Distribution of the stress per atom along the y direction in Graphene, with the lattice oriented in the arm-chair direction, at various times with Δt = 1 fs. The sub picture on the top shows a closeup around the crack tip and the sub picture on the bottom shows the location of the crack tip along with highlighting the atoms on the crack surface. 95

5.8 Distribution of the potential energy per atom on the atoms around the crack tip at various times, with the lattice oriented in the arm-chair direction and time step equal to 1 fs. 96

5.9 Variation of (a) the bond angle and (b) the bond length when the time step is equal to 1 fs and the lattice is oriented along the arm-chair direction. The corresponding atoms and the bonds around the crack tip actively involved in the bond stretching and the reorientation are shown in the sub-picture, highlighting the atom numbers shown in Fig. 5.8(a). Another sub-picture shows a closeup of the variation at the initiation of the crack propagation. Legends indicate the defined bond angles and the bond lengths in the atomic model. 97

5.10 Distribution of stress per atom along the y direction in Graphene, with the lattice oriented in the arm-chair direction, at various times with Δt = 0.1 fs. The sub picture on the top shows a closeup around the crack tip and the sub picture on the bottom shows the location of the crack tip along with highlighting the atoms on the crack surface. 99

5.11 Distribution of the potential energy per atom on the atoms around the crack tip at various times, with the lattice oriented in the arm-chair direction and time step equal to 0.1 fs. 101

5.12 Variation of (a) the bond angle and (b) the bond length when the time step is equal to 0.1 fs and the lattice is oriented along the arm-chair direction. The corresponding atoms and the bonds around the crack tip actively involved in the bond stretching and the reorientation are shown in the sub-picture, highlighting the atom numbers shown in Fig. 5.11(a). Another sub-picture shows a closeup of the variation at the initiation of the crack propagation. Legends indicate the defined bond angles and the bond lengths in the atomic model. 102

5.13 Distribution of the (a) strain with time, (b) potential energy with strain and (c) a closeup of (b) around the crack propagation zone. Variation of the (d) stress along the y direction with strain, (e) a closeup of (d) around the crack propagation zone and (f) distribution of the potential energy with time for the crack growth in zig-zag Graphene. 103

5.14 Figures (a)-(f): Distribution of stress per atom along the y direction in Graphene, with the lattice oriented along the zig-zag direction, with Δt = 1 fs. The sub picture on the top shows a closeup around the crack tip and the sub picture on the bottom shows the location of the crack tip along with highlighting the atoms on the crack surface. Figures (g)-(l): Distribution of the potential energy per atom on the atoms around the crack tip at various times, with the lattice oriented in the arm-chair direction and Δt = 1 fs. 104

5.15 Variation of (a) the bond angle and (b) the bond length when the time step is equal to 1 fs and the lattice is oriented along the zig-zag direction. The corresponding atoms and the bonds around the crack tip actively involved in the bond stretching and the reorientation are shown in the sub-picture, highlighting the atom numbers shown in Fig. 5.14(g). Another sub-picture shows a closeup of the variation at the initiation of the crack propagation. Legends indicate the defined bond angles and the bond lengths in the atomic model. 105

5.16 Figures (a)-(f): Distribution of stress per atom along the y direction in Graphene, with the lattice oriented along the zig-zag direction, with Δt = 0.1 fs. The sub picture on the top shows a closeup around the crack tip and the sub picture on the bottom shows the location of the crack tip along with highlighting the atoms on the crack surface. Figures (g)-(l): Distribution of the potential energy per atom on the atoms around the crack tip at various times, with the lattice oriented in the arm-chair direction and Δt = 0.1 fs. 106

5.17 Variation of (a) the bond angle and (b) the bond length when the time step is equal to 0.1 fs and the lattice is oriented along the zig-zag direction. The corresponding atoms and the bonds around the crack tip actively involved in the bond stretching and the reorientation are shown in the sub-picture, highlighting the atom numbers shown in Fig. 5.14(g). Another sub-picture shows a closeup of the variation at the initiation of the crack propagation. Legends indicate the defined bond angles and the bond lengths in the atomic model. 108

5.18 Variation of the crack speed with the location of the crack tip, when lattice is oriented along the (a) arm-chair direction, with time step equal to 1 fs, (b) arm-chair direction, with time step equal to 0.1 fs, (c) zig-zag direction, with time step equal to 1 fs and (d) zig-zag direction, with time step equal to 0.1 fs. 109

5.19 Crack propagation in (a) Graphene sheet, (b) Silicon. (c) Graphene on Silicon surface highlighting the bonds of the Silicon atoms connected to the Graphene atoms and (d) Crack propagation in the combined Graphene on Silicon surface. 110

5.20 Deformed configuration of the coarse model highlighting the initial and final positions of the nodes (a) in the front view and in an (b) an isometric view. . 111

List of Tables

2.1 Computational times of the MS model, MFC model and AMM in examples 1 and 2. 25

3.1 Range of centro symmetry parameter for various defects, normalized by square of the lattice parameter a_0^2. 41
3.2 Comparison of potential energies from Atomistic and CG models. 49
3.3 Comparison of potential energies from Atomistic and CG models. 56

4.1 Range of centro symmetry parameter for various defects, normalized by square of the lattice parameter a_0^2. 71
4.2 Computational times of the MS and the MAMMF models in examples 1, 2 and 3. 76

B.1 Parameters for Silicon and Carbon to be used in equation (B.2), adopted from [177]. $\mathcal{R}$ and $\mathcal{S}$ were not systematically optimized. 118

Chapter 1

Introduction

Understanding the microscopic processes behind material failure is critical for engineers and scientists developing new materials with higher strength and toughness, developing robust designs against failure, or for those concerned with an accurate estimate of a component's design life. Defects like cracks and dislocations evolve at nano scales and influence the macroscopic properties such as strength, toughness and ductility of a material. In engineering applications, the global response of the system is often governed by the behaviour at the smaller length scales. Hence, the subscale behaviour must be computed accurately for good predictions of the full scale behaviour. Molecular Dynamics (MD) simulations promise to reveal the fundamental mechanics of material failure by modeling the atom to atom interactions. Since the atomistic dimensions are of the order of Angstroms (Å), approximately 85 billion atoms are required to model a 1 μm^3 volume of Copper. Therefore, pure atomistic models are prohibitively expensive [1, 2] with everyday engineering computations involving macroscopic cracks and shear bands, which are much larger than the atomistic length and time scales.

To reduce the computational effort, multiscale methods are required, which are able to couple a continuum description of the structure with an atomistic description. In such paradigms, cracks and dislocations are explicitly modeled at the atomistic scale, whilst a self-consistent continuum model elsewhere. The coarse-scale model might be discretized with classical techniques like the finite element method (FEM), meshless methods (MM) [3–13] or partition-of-unity enriched methods such as the eXtended Finite Element Method (XFEM) [14–19], the Smooth Finite Element Method (SFEM) [20–22], the Generalized Finite Element Method (GFEM) [23–29], the Partition of Unity Finite Element Method (PUFEM) [30, 31], the eXtended Element Free Galerkin method (XEFG) [32–39], the Cracking Particles Method (CPM) [40–46], the Phantom Node Method (PNM) [47–53], the Numerical Manifold Method (NMM) [54, 55] or the isogeometric analysis with high-order approximation [56–62] of the exact geometry, to name a few. The fine scale and the coarse scale domains are coupled at the interface/handshake domain by enforcing the appropriate boundary conditions.

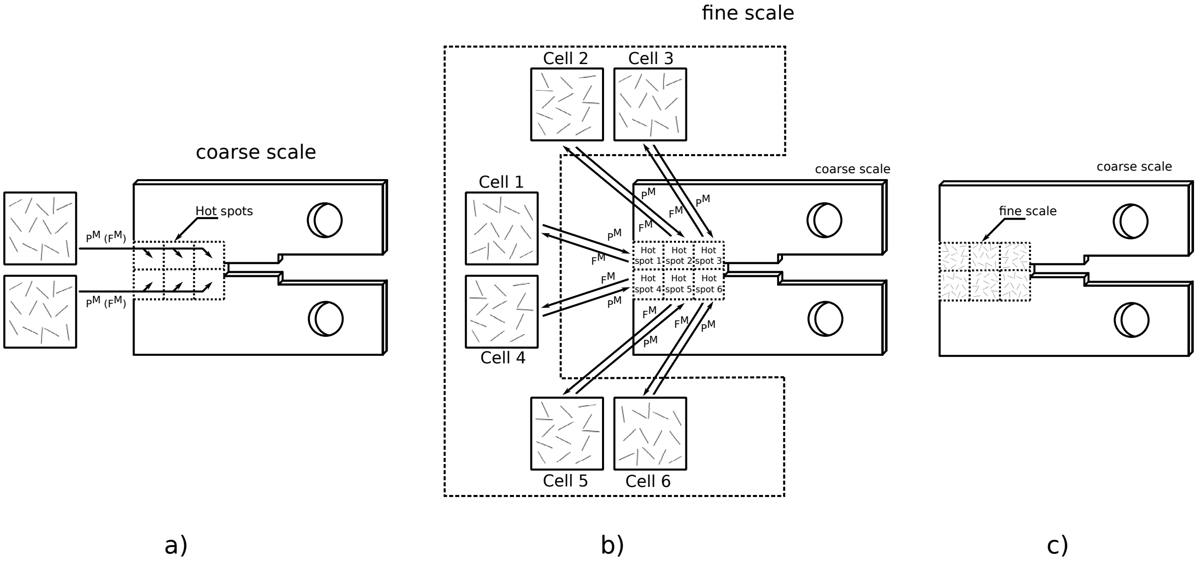

Figure 1.1: Schematic of a (a) hierarchical, (b) semi-concurrent and (c) concurrent multiscale methods; reproduced from [98].

1.1 Overview of multiscale methods

Multiscale methods can be categorized into hierarchical, semi-concurrent [63–66] and concurrent methods [67–95], as shown in Fig.1.1. In hierarchical multiscale methods, information is passed from the fine-scale to the coarse-scale; but not vice versa. Computational homogenization [96] is a classical up-scaling technique. Hierarchical multiscale approaches are very efficient. However, their extension to model fracture is complex, in particular for fracture and materials involving strain softening. One basic assumption for the application of homogenization theories is the existence of disparate length scales [97]: $\mathcal{L}_{Cr} \ll \mathcal{L}_{RVE} \ll \mathcal{L}_{Spec}$ where $\mathcal{L}_{Cr}$, $\mathcal{L}_{RVE}$ and $\mathcal{L}_{Spec}$ are the crack length, the representative volume element (RVE) and specimen-size, respectively. For problems involving fracture, the first condition is violated as $\mathcal{L}_{Cr}$ is of the order of $\mathcal{L}_{RVE}$. Moreover, periodic boundary conditions (PBC) often used at the fine scale, cannot be used when a crack touches a boundary as the displacement jump in that boundary violates the PBC. In semi-concurrent multiscale methods, information is passed from the fine-scale to the coarse-scale and vice versa. The basic idea of semi-concurrent multiscale methods is illustrated in Figure 1.1(b). Concurrent multiscale methods (refer to Fig.1.1(c)) can be classified into 'Interface' coupling methods and 'Handshake' coupling methods. Interface coupling methods seem to be less effective for dynamic applications as avoiding spurious wave reflections at the 'artificial' interface seem to be more problematic.

Numerous multiscale methods coupling the atomistic domain with continuum domain have been proposed, that include: quasi-continuum method (QCM) [78], discrete-to-continuum bridging [99, 100], the discontinuous enrichment method [101], bridging scale method (BSM) [69, 71, 73], bridging domain method (BDM) [67, 83], coupled atomistic discrete dislocation (CADD) [86–89], coarse grained molecular dynamics (CGMD) [90, 91], macroscopic atomistic

Ab initio dynamics (MAAD) [82, 92–95], to name a few. In the QCM, the continuum degrees of freedom need to be located at the positions of the atoms at the interface. Hence to match with the atomistic dimensions, a very fine grading of the continuum mesh is required around defects. Note that the QCM has also been very successful at linking two continuum scales, for example, for fibrous materials in [102] and is readily capable of including quantum effects through density functional theory (QCDFT) [103]. A classical semi-concurrent multiscale method is the FE^2 [63–66] originally developed for intact materials. Kouznetsova *et al.* [104] extended this method to problems involving material failure, see also Kouznetsova *et al.* [96] or recent contribution by Nguyen *et al.* [105], Verhoosel *et al.* [106] and Belytschko *et al.* [107]. Some of the multiscale methods have been extended to fracture [83–85, 99, 108, 108–110].

Belytschko *et al.* [107] have proposed the bridging domain method (BDM) which is based on a domain decomposition technique. The MD subdomain overlaps the original finite element (FE) mesh, similar to the Arlequin method [80, 81, 111]. The BDM relies upon a linear energy weighting in the bridging domain. Therefore, the continuum region is not required to be refined at the bridging domain. Compatibility of the displacement field between the continuum domain and the atomistic domain, in the bridging domain, is enforced by Lagrange multipliers. An advantage of the BDM is that the nodes on the "continuum-atomistic" region need not coincide with the atoms. Guidault *et al.* [68, 99, 100] enhanced the BDM by also enforcing the strain compatibility between the "atomistic" and the continuum in the bridging domain. Such a coupling can be useful for the development of error estimators to drive the adaptive refinement of the coarse scale. The method was extended to dynamic problems by Xiao *et al.* [67]. Xu *et al.* [112, 113] have addressed the difficulties of attenuating the spurious wave reflection at the interfaces and extended the BDM for composite lattices [114].

Gracie *et al.* [83, 84] have extended the bridging domain method (XBDM) to effectively account for dislocations and cracks. The XFEM was used to model the crack surfaces and slip planes in the continuum. A close agreement of the energies and energy distributions of the bridging domain model with the direct numerical solutions are reported. Aubertin *et al.* [108, 115] have proposed an XFEM based multiscale model for dynamic fracture. Talebi *et al.* [76] have extended the XBDM for three dimensional dynamic crack growth problems. A computational library for multiscale modeling of material failure was proposed in [75]. Shilkrot *et al.*, [86–89] have developed a multiscale method to automatically detect the dislocations as they move from the atomistic region to the continuum region and convert them into discrete dislocations in the coarse region and vice-versa.

Liu *et al.* [69–73] have developed the bridging scale method (BSM) based on the projection of the MD solution onto the coarse scale shape functions. BSM effectively addresses the spurious wave reflections in dynamic settings. In the bridging scale method, the continuum representation exists everywhere in the domain, including those areas in which MD is present. The projection operator helps to decompose the displacement field into orthogonal coarse and fine scales, resulting in a coupled but separate set of equations of motion describing the evolution of the MD and FE systems. These coupled equations of motion have three major benefits. Firstly, unlike the finite element method (FEM), MD equations of motion are not required to be integrated using the same time step. Hence, the coarse scale and fine scale problems can be solved separately. Secondly, it is possible to eliminate the unwanted MD degrees of freedom by accounting for them in the form of an impedance force which augments the standard MD equations of motion. Since the unwanted MD degrees of freedom are accounted for in a consistent manner, high-frequency waves which cannot be represented by the continuum mesh are dissipated naturally out of the MD region. Lastly, unlike the QCM, the bridging scale is valid for finite temperature dynamic problems. Therefore, BSM is a very efficient technique to model fracture.

1.2 Motivation

Many of the developed multiscale methods for fracture are applied for “fictitious” materials based on “simple” potentials such as the Lennard-Jones potential. Moreover, multiscale methods for evolving cracks are rare. Adaptive multiscale methods have been significantly improved after the works of Abraham *et al.* [82], Broughton *et al.* [92], Shenoy *et al.* [116] and Shan *et al.* [117]. Recently Gracie *et al.* [84] and Moseley *et al.* [118] have developed adaptive multiscale methods based on the XBDM. However, sufficient methods to coarse grain the fine scale defects are missing. Most methods, therefore only “enlarge” the fine scale domain and therefore drastically increase computational cost. Therefore, computationally efficient adaptive multiscale methods for fracture are very much required, where the fine scale domain needs to be adjusted by adaptive refinement *and* coarsening approaches as the crack propagates.

Lack of efficient coarse-graining techniques to convert the atomistic domain back to continuum will continuously increase computational costs. Additionally, the necessary modifications to the FE mesh are substantial, adding complexity and cost. Therefore, it is required to develop efficient coarse graining techniques to convert a given atomistic region into an equivalent coarse region. Finally, multiscale methods for fracture in “realistic” materials are in demand.

1.3 Objectives and the outline

The principal goal is to develop computationally efficient adaptive multiscale methods for fracture, where the crack tip is captured in the fine scale domain and the domain elsewhere is modeled by continuum. The fine scale domain needs to be adjusted by adaptive refinement *and* coarsening approaches as the crack propagates.

To achieve the objective, two different multiscale methods for fracture are developed. During the course of the work, it was realized that many substantially different problems have to be solved in order to approach the global goal. Therefore, the associated objectives along with the outline of presentation can be listed as follows:

1. Develop an adaptive multiscale method (AMM) for fracture by enhancing the BSM using the phantom node method so that cracks can be modeled at the coarse scale. To ensure self-consistency in the bulk, a virtual atom cluster (VAC) is devised providing the response of the intact material at the coarse scale. Details of the developed AMM [74] are explained in chapter 2. The material models of the coarse scale and fine scale domains are explained in section 2.1. Section 2.2 is dedicated to the algorithms of adaptive refinement and coarsening. The AMM is verified through three numerical examples in section 2.3.

2. Develop efficient coarse graining (CG) techniques to convert a given atomistic region into an equivalent coarse region. Details of the developed CG model [119] are presented in chapter 3. The coarse grained model is proposed in section 3.1. The developed coarse graining technique is validated through four numerical examples in Section 3.2.

3. Develop a meshless adaptive multiscale method for fracture (MAMMF) where the coarse scale domain is modeled based on a meshless method. The proposed MAMMF [77] is explained in chapter 4. Section 4.1 is dedicated to the mathematical modeling of coarse and fine scale domains. Details of the adaptive refinement and coarsening algorithms are explained in section 4.2. Section 4.3 is devoted to verify the developed MAMMF through three numerical example.

4. Finally, the presented approach should be applied to “realistic” materials. Therefore, crack growth in Graphene and Graphene on Silicon surface are considered. The fracture in 2D Graphene sheet is presented in chapter 5. The importance of simulation of fracture in Grahene is introduced in section 5.1. The developed multiscale methods in chapters 2 and 4 can further be extended to model fracture in Graphene on Silicon surface. Details of the mathematical modeling of the three dimensional multiscale method for fracture in Graphene on Silicon surface are discussed in section 5.2. Crack propagation in Graphene is studied through two numerical examples in Section 5.3. In the third example in section 5.3, the atomistic model of Graphene on Silicon surface and the coarse scale model of the Silicon are discussed.

5. Chapter 6 concludes the thesis mentioning the scope for the future.

Chapter 2

An Adaptive Multiscale Method for quasi-static crack growth

In this chapter[1], an adaptive multiscale method has been developed for quasi-static crack growth. A molecular statics (MS) model is employed in the fine scale where crack propagation is modeled by naturally breaking the bonds. To ensure self-consistency in the bulk, a virtual atom cluster is used to model the material of the coarse scale. Crack in the coarse scale domain is modeled based on the phantom node method. The coupling between the coarse scale and fine scale is realized through ghost atoms, based on the principles of the BSM. The ghost atom positions are interpolated from the coarse scale solution and enforced as boundary conditions on the fine scale. The fine scale region is adaptively refined and coarsened as the crack propagates. An energy criterion is used to detect the crack tip location. The triangular lattice in the fine scale region corresponds to the lattice structure of the (111) plane of an FCC crystal. The Lennard-Jones (LJ) potential is used to model the atom-atom interactions. The method is implemented in two dimensions. The results are compared to pure atomistic simulations; they show excellent agreement.

The virtual atom cluster [120, 121] is based on the symmetry in atomic arrangement in a periodic crystal lattice. In a periodic crystal every atom possess similar neighbours. Therefore, an atom surrounded by its neighbours can be considered as a representative atom cluster of the crystal lattice. As a result, the representative atom cluster can be used in all the calculations. Hence, a coarse scale equivalent to the fine scale can be developed using the VAC, by equating the energies of the fine scale and the coarse scale domains. Further details of the methodology are discussed in section 2.1.2. The VAC based continuum does not involve a stress update scheme employing the Cauchy-Born hypothesis, since there is no continuum measure in the VAC. Qian et al. [120] studied the carbon nanotubes based on the VAC. Yang et al. [122] extended the method to dynamic crack propagation.

---

[1] This work has been published in the Computational Mechanics journal [74].

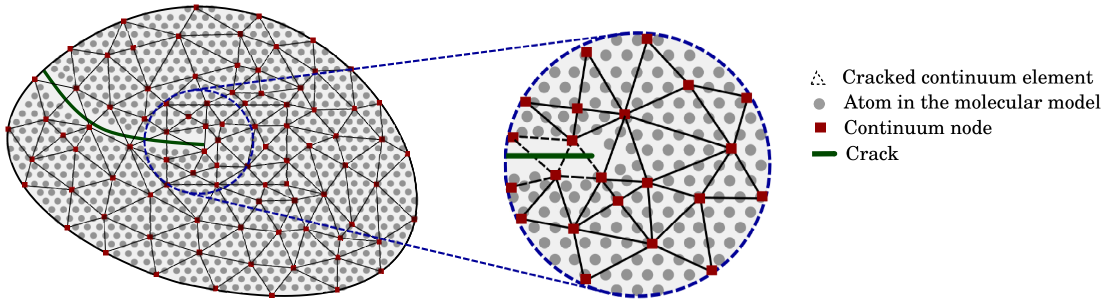

(a) (b)

Figure 2.1: (a) Multiscale partition of a cracked atomistic lattice. The solid circles represent the atoms from the cracked atomistic model. The coarse scale nodes are denoted by squares. (b) A zoom around the crack tip.

2.1 The Adaptive Multiscale Method

Consider a multiscale model with an initial crack and a discretized coarse region shown in Fig. 2.1(a). The solid circles represent the atoms from the cracked atomistic model. The shaded area corresponds to the coarse scale approximation. The squares denote the nodes of the phantom node discretization. A close up of the crack tip is shown in Fig. 2.1(b). The elements with edges in dotted lines denote the split elements and the edges of the normal elements are shown in solid lines. The AMM consisting of the coarse and fine scale regions along with the crack is shown in Fig. 2.2(a). The coarse scale model with the crack is shown in Fig. 2.2(b), the fine scale model is shown in Fig. 2.2(c). The material behaviour at the crack tip is expected to be highly non-linear and/or non-homogeneous, and away from the tip it is expected to be homogeneous.

The atoms on the crack surface are defined as the atoms on the 'surface' of the crack or at the "crack tip". The initial crack in the fine scale region is created by removing the bonds between the atoms on the crack surface and updating the neighbor list accordingly. The neighbour list is generated based on a radius of influence. Nodal displacements in the coarse scale region are estimated based on the VAC. The phantom node method [40, 50], explained in section 2.1.3, is used to model the crack surfaces in the coarse scale region. Ghost atoms are located in the coarse region but within the cutoff radius of the atoms in the fine region. Their positions are interpolated from the coarse scale solution and enforced as the boundary conditions for the fine scale solution. The crack originates from the coarse scale region with the crack tip in the fine region. The fine scale region is adaptively enlarged as the crack propagates and the model behind the crack tip is coarsened to reduce the size of the fine scale model [74, 84, 119]. The energy criterion [74, 84] as explained in 2.2.2, is used to identify the atoms on the crack surface and hence the location of the crack tip.

In the two scale model, the total displacement field $\mathbf{u}_\alpha$ of an atom α is decomposed into

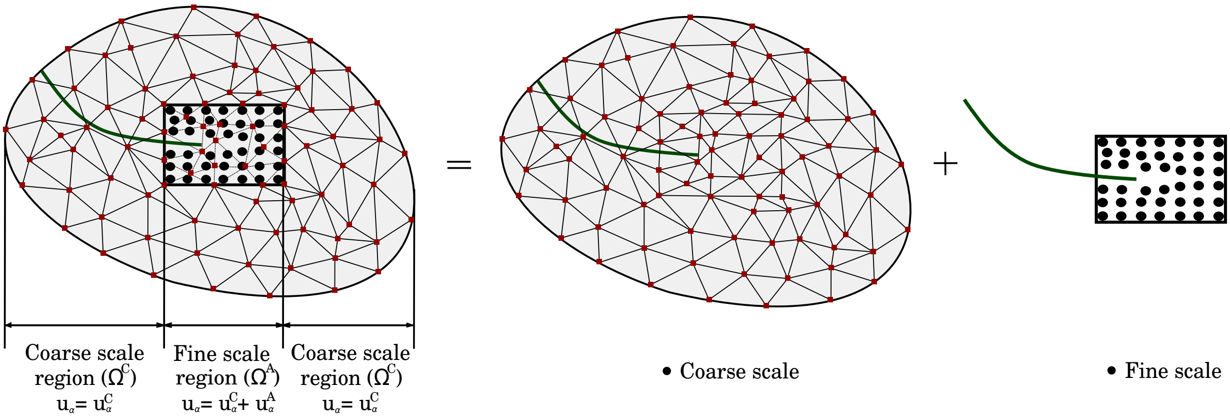
Coarse scale region (Ω^C) $u_\alpha = u_\alpha^C$
Fine scale region (Ω^A) $u_\alpha = u_\alpha^C + u_\alpha^A$
Coarse scale region (Ω^C) $u_\alpha = u_\alpha^C$
=
+
• Coarse scale
• Fine scale

(a) (b) (c)

Figure 2.2: (a) Schematic diagram of a coupled continuum-atomistic model. (b) Coarse scale domain with the crack. (c) Fine scale region containing the crack tip. The crack in the coarse scale region is modeled using the VAC and the fine scale model is embedded at the crack tip.

coarse and fine scale components:

$$\mathbf{u}_\alpha = \mathbf{u}_\alpha^{\mathrm{C}} + \mathbf{u}_\alpha^{\mathrm{A}} \tag{2.1}$$

where $\mathbf{u}_\alpha^{\mathrm{C}}$ is the coarse scale component and $\mathbf{u}_\alpha^{\mathrm{A}}$ is the fine scale component, whose projection onto the coarse scale is zero. The fine scale component $\mathbf{u}_\alpha^{\mathrm{A}}$, is the difference between the actual position of an atom α and the interpolated position of the coarse scale. In other words, $\mathbf{u}_\alpha^{\mathrm{A}}$ is insignificant in the regions far away from the crack tip, and hence, $\mathbf{u}_\alpha^{\mathrm{C}}$ is sufficient to model the deformation in the coarse scale region. On the other hand, in the fine scale region, both coarse and fine scale components are required. Let the coarse scale displacement $\mathbf{u}_\alpha^{\mathrm{C}}$ of an atom α be represented by a set of FEM basis functions defined over a set of n^{C} nodal points,

$$\mathbf{u}_\alpha^{\mathrm{C}} = \sum_{I=1}^{n^{\mathrm{C}}} N_I(\mathbf{X}_\alpha)\mathbf{u}_I^{\mathrm{C}} \tag{2.2}$$

where $N_I(\mathbf{X}_\alpha)$ is the shape function defined at node I, estimated at the α^{th} atom with the material coordinate $\mathbf{X}_\alpha$, and $\mathbf{u}_I^{\mathrm{C}}$ is the continuum displacement vector at node I.

The notation adopted is as follows: Greek indices refer to atoms and capital subscripts (such as I, J, K) will refer to the computational nodes. Quantities in the reference configuration are denoted by the same symbol but with a naught. For example, the reference configurations of the coarse scale domain Ω^{C} and the fine scale domain Ω^{A} are denoted by Ω_0^{C} and Ω_0^{A}, respectively. n^{C} are the total number of nodes in the coarse scale region Ω^{C}; the number of atoms in the fine scale region Ω^{A} is given by n^{A} and the number of ghost atoms by n^{Gh}. Ghost atoms are located in the coarse scale region Ω^{C} that are within the cut off radius of the atoms in Ω^{A}. The total number of Gauss points in the coarse scale region is given by n^{G}. The material coordinates of a point in Ω_0^{C} are denoted by $\mathbf{X}$ and the spatial coordinates by $\mathbf{x}$. The motion is defined as $\mathbf{x} = \phi(\mathbf{X})$ with $\mathbf{u}(\mathbf{x}) = \phi(\mathbf{X}) - \mathbf{X} = \mathbf{x} - \mathbf{X}$. The position vector of an atom in Ω^{A} is given by $\mathbf{r}$.

2.1.1 Fine scale model

The objective of the atomistic simulations is to determine the positions of the atoms for the given boundary conditions, either by minimizing the system potential energy in the molecular statics (MS) or based on the Lagrangian principles in the molecular dynamics. The system potential energy of the atomistic model is given by

$$\Pi = W^{\mathrm{int}} - W^{\mathrm{ext}} \tag{2.3}$$

where W^{int} represents the internal energy of the system and W^{ext} is the external work done on the system. Consider the simplest atom-atom interactions in which the potential energy is only a function of the distance between two atoms, the total internal energy of the system is given by summing the energies of all the atomic bonds over all the atoms, as given below:

$$W^{\mathrm{int}} = \frac{1}{2} \sum_{\alpha=1}^{n^{\mathrm{A}}} \sum_{\beta \neq \alpha}^{n^{\mathrm{A}}} V(r_{\alpha\beta}) \tag{2.4}$$

where $V(r_{\alpha\beta})$ is the bond potential between the atoms α and β, separated by distance $r_{\alpha\beta}$. The system potential energy will be minimum, when the first derivative of the potential function with respect to the positions of the atoms goes to zero. Therefore, for any given atom λ, the first derivative of the system potential energy with respect to the position vector $\mathbf{r}_\lambda$ is

$$\frac{\partial\left(\frac{1}{2}\sum_{\alpha=1}^{n^{\mathrm{A}}}\sum_{\beta\neq\alpha}^{n^{\mathrm{A}}} V(r_{\alpha\beta})\right)}{\partial \mathbf{r}_\lambda} - \frac{\partial W^{\mathrm{ext}}}{\partial \mathbf{r}_\lambda} = 0 \tag{2.5}$$

where the internal forces acting on atom λ are given by

$$\mathbf{F}_\lambda^{\mathrm{int}} = \frac{1}{2} \sum_{\alpha=1}^{n^{\mathrm{A}}} \sum_{\beta \neq \lambda}^{n^{\mathrm{A}}} - \frac{\partial V(r_{\alpha\beta})}{\partial r_{\alpha\beta}} \frac{\partial r_{\alpha\beta}}{\partial \mathbf{r}_\lambda} \tag{2.6}$$

and the external forces acting on atom λ are

$$\mathbf{F}_\lambda^{\mathrm{ext}} = -\frac{\partial W^{\mathrm{ext}}}{\partial \mathbf{r}_\lambda}. \tag{2.7}$$

The residual forces on each atom is

$$\mathbf{R} = \mathbf{F}^{\mathrm{int}} - \mathbf{F}^{\mathrm{ext}}. \tag{2.8}$$

The distance $r_{\alpha\beta}$ in (2.6) is defined as

$$r_{\alpha\beta} = |\mathbf{r}_\alpha - \mathbf{r}_\beta| = \sqrt{\sum_{j=1}^{3} (r_{\alpha j} - r_{\beta j})^2}. \tag{2.9}$$

where j is the free index. Substituting equation (2.9) into equation (2.6) yields

$$\mathbf{F}_\alpha^{\text{int}} = -\sum_{\beta \neq \alpha}^{n^{\text{A}}} \frac{\partial V(r_{\alpha\beta})}{\partial r_{\alpha\beta}} \left(\frac{\mathbf{r}_\alpha - \mathbf{r}_\beta}{r_{\alpha\beta}} \right). \tag{2.10}$$

The details of derivation of equation 2.10 are given in appendix A. The Lennard-Jones potential function is mentioned in section B.1. In the present work, the energy minimization is carried out using the conjugate gradient method and so a tangent stiffness matrix is not required.

2.1.2 Coarse scale model

Consider a periodic face centered cubic (fcc) crystal structure, which can be described in terms of a unit cell, as shown in Fig. 2.3. The unit cell of an fcc crystal is shown in Fig. 2.3(a). The space lattice of the fcc crystal can be obtained by stacking the unit cells in three dimensional space, as shown in Fig. 2.3(b). The resulting crystal structure when stacked in ABC layers, using the atoms in the close packed directions, as shown in Fig. 2.3(c), possess symmetry in three dimensions. The two dimensional projection of the atomic arrangement in ABC layers is shown in Fig. 2.3(d). The geometric parameters of the fcc crystal lattice are expressed using the lattice constant a, with reference to the atoms on the (111) and (100) planes, as shown in Fig. 2.3(e) and Fig. 2.3(f), respectively. Because of the symmetry of the crystal structure, a cluster of atoms can be taken as a representative model of the whole lattice structure [120]. As a result, all the calculations can be performed with reference to the cluster, which improves the computational efficiency. Since the locations of atoms in the cluster do not represent the exact locations of the atoms, it is called a virtual atom cluster. The same inter atomic potential as in the full scale MS model is used in the VAC. The VAC for fcc lattice structure is shown in Fig. 2.4.

The coarse scale displacement $\mathbf{u}_\alpha^{\text{C}}$ of an atom α in the VAC can be estimated using equation (2.2). The total potential energy of a fine scale system is given by the sum of all bond potentials ϕ_α (refer to equation (2.12)). Consider an equivalent coarse scale model based on the VAC, illustrated in Fig. 2.4. Since the fine scale and coarse scale models are equivalent, their potential energy must be equal. Hence, ϕ_ρ is defined as the distributed energy density function from the VAC. The discrete summation of the potential energy defined in the original

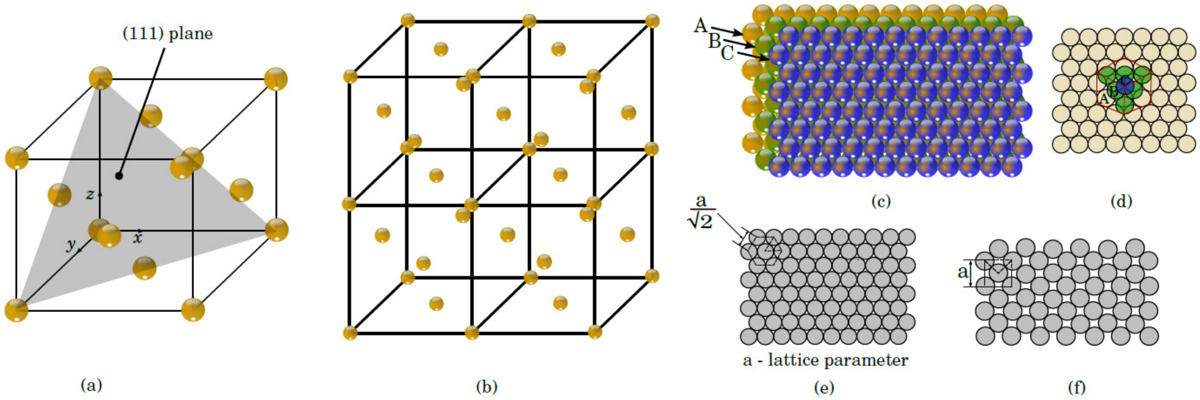
(111) plane
z
y
x
A
B
C
a
√2
a - lattice parameter
a

(a) (b) (c) (d) (e) (f)

Figure 2.3: Atomic arrangement in an fcc crystal; (a) in the unit cell (b) in the space lattice and (c) in the ABC layers. The atoms in the ABC layers when projected onto a two dimensional space; (d) and (e) onto the (111) plane and (f) onto the (100) plane.

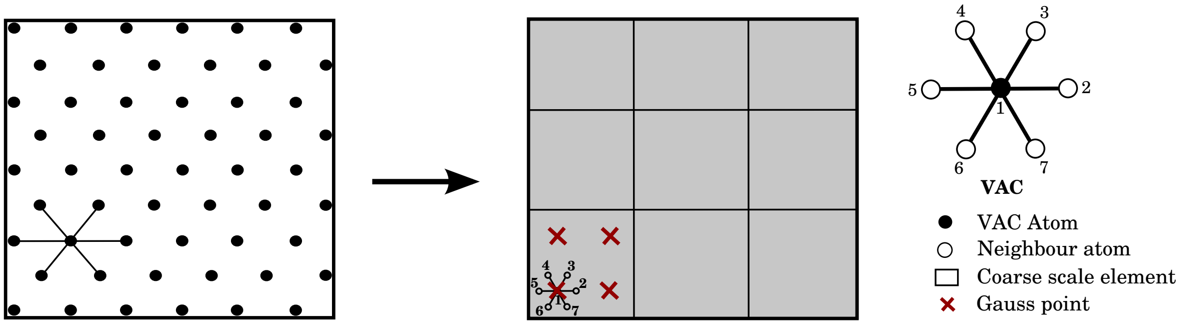
4
3
5
2
1
6
7
VAC
● VAC Atom
○ Neighbour atom
□ Coarse scale element
× Gauss point

(a) (b) (c)

Figure 2.4: A demonstration of VAC based coarse scale domain in two dimensions. (a) Atomistic model with triangular lattice as on the (111) plane of an fcc material. (b) Equivalent continuum model with the VAC being placed at a particular Gauss point. (c) Details of the VAC

molecular structure, can now be replaced with an integral based on the VAC, i.e.

$$W^{\text{int}} = \sum_{\alpha=1}^{n^{\text{A}}} \phi_\alpha = \int_{\Omega_0} \phi_\rho d\Omega_0 \approx \sum_G w_{\text{G}} \phi_\rho^{\text{G}} \tag{2.11}$$

where ϕ_α is the potential energy associated with atom α, as defined below

$$\phi_\alpha = \frac{1}{2} \sum_{\beta \neq \alpha}^{n^{\text{A}}} V(r_{\alpha\beta}). \tag{2.12}$$

Due to the periodic nature of the lattice, ϕ_ρ can be defined as the potential energy of a VAC divided by the volume of the VAC. For a homogeneous lattice, as considered in this chapter, each VAC consists of a single atom and its volume is that of the unit cell of the lattice. The volume of the VAC for a triangular lattice is $\text{V}_0 = \frac{\sqrt{3}}{2}a^2$. When only nearest neighbour interactions are considered, each atom in the triangular lattice interacts with six neighbouring atoms, as shown in Fig. 2.4(a). The energy attributed to a central atom involves summing the contributions from each bond with neighbouring atoms. The energy of the central atom is the energy of the VAC. The number of neighbours that the central atom has does not influence the volume/area attributed to the atom and therefore does not effect the volume/area attributed to the VAC. In other words, the volume/area of the VAC do not increase if more neighbours are considered in the computation of the potential energy of the central atom. Using the numbering scheme shown in Fig. 2.4(c), the potential energy of the VAC is given by

$$\phi_{\text{VAC}} = \frac{1}{2} \sum_{\beta=2}^{7} V(r_{1\beta}). \tag{2.13}$$

Therefore, the distributed energy density function ϕ_ρ can be defined as

$$\phi_\rho = \frac{\phi_{\text{VAC}}}{\text{V}_0} = \frac{1}{2} \sum_{\beta=2}^{7} \frac{V(r_{1\beta})}{\sqrt{3}a^2/2} = \frac{1}{2} \sum_{\beta=2}^{7} \phi_{1\beta} \tag{2.14}$$

where

$$\phi_{1\beta} = \frac{V(r_{1\beta})}{\sqrt{3}a^2/2}. \tag{2.15}$$

Therefore, the energy density function ϕ_ρ becomes

$$\phi_\rho = \frac{1}{2}(\phi_{12} + \phi_{13} + \phi_{14} + \phi_{15} + \phi_{16} + \phi_{17}). \tag{2.16}$$

in which $\phi_{1\beta}$ are the bonding energy densities. w_{G} denote the quadrature weight and ϕ_ρ^{G} is the corresponding energy density function evaluated at a quadrature point. The internal forces on node 'I' in the coarse scale region, can be estimated by taking the derivative of equation (2.11) with respect to the nodal displacements $\mathbf{u}_I^{\mathrm{C}}$

$$\mathbf{F}_I^{\mathrm{int}} = -\frac{\partial W^{\mathrm{int}}}{\partial \mathbf{u}_I^{\mathrm{C}}} = \int_{\Omega_0} -\frac{\partial \phi_\rho}{\partial \mathbf{u}_I^{\mathrm{C}}} d\Omega_0 = \int_{\Omega_0} -\frac{\partial \phi_\rho}{\partial \mathbf{u}}\frac{\partial \mathbf{u}}{\partial \mathbf{u}_I^{\mathrm{C}}} d\Omega_0 \approx -\sum_{\mathrm{G}} w_{\mathrm{G}} \frac{\partial \phi_\rho^{\mathrm{G}}}{\partial \mathbf{u}}\frac{\partial \mathbf{u}}{\partial \mathbf{u}_I^{\mathrm{C}}}. \tag{2.17}$$

Therefore, the internal forces are calculated from the potential energy density of the VAC, which is placed at each Gauss point. As shown in Fig. 2.4(c), there are 7 atoms including the central VAC atom and its neighbours. Therefore, the energy density function $\phi_\rho^{\mathrm{G}} = \phi_\rho^{\mathrm{G}}(\mathbf{r}_1, \mathbf{r}_2, \mathbf{r}_3, \mathbf{r}_4, \mathbf{r}_5, \mathbf{r}_6, \mathbf{r}_7)$. Since the VAC is used in the coarse scale equation which assumes $\mathbf{u}_\alpha = \mathbf{u}_\alpha^{\mathrm{C}}$, for $\alpha = 1$–7. Therefore,

$$\mathbf{F}_I^{\mathrm{int}} \approx -\sum_{\mathrm{G}} w_{\mathrm{G}} \frac{\partial \phi_\rho^{\mathrm{G}}}{\partial \mathbf{u}}\frac{\partial \mathbf{u}}{\partial \mathbf{u}_I^{\mathrm{C}}} \approx -\sum_{\mathrm{G}} w_{\mathrm{G}} \sum_{\alpha=1}^{7} \frac{\partial \phi_\rho^{\mathrm{G}}}{\partial \mathbf{u}_\alpha^{\mathrm{C}}}\frac{\partial \mathbf{u}_\alpha^{\mathrm{C}}}{\partial \mathbf{u}_I^{\mathrm{C}}}. \tag{2.18}$$

Using the definition of $\mathbf{u}_\alpha^{\mathrm{C}}$ from equation (2.2), the second term on the right hand side of equation (2.18) can be reduced to

$$\frac{\partial \mathbf{u}_\alpha^{\mathrm{C}}}{\partial \mathbf{u}_I^{\mathrm{C}}} = N_I(\mathbf{X}_\alpha). \tag{2.19}$$

Therefore, after substituting equation (2.19) into equation (2.18), the nodal internal forces in the coarse scale domain are given by

$$\mathbf{F}_I^{\mathrm{int}} = -\sum_{\mathrm{G}=1}^{n^{\mathrm{G}}} w_{\mathrm{G}} \sum_{\alpha=1}^{7} \frac{\partial \phi_\rho^{\mathrm{G}}}{\partial \mathbf{u}_\alpha^{\mathrm{C}}} N_I(\mathbf{X}_\alpha). \tag{2.20}$$

The term $\frac{\partial \phi_\rho}{\partial \mathbf{u}_\alpha^{\mathrm{C}}}$ in equation (2.20) can be evaluated for each α as given below:
$\alpha = 1$

$$\begin{aligned} \frac{\partial \phi_\rho}{\partial u_{1i}^{\mathrm{C}}} = & \frac{\partial \phi_{12}}{\partial r_{12}}\frac{r_{12i}}{r_{12}} + \frac{\partial \phi_{13}}{\partial r_{13}}\frac{r_{13i}}{r_{13}} + \frac{\partial \phi_{14}}{\partial r_{14}}\frac{r_{14i}}{r_{14}} \\ & + \frac{\partial \phi_{15}}{\partial r_{15}}\frac{r_{15i}}{r_{15}} + \frac{\partial \phi_{16}}{\partial r_{16}}\frac{r_{16i}}{r_{16}} + \frac{\partial \phi_{17}}{\partial r_{17}}\frac{r_{17i}}{r_{17}} \end{aligned} \tag{2.21}$$

$\alpha = 2$

$$\frac{\partial \phi_\rho}{\partial u_{2i}^{\mathrm{C}}} = -\frac{\partial \phi_{12}}{\partial r_{12}}\frac{r_{12i}}{r_{12}} \tag{2.22}$$

$\alpha = 3$

$$\frac{\partial \phi_\rho}{\partial u_{3i}^{\mathrm{C}}} = -\frac{\partial \phi_{13}}{\partial r_{13}}\frac{r_{13i}}{r_{13}} \tag{2.23}$$

$\alpha = 4$

$$\frac{\partial \phi_\rho}{\partial u^{\mathrm{C}}_{4i}} = -\frac{\partial \phi_{14}}{\partial r_{14}} \frac{r_{14i}}{r_{14}} \tag{2.24}$$

$\alpha = 5$

$$\frac{\partial \phi_\rho}{\partial u^{\mathrm{C}}_{5i}} = -\frac{\partial \phi_{15}}{\partial r_{15}} \frac{r_{15i}}{r_{15}} \tag{2.25}$$

$\alpha = 6$

$$\frac{\partial \phi_\rho}{\partial u^{\mathrm{C}}_{6i}} = -\frac{\partial \phi_{16}}{\partial r_{16}} \frac{r_{16i}}{r_{16}} \tag{2.26}$$

$\alpha = 7$

$$\frac{\partial \phi_\rho}{\partial u^{\mathrm{C}}_{7i}} = -\frac{\partial \phi_{17}}{\partial r_{17}} \frac{r_{17i}}{r_{17}} \tag{2.27}$$

where i is the index of the coordinate axes. In equations (2.21) to (2.27) $r_{\alpha\beta i}$ is the component of $r_{\alpha\beta}$ in the i^{th} direction, which is defined as

$$r_{\alpha\beta i} = r_{\alpha i} - r_{\beta i}. \tag{2.28}$$

The detailed derivation of the term $\frac{\partial \phi_\rho}{\partial \mathbf{u}^{\mathrm{C}}_\alpha}$ for the fcc lattice structure, is given in appendix C. Equations (2.21) to (2.28) are substituted into equation (2.20) to calculate the internal nodal forces. The minimization problem can be solved for the coarse scale solution by minimizing the potential energy for the given boundary conditions.

2.1.3 The Phantom node method

In the phantom node method, when an element is completely cut by a crack, the displacement field is continuous on each part of the cracked element, but discontinuous across the crack. Therefore, the crack kinematics can be obtained by overlapping elements [49, 50]. The theoretical framework for the above idea was given by Hansbo and Hansbo [51], and was implemented by Mergheim et al. [52, 53] for statics and dynamics by Song et al. [50], who called the method the Phantom node method. The advantages of the phantom node method are: First, the displacement field is discontinuous across the crack but independently continuous on each part of the cracked element. Hence, the discontinuous element is replaced by two elements with the additional phantom nodes, which requires only a small modification in existing finite element codes. Secondly, the associated shape functions in a cracked element are the same as the shape functions of an intact element. Finally, the elements adjacent to the cracked elements do not require any modification. Because of the above advantages, the computer implementation of the phantom node method is particularly easy. The phantom-

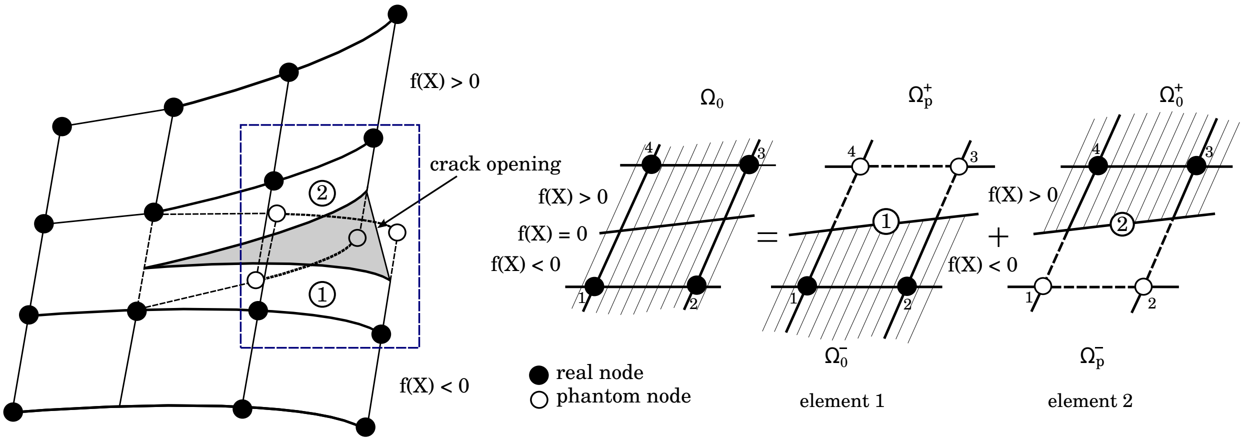

(a) (b)

Figure 2.5: The principle of the phantom node method where the hashed region is integrated to build the energy equation (2.11). (a) Crack opening and propagation after the phantom nodes are placed on the cracked elements. (b) Equivalence of a cracked element in the real domain to, two elements with phantom nodes.

node method was extended by Rabczuk et al. [49] to model crack tips within an element, for triangular and quadrilateral elements. Chau–Dinh et al. [48] applied the phantom node method to shell models with arbitrary cracks.

Consider a cracked body as shown in Fig. 2.5, and the corresponding finite element discretization; Ω_0 is the real domain, i.e. the domain to be cut by the crack and Ω_p is the phantom domain, $\Omega_\mathrm{p} = \Omega_\mathrm{p}^+ \bigcup \Omega_\mathrm{p}^-$. The part of the cracked elements which belong to the real domain Ω_0 are extended to the phantom domain Ω_p, so that the interpolation basis is full. Now the displacement in the real domain Ω_0 can be interpolated using the degrees of freedom for the nodes in the phantom domain Ω_p. The nodes in the phantom domain are called the phantom nodes and denoted by empty circles in Fig. 2.5(a). In other words, the approximation of the cut element is the superposition of the two approximations ($\Omega_0^+ \bigcup \Omega_\mathrm{p}^-$ and $\Omega_0^- \bigcup \Omega_\mathrm{p}^+$) over the cracked elements, as shown in Fig. 2.5(b). Defining f as the signed distance measured from the crack, W_0^+, W_p^-, W_0^- and W_p^+ as the nodes belonging to $\Omega_0^+, \Omega_\mathrm{p}^-, \Omega_0^-$ and Ω_p^+, respectively; H as the Heaviside function, the approximation of the displacement field is then given by [49]:

$$\mathbf{u}(\mathbf{X},t) = \sum_{I\in\{W_0^+,W_\mathrm{p}^-\}} \mathbf{u}_I(t) N_I(\mathbf{X}) H(f(\mathbf{X})) + \sum_{J\in\{W_0^-,W_\mathrm{p}^+\}} \mathbf{u}_J(t) N_J(\mathbf{X}) H(-f(\mathbf{X})). \tag{2.29}$$

The cracked elements have both real nodes and phantom nodes as shown in Fig. 2.5(b). The discontinuity in the displacement field is realized by simply integrating only over the area from the side of the real nodes up to the crack, i.e. the hashed areas in element 1 and element 2, Ω_0^- and Ω_0^+, respectively.

The initial phantom nodes are created on the completely cracked elements. The crack tip

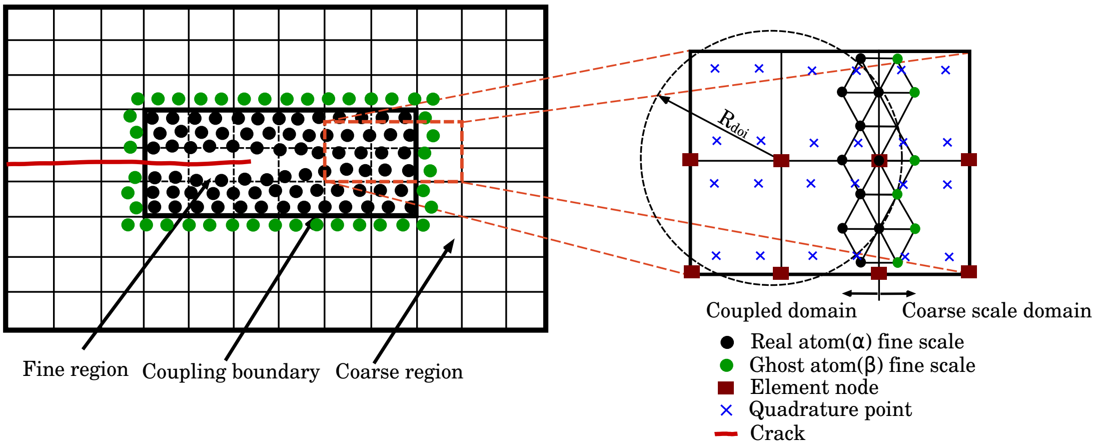

Figure 2.6: Schematic of the AMM for two dimensional problems. (a) The coarse and fine scale discretization along with the ghost atoms and the coupling boundary. (b) A zoom around the coupling boundary.

location is captured at every load step, from the fine scale model. Based on the location of the crack tip, the elements are checked for complete fracture. If an element is completely cracked, the crack is propagated in the coarse scale domain. To do so, the new phantom nodes are created on the newly cracked element, and their positions are initialized by interpolation from the coarse scale solution. The nodal connectivity table is updated with the phantom nodes, for the next load step.

2.1.4 Coupling the coarse and fine scales

The positions of the ghost atoms are interpolated from the coarse scale solution, as illustrated in Fig. 2.6. Let β be the index of the ghost atoms; the corresponding ghost atom displacements are given by

$$\mathbf{u}_{\beta}^{\mathrm{C}} = \sum_{I=1}^{n^{\mathrm{C}}} N_I(\mathbf{X}_{\beta})\mathbf{u}_I^{\mathrm{C}}. \tag{2.30}$$

The ghost atom positions estimated from equation (2.30) are applied as the boundary conditions for the fine scale model. The estimation of the ghost atom positions using only the coarse scale component of the displacement will impose a constraint that does not exist in the original problem, as explained in [120]. However for quasi-static problems, such an error can be controlled by properly choosing the interface of the coupling region. Additionally, care must be taken while calculating the nodal forces in the coarse scale region. At the interface region there are two sets of atoms. The first set from the underlying VAC and the second set from the fine scale region. Hence, both sets of atoms within the radius of influence $\mathrm{R}_{\mathrm{doi}}$ (Fig. 2.6) must be considered while estimating the nodal forces in the coupling region.

2.2 Adaptivity

The crack tip is contained within the fine scale region Ω^{A}, while the fine scale regions are coarse-grained as the crack propagates. The adaptivity scheme consists of the following steps:

1. Identify the coarse region Ω^{C} to be refined. Refine the model by expanding the atomistic region Ω^{A}, i.e by converting the estimated coarse scale region into a fine scale region.
2. Identify the fine region Ω^{A} to be coarse grained. Coarsen the model by shrinking the atomistic region Ω^{A}, i.e by converting the estimated fine scale region into a coarse scale region.

The details of refinement and coarsening algorithms are discussed below.

2.2.1 Preliminaries

In the present work, the fine scale region is embedded within the 'boundaries' of elements around the crack tip. The initial size of the fine scale region in the AMM boundaries is decided based on the following conditions: The refinement algorithm is activated sufficiently often such that a buffer layer of elements is always maintained between the crack tip and the coupling boundary. Secondly, to ensure that the refinement operation is not activated in the first load step itself, at least one element layer is considered between the crack tip and the buffer element layer. Finally, the crack tip element layer is sandwiched by at least one layer of elements. In other words, the minimum initial fine scale region is embedded within a 3×3 element mesh.

In the AMM, the fine scale contains the crack tip. The length of the initial crack contained in the fine scale is calculated based on the dimensions of the fine scale region. Therefore, the initial crack in the fine scale is modeled by removing the bonds between the atoms on the crack surface. The atoms on the crack surface possess the highest energy in the entire lattice. Hence, the high energy atoms and elements (discussed in section 2.2.2) can be used to identify the atoms on the crack surface. When the crack tip reaches the boundary of the buffer region, the adaptive refinement and/or coarsening schemes are activated. As a first step, adaptive refinement operation is carried out by creating the atoms in the elements to be refined, identified based on algorithm 1. The newly created atoms are initialized by interpolation from the coarse scale solution based on equation (2.2). In the next step, the crack is propagated in the coarse scale. In the phantom node method, whenever a refinement operation is activated the crack is incremented by an element length in the coarse scale. Therefore a new element is created along with two new phantom nodes. The elements to be coarsened are identified based on algorithm 2. In the adaptive coarsening operation, the atoms in the elements to be coarsened are deleted. The neighbourlist is regenerated after an adaptivity operation.

Let $\mathcal{E}$ be the total number of elements in the AMM. The load step just before an adaptive operation is denoted with subscript n, and subscript $n+1$ indicates the load step just after an adaptive operation. Therefore, $\mathcal{E}_n^{\mathrm{C}}$ is the set of elements in the coarse scale domain and $\mathcal{E}_n^{\mathrm{A}}$ is the set of fine scale elements, in load step n just before an adaptive operation; where $\mathcal{E}_n^{\mathrm{A}} \subset \mathcal{E}$ and $\mathcal{E}_n^{\mathrm{A}} \cap \mathcal{E}_n^{\mathrm{C}} = \emptyset$. And the sets $\mathcal{E}_{n+1}^{\mathrm{refA}}$, $\mathcal{E}_{n+1}^{\mathrm{refC}}$ and $\mathcal{E}_{n+1}^{\mathrm{coaA}}$, $\mathcal{E}_{n+1}^{\mathrm{coaC}}$ represent the fine scale and coarse scale elements at load step $n+1$, just after adaptive refinement and coarsening operations, respectively. The set $\mathcal{E}_{n+1}^{\mathrm{minA}}$ is the minimum set of elements in the fine scale domain after refinement, required to accurately capture the physics of the defects in the fine scale region.

2.2.2 Detection of the crack tip

The refinement/coarsening of an element in the coarse scale region is governed based on the atoms on the crack surface. Atoms on the crack surface helps in locating the position of the crack tip in Ω_A. Since the energies of the atoms around the crack tip are significantly higher than the other atoms, the potential energy provides an indication of the location of the crack tip. The energy criterion has been successfully applied to detect the locations of dislocations in dynamic propagation [74, 84]. Let $\mathcal{E}_n^{\mathrm{HE}}$ be the set of elements containing at least one atom with high potential energy, i.e.

$$\mathcal{E}_n^{\mathrm{HE}} = \{\mathrm{e} \in \mathcal{E}_n^{\mathrm{A}} \mid \text{energy of an atom in e} > \mathrm{tol}^{\mathrm{E}}\} \tag{2.31}$$

where $\mathrm{tol}^{\mathrm{E}}$ is the specified energy tolerance. As a guideline, $\mathrm{tol}^{\mathrm{E}}$ can be specified in the range of 15 and 30% [84] higher than the energy of an atom in equilibrium in a perfect lattice. The potential energy of an atom can be estimated from equation (4.30). In the present work 30% $\mathrm{tol}^{\mathrm{E}}$ values are considered in the MFC and AMM, respectively.

2.2.3 Adaptive refinement

The major steps of the refinement operation (Fig. 2.7) are:

1. Identify the elements to be refined.
2. Create and initialize the atoms in the elements to be refined.
3. Create and initialize the phantom nodes on the newly cracked elements.
4. Update the fine and coarse scale regions.

Figure 2.7(a) shows the elements containing high energy atoms flagged for refinement and the enlarged atomistic region after the refinement operation is shown in Fig. 2.7(b). Let $\mathcal{E}_n^{\mathrm{split}}$ be the set of completely cracked elements in the fine scale region, where $\mathcal{E}_n^{\mathrm{split}} \subset \mathcal{E}_n^{\mathrm{A}}$ and $\mathcal{E}_n^{\mathrm{tip}}$ be the element containing the crack tip, before refinement. Let $\mathcal{E}_{n+1}^{\mathrm{refA}}$ be the set of elements in the fine scale region and let $\mathcal{E}_{n+1}^{\mathrm{refC}}$ be the set of elements in the coarse scale region, immediately after an adaptive refinement operation.

In the current work, the crack is to be propagated in both the coarse scale and the fine scale regions. Hence, first the newly cracked elements in the coarse scale region are identified based on the position of the crack tip. The phantom nodes are created on the newly cracked elements. Crack propagation in the fine scale region depends on the number of broken bonds, identified based on the bond distance. The newly created atoms in the refined elements are initialized using equation (2.2).

The detailed algorithm of selecting the elements to be refined, initializing the newly created atoms in the elements identified for refinement and propagating the crack in the coarse scale region is explained in algorithm 1 in appendix D. The process is:

1. Store the fine scale elements in the element set $\mathcal{E}_n^{\mathrm{A}}$, the coarse scale elements in the element set $\mathcal{E}_n^{\mathrm{C}}$ and the completely cracked elements in the fine scale region into the element set $\mathcal{E}_n^{\mathrm{split}}$.

2. Calculate the high energy elements in the fine scale region using equation (2.31) and store in the element set $\mathcal{E}_n^{\mathrm{HE}}$.

3. Estimate the neighbours of the high energy elements in $\mathcal{E}_n^{\mathrm{HE}}$ and store them in $\mathcal{E}_{n+1}^{\mathrm{minA}}$.

4. Calculate the elements to be refined, $\mathcal{E}_{n+1}^{\mathrm{refine}}$ by removing the atomistic elements $\mathcal{E}_n^{\mathrm{A}}$ from the element set $\mathcal{E}_{n+1}^{\mathrm{minA}}$.

5. Flag the elements to be refined and increase the atomistic domain by creating the atoms in the flagged elements.

6. Initialize the positions of the newly created atoms using equation (2.2).

7. Update the fine scale elements ($\mathcal{E}_{n+1}^{\mathrm{refA}}$) after the refinement operation, by including the element set $\mathcal{E}_n^{\mathrm{refine}}$ into the set $\mathcal{E}_n^{\mathrm{A}}$.

8. Update the coarse scale element set ($\mathcal{E}_{n+1}^{\mathrm{refC}}$) after the refinement operation by deducting the atomistic elements $\mathcal{E}_{n+1}^{\mathrm{refA}}$ from the total elements $\mathcal{E}$.

9. Update the neighbour list ($nlist_{n+1}$) of the fine scale atoms in the element set $\mathcal{E}_{n+1}^{\mathrm{refA}}$.

10. Identify the newly cracked elements in the fine scale region ($\mathcal{E}_{n+1}^{\mathrm{nsplit}}$) by removing the split ($\mathcal{E}_n^{\mathrm{split}}$) and tip ($\mathcal{E}_n^{\mathrm{tip}}$) elements from the high energy element set $\mathcal{E}_n^{\mathrm{HE}}$.

11. Place the phantom nodes on the newly cracked elements ($\mathcal{E}_{n+1}^{\mathrm{nsplit}}$) and initialize their positions by interpolation.

12. Update the nodal connectivity table.

13. Update the split ($\mathcal{E}_{n+1}^{\mathrm{split}}$) and tip ($\mathcal{E}_{n+1}^{\mathrm{tip}}$) elements.

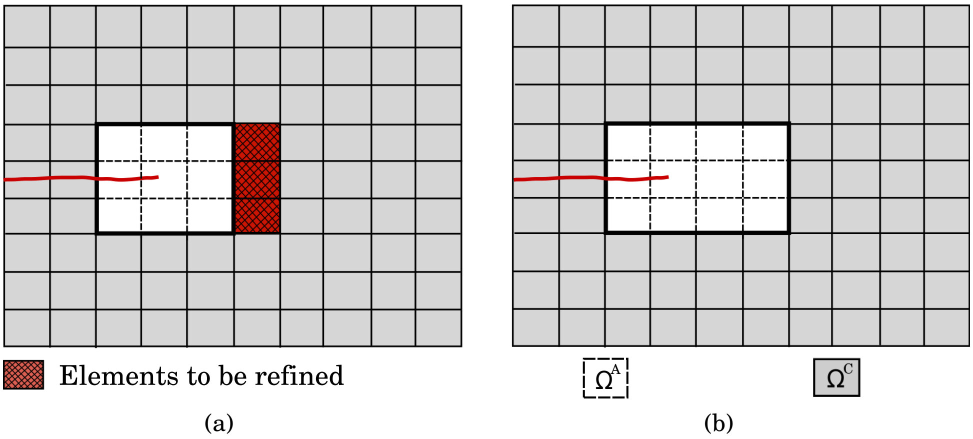

Figure 2.7: Sketch of the adaptive refinement operation. (a) Flagged elements to be refined are hatched in red color. (b) Increased atomistic region after the refinement operation.

Now the atomistic domain is enlarged to handle the elongated crack. To improve the computational efficiency, the atomistic elements behind the crack tip can be coarsened as explained in section 2.2.4.

2.2.4 Adaptive coarsening

The fine scale region is only needed close to the crack tip, the region away from the crack tip is coarse-grained. This reduces the size of the atomistic region and improves the computational efficiency. The major steps of an adaptive coarsening operation are:

1. Identify the elements to be coarsened.
2. Delete the atoms in the elements to be coarsened.
3. Update the fine and coarse scale regions.

The process of the adaptive coarsening operation is explained in Fig. 2.8. Figure 2.8(a) shows the elements containing low energy inactive atoms being flagged and the elements after coarsening are shown in Fig. 2.8(b). The algorithm explaining the coarsening steps is shown in algorithm 2 in appendix D.

Let $\mathcal{E}_n^{\mathrm{LE}}$ be the set of elements not containing any high energy atoms in the load step n, $\mathcal{E}_n^{\mathrm{LE}} \subset \mathcal{E}_n^{\mathrm{A}}$. Let $\mathcal{E}_n^{\mathrm{BA}}$ be the set of elements which are in the fine scale domain and are attached to the coupling 'boundary', $\mathcal{E}_n^{\mathrm{BA}} \subset \mathcal{E}_n^{\mathrm{A}}$. The elements to be coarsened are the elements which are in both set $\mathcal{E}_n^{\mathrm{LE}}$ and set $\mathcal{E}_n^{\mathrm{BA}}$ in front of the crack tip, $\mathcal{E}_n^{\mathrm{coarsen}} = \mathcal{E}_n^{\mathrm{LE}} \cap \mathcal{E}_n^{\mathrm{BA}}$. The process of adaptive coarsening operation is given below:

1. Store the atomistic elements in $\mathcal{E}_n^{\mathrm{A}}$ and the coarse scale elements in $\mathcal{E}_n^{\mathrm{C}}$.
2. Calculate the high energy elements in the fine scale region using equation (2.31) and store them in the element set $\mathcal{E}_n^{\mathrm{HE}}$.

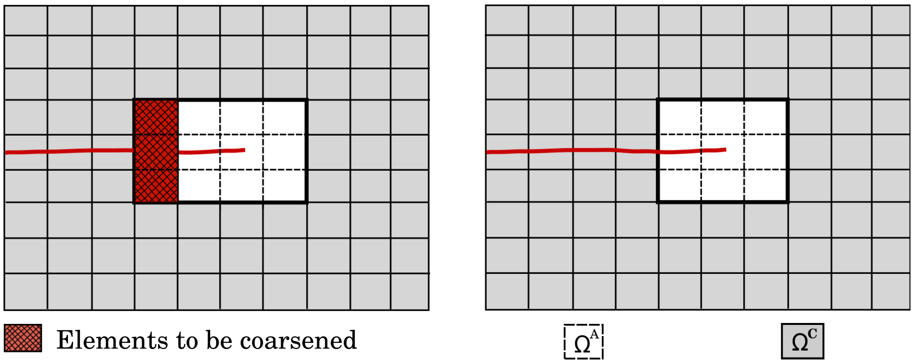

(a) (b)

Figure 2.8: Sketch of the adaptive coarsening operation. (a) Flagged elements to be coarsened are hatched in red color. (b) Reduced atomistic region after the coarsening operation.

3. Estimate and store the elements which do not contain at least one high energy atom in $\mathcal{E}_n^{\mathrm{LE}}$.
4. Find the fine scale elements attached to the coupling boundary and store them in $\mathcal{E}_n^{\mathrm{BA}}$.
5. The elements to be coarsened ($\mathcal{E}_{n+1}^{\mathrm{coarsen}}$) are given by $\mathcal{E}_n^{\mathrm{LE}} \cap \mathcal{E}_n^{\mathrm{BA}}$.
6. Flag the elements to be coarsened and decrease the atomistic domain by deleting the atoms in the flagged elements.
7. Update the element set in the fine scale region after the coarsening operation $\mathcal{E}_{n+1}^{\mathrm{coaA}}$ by deducting the element set $\mathcal{E}_n^{\mathrm{coarsen}}$ from the element set $\mathcal{E}_{n+1}^{\mathrm{refA}}$.
8. Update the element set in the coarse scale region after the coarsening operation $\mathcal{E}_{n+1}^{\mathrm{coaC}}$ by deducting the atomistic elements $\mathcal{E}_{n+1}^{\mathrm{coaA}}$ from the total elements $\mathcal{E}$.
9. Update the neighbour list of the fine scale atoms in the element set $\mathcal{E}_{n+1}^{\mathrm{coaA}}$.
10. Update the fine scale, coarse scale and the split elements for the next iteration.

The computer implementation steps for solving the crack propagation problem in the MFC and AMM are explained in Fig. 2.9.

2.3 Numerical Examples

In this example, the multiscale method developed in this chapter is validated through three numerical examples on quasi-static crack growth. In the first example, a very small displacement is prescribed on an edge crack model so that the crack does not propagate. Displacements and energies for selected atoms around the crack tip from the molecular statics model, the Multiscale model with the Fine scale region containing the whole Crack (MFC) and the AMM are compared. In the second example, sufficiently large displacements are applied so

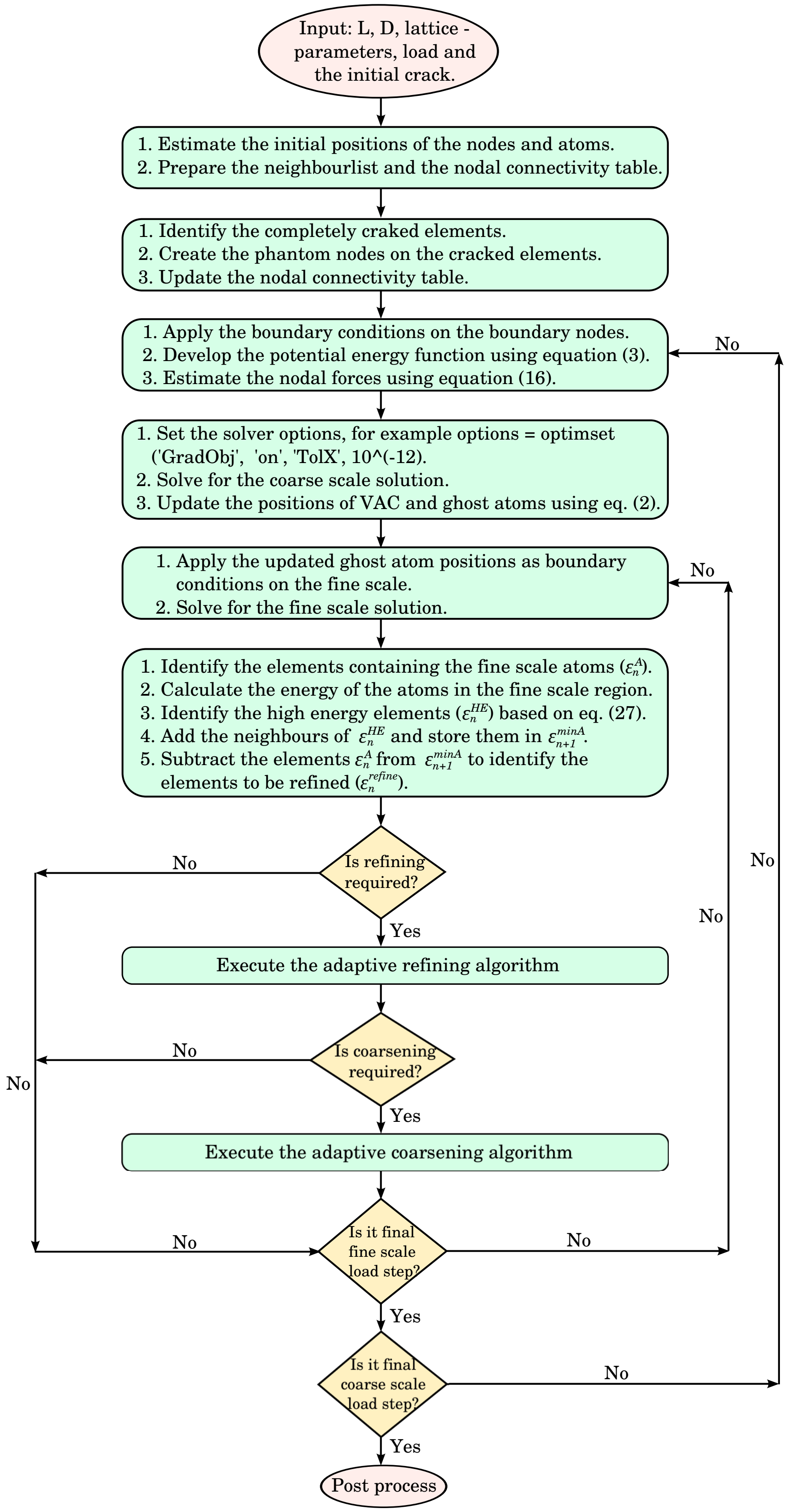
Input: L, D, lattice - parameters, load and the initial crack.
1. Estimate the initial positions of the nodes and atoms.
2. Prepare the neighbourlist and the nodal connectivity table.
1. Identify the completely craked elements.
2. Create the phantom nodes on the cracked elements.
3. Update the nodal connectivity table.
1. Apply the boundary conditions on the boundary nodes.
2. Develop the potential energy function using equation (3).
3. Estimate the nodal forces using equation (16).
No
1. Set the solver options, for example options = optimset ('GradObj', 'on', 'TolX', 10^(-12).
2. Solve for the coarse scale solution.
3. Update the positions of VAC and ghost atoms using eq. (2).
1. Apply the updated ghost atom positions as boundary conditions on the fine scale.
2. Solve for the fine scale solution.
No
1. Identify the elements containing the fine scale atoms (ε_n^A).
2. Calculate the energy of the atoms in the fine scale region.
3. Identify the high energy elements (ε_n^{HE}) based on eq. (27).
4. Add the neighbours of ε_n^{HE} and store them in ε_{n+1}^{minA}.
5. Subtract the elements ε_n^A from ε_{n+1}^{minA} to identify the elements to be refined (ε_n^{refine}).
No
Is refining required?
Yes
No
No
Execute the adaptive refining algorithm
No
Is coarsening required?
No
Yes
Execute the adaptive coarsening algorithm
No
Is it final fine scale load step?
No
Yes
Is it final coarse scale load step?
No
Yes
Post process

Figure 2.9: Flow chart indicating the computer implementation steps for solving the crack propagation problem in the MFC and AMM.

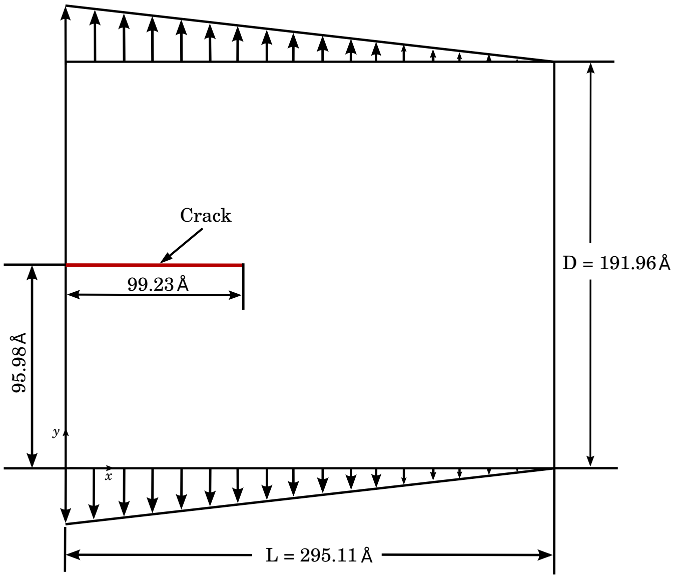

Figure 2.10: Schematic diagram of the edge crack model used in examples 1 and 2. A triangular displacement load is applied on the top and bottom boundaries.

that the crack propagates. The displacements and the energies of the MS, MFC and the AMM models are compared. In the final example, kinked crack propagation is studied by prescribing a displacement on the right edge of a cantilever beam with a pre-notch.

2.3.1 Example 1: Edge crack simulations

Consider a two dimensional atomistic model with dimensions 295.11Å×191.96Å as shown in Fig. 2.10. The triangular lattice corresponding to the (111) plane of the copper crystal with lattice constant 3.645Å is adopted to model the fine scale region. The ghost atoms are created all along the four edges. The LJ potential (given in equation (B.1)) is used to model the atomistic interactions with $\sigma = 2.29621$Å and $\epsilon = 0.467$ eV.

The full MS model consists of 10005 active atoms and 408 ghost atoms. The ghost atoms are placed all along the four edges just on the top of the coupling boundary in the MFC and the AMM. In this example, the crack propagation is not considered. Hence, a small triangular displacement load of 0.875Å with maximum amplitude on the left boundary is applied on the top and bottom edges, in the y direction. Both the top and bottom edge atoms are fixed in the x and y directions, and the left and right edge atoms are fixed in the x direction. The initial crack in the MS model is created by breaking the bonds. The initial crack is created at 95.98Å from the bottom edge with a length of 99.23Å along the x direction. In order to achieve a brittle fracture, the neighbours are not updated after each load step. Also only immediate neighbors are considered for the atom to atom interaction. The computer implementation steps for solving the crack propagation problem in the MFC and AMM are explained in Fig. 2.9.

Example	Normalized time		
	MS	MFC	AMM
1	1.0	0.19	0.13
2	1.0	0.79	0.39

Table 2.1: Computational times of the MS model, MFC model and AMM in examples 1 and 2.

Next, consider a coarse scale model with dimensions 295.11Å×191.96Å. The initial crack of length 99.23Å in the x direction located at 95.98Å in the y direction, is created in the coarse scale model. The model is discretized with the 12×8 elements in the x and y directions, respectively. The crack in the coarse scale domain is modeled by the phantom node method. Therefore, the phantom nodes are created on the completely cracked elements. In the current model there are three cracked elements with six phantom nodes. The fine scale regions measuring 163.66Å×84.82Å with 2294 active atoms and 202 ghost atoms, refer to Fig. 2.11(b) and 112.11Å×84.82Å with 1554 active atoms and 162 ghost atoms, refer to Fig. 2.11(c), have been created for the MFC and the AMM, respectively. A triangular displacement load of 0.875Å is applied on the top and bottom edge nodes. Both the top and bottom edge nodes are fixed in the x and y directions, whereas the left and right edge nodes are fixed in the x direction. Figure 2.11(d) compares the atom positions around the crack tip from the MS, MFC and AMM after the final load step. Six rows, on either side of the crack around the tip are captured from the three models for comparison. There are 360 atoms in total in twelve equal rows. The LJ potential energy and the ratio of the potential energy (PE) to the initial potential energy (PE0) of the three models, for the atoms in Fig. 2.11(d) are compared in Fig. 2.12(a). Fig. 2.12(b) shows a zoom of Fig. 2.12(a), around the crack tip. The numbering of atoms in Fig. 2.12, is mentioned in Fig. 2.11(d). The results from the MS model are assumed to be the accurate results. The error of a quantity is defined as the difference with respect to the accurate results. And the percentage error is 100 times the ratio of the error to the accurate results. The percentage error in the displacement and the potential energy are shown in Fig. 2.13(a) and Fig. 2.13(b), respectively. We notice that the maximum displacement percentage error is 0.208 and the maximum energy percentage error is 0.824, occurs around the crack tip. The normalized computational times are calculated as the ratio of the computational time with respect to the MS model. The normalized computational times for the MS, MFC and AMM are mentioned table 2.1. From the first row of the table, the computational cost of the AMM is 13% of the MS model.

2.3.2 Example 2: Edge crack propagation studies

In this example, the mode I crack propagation of an edge crack as shown in Fig. 2.10 is considered. Therefore, the displacement loads are applied in small increments. In order to propagate the crack in a brittle fashion, the neighbours are not updated after each load step.

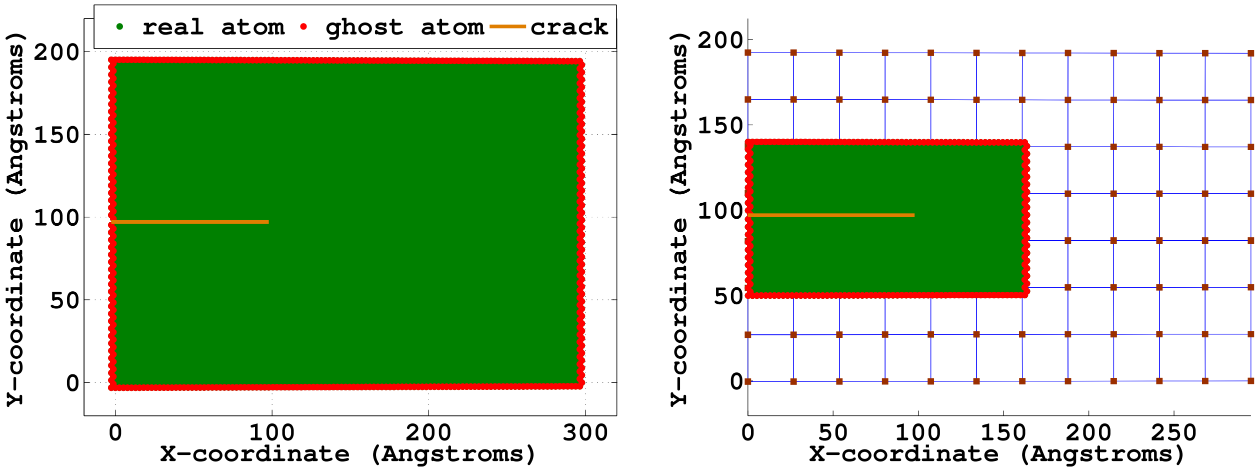

(a) MS model.

(b) MFC model.

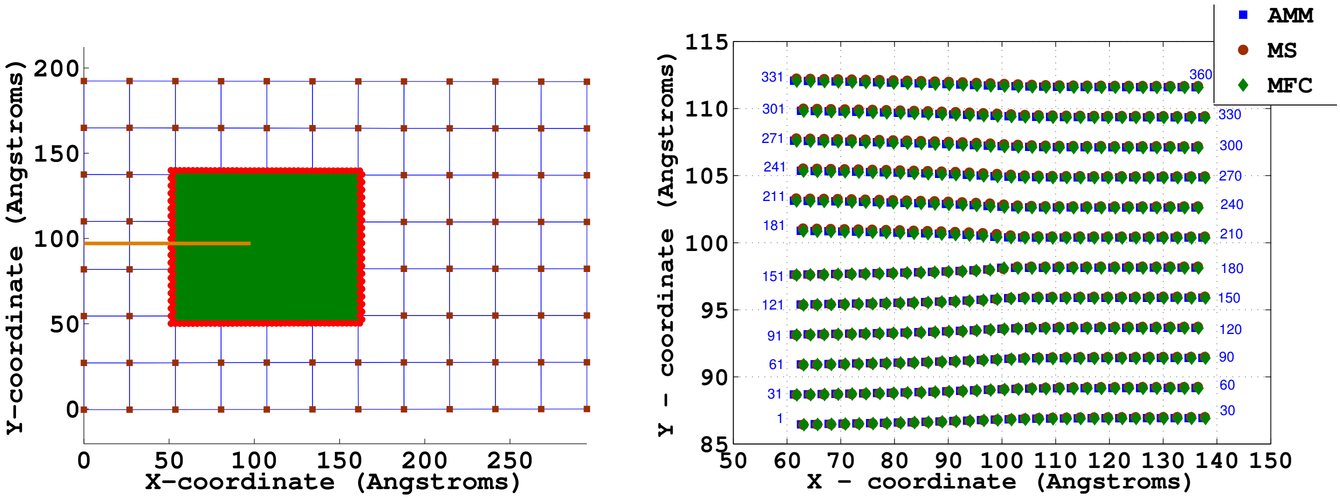

(c) AMM.

(d) Comparison of atom positions around the crack tip.

Figure 2.11: Deformed configurations of the (a) MS (b) MFC (c) AMM after the final load step and (d) comparison of atom positions around the crack tip, from the MS, MFC and AMM.

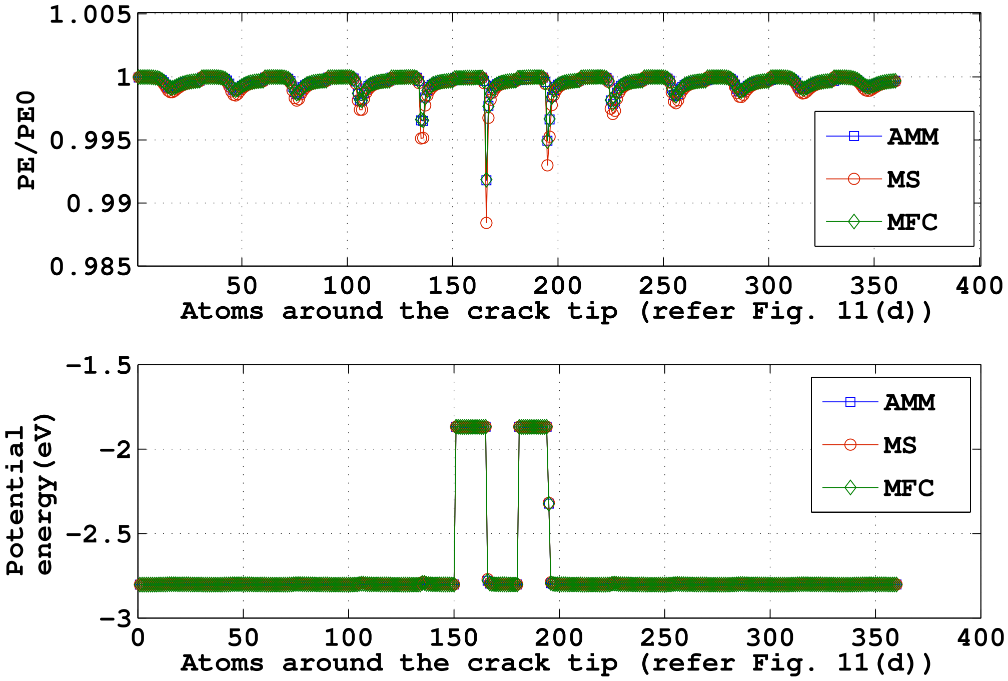

(a) Comparison of potential energy.

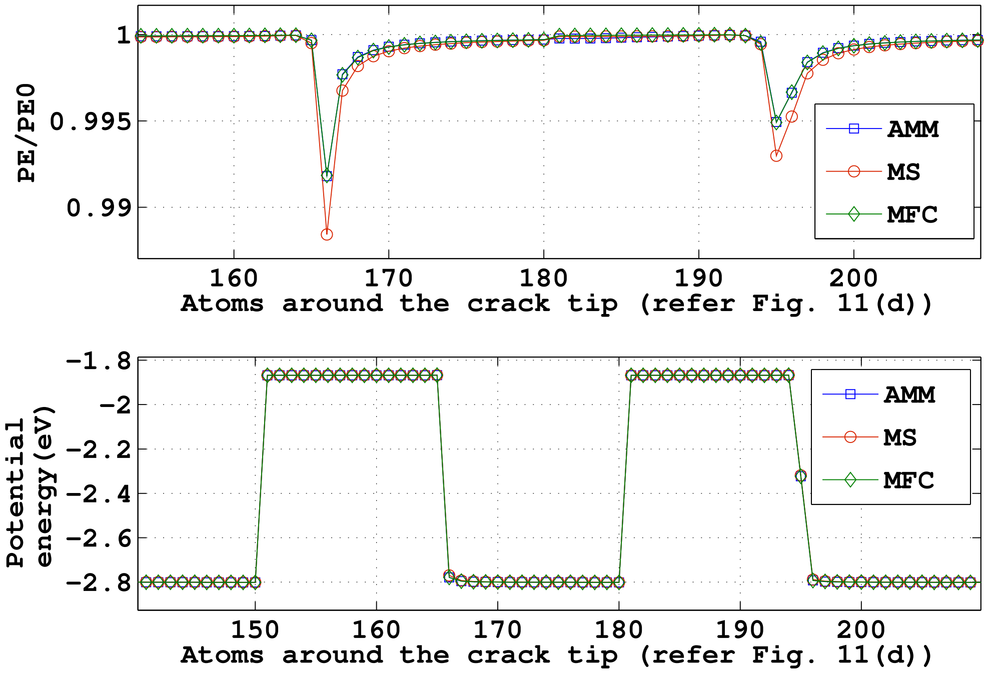

(b) Comparison of potential energy, zoom around the crack tip.

Figure 2.12: (a) Comparison of the LJ potential energy from the MS, MFC and AMM for the atoms around the crack tip, see Fig. 2.11(d); after the final load step. The bottom picture shows the LJ potential energy in eV and the ratio $\frac{\mathrm{PE}}{\mathrm{PE0}}$ is plotted in the top picture. (b) A zoom around the crack tip.

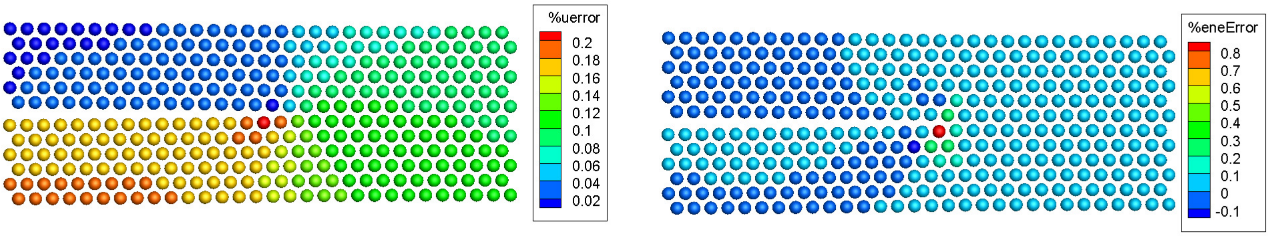

(a) Percentage displacement error.

(b) Percentage energy error.

Figure 2.13: Percentage errors in (a) displacement and (b) the potential energy, between the MS and AMM.

Only immediate neighbors are considered for the atom to atom interaction.

A triangular displacement load of 5.892Å is applied in the y direction, on the top and bottom rows of atoms/nodes, in 8 equal load steps. The coarse scale solution is in turn transferred to the fine scale model in 8 equal load steps. The same initial models as described in the MFC and AMM of example 1 are used. The fine scale region in the AMM is adaptively refined (refer to section 2.2.3) in the MFC model and adaptively refined and coarsened (refer to section 2.2.4) in the AMM. At the end of the final load step, it was observed that the refinement operations are carried out three times for the MFC model and the final fine scale model in MFC consists of 4305 atoms with 290 ghost atoms. In the AMM, the refinement and coarsening operations are carried out three times as well and there is no change in the number of atoms of the fine scale model.

Atom positions in the deformed configuration after the final load step from the MS, MFC and AMM are plotted in Fig. 2.14. The first row in Fig. 2.14 corresponds to the deformed configuration after the first load step. Fig. 2.14$(d-i)$ show the deformed configuration at the end of the simulation. The ratio of PE to PE0 is plotted in the top picture of Fig. 2.16(a), and the bottom picture shows the absolute value of the potential energy. The two peaks in the energy distribution in Fig. 2.16(a) corresponds to the energies of the crack tip atoms immediately on either side of the crack, indicating that the crack tip atoms possess the highest energy in the entire lattice. Figure 2.16(b) shows a zoom of Fig. 2.16(a), around the crack tip. The numbering of atoms in Fig. 2.16, is mentioned in Fig. 2.15. Figure 2.15 compares the atom positions from the three models. Six rows, on either side of the crack around the tip, are captured from the three models for comparison. There are 360 atoms in total in twelve equal rows. The percentage displacement error between the MS and the AMM is shown in Fig. 2.17(a). Similarly the percentage potential energy error is plotted in Fig. 2.17(b). From the results, a close agreement among the three models can be observed.

The change in average potential energy per atom for the MS, VAC and AMM at each load step is plotted in Fig. 2.18. The change in average potential energy per atom is defined as the difference of the potential energy per atom, in the current load step to the undeformed

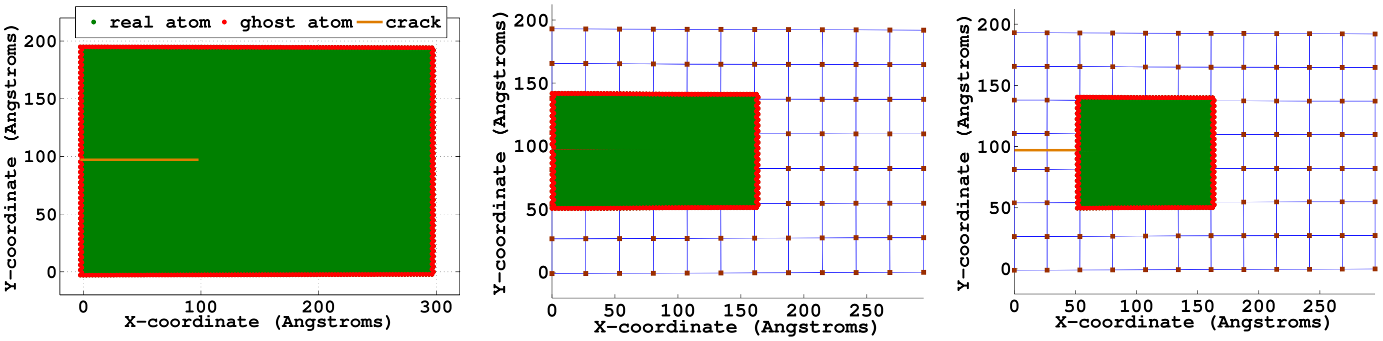

(a) MS model after the first LS (b) MFC model after the first LS (c) AMM after the first LS

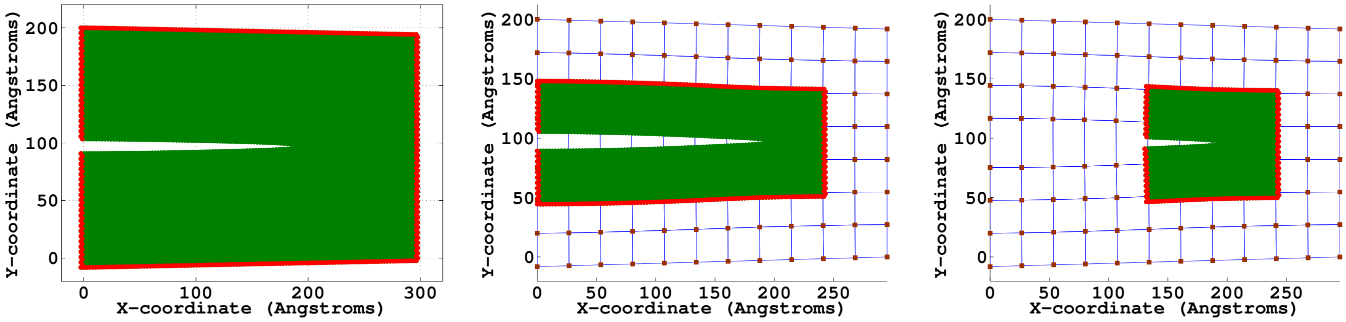

(d) MS model after the final LS (e) MFC model after the final LS (f) AMM after the final LS

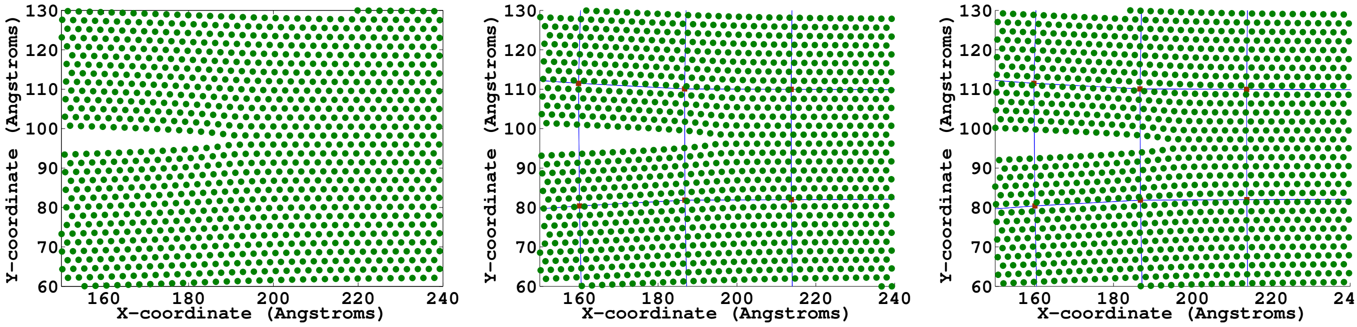

(g) zoom of MS model after the final LS (h) zoom of MFC model after the final LS (i) zoom of AMM after the final LS

Figure 2.14: Atom positions at the end of the simulation, from the MS, MFC and AMM with ghost atoms in red color. The first row corresponds to deformed configurations of the MS, MFC and AMM at the end of the first load step. Figures (d–i) correspond to the deformed configuration at the end of the simulation.

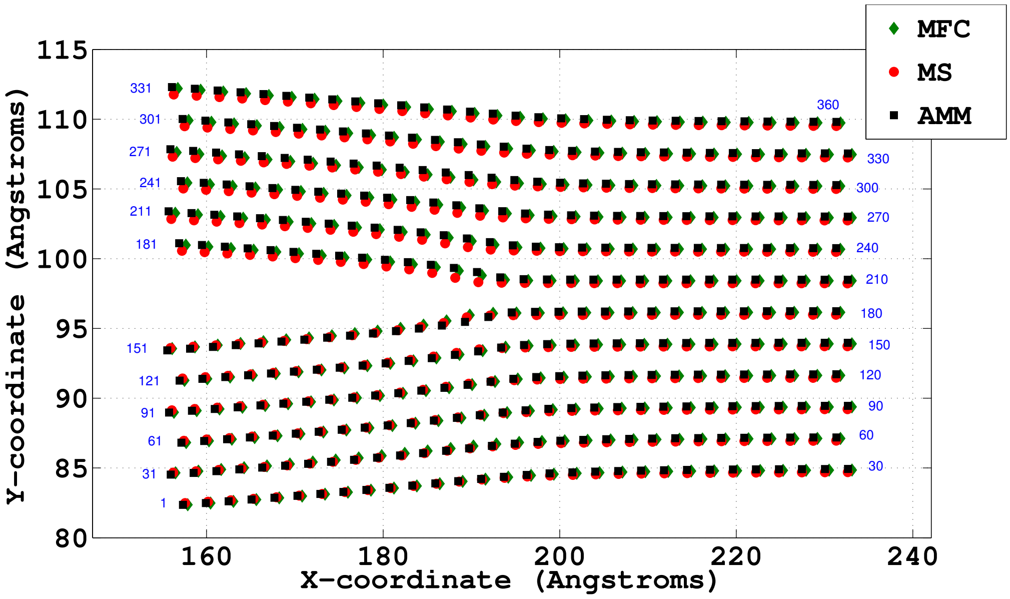

Figure 2.15: Comparison of the atom positions around the crack tip from the MS, MFC and AMM.

configuration. The average potential energy is calculated by dividing the total potential energy with the number of atoms. To generate a smooth curve, the displacement load is applied in 50 equal steps. The total potential energy decreases as the crack starts to propagate. Therefore, a jump in potential energy can be observed during load step 35. In other words, the crack starts to propagate from load step 35. A second jump was occurred during load step 42. The displacement field of the VAC does not contain the fine scale component ($\mathbf{u}_\alpha^\mathrm{A}$). Hence, a deviation of the VAC with the MS and AMM can be observed as the crack started to propagate, whilst the AMM and MS models always agree with each other. From the results, a close agreement among the three models can be observed. From table 2.1, the computational cost of the AMM is 39% of the MS model.

2.3.3 Example 3: Kinked crack propagation

The final example is a problem involving a kinked crack propagation. In this problem, the crack is not propagated in the fine scale region. Consider a 440Å×180Å beam with an initial pre-notch of 35Å in length at the center as shown in Fig. 2.19. A displacement load of 24.789Å at a 60° angle to the horizontal is applied on the right edge of the beam in 30 equal steps. The MFC and AMM are compared. The coarse scale solution at each load step is in turn transferred to the fine scale in 9 equal load steps. A 12×8 rectangular mesh is used to discretize the continuum. In the MFC model, initially the fine scale region is created between the 3rd and 10th nodes in the x direction and from the 1st to the 7th node in the y direction, with a domain size of 280Å×154.28Å as shown in Fig. 2.20(a) so that the crack is completely immersed in the fine scale region. In the AMM, initially the fine scale region is

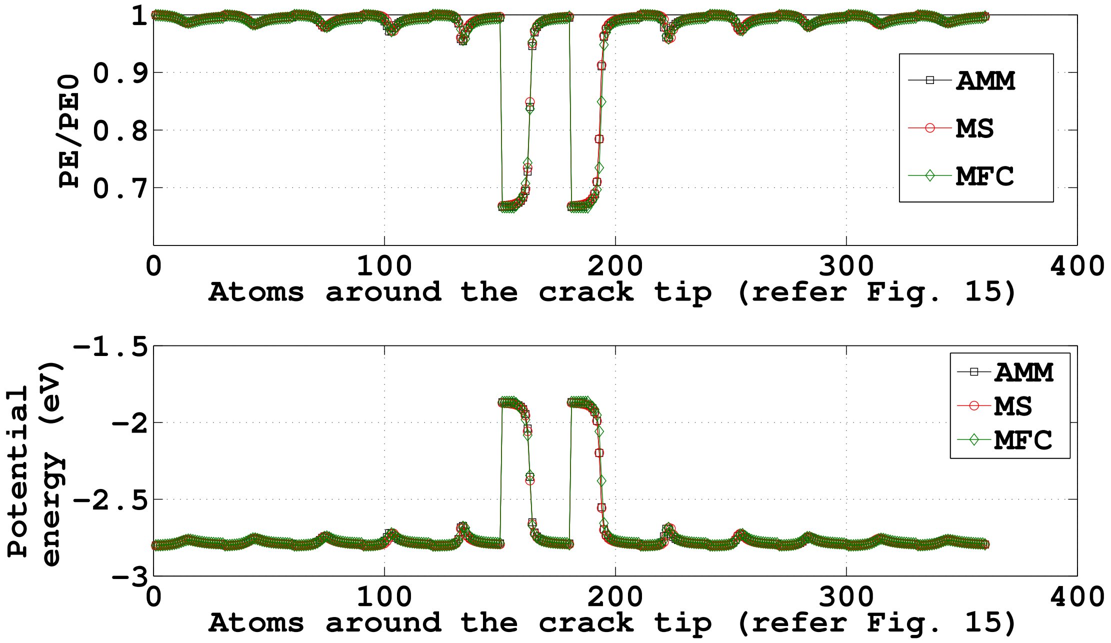

(a) Comparison of potential energy.

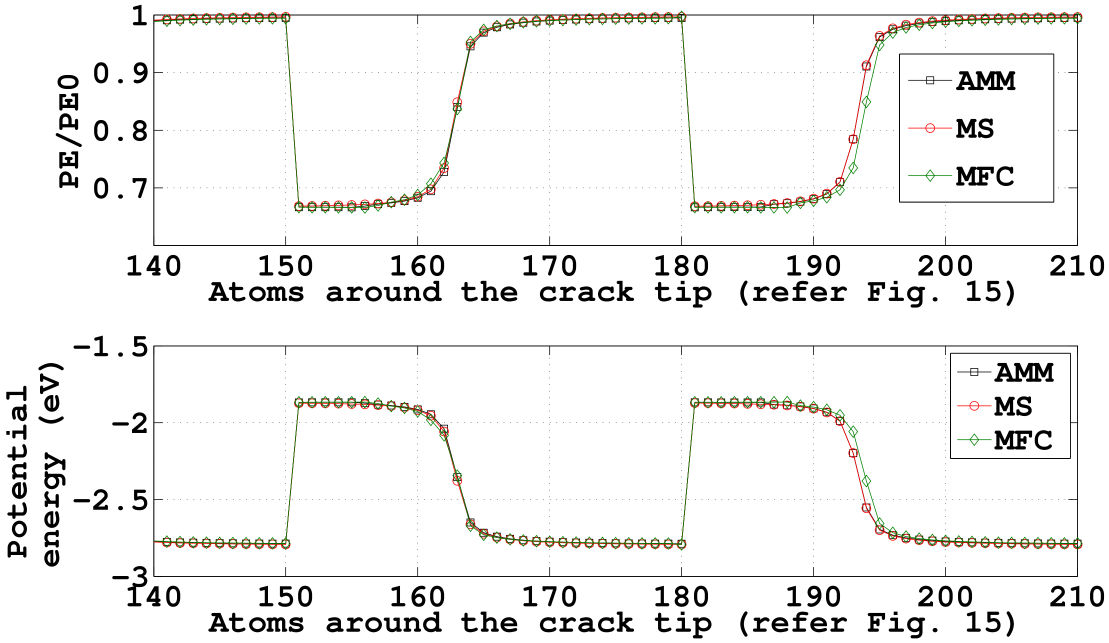

(b) Comparison of potential energy, a zoom around the crack tip.

Figure 2.16: (a) Comparison of the LJ potential energy from the MS, MFC and AMM for the atoms around the crack tip, see Fig. 2.15; after the final load step. The bottom picture shows the LJ potential energy in eV and the ratio $\frac{\text{PE}}{\text{PE0}}$ is plotted in the top picture. (b) A zoom around the crack tip.

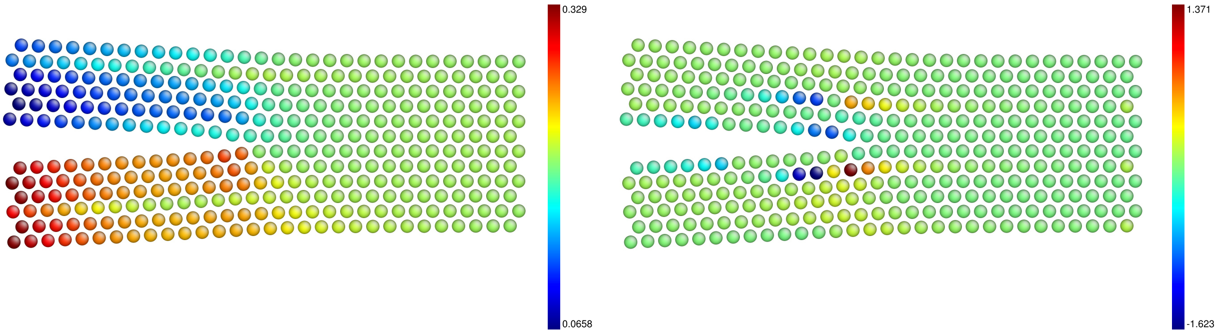

(a) Percentage displacement error.

(c) Percentage energy error.

Figure 2.17: Percentage errors in (a) displacement and (b) the potential energy, between the MS and AMM.

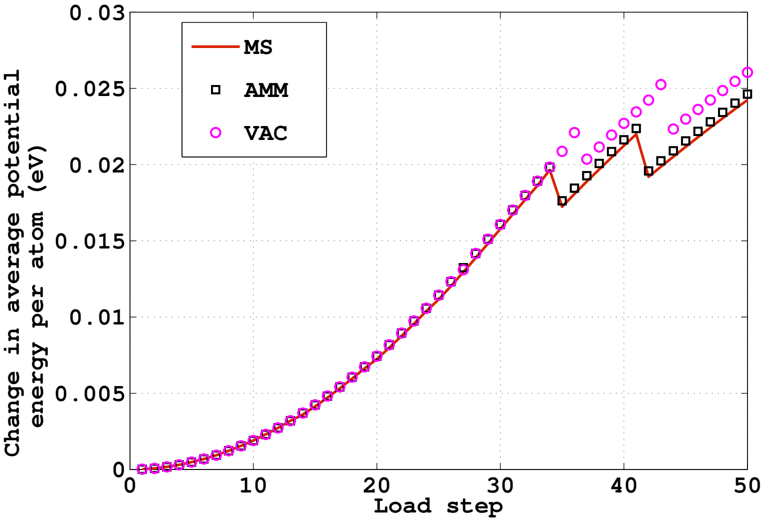

Figure 2.18: Change in average potential energy per atom with the load step.

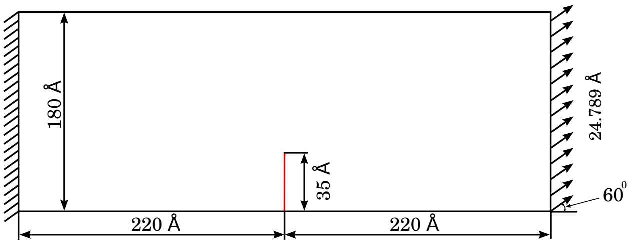

Figure 2.19: Schematic of the cantilever beam with the pre-notch, considered for the third example.

created between the 5th and 8th nodes in the x direction and from the 1st to the 4th nodes in the y direction, with a size of 120Å×77.14Å as shown in Fig. 2.20(b).

The load is quasi-statically incremented at each load step and the crack starts propagating in the y direction. After the 18th load step the crack takes a kink at an angle of 33.12° degrees to the horizontal axis towards the left boundary. The deformation pattern of the AMM model after the 18th and 24th load steps are plotted in Fig. 2.20(c) and Fig. 2.20(e), respectively. The adaptive refining and coarsening operations are carried out in the x and y directions based on the location of the crack tip. The atoms around the crack and the kink from the MFC and AMM models after the 18th and 24th load steps are plotted in Fig. 2.20(d) and Fig. 2.20(f), respectively. The percentage error in displacement for the the atoms around the crack tip after the 18th and the 24th load step, are plotted in Fig. 2.20(g) and Fig. 2.20(h), respectively. The results between the MFC and the AMM models closely agree with each other.

2.4 Discussion

The continuum based phantom node method was coupled with a molecular statics model to generate a multiscale framework for the simulation of fracture. The framework was developed to perform energy minimization of a triangular lattice which contains stably propagating fractures. Coupling of the continuum and atomistic models was realized through the use of a bridging scale method and a virtual atom cluster method. The BSM is enhanced so that arbitrary cracks are admissible at the coarse scale using the phantom node method leading to an adaptive multiscale method. The crack was incorporated into the fine scale model by breaking atomic bonds. The phantom node method was used to incorporate the crack in the coarse scale model. The fine scale and coarse scale models are coupled by enforcing the displacement boundary conditions on the ghost atoms.

The AMM was used to study the crack propagation in three examples. In the first example, a small displacement was prescribed to a domain containing an edge crack. The value of the prescribed displacement was chosen small enough that the crack does not propagate. The atom positions around the crack tip from the MS, MFC and AMM were compared. The error

3

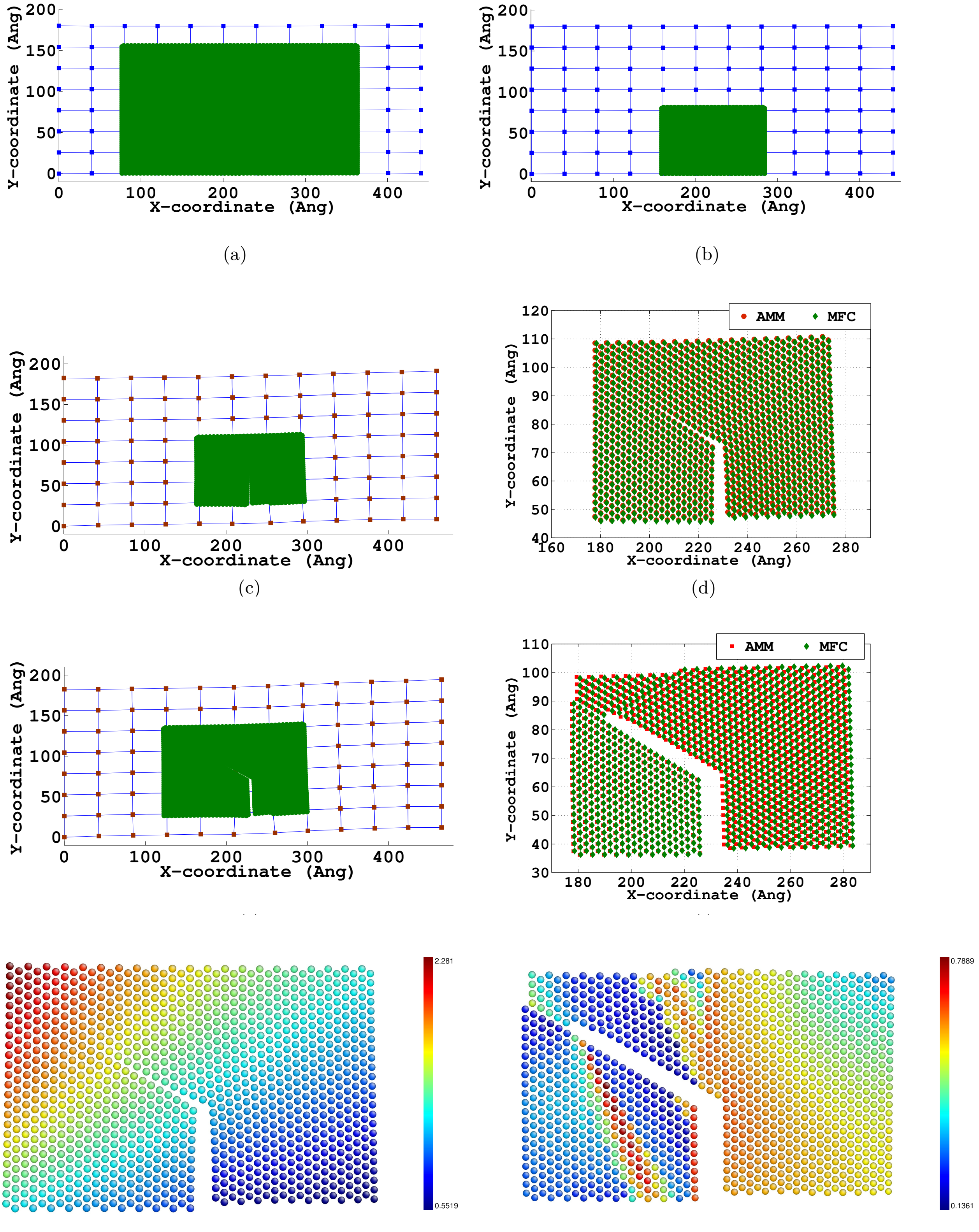

(a) (b)

(c) (d)

(g) (i)

Figure 2.20: Deformation plots of the MFC and AMM models with angular loading. (a) and (b) shows the initial configuration of the MFC and AMM models. (c) and (e) shows the deformed configuration of the AMM model after the 18th and 24th load steps. Atom positions around the crack tip, after the the 18th and 24th load steps from the MFC and AMM models are compared in figures (d) and (f), respectively. The percentage displacement errors for the atoms in (d) and (f) are shown in (g) and (h), respectively.

in displacement and the potential energy between the MS and AMM was found to be 0.208% and 0.824%, respectively. In the second example, the crack was made to propagate in the horizontal direction. Adaptive refinement and coarsening schemes were implemented during crack propagation. Very close agreement in the atom positions and the potential energy is observed across the three models. In the final example, the AMM was used to simulate the propagation of a kinked crack in a cantilever beam. The positions of atoms around the crack tip were compared between the MFC and AMM. The AMM was between 3 and 9 times more computationally efficient than the other methods to which it was compared.

The multiscale framework has been here introduced; it serves as a sound basis for further studies of more complex crack patterns.

Chapter 3

Efficient Coarse Graining in Multiscale Modeling of Fracture

In this chapter[2], a coarse-graining technique to reduce a given atomistic model into an equivalent coarse grained continuum model is discussed. The developed technique is applied on problems involving complex crack patterns in 2D and 3D including crack branching and coalescence. Atoms on the crack surface are separated from the atoms not on the crack surface by employing the centro symmetry parameter. A rectangular grid is superimposed on the atomistic model. Atoms on the crack surface in each cell are used to estimate the equivalent coarse-scale crack surface of that particular cell. The crack path in the coarse model is produced by joining the approximated crack paths in each cell.

One of the major difficulties in multiscale methods for fracture is to upscale fracture-related material information from the fine-scale to the coarse-scale, in particular for complex crack problems. Sufficient methods to coarse grain the fine scale defects are missing. Most methods, therefore only "enlarge" the fine scale domain and therefore drastically increase computational cost. In this chapter, a robust and simple coarse graining technique is presented in the context of multiscale modeling for fracture to reduce a given fine-scale model into an equivalent coarse-grained model. Only an atomistic model is considered at the fine-scale. The coarse-scale model might be discretized with classical techniques like the FEM, XFEM, GFEM, MM, to name a few. The developed technique is applied in the context of hierarchical upscaling though an extension to concurrent or semi-concurrent multiscale method is straight forward.

3.1 Coarse grained model

The goal of the present coarse-graining scheme is to develop an equivalent CG model for fracture based on a fine scale model containing defects. The CG scheme is employed for coarse scale models based on Finite Element/eXtended Finite Element (FE/XFE) or particle discretizations, whereas fracture on the fine scale occurs naturally by breaking the bonds between adjacent atoms. The CG approach is applicable to concurrent, semi-concurrent and hierarchical multiscale methods, though we present results only for the latter multiscale approach. The ingredients of the CG model are:

---

[2] This work has been published in the Theoretical and Applied Fracture Mechanics journal [119].

1. Identify the atoms on the crack surface in the fine scale model and approximate the crack surface in the equivalent CG representation.
2. Estimate the elastic potential functions and parameters of the CG model from an atomistic scale system.
3. Verify the results from the CG model with standards like full scale atomic calculations and/or empirical models.

3.1.1 Crack surface approximation

Consider a fine-scale model containing a crack in a particular deformed configuration. We define the “crack region” as the area created by connecting four nodes/particles in the rectangular discretization of the CG model, containing at least one atom on the crack surface. As a first step, the fine domain is discretized with a rectangular mesh. The scheme of such a rectangular discretization based on the finite element or meshfree methods is shown in Fig. 3.1 and Fig. 3.2, respectively. The hollow circles in Fig. 3.1(a) and Fig. 3.2(a) denote the atoms on the crack surface and the filled circles are the atoms not on the crack surface. The steps for the crack surface approximation are:

1. Determine the atoms on the crack surface using e.g. the Centro Symmetry Parameter (CSP), explained in section 3.1.2.
2. Identify the crack regions based on the positions of the atoms on the crack surface and the positions of the nodes or meshfree particles of the background discretization, as shown in Fig. 3.1(b) and Fig. 3.2(b).
3. Estimate the normal and Center of Gravity (CoG) of the atoms on the crack surface. Calculate the effective CoG of a crack surface by averaging the CoGs of the atoms on the crack surface in that crack region.
4. Approximate the crack path in each crack region by joining the effective normal and CoG of the atoms on the crack surface, as shown in Fig. 3.1(d) and Fig. 3.2(d).
5. Estimate the nodes or particles on either side of the crack surface or around the tip, refer Fig. 3.1(c) and Fig. 3.2(c).

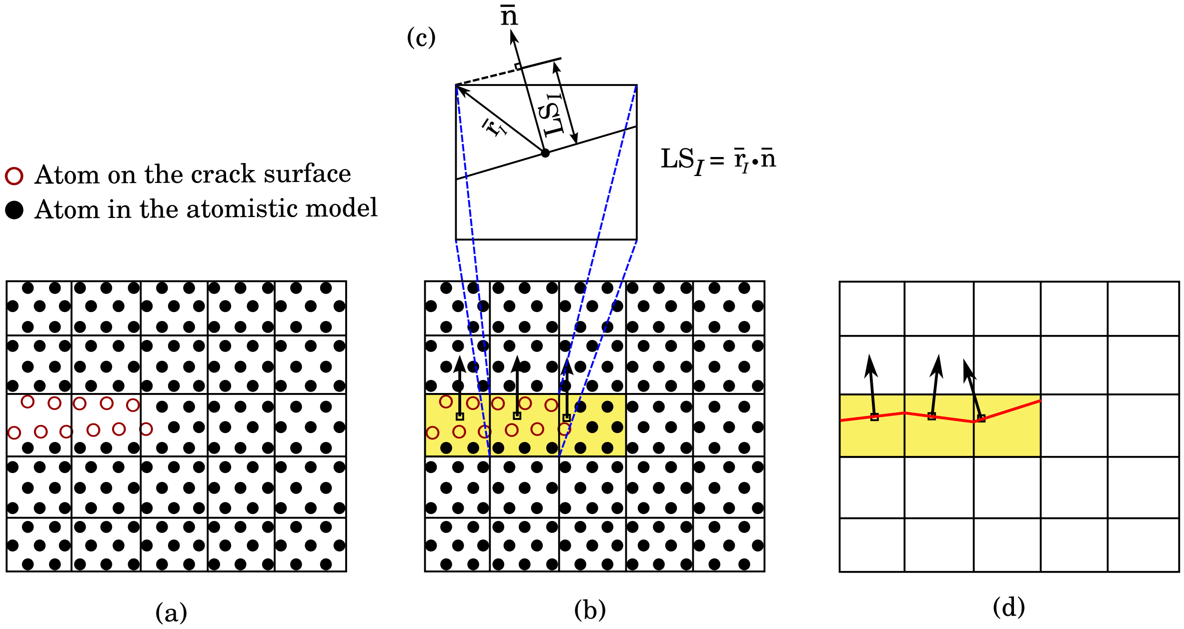

Figure 3.1: Schematic of mesh based equivalent coarse scale model. (a) Coarse mesh superimposed on the atomistic model (b) elements containing the atoms on the crack surface are highlighted along with the normals of the crack surface in each element (c) calculation of level sets and (d) approximation of crack surface by joining the crack path in the regions containing the crack.

The details of approximating the crack path is explained in section 3.1.3. The crack path is a continuous surface when extended mesh-free methods [3–13] or partition-of-unity enriched methods such as the eXtended Finite Element Method [14–19], the Generalized Finite Element Method [23–29], the Partition of Unity Finite Element Method [30, 31], the eXtended Element Free Galerkin method [32–39], the Cracking Particles Method [40–46], the phantom node method [47–53] or the Numerical Manifold Method [54, 55] are used on the coarse scale. Hence, the crack in the CG model is approximated by joining the crack paths in each crack region, shown in Fig. 3.1(d) and Fig. 3.2(d). However, when the CG model is based on the 'cracking particles' method [40–46], crack path continuity is not required. This facilitates the multiscale approach tremendously as no detection of branching or joining cracks need to be considered.

3.1.2 Centro symmetry parameter

The CSP is employed to detect the atoms on the crack surface. Consider an atom α in a fine scale model with the face centered cubic (fcc) lattice structure. Let β denote the neighbours

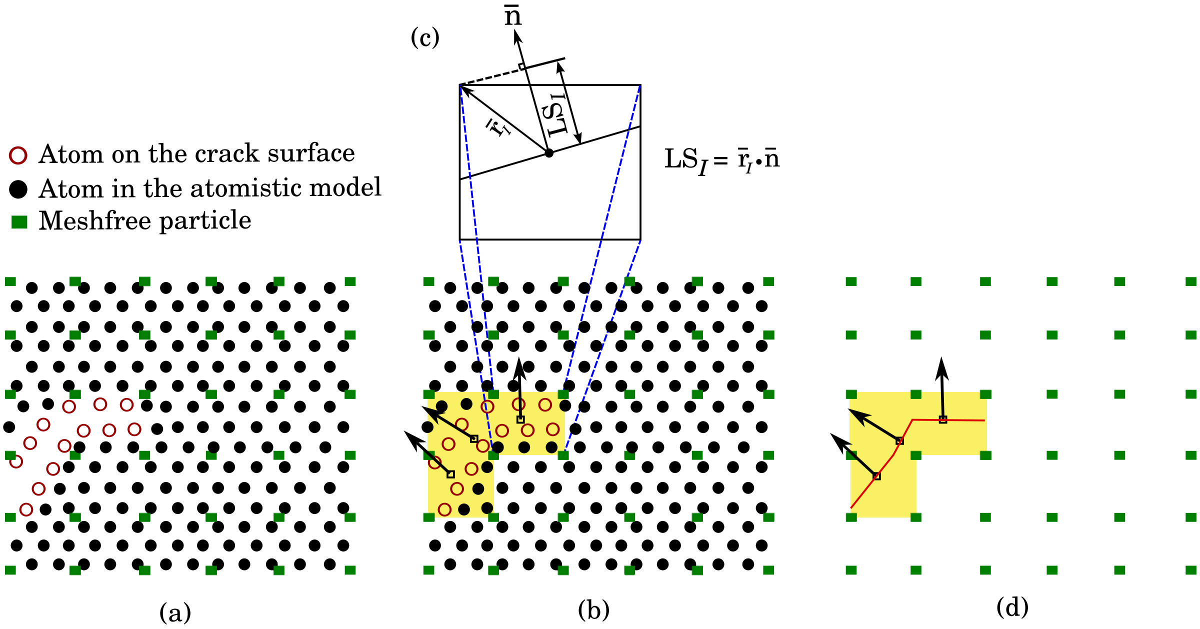
(c)
$\bar{n}$
$\bar{r}_I$
LS_I
$LS_I = \bar{r}_I \cdot \bar{n}$
○ Atom on the crack surface
● Atom in the atomistic model
■ Meshfree particle
(a)
(b)
(d)

Figure 3.2: Schematic of meshless equivalent coarse scale model. (a) Meshfree particles superimposed on the atomistic model (b) regions containing the atoms on the crack surface are highlighted along with the normals of the crack surface in each region (c) calculation of level sets and (d) approximation of crack surface by joining the crack path in the regions containing the crack.

of α. The centro symmetry parameter of an atom α is defined as [123]

$$\mathrm{CSP}_\alpha = \sum_{\beta=1}^{n^{\mathrm{nb}}/2} |\mathbf{r}_{\alpha\beta} + \mathbf{r}_{\alpha(\beta+n^{\mathrm{nb}}/2)}|^2 \tag{3.1}$$

where n^{nb} are the total number of nearest neighbours of atom α and $\mathbf{r}_{\alpha\beta}$ and $\mathbf{r}_{\alpha(\beta+n^{\mathrm{nb}}/2)}$ are the distance between the atoms α and β and α and $(\beta + n^{\mathrm{nb}}/2)$, respectively. In an fcc lattice structure there are 6 nearest neighbours (n^{nb}) for any atom α in the fine scale domain. Therefore, the CSP of the atom α in the fcc lattice is given by

$$\mathrm{CSP}_\alpha = \sum_{\beta=1}^{3} |\mathbf{r}_{\alpha\beta} + \mathbf{r}_{\alpha(\beta+3)}|^2 \tag{3.2}$$

From equation (4.34), the CSP of an atom α in the fcc lattice, is the summation of the square of the sum of the distances between the opposing neighbours. We consider periodic crystal structures with symmetry in atomic arrangement for full scale atomistic models. Because of the symmetry of the lattice structure in a perfect crystal, the CSP of an atom in a perfect lattice is zero. In other words, the atoms on the crack surface will possess CSP values other than zero. Atoms on the crack surface can be selected corresponding to the range of CSP values normalized with the square of the lattice parameter, listed in table 4.1. In the present

Defect	$\mathrm{csp}_\alpha/a_0^2$	Range $\Delta\mathrm{csp}_\alpha/a_0^2$
Perfect lattice	0.0000	$\mathrm{csp}_\alpha < 0.1$
Partial dislocation	0.1423	$0.01 \le \mathrm{csp}_\alpha < 2$
Stacking fault	0.4966	$0.2 \le \mathrm{csp}_\alpha < 1$
Surface atom	1.6881	$\mathrm{csp}_\alpha > 1$

Table 3.1: Range of centro symmetry parameter for various defects, normalized by square of the lattice parameter a_0^2.

work, atoms on the crack surface are the atoms possessing normalized CSP values greater than or equal to 1.6881.

3.1.3 Crack surface orientation

Consider a deformed configuration of the fine scale model and the discretized coarse scale model as shown in Fig. 3.1(a) or Fig. 3.2(a). Atoms on the crack surface in the fine scale model can be separated based on the CSP values estimated from equation (4.34). Let the atoms in the fine model be separated into small rectangular cells surrounded by four nodes/particles in the coarse model. These cells are categorized into cells containing atoms on the crack surface and atoms not on the crack surface.

The CoG of the neighbours of a particular atom on the crack surface α is calculated as the average position of the neighbours of α. If β are the neighbours of α, the CoG of the neighbours of α is given by

$$\mathbf{r}_\alpha^{\mathrm{cog}} = \frac{\sum_{\beta=1}^{n^{\mathrm{nb}}} \mathbf{r}_\beta}{n^{\mathrm{nb}}} \tag{3.3}$$

where $\mathbf{r}_\alpha^{\mathrm{cog}}$ is the position vector of the CoG of atom α and n^{nb} are the total number of neighbours of α. The normal to the crack surface of atom α is estimated by vectorially adding the position vector of α with its CoG vector:

$$\mathbf{n}_\alpha^{\mathrm{cog}} = \mathbf{r}_\alpha - \mathbf{r}_\alpha^{\mathrm{cog}} \tag{3.4}$$

where $\mathbf{n}_\alpha^{\mathrm{cog}}$ is the normal to the crack surface at atom α. The normalized normal to the crack surface at atom α is given by

$$\mathbf{n}_{\alpha\mathrm{n}}^{\mathrm{cog}} = \frac{\mathbf{n}_\alpha^{\mathrm{cog}}}{|\mathbf{n}_\alpha^{\mathrm{cog}}|}. \tag{3.5}$$

In this work, we pointed all the normals in the positive y direction. This is achieved by changing the sign of the normals pointing in the negative y direction. The process is repeated to estimate the CoGs and normals of all the atoms on the crack surface in a particular cell. Hence, the center of gravity of a cell can be calculated by averaging the positions of center

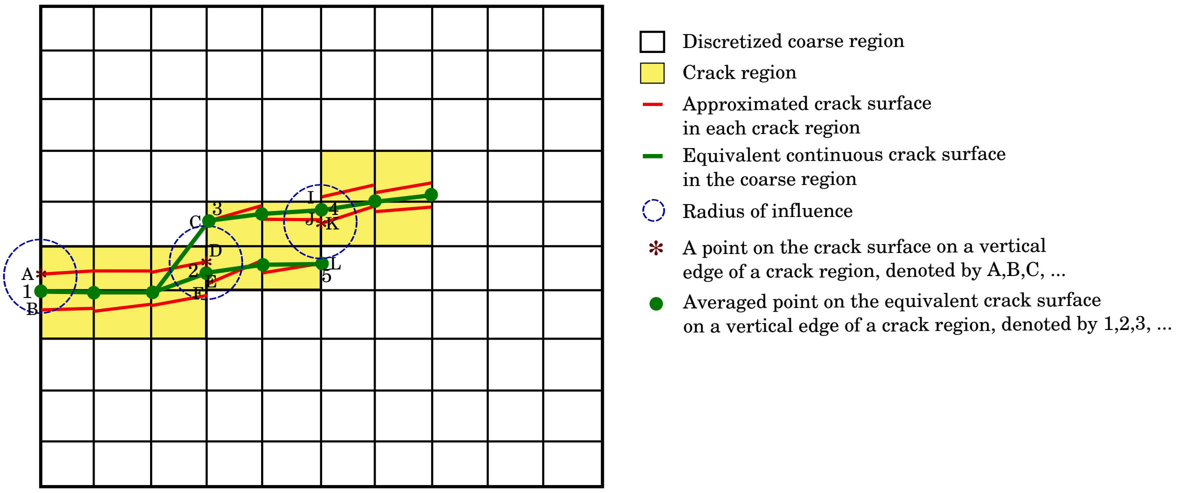
A
1
B
C
3
D
2
E
F
I
4
J
K
L
5
Discretized coarse region
Crack region
Approximated crack surface in each crack region
Equivalent continuous crack surface in the coarse region
Radius of influence
A point on the crack surface on a vertical edge of a crack region, denoted by A,B,C, ...
Averaged point on the equivalent crack surface on a vertical edge of a crack region, denoted by 1,2,3, ...

Figure 3.3: Schematic of averaging the approximated individual crack surface orientation in each crack region, to generate a smooth continuous equivalent crack surface.

of gravities of the atoms on the crack surface in that cell

$$\mathbf{r}_{\mathrm{cr}}^{\mathrm{cog}} = \frac{\sum_{\alpha=1}^{n^{\mathrm{cacr}}} \mathbf{r}_{\alpha}^{\mathrm{cog}}}{n^{\mathrm{cacr}}} \tag{3.6}$$

where $\mathbf{r}_{\mathrm{cr}}^{\mathrm{cog}}$ is the approximated position of the center of gravity of the atoms on the crack surface and n^{cacr} are the total number of atoms on the crack surface, in a crack region. The normal of the approximated crack surface in the crack region is computed as the average of the normals of the atoms on the crack surface

$$\mathbf{n}_{\mathrm{cr}}^{\mathrm{cog}} = \frac{\sum_{\alpha=1}^{n^{\mathrm{cacr}}} \mathbf{n}_{\alpha}^{\mathrm{cog}}}{n^{\mathrm{cacr}}} \tag{3.7}$$

where $\mathbf{n}_{\mathrm{cr}}^{\mathrm{cog}}$ is the normal vector of the approximated crack surface in a crack region. The crack surfaces in the crack regions are obtained by the planes passing through $\mathbf{r}_{\mathrm{cr}}^{\mathrm{cog}}$, whose normals are estimated from equation (3.7). Therefore, the approximated crack surface in the CG model is obtained by joining the crack surfaces in each crack region.

However, to generate a smooth and continuous crack surface in the CG domain, we average the start/end positions of the crack surfaces on the vertical edges of the crack regions, illustrated in the schematic Fig. 3.3. To achieve the goal, first, identify the number and locations of the start/end points on a vertical edge of a CG domain. Secondly, estimate the points separated by the largest distance. Thirdly, if the points separated by the largest distance fall within the domain influence, then the point on the equivalent crack surface on that edge is given by averaging the positions of the identified points in the first step. If not, there exists more than one point on the equivalent crack surface. In other words, the crack has a different orientation on that particular edge. The suggested radius of domain of influence is between 1 to 1.5 times the element length in the y direction.

A simple example of a continuous crack surface is shown in Fig. 3.3. We discuss the construction of points 1 to 5. Consider two crack surfaces at the left vertical edge of the CG domain; the crack surfaces start at points A and B, respectively. The (largest) distance between point A and point B falls within the domain of influence. The coordinates of point 1 on the equivalent crack surface are obtained by averaging the coordinates of points A and B. Secondly, consider the vertical edge containing points C,D E, and F. The points D and E correspond to end points of two crack surfaces and the points C and F are the starting points of new crack surfaces. The largest distance between these points is the distance between the points C and F, which is larger than the domain of influence. Therefore, there exists more than one point on the equivalent crack surface on this particular edge. The total number of points on the equivalent crack surface on this vertical edge can be estimated by recursively checking if the distance between the neighbours of points C,D,E and F falls within the domain of influence. Hence, for the scheme mentioned in Fig. 3.3, two points, point 2 and point 3 exist on the equivalent crack surface. The coordinates of points 2 and 3 is estimated by the averaging procedure as in the first step. Thirdly, a similar procedure is used for the edge containing points I,J,K and L to arrive at points 4 and 5 on the equivalent crack surface. The final path of the equivalent crack surface is obtained by joining points 1,2,3,...,n.

In this thesis, a cell containing at least 12 atoms on the crack surface is considered as crack region. Therefore, the adopted minimum size of the cell as 13 times the lattice parameter. However, the size of the cell or the fine-scale domain in general can be determined by a-posteriori error estimators and an adaptive refinement procedure. An alternative simpler procedure might be based on the change in the crack orientation of neighboring cells. The proposed CG model is equivalent to the fine scale. Therefore, the CG and the atomistic models can be validated through their potential energy.

3.1.4 Validation

The proposed CG model is equivalent to the fine scale. Therefore, their potential energy must be equal. The total potential energy of a fine scale system as shown in Fig. 3.1(a) is given by the sum of all bond potentials ϕ_α, where ϕ_α is the potential energy associated with atom α, defined below

$$\phi_\alpha = \frac{1}{2} \sum_{\beta \neq \alpha}^{n^A} \mathrm{V}(r_{\alpha\beta}) \tag{3.8}$$

where $\mathrm{V}(r_{\alpha\beta})$ is the bond potential between the atoms α and β, separated by distance $r_{\alpha\beta}$. Therefore, the total potential energy of the fine scale model is given by

$$\mathrm{U_A} = \sum_{\alpha=1}^{n^{\mathrm{A}}} \phi_\alpha = \frac{1}{2} \sum_{\alpha=1}^{n^{\mathrm{A}}} \sum_{\beta \neq \alpha}^{n^A} \mathrm{V}(r_{\alpha\beta}) \tag{3.9}$$

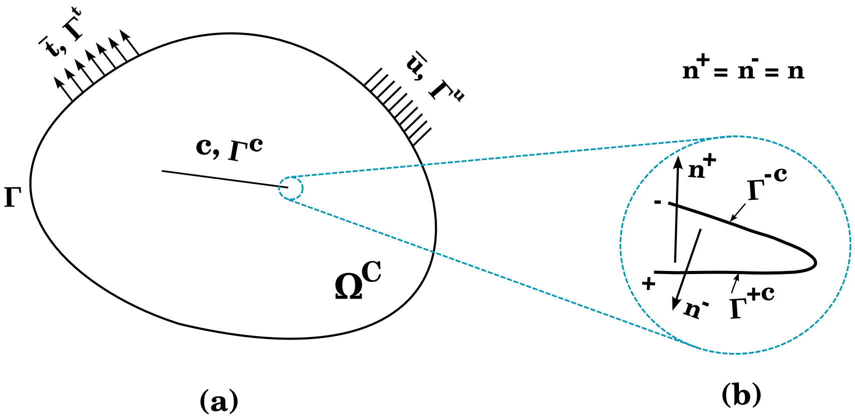

Figure 3.4: Schematic of domain and surface descriptions of a body in coarse region (a) displacements, tractions and the crack along with their surfaces (b) a closeup of the crack tip indicating the directions on the normals on the crack surfaces.

where $\mathrm{U_A}$ represents the total potential energy of the atomistic model.

Consider an equivalent CG model, illustrated in Fig. 3.1 or Fig. 3.2. Since the fine scale and CG models are equivalent, their potential energy must be equal. Hence, we define ϕ_ρ as the energy density function from the CG model. The discrete summation of the potential energy defined in the original molecular structure, can now be replaced with an integral based on the CG model, i.e.

$$\mathrm{U_{CG}} = \int_{\Omega_0^{\mathrm{C}}} \phi_\rho d\Omega_0^{\mathrm{C}} \approx \sum_{\mathrm{G}} w_{\mathrm{G}} \phi_\rho^{\mathrm{G}}. \tag{3.10}$$

In case of a periodic crystal structure, ϕ_ρ can be evaluated using a VAC [74, 120] like model. For an elastic isotropic material to ensure the consistent mechanical behaviour the strain energy of a coarse grained model can be estimated from

$$\mathrm{U_{CG}} = \int_{\Omega^{\mathrm{C}}} \boldsymbol{\sigma} \ \boldsymbol{.} \ \delta\boldsymbol{\epsilon} \ d\Omega^{\mathrm{C}}. \tag{3.11}$$

We consider a displacement field which is discontinuous at the cracks and continuous elsewhere in the coarse domain Ω^{C}, see Fig. 3.4. The displacement field is decomposed into continuous and discontinuous components,

$$\mathbf{u}^{\mathrm{C}} = \mathbf{u}^{\mathrm{CC}} + \mathbf{u}^{\mathrm{CD}} = \sum_{I \in \mathcal{S}} N_I(\mathbf{X})\mathbf{u}_I + \sum_{K \in \mathcal{E}} \sum_{I \in \mathcal{S}^{\mathrm{C}}} \hat{N}_I^{\mathrm{K}}(\mathbf{X})\psi_I^{\mathrm{K}}(\mathbf{X})\mathbf{a}_I^{\mathrm{K}} \tag{3.12}$$

where $\mathbf{u}^{\mathrm{C}}$ is the coarse scale displacement, $\mathbf{u}^{\mathrm{CC}}$ is the continuous component and $\mathbf{u}^{\mathrm{CD}}$ is the discontinuous component, in the coarse scale; $\mathcal{S}$ is the set of nodes in the entire discretization, $\mathcal{S}^{\mathrm{C}}$ is the set of enriched nodes that are influenced by the interface, N_I and $\hat{N}_I$ are the 'standard' and 'enriched' shape functions; $\mathbf{a}_I$ are additional degrees of freedom and $\mathcal{E}$ denotes the total number of interfaces. The shifted enrichment function $\psi_I(\mathbf{X})$ is chosen according to the problem:

$$\psi_I(\mathbf{X}) = \psi(\mathbf{X}) - \psi(\mathbf{X}_I). \tag{3.13}$$

A continuum model based on the VAC [74, 120] model combined with the XFEM, is used to estimate the potential energy of the CG model. XFEM is used for the discretization of the displacement field in equation (3.12). Equation (3.12) is used in equation (3.15) to estimate the potential energy of the CG model, which in turn is compared with the potential energy of the atomistic model in equation (3.9).

3.2 Numerical examples

In this section, the proposed CG model is validated with four numerical examples. The quasi-static crack propagation in two dimensions with an initial angular edge crack is studied in the first example. In the second example, we study two dimensional dynamic crack growth in a double notched specimen. Quasi-static crack propagation including crack branching and crack coalescence in two dimensions is studied in the third example. In the final example, we study three dimensional dynamic crack growth of an edge cracked specimen.

In order to directly compare the fine scale solution to the coarse scale solution, we ensure identical boundary conditions of the fine and coarse-scale models. Therefore, ghost atoms are placed all along the four edges of the fine scale model. The initial crack in the fine scale region is created by deleting the bonds between the atoms on the crack surface and updating the neighbor list accordingly. The neighbour list is generated based on a radius of influence. To model brittle material behaviour, the neighbour list is not updated at each load step and only immediate neighbours are considered while estimating the potential energy. The crack pattern at each load step is then used in the coarse-grained model and the solution of both models is compared. In future, the CG algorithm will be employed in the context of a concurrent multiscale method [74, 76].

3.2.1 Example 1: Angular crack propagation

Let us consider the mode I quasi-static crack propagation of a slanted edge crack, as shown in Fig. 3.5. The triangular lattice corresponding to the (111) plane of an fcc crystal and a lattice constant 3.645Å is adopted in the fine scale. The Lennard-Jones potential is used to model the atomistic interactions with $\sigma = 2.29621$Å and $\epsilon = 0.467$ eV. The full scale molecular statics model consists of 36157 active atoms and 768 ghost atoms. To propagate the crack quasi-statically, a total triangular displacement load of 15.678Å is applied on the top and bottom edges, in 25 equal load steps. Both the top and bottom edge atoms are fixed in the x and y directions, whereas the left and right edge atoms are fixed only in the x direction.

In this example, we want to develop a hierarchical CG model corresponding to a particular

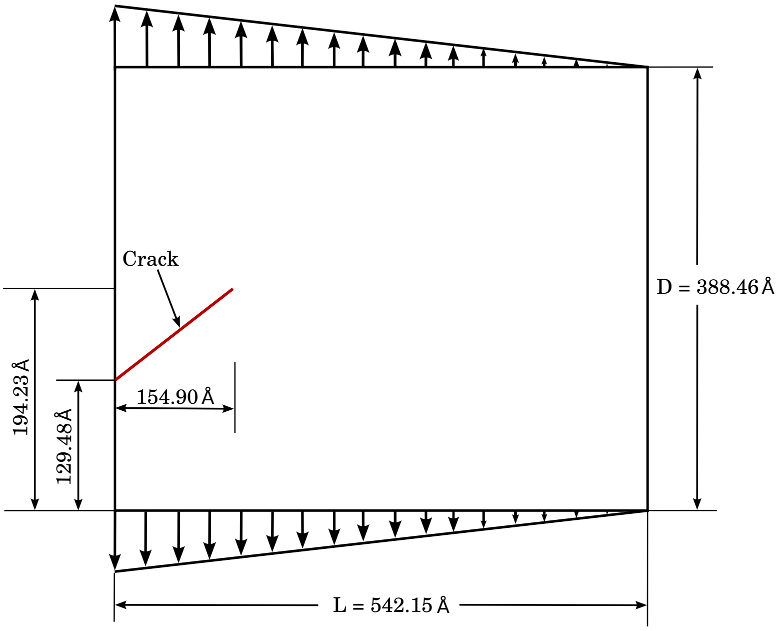

Figure 3.5: Schematic of fine scale model with initial crack used in example 1.

deformed configuration of the atomistic model. Therefore, the dimensions of the CG model are calculated based on the atom positions in the atomistic model for each load step. The CG model is discretized with 12×10 nodes in the x and y directions, respectively. The CG background cells are identical to the element size and the potential energy of the CG model is estimated from equation (3.15).

The initial configuration of the MS model is shown in Fig. 3.6(a). The deformed configuration of the MS model at the 15th load step is plotted in Fig. 3.6(b), highlighting the ghost atoms and the atoms on the crack surface. Fig. 3.6(c) shows the rectangular discretization created on the deformed configuration in Fig. 3.6(b). The discretization helps to capture the cells containing the atoms on the crack surface. Two particular atoms on the crack surface are identified and their neighbours and normals estimated based on equation (3.5), see Fig. 3.6(d). Fig. 3.6(e) shows the normals (estimated by equation (3.7)) of all the regions in the coarse scale, containing the atoms on the crack surface. Highlighted crack regions along with their center of gravities and normals are plotted in Fig. 3.6(f).

Since the fine scale and the CG models are equivalent, their potential energy must be equal. Hence, we define ϕ_ρ as the energy density function from the CG model. The discrete summation of the potential energy defined in the original molecular structure, can now be replaced with an integral based on the CG model, i.e.

$$\mathrm{U}_{\mathrm{CG}} = \int_{\Omega_0^{\mathrm{C}}} \phi_\rho d\Omega_0^{\mathrm{C}} \approx \sum_{\mathrm{G}} w_{\mathrm{G}} \phi_\rho^{\mathrm{G}}. \tag{3.14}$$

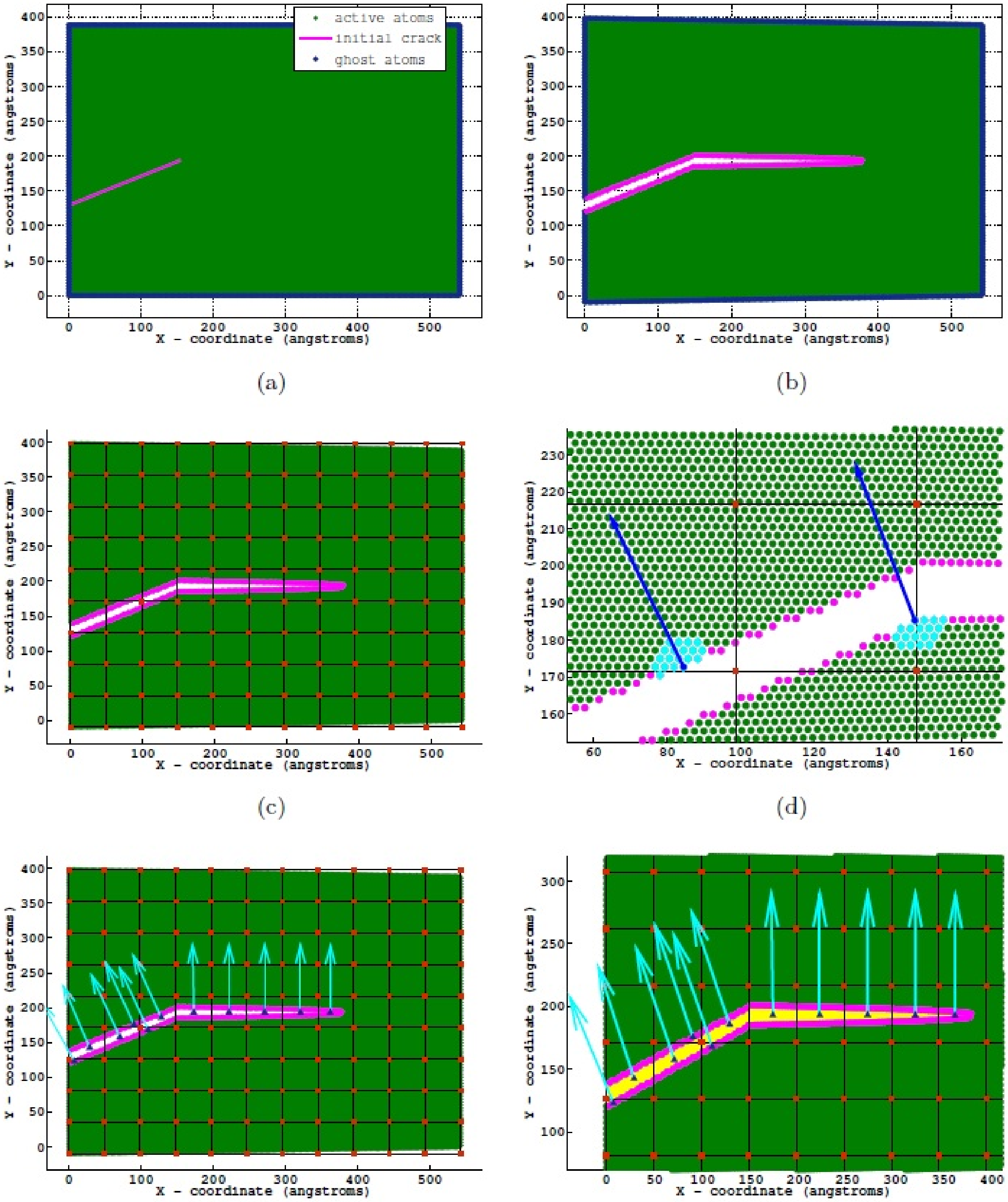

(a) (b) (c) (d) (e) (f)

Figure 3.6: Development of a CG model of a given fine scale model, for a quasi-static crack propagation of an angular edge crack. (a) Initial configuration of the fine scale model. (b) Fine scale model at the 15th load step highlighting the ghost atoms and the atoms on the crack surface. (c) Fine scale model at the 15th load step, superimposed with the rectangular discretization. (d) Normals and neighbours of two particular atoms on the crack surface. (e) Normals of all the crack regions. (f) Rectangular discretization of the fine scale model at the 15th load step, highlighting the crack regions and their CoGs and normals.

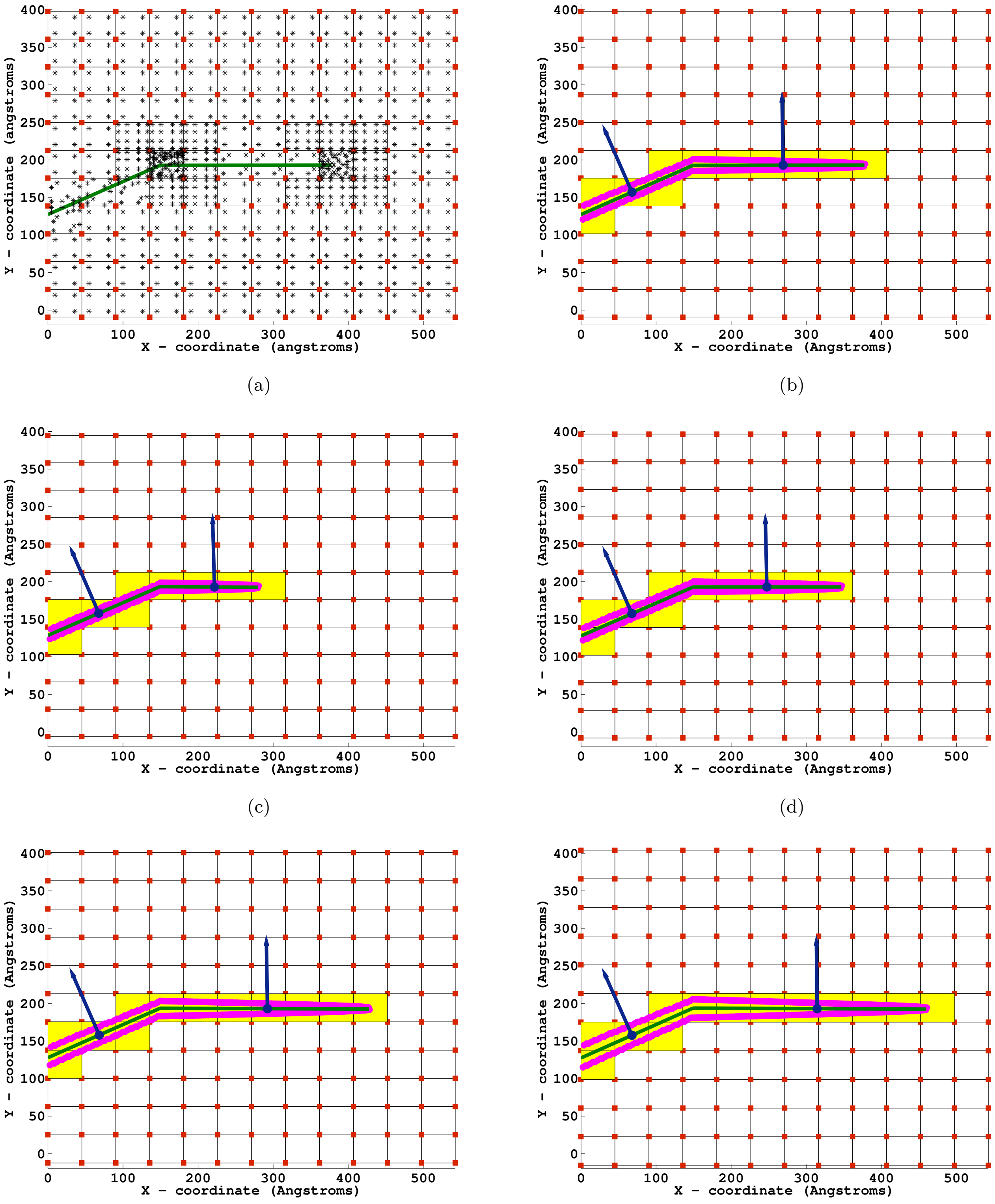

(a)

(b)

(c)

(d)

(e)

(f)

Figure 3.7: Equivalent CG models, atoms on the crack surface and the approximated crack surface along with their normals. (a) Distribution of Gauss points on the CG model in (b), used to calculate the potential energy. (b) Equivalent CG model of the fine scale model in Fig. 3.6(b). Equivalent CG model of the fine scale model at the (c) 10th load step (d) 13th load step (e) 20th load step and (f) 25th load steps.

Load step	Potential energy from the		% error
	fine model ($\mathrm{E_{FS}}$)	CG model ($\mathrm{E_{CS}}$)	
0	1.0265e+05	1.029e+05	3.01
10	1.0241e+05	1.059e+05	3.29
13	1.0236e+05	1.069e+05	4.24
15	1.0233e+05	1.075e+05	4.80
20	1.0225e+05	1.092e+05	6.36
25	1.0218e+05	1.109e+05	7.86

Table 3.2: Comparison of potential energies from Atomistic and CG models.

For an elastic isotropic material to ensure the consistent mechanical behaviour the strain energy of a coarse grained model can be estimated from

$$\mathrm{U_{CG}} = \int_{\Omega^{\mathrm{C}}} \boldsymbol{\sigma} \;.\; \delta\boldsymbol{\epsilon} \; d\Omega^{\mathrm{C}}. \tag{3.15}$$

Fig. 3.7(a) shows the Gauss point distribution used to calculate the potential energy of the CG model. Fig. 3.7(b) depicts atoms on the crack surface and the final approximated crack surface orientation at the 15th load step. Similarly, the final approximated crack surface orientations along with the atoms on the crack surface, at the 10th, 13th, 20th and 25th load steps are plotted in Figures 3.7(c), 3.7(d), 3.7(e) and 3.7(f), respectively. The potential energies of the fine scale model and the CG model at the 10th, 13th, 15th, 20th and 25th load steps are compared in table 3.2. The percentage error in the potential energy is estimate as: $\frac{|\mathrm{E_{CG}}-\mathrm{E_{FS}}|}{\mathrm{E_{CG}}} \times 100$, where $\mathrm{E_{CG}}$ is the potential energy of the CG model and $\mathrm{E_{FS}}$ is the potential energy of the fine scale model. The minimum and maximum percentage errors are observed to be 3.29% and 7.86%, at the 10th and 25th load steps, respectively.

3.2.2 Example 2: Dynamic crack propagation in a double notched specimen

The second example is a dynamic crack propagation problem in a double-notched specimen as shown in Fig. 3.8. The initial left and right edge cracks are located at 270Å and 538Å, respectively from the bottom edge with an initial length of 102.1Å each along the x direction, as shown in Fig. 3.8. The fine scale model consists of 168551 atoms and 2604 ghost atoms. Initial velocities are prescribed on the bottom and top rows of atoms at the rate of 8.8 m/s, whereas the atoms in between the top and bottom rows are ramped with a maximum velocity of 8.8 m/s, refer to Fig. 3.8. The velocity is applied in 20000 time steps; each time step is equal to 8 pico-seconds. Fig. 3.9(a) shows the initial configuration of the fine scale model highlighting the atoms on the crack surface.

The deformed configuration at 48 pico-seconds is plotted in Fig. 3.9(b). We observed several regions in Fig. 3.9(b) containing less than 12 atoms on the crack surface. Therefore, they are not identified as the regions containing the atoms on the crack surface. The su-

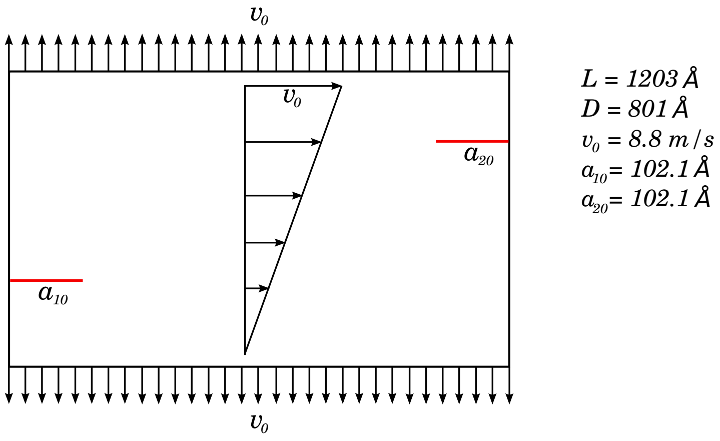

Figure 3.8: Schematic of double notched specimen used in example 2.

perimposed rectangular discretization highlighting the regions containing the atoms on the crack surface and their normals are also shown in Fig. 3.9(b). Note that all normals are pointing in the y direction and the changes in the crack surface orientation along the x direction are accurately captured. Fig. 3.9(c) shows the deformed configuration just before the two cracks join at 78 pico-seconds. The number of atoms on the crack surface have significantly reduced at 78 pico-seconds compared to 48 pico-seconds due to the coalescence of many small cracks/dislocations. The deformed configuration after crack coalescence is shown in Fig. 3.9(d). Fig. 3.9(d) also shows the superimposed rectangular discretization of the CG model highlighting the regions containing the atoms on the crack surface and their normals. The deformed configuration at 108 seconds and 180 pico-seconds (Fig. 3.9(e) and Fig. 3.9(f)) shows the separation of the united crack surfaces.

A closeup of the deformed configuration at 108 pico-seconds is shown in Fig. 3.10. Fig. 3.10(a) shows a closeup of the Fig. 3.9(e) on the top half of the crack surface. Small cracks and dislocation cores can be observed. Two particular atoms on the branch crack formed in Fig. 3.9(d) are selected to estimate the neighbours and the normals. Fig. 3.10(b) shows the normals of the selected two atoms on the crack surface along with their neighbours. Fig. 3.10(c) and Fig. 3.10(d) shows a closeup of Fig. 3.9(e), on the left and right halfs, respectively. The change in the direction of the normals according to the orientation of the crack surface can be closely observed in Figures 3.10(c) and 3.10(d).

The approximated equivalent crack surface with varying discretizations is studied in Fig. 3.12. The deformed configuration of the fine scale model in Fig. 3.9(e) and the CG model discretizations of 7×5, 14×8, 21×12 and 21×16 nodes along the x and y directions, are selected in the study. Fig. 3.12(a) shows the CG model with discretization of 7×5 nodes, superimposed on the fine scale model. The corresponding CG model with the approximated equivalent crack is given in Fig. 3.12(b). Since the discretization is very coarse, details of the branch crack and the changes in the crack surface orientation are not accurately captured in the CG model. Secondly, a discretization of 14×8 nodes is considered, as shown in

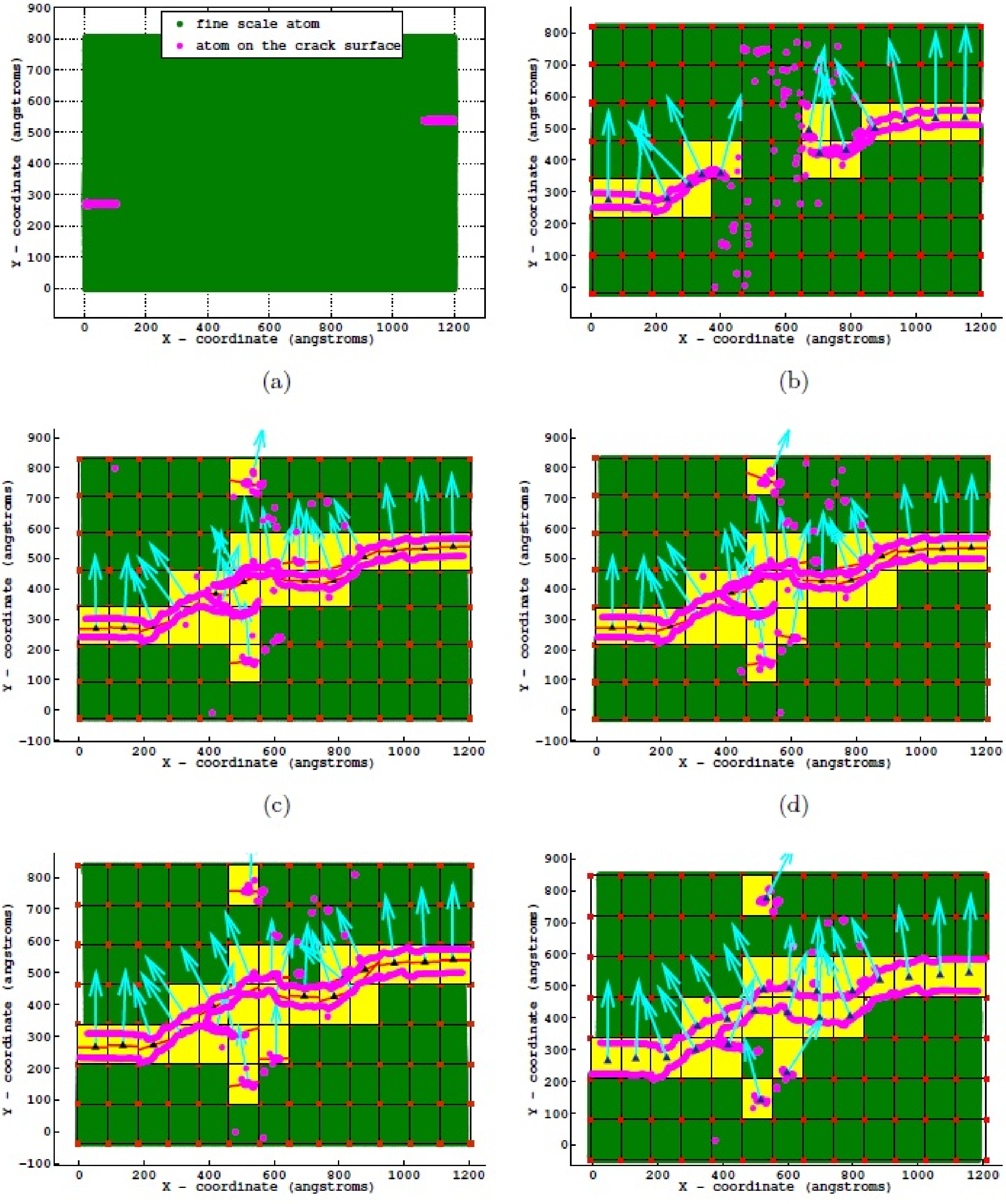

(a) (b) (c) (d) (e) (f)

Figure 3.9: Development of an equivalent coarse scale model of a given fine scale model, for a dynamic crack propagation of double edge crack model. (a) Initial configuration of the fine model. Fine model at (b) 48 pico-seconds (c) 78 pico-seconds (d) 88 pico-seconds (e) 108 pico-seconds and (f) 180 pico-seconds, along with the highlighted atoms on the crack surface, crack regions and their normals.

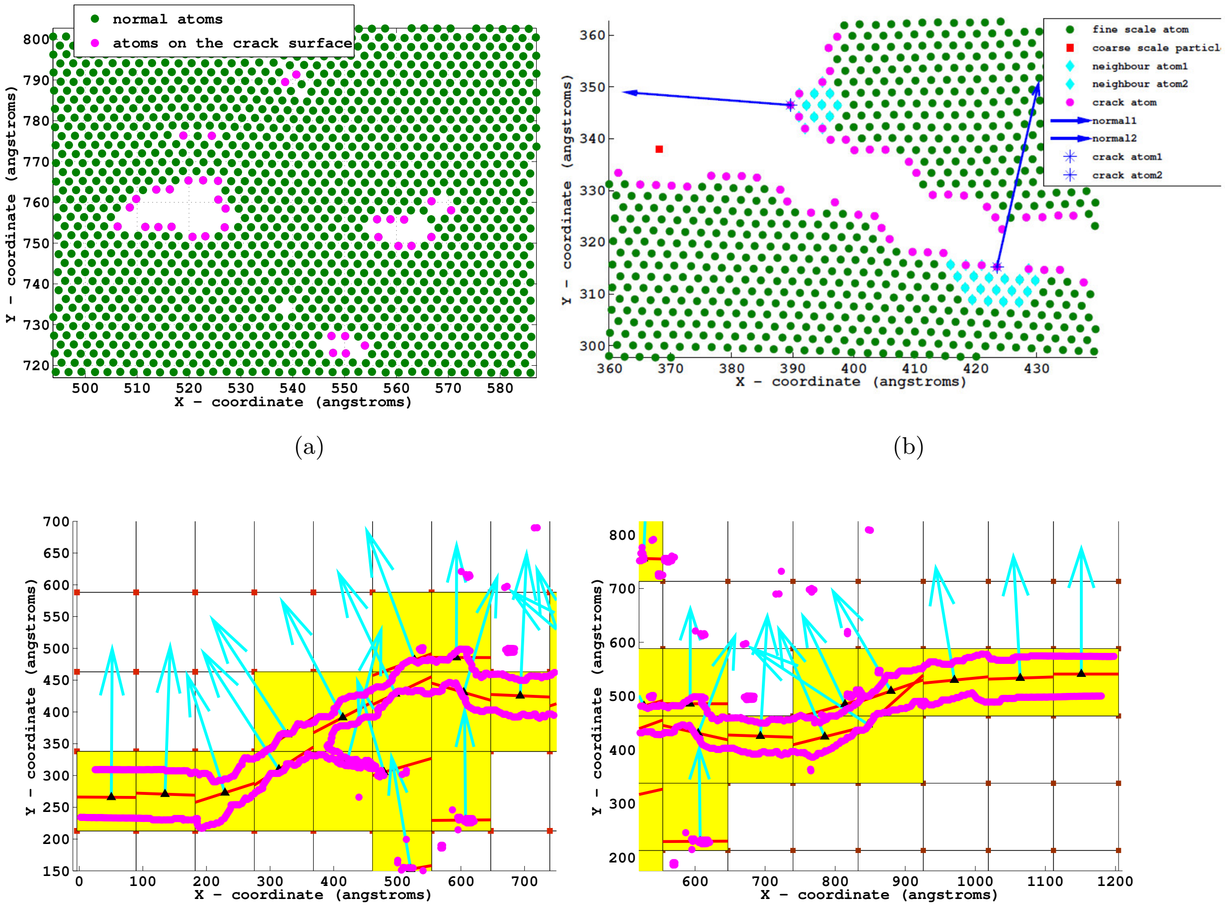

(a) (b)

(c) (d)

Figure 3.10: A closeup of the deformed configuration at 108 pico-seconds. (a) Upper right area of fine scale model in Fig. 3.9(e), displaying small cracks and dislocation cores. (b) Normals of two atoms on the crack surface on the crack surface along with their neighbours. (c) A closeup of Fig. 3.9(e) on the left half. (d) A closeup of Fig. 3.9(e) on the right half.

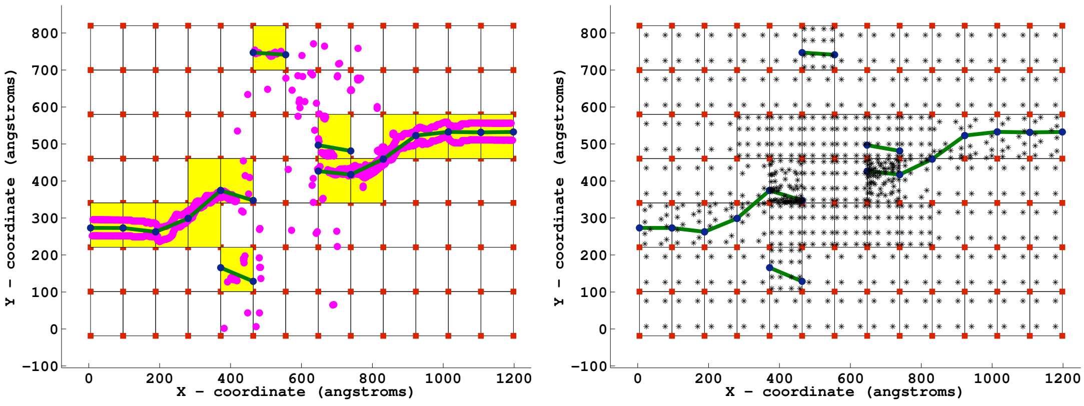

(a) (b)

Figure 3.11: CG model with approximated equivalent crack surface at 48 pico-seconds. (a) Atoms on the crack surface along with the highlighted regions containing the atoms on the crack surface and the approximated equivalent crack. (b) Gauss point distribution used to calculate the system energy.

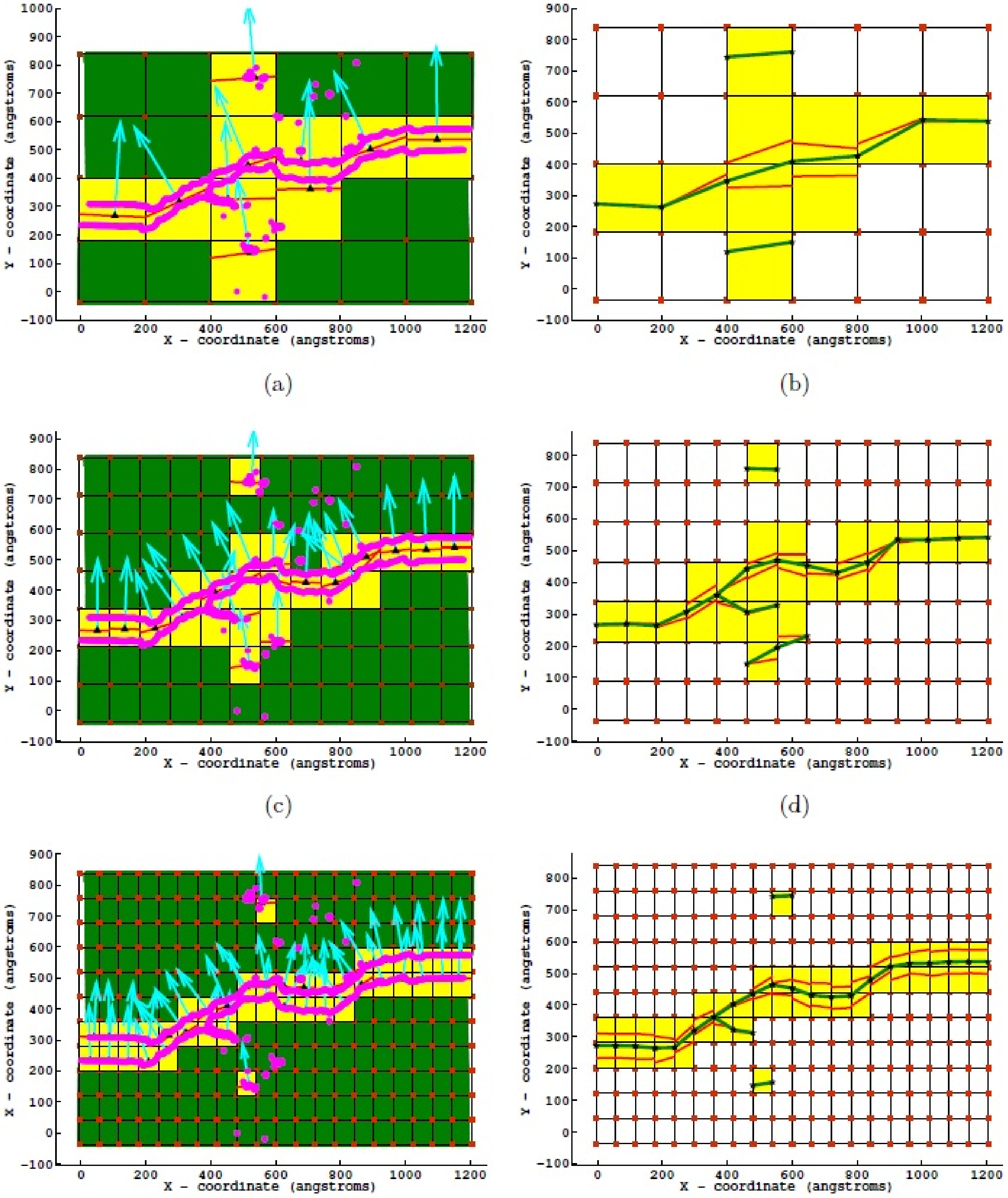

(a) (b)

(c) (d)

(e) (f)

Figure 3.12: Approximated crack surface with different discretizations of (a) 7×5 (c) 14×8 and (d) 21×12 nodes, along the x and y directions, respectively. The corresponding approximated equivalent crack surfaces are shown in subplots (b), (d) and (f), respectively.

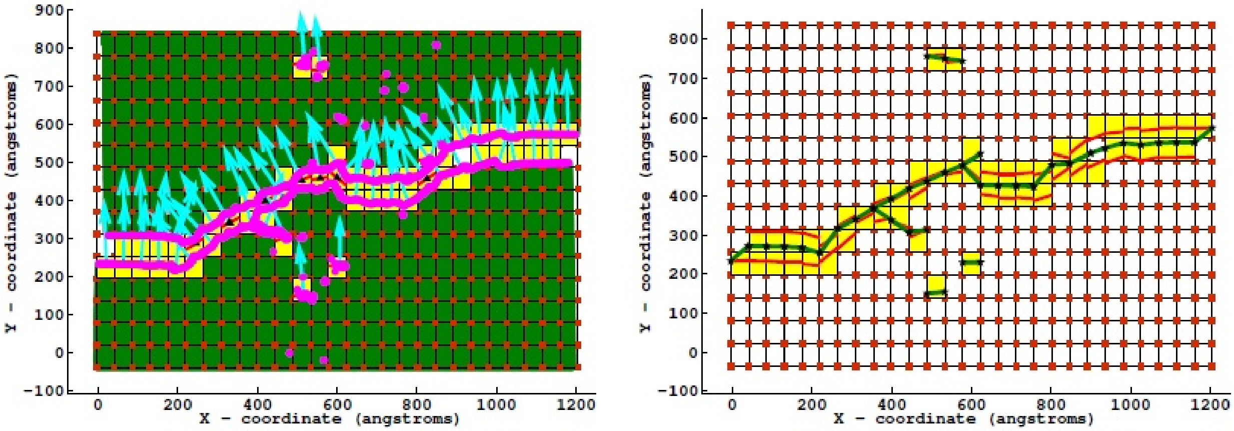

(a) (b)

Figure 3.13: Approximated crack surface with different discretizations of (a) 28×16 nodes, along the x and y directions, respectively. (b) The corresponding approximated equivalent crack surface.

Fig. 3.12(c). The discretization is selected so that in majority of the cases, the top and bottom surfaces of the crack lies in the same identified region containing the atoms on the crack surface. The corresponding approximated equivalent crack surface is plotted in Fig. 3.12(d). In this case, some of the branch cracks are captured and the crack surface orientation is reasonably approximated. Thirdly, a discretization of 21×12 nodes is selected, refer Fig. 3.12(e). Note that the selected discretization allows the top and bottom surfaces of the crack to lie in two different adjacent identified regions containing the atoms on the crack surface. Therefore, for a given location in the x direction, two normals of the crack regions are observed; refer to Fig. 3.12(f) for the corresponding approximated equivalent crack surface. The crack surface orientation and the branch cracks are accurately captured here. Finally, consider a discretization of 21×16 nodes, refer to Fig. 3.13(a). Similar to the third case, the top and bottom surfaces of the crack lie in two different identified regions containing the atoms on the crack surface. Due to the sufficiently refined discretization, the approximated equivalent crack surface in Fig. 3.13(b), closely agrees with the fine scale model. Subsequently, we consider the discretization of 14×8 nodes in all the calculations for the CG model. Table 3.3 gives the system energy estimated from the fine scale model and the CG model at different times. The minimum and maximum percentage errors are range from -2.79% and 6.01%, respectively.

The effect of the value of CSP in identifying the atoms crack surface is studied in Fig. 3.14. Varying CSP values of 1.5, 2.0, 2.5, 3.1, 3.25 and 3.5 are considered and the corresponding atoms on the crack surface are plotted in Fig. 3.14(a), Fig. 3.14(b), Fig. 3.14(c), Fig. 3.14(d), Fig. 3.14(e) and Fig. 3.14(f), respectively. The number of atoms on the crack surface starts reducing when the CSP value is greater than 2.0. The number of atoms on the crack surface

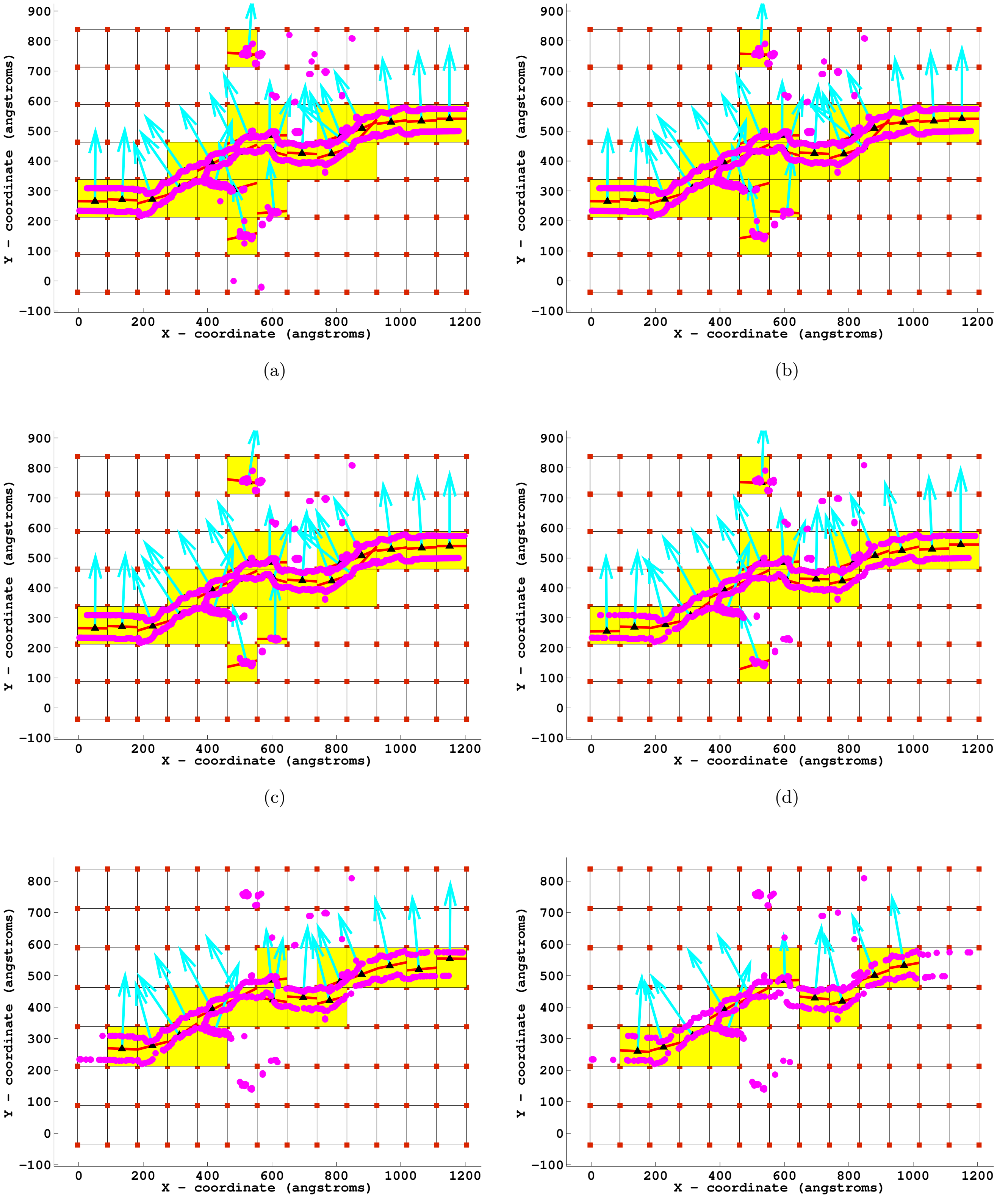

(a) (b) (c) (d) (e) (f)

Figure 3.14: Atoms on the crack surface based on different values CSP (a) 1.5 (b) 2.0 (c) 2.5 (d) 3.1 (e) 3.25 and (f) 3.5. The number of atoms on the crack surface starts reducing the CSP values more than 2.0.

Time (pico-seconds)	System energy from the fine model (E_{FS})	System energy from the CG model (E_{CS})	% error
0	2.320246e+05	2.257086e+05	-2.79
48	2.267228e+05	2.275007e+05	0.34
78	2.275510e+05	2.306417e+05	1.34
88	2.272985e+05	2.344631e+05	3.05
108	2.275401e+05	2.373267e+05	4.12
180	2.274723e+05	2.420270e+05	6.01

Table 3.3: Comparison of potential energies from Atomistic and CG models.

significantly reduced for the CSP values greater than 3.0, which in turn will result in poor approximation of the crack surface in the CG model.

3.2.3 Example 3: Crack branching and coalescence

In this example, we study a two dimensional crack branching problem. The atomistic simulations are carried out with the open source software Large-scale Atomic/Molecular Massively Parallel Simulator (LAMMPS). Consider a rectangular region with dimensions of 100.00Å×60.00Å in the x and y directions, respectively. LJ units are considered in all the calculations. The hexagonal lattice with lattice constant 0.8Å and unit atomic mass, is adopted in the fine scale. The Lennard-Jones potential is used to model the atomistic interactions with $\sigma = 1$Å and $\epsilon = 1$ eV. Neighbours within the domain of influence of 2.5Å are considered. The neighbourlist is updated after every 5 load steps. The full scale molecular statics model consists of 12161 atoms. A total displacement load of 30.65Å is applied in the y direction on the top and bottom edges, in 3065 equal load steps. Both the top and bottom edge atoms are fixed in the x and y directions, whereas the left and right edge atoms are fixed only in the x direction.

Deformed configurations at particular load steps and the corresponding approximated equivalent crack surfaces are plotted in Fig. 3.15. Fig. 3.15(a) shows the configuration of the fine-scale model at the final load step with a superimposed 12×9 rectangular discretization. Fig. 3.15(b) depicts the highlighted atoms on the crack surface, regions containing the atoms on the crack surface and their normals. The approximated crack surfaces in each crack region are plotted in Fig. 3.15(c). Fig. 3.15(d) shows the corresponding approximated equivalent CG model. To study the effect of the mesh size on the equivalent CG model, the atomistic model in Fig. 3.15(a) is discretized with 8×10 nodes in the x and y directions respectively, plotted Fig. 3.15(e). The corresponding equivalent CG model is shown in Fig. 3.15(f). The equivalent CG models in Fig. 3.15(e) and Fig. 3.15(f) are in agreement.

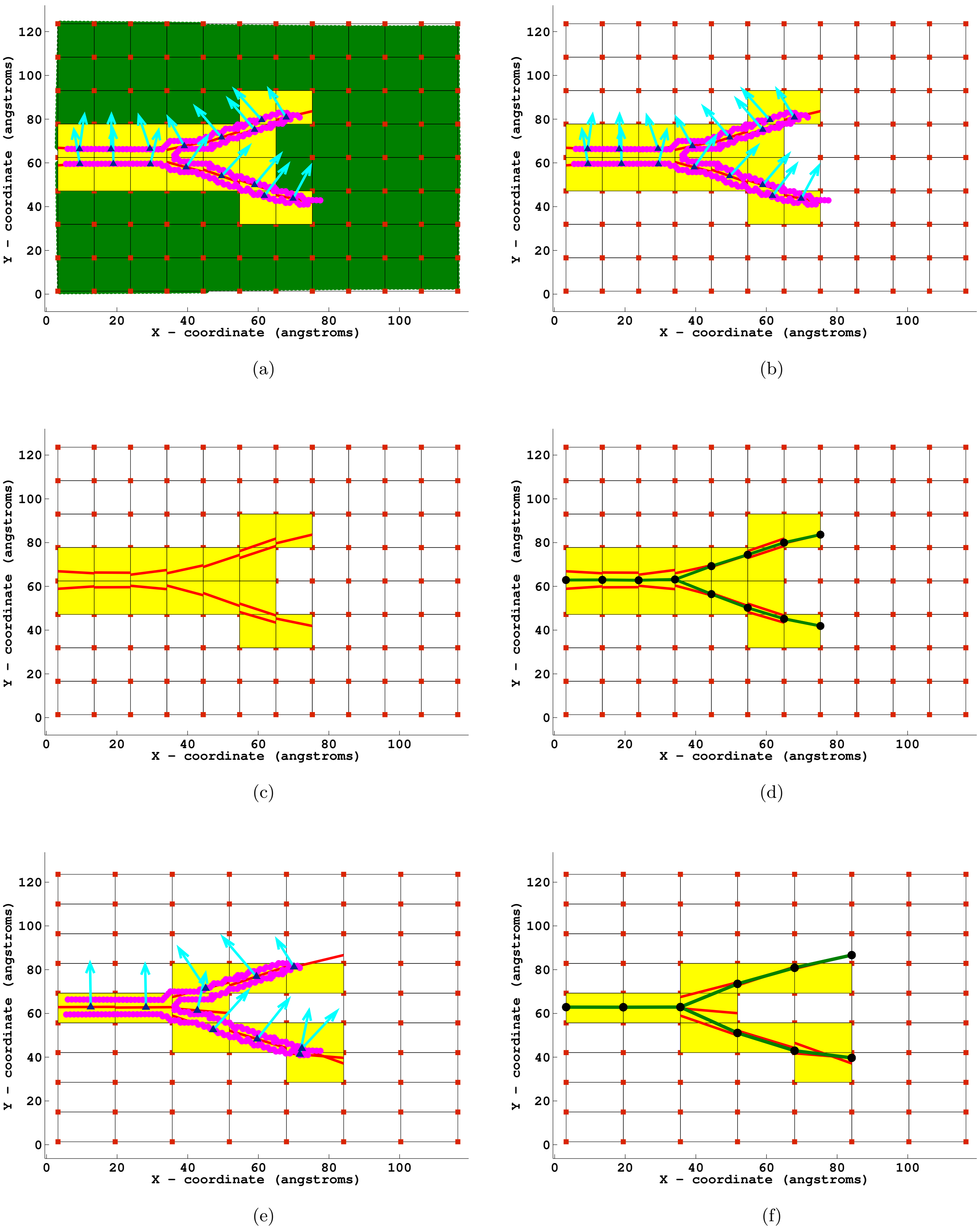

(a) (b) (c) (d) (e) (f)

Figure 3.15: Equivalent CG model of the crack propagation through branching. (a) Deformed configuration of the fine model at the final load step, superimposed with CG model discretization of 12×9 nodes along the x and y directions, respectively. (b) Highlighted atoms on the crack surface, crack regions and their normals of the fine model in Fig. 3.15(a) (c) crack paths in each crack region (d) equivalent approximated crack surface. (e) Configuration in Fig. 3.15(a) discretized with 8×10 nodes in the x and y directions, respectively (f) equivalent approximated crack surface of Fig. 3.15(e).

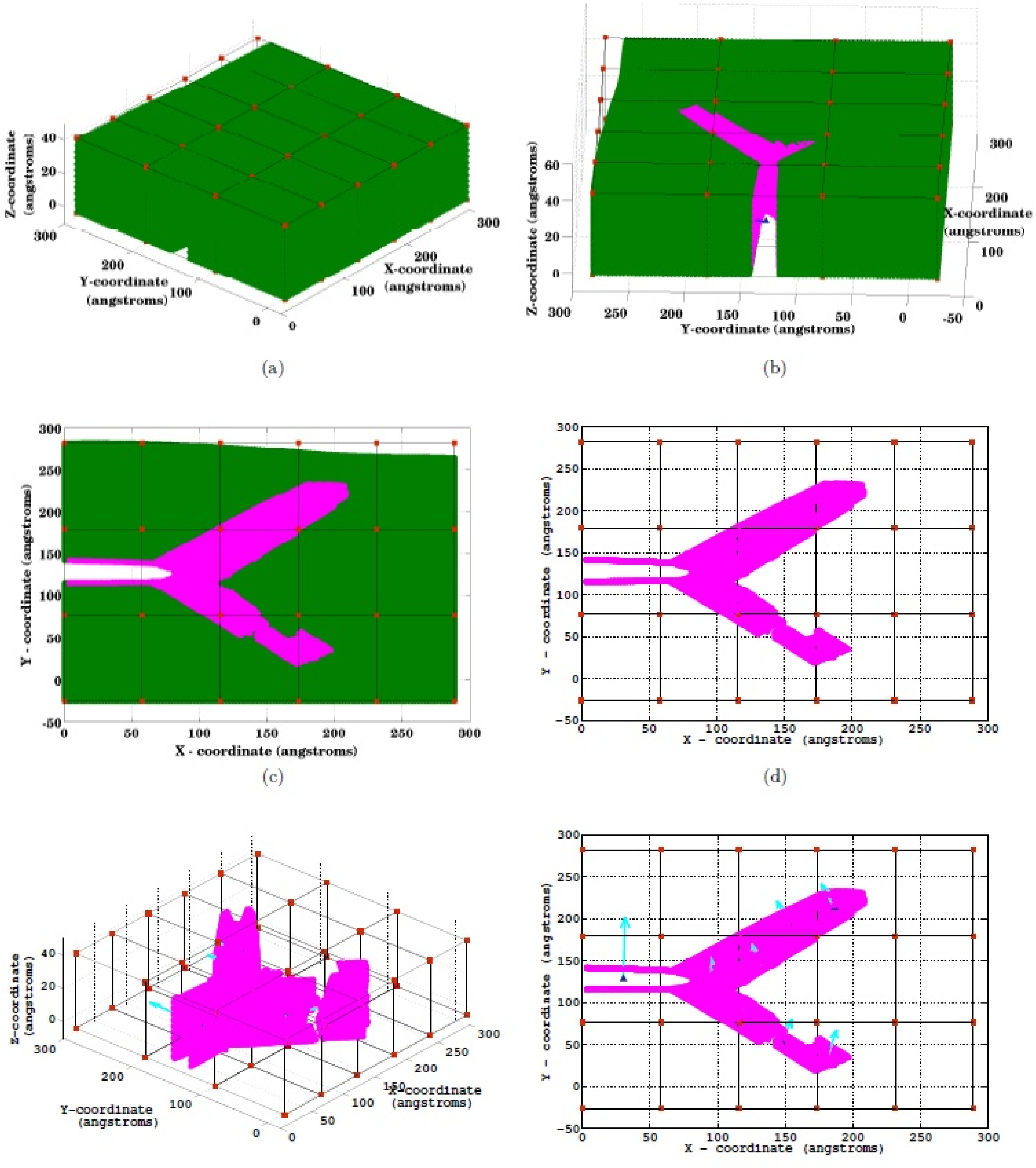

(a) (b)

(c) (d)

(e) (f)

Figure 3.16: Equivalent CG model of a 3D crack propagation with a discretization of 6×4×2. (a) Deformed configuration of the atomistic model at 18 pico-seconds. (b) Another view of Fig. 3.16(*a*) highlighting the atoms on the crack surface. (c) and (d) Two dimensional projection of Fig. 3.16(*a*). (e) Atoms on the crack surface and the normals of the crack regions in 3D. (f) Two dimensional projection of Fig. 3.16(*e*).

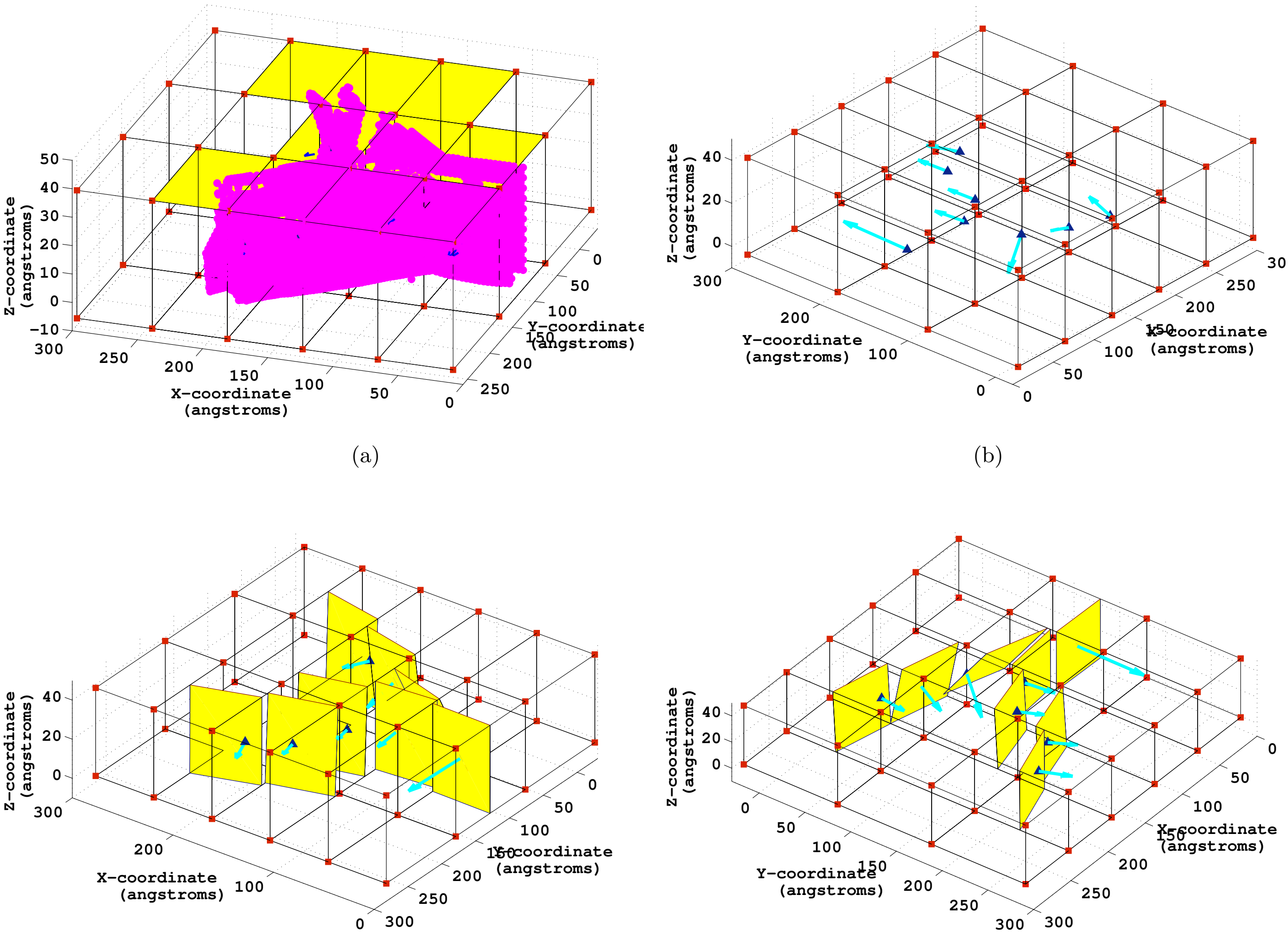

(a)

(b)

(c)

(d)

Figure 3.17: Equivalent CG model of a 3D crack propagation with a discretization of 6×4×2, showing crack surfaces and their normals. (a) Highlighted crack regions in 3D. (b), (c) and (d) The crack surfaces in each crack region and their normals in different views.

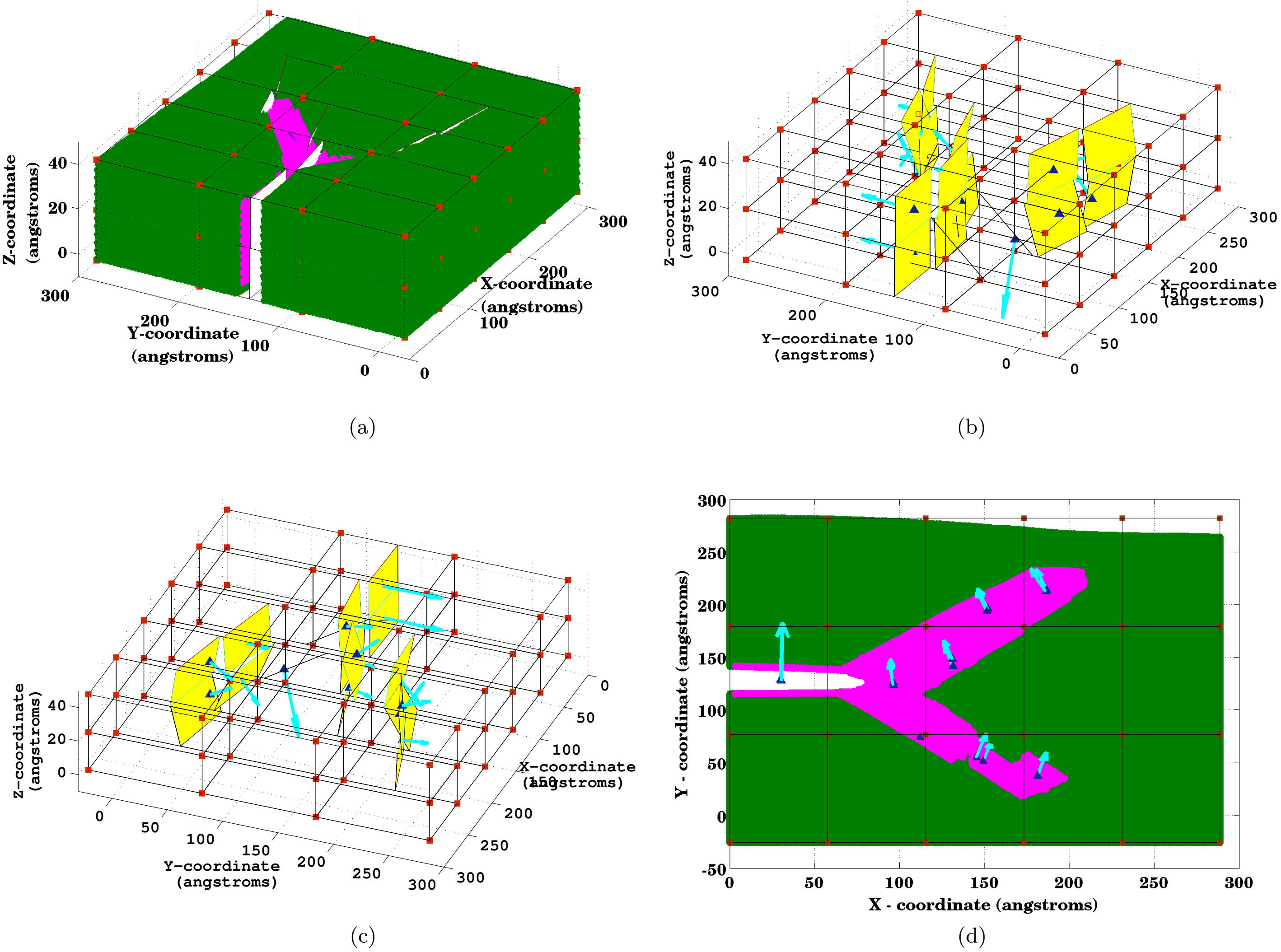

(a) (b)

(c) (d)

Figure 3.18: Equivalent CG model of a 3D crack propagation with a discretization of 6×4×3, showing crack surfaces and their normals. (a) The deformed configuration at 18 pico-seconds. (b) and (c) The crack surfaces in each crack region and their normals in different views. (d) Two dimensional projection of Fig. 3.18(a).

3.2.4 Example 4: Three dimensional crack growth

We study the three dimensional crack growth in the final example. Therefore, consider a three dimensional domain of dimensions 288.83Å×288.83Å×43.32Åwith an initial edge crack of length 72Å along the x direction, located at 144.415Å from the bottom surface, cutting through the entire thickness in the z direction. We consider the fcc lattice structure of copper with embedded atom model (eam) potential to simulate the atom-to-atom interactions in the fine scale. The adopted atomic weight of copper is 63.546 amu. Neighbours within the radius of 4.949Å are considered in building the neighbour list. The neighbour list is updated after every 5 load steps. The left and right edges are constrained in the x direction, whereas the top and bottom edges are moved with a velocity of 40 m/s. The forces in the x, y and z directions on the bottom edge atoms are fixed at 0.0. The atoms in between the top and bottom edges are ramped with minimum and maximum velocities of 0 m/s and 40 m/s, respectively.

Fig. 3.16(a) shows the deformed configuration of the atomistic model superimposed with the coarse scale discretization of 6×4×2 nodes along the x, y and z directions respectively, after 18000 time steps; the time step is equal to 1 pico-second. Another view of Fig. 3.16(a), highlighting the atoms on the crack surface is illustrated in Fig. 3.16(b). The two dimensional projection of Fig. 3.16(a) in the xy plane is plotted in Fig. 3.16(c). Fig. 3.16(d) highlights the atoms on the crack surface in the CG discretization. Fig. 3.16(e) plots the atoms on the crack surface and the normals of the crack regions in the 3D discretization. A 2D projection of Fig. 3.16(e) is shown in Fig. 3.16(f). The crack regions are highlighted in Fig. 3.17(a). The crack surfaces in each crack region and their normals, in different views are plotted in Fig. 3.17(b) to Fig. 3.17(d).

In order to study the effect of the discretization, the deformed configuration in Fig. 3.16(a) is discretized with 6×4×2 nodes along the x, y and z directions, respectively, as shown in Fig. 3.18(a). The crack surfaces, along with the normals in two different orientations are plotted in Fig. 3.18(b) and Fig. 3.18(c), respectively. The two dimensional projection of Fig. 3.18(a) in the xy plane is shown in Fig. 3.18(d), along with the normals of the crack surfaces.

3.3 Discussion

A coarse graining technique to upscale fracture pattern from an atomistic model to an equivalent CG model has been presented. The present method is the first of its kind. The developed CG technique can be applied to identify and upscale the defects like: cracks, dislocations and shear bands. Atoms lying on the crack surface in the fine scale model are separated from the atoms not on the crack surface through the centro symmetry parameter. A rectangular discretization is superimposed on the fine scale model to capture the atoms into rectangular cells. The crack path in each cell is approximated using the atoms on the crack surface and their neighbours. An equivalent crack surface in the coarse scale model is obtained by joining the cellular crack paths.

The performance of the method is demonstrated through four examples. In the first example, quasi-static propagation of an edge crack is considered. The upscaled crack pattern agree well with the deformed crack pattern in the fine scale. Also the error in the potential energies of both models agree reasonably well. The second example shows the CG approach for a complex crack pattern. The developed technique is tested for a crack branching and crack coalescence problem in the third example. In the final example, the present method is applied to a three dimensional problem. In all examples, the coarse-grained crack patterns agree well with the crack pattern from the fine-scale simulations.

The presented CG technique serves as a sound basis for future studies of adaptive propagation of complex crack patterns. The developed CG technique will be employed in the context of a concurrent multiscale models [74, 76, 84]. In future, we plan to develop an error estimator to determine the size of the fine scale domain (inside the coarse scale domain) and to drive an adaptive refinement in the context of concurrent multiscale methods for fracture.

Chapter 4

A meshless adaptive multiscale method for fracture

In this chapter[3], a meshless adaptive multiscale method for crack propagation is discussed. The coarse region is modeled by the differential reproducing kernel particle method. The crack in the coarse scale region is modeled by node enrichment. A molecular statics approach is employed in the fine scale where crack propagation is modeled naturally by breaking of bonds. The triangular lattice corresponds to the lattice structure of the (111) plane of an FCC crystal in the fine scale region. The Lennard-Jones potential is used to model the atom-atom interactions. The coupling between the coarse scale and fine scale is realized through ghost atoms. The ghost atom positions are interpolated from the coarse scale solution and enforced as boundary conditions on the fine scale. The fine scale region is adaptively refined and coarsened as the crack propagates. The centro symmetry parameter is used to detect the crack tip location. The method is implemented in two dimensions. The results are compared to pure atomistic simulations and show excellent agreement.

Meshless methods (MM) [3, 4, 38, 42, 46, 111, 124] are based on the idea of using the nodes in the zone of influence of a selected point to construct its approximation space. Popular meshless methods include the Element Free Galarkin (EFG) method [6], reproducing kernel particle method (RKPM) [8, 9], radial point interpolation method (RPIM) [5, 125], Meshless Local Petrov-Galerkin (MLPG) [126, 127], to name a few. Yang *et al* [128] have proposed a meshless collocation method based on the differential reproducing kernel (DRK) approximation. The main feature of the DRK is that the shape function of reproducing kernel (RK) approximants is replaced by a set of differential reproducing conditions. Therefore, it is not required to be directly differentiated, whereas in the EFG [6, 129] method the shape functions are directly differentiated. As a result, the number of degrees of freedom are reduced, improving the computational efficiency of the differential reproducing kernel particle (DRKP) method as compared to the RKPM. On the otherhand, the shape functions of the RK approx-

---

[3] This work is published in the Computational Material Science Journal [77].

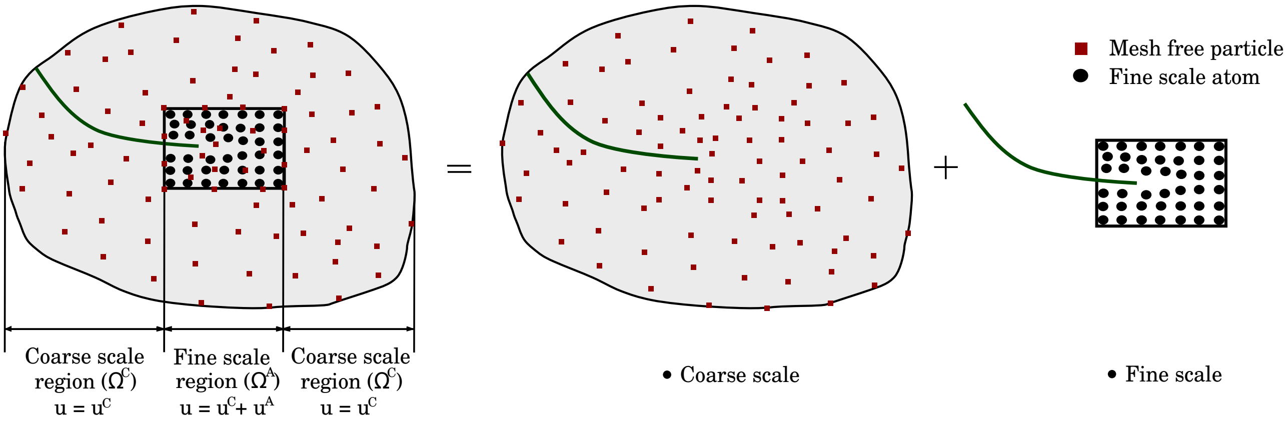
■ Mesh free particle
● Fine scale atom
Coarse scale region (Ω^C) u = u^C
Fine scale region (Ω^A) u = u^C+ u^A
Coarse scale region (Ω^C) u = u^C
=
+
• Coarse scale
• Fine scale

(a) (b) (c)

Figure 4.1: (a) Schematic of a coupled continuum-atomistic model. (b) Coarse scale domain with the crack. (c) Fine scale region containing the crack tip.

imants do not satisfy the Kronecker delta property, which necessitates to post possess. To resolve the difficulty in the DRK approximation, Chih Ping *et al.* [130–132] have proposed a meshless collocation method based on the DRKP method [130–133] satisfying the Kronecker delta property. The DRKP method is comparatively more expensive but allows for a more "natural" coupling between the two scales due to the meshless interpolation functions. The higher order continuity is also beneficial.

4.1 Meshless Adaptive Multiscale Method for Fracture (MAMMF)

The basic idea of the MAMMF is based on the decomposition of the domain into coarse and fine scale regions as shown in Fig. 4.1. The crack originates from the coarse scale region with the crack tip in the fine region. The coarse region is discretized by the DRKP method. The crack in the coarse scale region is modeled by node enrichment. Fracture in the fine scale is realized by restricting the interactions between the atoms on the crack surface. This is achieved by updating the neighbor list accordingly. The neighbour list is generated based on a radius of influence. The neighbourlist is not updated after each load step. As the crack starts to propagate, the centro symmetry parameter explained in section 3.1.2, is employed to identify the atoms on the crack surface and hence the location of the crack tip. Ghost atoms are located in the coarse region but within the cutoff radius of the atoms in the fine region. Their positions are interpolated from the coarse scale solution and enforced as the boundary conditions for the fine scale solution [69, 71, 73]. The fine scale region is adaptively refined and coarsened when the crack propagates [34, 74, 84].

4.1.1 Coarse scale model

The governing equations for large deformation problems will first be presented in the total Lagrangian formulation, where the conservation equations and constitutive equations are expressed in terms of the material coordinates $\mathbf{X}$. They will then be presented in the updated Lagrangian formulation, where the equations are described in the current configuration, see Rabczuk *et al.* [4].

Governing equations

Consider a body Ω in two dimensional vector space $\mathcal{R}^2$ with boundary Γ, as shown in Fig. 3.4. The crack is denoted by c on the surface Γ_c. The strong form of the equilibrium equation in the total Lagrangian description is given by

$$\nabla_0 \cdot \boldsymbol{\sigma}_e + \rho_0 \mathbf{b} = 0 \qquad \text{in } \Omega_0 \backslash \Gamma_0 \tag{4.1}$$

with the boundary conditions

$$\mathbf{n}_0 \cdot \boldsymbol{\sigma}_e = \bar{\mathbf{t}}_0 \qquad \text{on } \Gamma_0^{\mathrm{n}} \tag{4.2}$$

$$\mathbf{u} = \bar{\mathbf{u}} \qquad \text{on } \Gamma_0^{\mathrm{u}} \tag{4.3}$$

$$\mathbf{n}_0 \cdot \boldsymbol{\sigma}_e^- = \mathbf{n}_0 \cdot \boldsymbol{\sigma}_e^+ = 0 \qquad \text{on } \Gamma_0^{\mathrm{c}} \tag{4.4}$$

where $\boldsymbol{\sigma}_e$ is the engineering stress, $\mathbf{b}$ are the body forces, ρ_0 is the initial density, $\mathbf{u}$ is the displacement vector, $\mathbf{n}_0$ is the normal to the boundary in the initial configuration and $\bar{\mathbf{u}}$ and $\bar{\mathbf{t}}$ are the specified displacement and traction on the surfaces Γ_0^{u} and Γ_0^{n}, respectively.

Displacement field

We consider a displacement field which is discontinuous at the cracks and continuous elsewhere in the domain Ω, as shown in Fig. 3.4. The displacement field is decomposed into standard/continuous and discontinuous/enriched part;

$$\mathbf{u} = \mathbf{u}^{\mathrm{cont}} + \mathbf{u}^{\mathrm{enr}} \tag{4.5}$$

where $\mathbf{u}^{\mathrm{cont}}$ is the continuous component and $\mathbf{u}^{\mathrm{enr}}$ is the discontinuous component. The meshfree approximation of equation (4.5) is given by

$$\mathbf{u}^{\mathrm{h}}(\mathbf{X}) = \sum_{I \in \mathcal{S}} N_I^{\mathrm{cont}}(\mathbf{X}) \mathbf{u}_I + \sum_{I \in \mathcal{S}^{\mathrm{c}}} N_I^{\mathrm{enr}}(\mathbf{X}) \mathbf{q}_I \tag{4.6}$$

where N_I^{cont} and N_I^{enr} are the displacement interpolation functions in the continuous and discontinuous domains, respectively, as shown in Fig. 4.2. The nodal parameters associated to the continuous and discontinuous displacement field are denoted by $\mathbf{u}_I$ and $\mathbf{q}_I$, respectively.

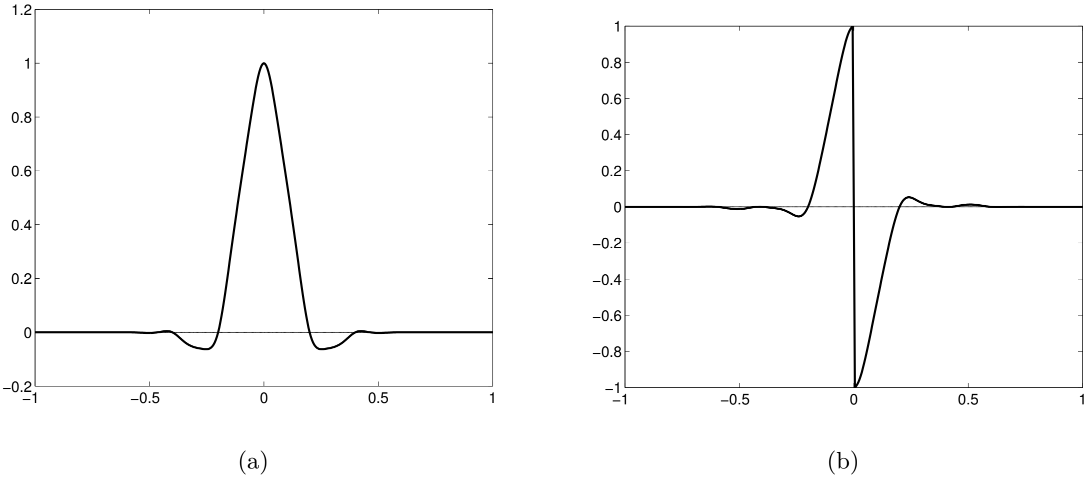

Figure 4.2: Shape functions in (a) the continuous domain and (b) the discontinuous domain.

In the DRKP method, it is assumed that there are n^{P} discrete nodes randomly selected and located at $\mathbf{x} = \mathbf{x}_1, \mathbf{x}_2, ..., \mathbf{x}_{n^{\mathrm{P}}}$, respectively in the domain Ω^{C}. The DRKP interpolant function $N_I^{\mathrm{cont}}(\mathbf{X})$ is defined as

$$N_I^{\mathrm{cont}}(\mathbf{X}) = \hat{N}_I(\mathbf{X}) + \bar{N}_I(\mathbf{X}). \tag{4.7}$$

We choose the quartic spline given by

$$\hat{N}(s) = \begin{cases} -3s^4 + 8s^3 - 6s^2 + 1 & for \;\; s \leq 1 \\ 0 & for \;\; s > 1 \end{cases} \tag{4.8}$$

with

$$s = \frac{\sqrt{(\mathrm{X} - \mathrm{X}_I)^2 + (\mathrm{Y} - \mathrm{Y}_I)^2 (\frac{a_x}{a_y})^2}}{a_x} \tag{4.9}$$

in which a_x and a_y denote the principle radii of curvature of the elliptic zone of influence. $\bar{N}_I(\mathbf{x})$ in equation (4.6), is introduced to impose the n^{th} order reproducing conditions and is given by

$$\bar{N}_I(\mathbf{X}) = w_a(\mathbf{X} - \mathbf{X}_I)\mathbf{P}^{\mathrm{T}}(\mathbf{X} - \mathbf{X}_I)\bar{\mathbf{z}}(\mathbf{X}) \tag{4.10}$$

where the weight function $w_a(\mathbf{X} - \mathbf{X}_I)$ is centered at $\mathbf{X}_I$, defined by the normalized Gaussian function given by

$$w_a(s) = \begin{cases} \frac{e^{-(\frac{s}{\alpha})^2} - e^{-(\frac{1}{\alpha})^2}}{1 - e^{-(\frac{1}{\alpha})^2}} & for \;\; s \leq 1 \\ 0 & for \;\; s > 1 \end{cases} \tag{4.11}$$

where α is 0.3. The set of complete n^{th} order polynomial functions are given by

$$\mathbf{P}^{\mathrm{T}}(\mathbf{X}-\mathbf{X}_I) = \left[1, (\mathrm{X}-\mathrm{X}_I), (\mathrm{Y}-\mathrm{Y}_I), (\mathrm{X}-\mathrm{X}_I)^2, (\mathrm{X}-\mathrm{X}_I)(\mathrm{Y}-\mathrm{Y}_I), (\mathrm{Y}-\mathrm{Y}_I)^2, ...(\mathrm{X}-\mathrm{X}_I)^n\right] \tag{4.12}$$

For an n^{th} order complete polynomial basis, a set of reproducing conditions can be obtained to determine $\bar{\mathbf{z}}_i(\mathbf{X}), i = 1, 2, ..., n^{\mathrm{B}}$, where n^{B} are the total number of basis functions given by (n+1)(n+2)/2. It can be shown that the reproducing conditions are given by

$$\sum_{I=1}^{n^{\mathrm{P}}} [\hat{N}_I(\mathbf{X}) + \bar{N}_I(\mathbf{X})] x_I^g y_I^h = x^g y^h, \quad \text{where} \quad g + h \leq n. \tag{4.13}$$

The reproducing conditions in equation (4.13) can be explicitly estimated for several combinations of g and h values ChihPing2011, and expressed in matrix form by

$$\sum_{I=1}^{n^{\mathrm{P}}} \mathbf{P}(\mathbf{X}-\mathbf{X}_I)\bar{N}_I(\mathbf{X}) = \mathbf{P}(\mathbf{0}) - \sum_{I=1}^{n^{\mathrm{P}}} \mathbf{P}(\mathbf{X}-\mathbf{X}_I)\hat{N}_I(\mathbf{X}) \tag{4.14}$$

where $\mathbf{P}(\mathbf{0}) = [1 \ 0 \ 0 \ ... \ 0]^{\mathrm{T}}$. Substituting the expression for $\bar{N}_I(\mathbf{X})$ from equation (4.10) into equation (4.14), the undetermined function $\bar{\mathbf{z}}(\mathbf{X})$ can be estimated as

$$\bar{\mathbf{z}}(\mathbf{X}) = \mathbf{A}^{-1}(\mathbf{X}) \left[\mathbf{P}(\mathbf{0}) - \sum_{I=1}^{n^{\mathrm{P}}} \mathbf{P}^{\mathrm{T}}(\mathbf{X}-\mathbf{X}_I)\hat{N}_I(\mathbf{x}) \right] \tag{4.15}$$

where

$$\mathbf{A}(\mathbf{X}) = \sum_{I=1}^{n^{\mathrm{P}}} \mathbf{P}(\mathbf{X}-\mathbf{X}_I) w_a(\mathbf{X}-\mathbf{X}_I) \mathbf{P}^{\mathrm{T}}(\mathbf{X}-\mathbf{X}_I). \tag{4.16}$$

The enriched shape functions in equation (4.6), are expressed by the product of the standard shape function and the sign function $\mathcal{H}$,

$$N_I^{\mathrm{enr}}(\mathbf{X}) = N_I^{\mathrm{cont}}(\mathbf{X})\mathcal{H}(f_I(\mathbf{X})) \tag{4.17}$$

where

$$\mathcal{H}(\xi) = \begin{cases} 1 & \forall \ \xi > 0 \\ -1 & \forall \ \xi < 0. \end{cases} \tag{4.18}$$

and

$$f_I(\mathbf{X}) = \mathbf{n}_0 \cdot (\mathbf{X} - \mathbf{X_I}) \tag{4.19}$$

where $\mathbf{n}_0$ is the normal of the split nodes in the initial configuration, which is estimated from the fine scale.

Variational formulation

The governing equations in weak form can be stated as:

$$\text{find} \quad \mathbf{u} \in U \quad \forall \delta\mathbf{u} \in U_0, \tag{4.20}$$

such that

$$\delta W = \delta W_{\text{int}} - \delta W_{\text{ext}} = 0 \tag{4.21}$$

where $\mathbf{u} = \bar{\mathbf{u}}$ on Γ_u and $\mathbf{u} \in \mathcal{H}^1(\Omega)$, δW_{int} is the first variation of the internal energy

$$\delta W_{\text{int}} = \int_{\Omega_0 \backslash \Gamma_0^{\text{c}}} (\nabla \delta \mathbf{u})^T \boldsymbol{\sigma}_e d\Omega \tag{4.22}$$

and δW_{ext} is the virtual work from the external forces

$$\delta W_{\text{ext}} = \int_{\Omega_0 \backslash \Gamma_0^{\text{c}}} \rho_0 \delta \mathbf{u} \cdot \mathbf{b} d\Omega_0 + \int_{\Gamma_0^{\text{n}}} \delta \mathbf{u} \cdot \bar{\mathbf{t}}_0 d\Gamma. \tag{4.23}$$

The test functions $\delta\mathbf{u}^{\text{h}}(\mathbf{X})$ have a similar structure as the trial functions

$$\delta\mathbf{u}^{\text{h}}(\mathbf{X}) = \sum_{I \in \mathcal{S}} N_I^{\text{cont}}(\mathbf{X}) \delta \mathbf{u}_I + \sum_{I \in \mathcal{S}^c} N_I^{\text{enr}}(\mathbf{X}) \delta \mathbf{q}_I. \tag{4.24}$$

Substituting equations (4.6) and (4.24) into equation (4.21) and noting that $\delta\mathbf{u}_I$ and $\delta\mathbf{q}_I$ are arbitrary, we obtain the discrete system of equations as

$$\mathbf{K}_{IJ} \cdot \mathbf{d}_J = \mathbf{f}_I^{\text{ext}} \tag{4.25}$$

where $\mathbf{K}_{IJ}$ is the stiffness matrix and $\mathbf{f}_I^{\text{ext}}$ denote the external force vector and $\mathbf{d}_J$ is the vector containing the nodal parameters. The stiffness matrix is given by

$$\mathbf{K}_{IJ} = \int_{\Omega_0 \backslash \Gamma_0{}^c} \begin{bmatrix} \mathbf{K}_{IJ}^{uu} & \mathbf{K}_{IJ}^{uq} \\ \mathbf{K}_{IJ}^{qu} & \mathbf{K}_{IJ}^{qq} \end{bmatrix} \mathrm{d}\Omega \tag{4.26}$$

where

$$\begin{aligned} \mathbf{K}_{IJ}^{uu} &= \frac{\partial N_I^{\text{cont}}(\mathbf{X})}{\partial \mathbf{X}} \mathbf{C} \frac{\partial N_J^{\text{cont}}(\mathbf{X})}{\partial \mathbf{X}}, \\ \mathbf{K}_{IJ}^{uq} &= \frac{\partial N_I^{\text{cont}}(\mathbf{X})}{\partial \mathbf{X}} \mathbf{C} \frac{\partial N_J^{\text{cont}}(\mathbf{X}) \mathcal{H}(\mathbf{f}_J(\mathbf{X}))}{\partial \mathbf{X}}, \\ \mathbf{K}_{IJ}^{qu} &= \frac{\partial N_I^{\text{cont}}(\mathbf{X}) \mathcal{H}(\mathbf{f}_I(\mathbf{X}))}{\partial \mathbf{X}} \mathbf{C} \frac{\partial N_J^{\text{cont}}(\mathbf{X})}{\partial \mathbf{X}}, \\ \mathbf{K}_{IJ}^{qq} &= \frac{\partial N_I^{\text{cont}}(\mathbf{X}) \mathcal{H}(\mathbf{f}_I(\mathbf{X}))}{\partial \mathbf{X}} \mathbf{C} \frac{\partial N_J^{\text{cont}}(\mathbf{X}) \mathcal{H}(\mathbf{f}_J(\mathbf{X}))}{\partial \mathbf{X}}, \end{aligned} \tag{4.27}$$

where **C** is the matrix of material constants. The expressions for the nodal forces can be obtained as Rabczuk2004IJNME

$$\mathbf{f}_I^{\mathrm{ext}} = \int_{\Omega_0 \backslash \Gamma_0^{\mathrm{c}}} N_I^{\mathrm{cont}}(\mathbf{X})^{\mathbf{T}} \mathbf{b} \, \mathrm{d}\Omega + \int_{\Omega_0 \backslash \Gamma_0^{\mathrm{c}}} N_J^{\mathrm{enr}}(\mathbf{X})^{\mathbf{T}} \mathbf{b} \, \mathrm{d}\Omega. \tag{4.28}$$

4.1.2 Fine scale model

In molecular statics (MS) the objective is to determine the positions of the atoms for the given boundary conditions, by minimizing the system's potential energy. The total potential energy of the system is given by

$$\Pi = W^{\mathrm{int}} - W^{\mathrm{ext}} \tag{4.29}$$

where W^{int} represents the internal energy of the system and W^{ext} is the external work done on the system. Consider the simplest atom-atom interactions in which the potential energy is only a function of the distance between two atoms, the total internal energy of the system is given by summing the energies of all the atomic bonds over all the atoms, as given below:

$$W^{\mathrm{int}} = \frac{1}{2} \sum_{\alpha=1}^{n^{\mathrm{A}}} \sum_{\beta \neq \alpha}^{n^{\mathrm{A}}} V(r_{\alpha\beta}) \tag{4.30}$$

where $V(r_{\alpha\beta})$ is the bond potential between the atoms α and β, separated by distance $r_{\alpha\beta}$. The system potential energy will be minimum, when the first derivative of the potential function with respect to the positions of the atoms goes to zero. We use the Lennard-Jones potential given by

$$V(r_{\alpha\beta}) = 4\epsilon \left[\left(\frac{\sigma}{r_{\alpha\beta}} \right)^{12} - \left(\frac{\sigma}{r_{\alpha\beta}} \right)^{6} \right] \tag{4.31}$$

where σ and ϵ are the specific Lennard-Jones parameters. The energy minimization is carried out using the conjugate gradient method.

4.1.3 Coupling the coarse and fine scales

The coupling is realized through ghost atoms. The positions of the ghost atoms are interpolated from the coarse scale solution, as illustrated in Fig. 4.3. Let β be the index of the ghost atoms; the corresponding ghost atom displacements are given by

$$\mathbf{u}_\beta = \sum_{I \in \mathcal{S}} N_I^{\mathrm{cont}}(\mathbf{X}_\beta) \mathbf{u}_I + \sum_{I \in \mathcal{S}^{\mathrm{C}}} N_I^{\mathrm{cont}}(\mathbf{X}_\beta) \mathcal{H}(f_I(\mathbf{X}_\beta)) \mathbf{q}_I. \tag{4.32}$$

The ghost atom positions estimated from equation (4.32), are applied as boundary conditions on the fine scale model. The estimation of the ghost atom positions using only the coarse scale

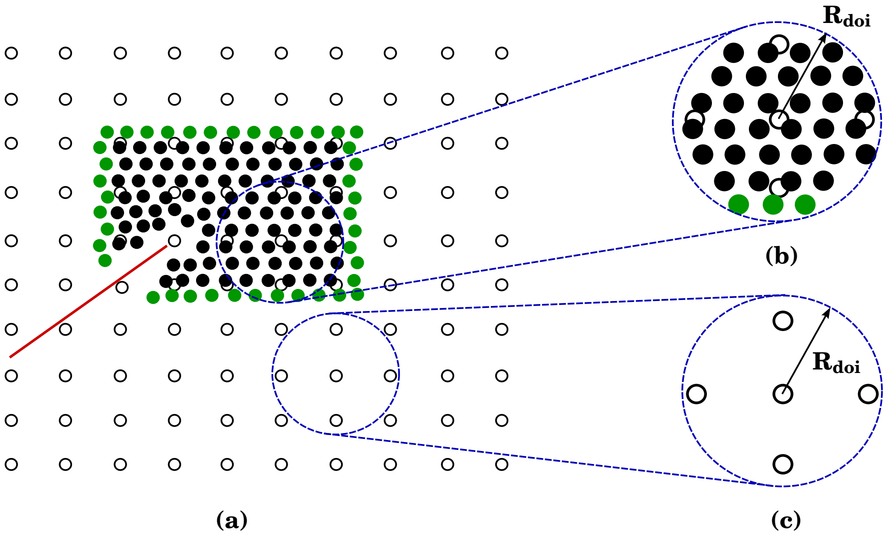

Figure 4.3: (a) Schematic of a multiscale model with initial crack. Unfilled circles denote the nodes in the coarse scale and the filled circles are the fine scale atoms. (b) A closeup of the coupling region within the radius of influence and (c) a closeup of the coarse region within the domain of influence.

component of the displacement will impose a constraint that does not exist in the original problem Qian2003. However for quasi-static problems, such an error can be controlled by properly choosing the interface of the coupling region.

4.1.4 Cracking criteria

The atoms on the crack surface and hence the atoms around the crack tip are identified by the CSP in the fine scale region. Therefore, consider an atom α in the fine scale model with the face centered cubic (fcc) lattice structure. Let β denote the neighbours of α. The centro symmetry parameter of an atom α is defined as Plimpton1998

$$\mathrm{CSP}_{\alpha} = \sum_{\beta=1}^{n^{\mathrm{nb}}/2} |\mathbf{r}_{\alpha\beta} + \mathbf{r}_{\alpha(\beta+n^{\mathrm{nb}}/2)}|^2 \tag{4.33}$$

where n^{nb} are the total number of nearest neighbours of atom α and $\mathbf{r}_{\alpha\beta}$ and $\mathbf{r}_{\alpha(\beta+n^{\mathrm{nb}}/2)}$ are the distance between the atoms α and β and α and $(\beta + n^{\mathrm{nb}}/2)$, respectively. In an fcc lattice structure there are 6 nearest neighbours (n^{nb}) for any atom α in the fine scale domain. Therefore, the CSP of the atom α is given by

$$\mathrm{CSP}_{\alpha} = \sum_{\beta=1}^{3} |\mathbf{r}_{\alpha\beta} + \mathbf{r}_{\alpha(\beta+3)}|^2 \tag{4.34}$$

We consider periodic crystal structures with symmetry in atomic arrangement for full scale atomistic models. Because of the symmetry of the lattice structure in a perfect crystal, the

Defect	$\mathrm{csp}_\alpha/a_0^2$	Range $\Delta\mathrm{csp}_\alpha/a_0^2$
Perfect lattice	0.0000	$\mathrm{csp}_\alpha < 0.1$
Partial dislocation	0.1423	$0.01 \leq \mathrm{csp}_\alpha < 2$
Stacking fault	0.4966	$0.2 \leq \mathrm{csp}_\alpha < 1$
Surface atom	1.6881	$\mathrm{csp}_\alpha > 1$

Table 4.1: Range of centro symmetry parameter for various defects, normalized by square of the lattice parameter a_0^2.

CSP of an atom in a perfect lattice is zero. Atoms on the crack surface will possess CSP values other than zero. Atoms on the crack surface can be selected corresponding to the range of CSP values normalized with the square of the lattice parameter, listed in table 4.1. In the present work, atoms on the crack surface are the atoms possessing normalized CSP values greater, or equal than 1.6881. The crack path in the coarse scale is obtained by a coarsening procedure as explained in Budarapu2014TAFM.

4.2 Adaptivity

The atoms on the crack surface and the hence the atoms around the crack tip are identified by the CSP in the fine scale region. The crack path in the coarse scale is approximated based on the CG technique [119], as explained in section 3.1.2. The two step adaptive procedure consists of an adaptive refinement and coarse graining:

1. Estimate the region in the coarse model Ω^{C} to be refined. Refine the model by expanding the atomistic region, i.e by converting the estimated coarse scale region into a fine scale region.
2. Estimate the region in the fine model Ω^{A} to be coarse grained. Coarsen the model by shrinking the fine scale region, i.e by converting the estimated fine scale region into a coarse scale region.

The fine scale domain is embedded within the 'boundaries' of the particles around the crack tip.The fine scale region contains the crack tip with a "sufficient" distance to the coupling boundary. At least one element layer is considered between the crack tip and the buffer layer and the minimum fine scale region is embedded within a 4×4 particle background mesh.

Let $\mathcal{P}$ be the set containing the total particles in the MAMMF. The load step just before an adaptive operation is denoted with subscript n, and subscript n+1 indicates the load step just after an adaptive operation. Therefore, $\mathcal{P}_{\mathrm{n}}^{\mathrm{C}}$ is the set of particles in the coarse scale domain and $\mathcal{P}_{\mathrm{n}}^{\mathrm{A}}$ is the set of fine scale atoms, at load step 'n' just before an adaptive operation; where $\mathcal{P}_{\mathrm{n}}^{\mathrm{A}} \subset \mathcal{P}$ and $\mathcal{P}_{\mathrm{n}}^{\mathrm{A}} \cap \mathcal{P}_{\mathrm{n}}^{\mathrm{C}} = \emptyset$. Let $\mathcal{P}_{\mathrm{n}}^{\mathrm{split}}$ be the set of completely split particles in the fine scale region, where $\mathcal{P}_{\mathrm{n}}^{\mathrm{split}} \subset \mathcal{P}_{\mathrm{n}}^{\mathrm{A}}$ and $\mathcal{P}_{\mathrm{n}}^{\mathrm{tip}}$ be the set of particles containing the crack tip before refinement. The sets $\mathcal{P}_{\mathrm{n+1}}^{\mathrm{refA}}$, $\mathcal{P}_{\mathrm{n+1}}^{\mathrm{refC}}$ and $\mathcal{P}_{\mathrm{n+1}}^{\mathrm{coaA}}$, $\mathcal{P}_{\mathrm{n+1}}^{\mathrm{coaC}}$ represent the fine scale and coarse

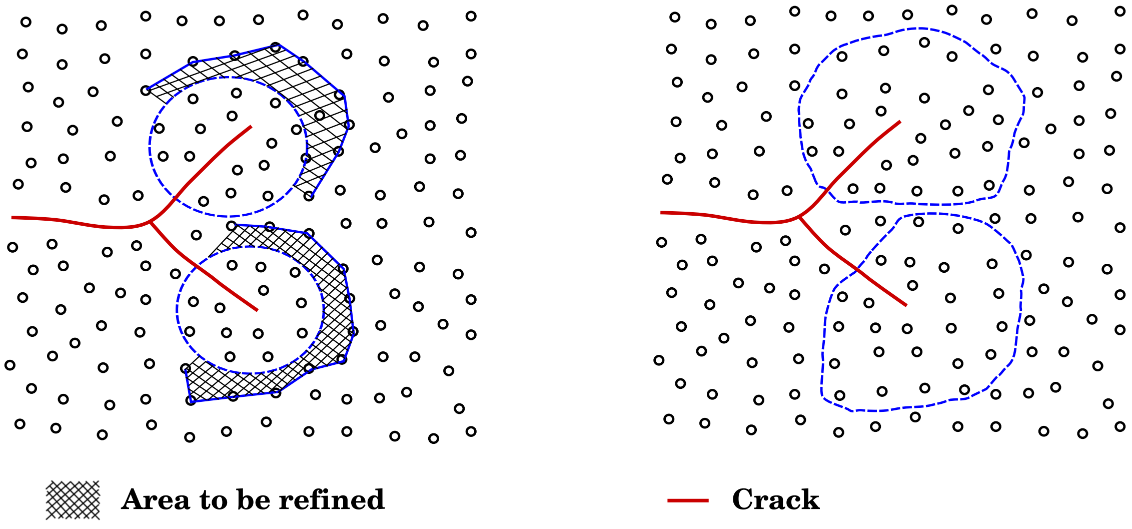

(a) **(b)**

Figure 4.4: Sketch of the adaptive refinement operation. (a) Flagged particles to be refined are hashed. (b) Increased atomistic region after the refinement operation.

scale particles at load step n + 1, just after adaptive refinement and coarsening operations, respectively. The set $\mathcal{P}^{\mathrm{minA}}_{\mathrm{n+1}}$ is the minimum set of particles in the fine scale domain after refinement, required to accurately capture the physics of the defects in the fine scale region.

4.2.1 Adaptive refinement

The major steps of the refinement operation (Fig. 4.4) are:

1. Identify the region to be refined.
2. Create and initialize the atoms in the region to be refined.
3. Identify and update the newly cracked atoms.
4. Update the fine and coarse scale regions.

Figure 4.4(a) shows the area to be refined. The final atomistic region is shown in Fig. 4.4(b). The steps of adaptive refinement operation are summarized as follows:

1. Store the particles before refining; in the fine scale region into the set $\mathcal{P}^{\mathrm{A}}_{n}$, in the coarse scale region into the set $\mathcal{P}^{\mathrm{C}}_{n}$ and the completely cracked particles in the fine scale region into the set $\mathcal{P}^{\mathrm{split}}_{n}$.
2. Calculate the atoms on the crack surface based on the CSP and store the regions containing the atoms on the crack surface into the set $\mathcal{P}^{\mathrm{csp}}_{n}$.
3. Estimate the neighbours of the regions containing the atoms on the crack surface in $\mathcal{P}^{\mathrm{csp}}_{n}$ and store them in $\mathcal{P}^{\mathrm{minA}}_{n+1}$.

4. Calculate the regions to be refined, $\mathcal{P}_{n+1}^{\text{refine}}$ by removing the fine scale region $\mathcal{P}_n^{\text{A}}$ from the set $\mathcal{P}_{n+1}^{\text{minA}}$.
5. Flag the regions to be refined and increase the atomistic domain by creating the atoms in the flagged elements.
6. Initialize the positions of the newly created atoms using equation (4.32).
7. Update the fine scale regions ($\mathcal{P}_{n+1}^{\text{refA}}$) after the refinement operation, by including the particle set $\mathcal{P}_n^{\text{refine}}$ into the set $\mathcal{P}_n^{\text{A}}$.
8. Update the coarse scale regions ($\mathcal{P}_{n+1}^{\text{refC}}$) after the refinement operation by deducting the atomistic regions $\mathcal{P}_{n+1}^{\text{refA}}$ from the total cells $\mathcal{P}$.
9. Update the neighbour list ($nlist_{n+1}$) of the fine scale atoms in the set $\mathcal{P}_{n+1}^{\text{refA}}$.
10. Identify the newly cracked particles in the fine scale region ($\mathcal{P}_{n+1}^{\text{nsplit}}$) by removing the split ($\mathcal{P}_n^{\text{split}}$) and tip ($\mathcal{P}_n^{\text{tip}}$) regions from the CSP particle set $\mathcal{P}_n^{\text{csp}}$.
11. Update the split nodes and the nodal connectivity table.
12. Update the split ($\mathcal{P}_{n+1}^{\text{split}}$) and tip ($\mathcal{P}_{n+1}^{\text{tip}}$) regions.

The detailed algorithm of selecting the particles to be refined, initializing the newly created atoms in the region identified for refinement and propagating the crack in the coarse scale region is explained in algorithm 3.

4.2.2 Adaptive coarsening

The major steps of the adaptive coarsening operation are:

1. Identify the region to be coarsened.
2. Delete the atoms in the region to be coarsened.
3. Update the fine and coarse scale particles.

The process of the adaptive coarsening operation is explained in Fig. 4.5. Let $\mathcal{P}_{\text{n}}^{\text{LP}}$ be the regions containing atoms on the crack surface at load step n, $\mathcal{P}_{\text{n}}^{\text{LP}} \subset \mathcal{P}_{\text{n}}^{A}$. Let $\mathcal{P}_{\text{n}}^{\text{BA}}$ be the regions which are in the fine scale domain attached to the coupling 'boundary', $\mathcal{P}_{\text{n}}^{\text{BA}} \subset \mathcal{P}_{\text{n}}^{A}$. The particles to be coarsened are the particles which are in both set $\mathcal{P}_{\text{n}}^{\text{LP}}$ and the set $\mathcal{P}_{\text{n}}^{\text{BA}}$ in front of the crack tip, $\mathcal{P}_{\text{n}}^{\text{coarsen}} = \mathcal{P}_{\text{n}}^{\text{LP}} \cap \mathcal{P}_{\text{n}}^{\text{BA}}$. The steps of the adaptive coarsening operation are:

1. Store the particles before refinement in the fine scale region into the set $\mathcal{P}_n^{\text{A}}$. Store the particles in the coarse scale region into the set $\mathcal{P}_n^{\text{C}}$ and the completely cracked particles in the fine scale region into the set $\mathcal{P}_n^{\text{split}}$.

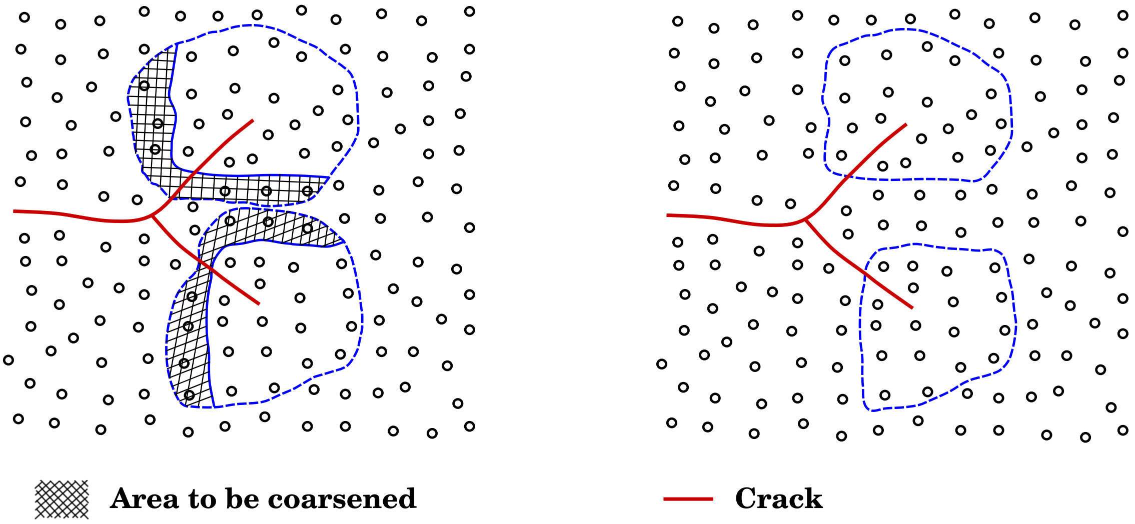

(a) **(b)**

Figure 4.5: Schematic of the adaptive coarsening operation. (a) Flagged particles to be coarsened are hashed. (b) Reduced atomistic region after the coarsening operation.

2. Calculate the atoms on the crack surface based on the CSP and store the regions containing the atoms on the crack surface into the set $\mathcal{P}_n^{\mathrm{csp}}$.
3. Estimate and store the regions containing the elements on the crack surface (far away from the crack tip) into $\mathcal{P}_n^{\mathrm{LE}}$.
4. Find the fine scale regions attached to the coupling boundary and store them in $\mathcal{P}_n^{\mathrm{BA}}$.
5. The regions to be coarsened ($\mathcal{P}_{n+1}^{\mathrm{coarsen}}$) are given by $\mathcal{P}_n^{\mathrm{LE}} \cap \mathcal{P}_n^{\mathrm{BA}}$.
6. Flag the regions to be coarsened and decrease the atomistic domain by deleting the atoms in the flagged regions.
7. Update the particle set in the fine scale region after the coarsening operation $\mathcal{P}_{n+1}^{\mathrm{coaA}}$ by deducting the set $\mathcal{P}_n^{\mathrm{coarsen}}$ from the set $\mathcal{P}_{n+1}^{\mathrm{refA}}$.
8. Update the particle set in the coarse scale region after the coarsening operation $\mathcal{P}_{n+1}^{\mathrm{coaC}}$ by deducting the atomistic regions $\mathcal{P}_{n+1}^{\mathrm{coaA}}$ from the total set $\mathcal{P}$.
9. Update the neighbour list of the fine scale atoms in the element set $\mathcal{P}_{n+1}^{\mathrm{coaA}}$.
10. Update the fine scale, coarse scale and the split particles for the next iteration.

To deduce the crack surface in the coarse scale domain, consider a deformed configuration of the fine scale model and the discretized coarse scale model as shown in Fig. 3.2(a). Atoms on the crack surface in the fine scale model can be separated based on the CSP values estimated from equation (4.34). Let the atoms in the fine model be separated into small rectangular cells surrounded by four nodes/particles in the coarse model. These cells are categorized into

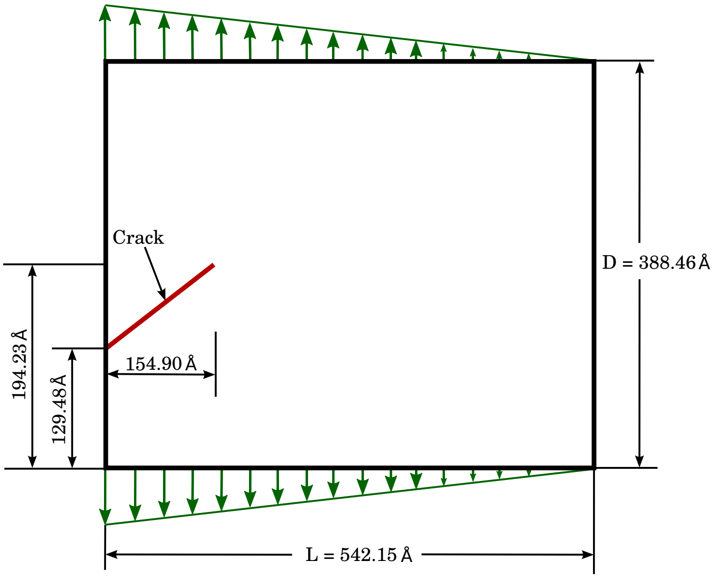

Figure 4.6: Geometry of the initial angled edge crack specimen along with the prescribed displacements studied in example 1.

cells containing atoms on the crack surface and atoms not on the crack surface. Refer [119] for details on obtaining an equivalent crack surface orientation in the coarse scale model. The algorithm explaining the coarsening steps is shown in algorithm 4.

4.3 Numerical examples

In this section we present three numerical examples. In the first example we consider the crack propagation of an initial angled edge crack. We study the crack propagation in a double edge notched specimen in the second example. The final example is on the mixed mode propagation of an edge crack.

4.3.1 Example 1: Angled edge crack propagation

Consider a specimen with a slanted edge crack as shown in Fig. 4.6. The triangular lattice corresponding to the (111) plane of an fcc crystal and a lattice constant 3.645Å is adopted in the fine scale. The distribution of the atoms in the fine scale region is based on the arrangement of the atoms on the the (111) plane of an fcc crystal. The Lennard-Jones potential is used with $\sigma = 2.29621$Å and $\epsilon = 0.467$ eV. As reference solution, we provide results based on a "pure" MS model. The full scale molecular statics model consists of 36157 active atoms and 768 ghost atoms. A total triangular displacement (refer to Fig. 4.6) of 15.678Å is prescribed on the top and bottom edges, in 42 equal load steps. Both the top and bottom edge atoms are fixed in the x and the y directions, whereas the left and right edge atoms are fixed only in the x direction. In our multiscale model, the coarse scale domain is discretized with 13×12 nodes, along the x and y direction, respectively. The initial set up including the fine scale

Example	Normalized time	
	MS	MAMMF
1	1.0	0.16
2	1.0	0.42
3	1.0	0.54

Table 4.2: Computational times of the MS and the MAMMF models in examples 1, 2 and 3.

region is illustrated in Fig. 4.7(d). The fine scale region consists of 3723 atoms in total containing 244 ghost atoms. As in the "pure" atomistic model, a total triangular displacement of 15.678Å is prescribed on the top and bottom edges, in 42 equal load steps.

The initial configuration of the full scale atomistic model is plotted in Fig. 4.7(a), highlighting the initial crack and the ghost atoms. Deformed configurations after the 16th and 42nd load steps are plotted in Fig. 4.7(b) and Fig. 4.7(c), respectively. Figure 4.7 shows the results of our multiscale model and Fig. 4.8 shows some closeups around the crack tip. The results of our multiscale methods are similar to those of the atomistic model. The atom positions from the atomistic and the coupled models are compared in Fig. 4.7(i). The normals and the CoG of the each coarse region containing the atoms on the crack surface are shown in Fig. 4.7(e). The normalized computational times are calculated as the ratio of the computational time with respect to the MS model. They are summarized in table 4.2. The computational cost of the MAMMF model is 16% of the MS model.

4.3.2 Example 2: Crack propagation in double-notched specimen

In the second example, we study the crack growth in a double-notched specimen as shown in Fig. 4.9. In the fine scale, we use the same lattice and the potential functions as in the first example. The pure atomistic model consists of 12870 atoms in total along with 454 ghost atoms. A total triangular displacement of 10.789Å is prescribed on the top and bottom edges as shown in Fig. 4.9, in 32 equal load steps. The left and right edge atoms are fixed only in the x direction, whereas the top and bottom edge atoms are fixed in both the x and the y directions.

In the multiscale model, the coarse scale domain is discretized with 15×15 nodes. The initial fine scale regions are specified around the crack tips as shown in Fig. 4.10(d). Each of the fine scale regions consists of 975 atoms in total containing 124 ghost atoms. Similar to the atomistic model, a total triangular displacement of 10.789Å is prescribed on the top and bottom edges, as shown in Fig. 4.9, in 32 equal load steps. The top and bottom edge nodes are fixed in the x and y directions, whereas the left and right edge nodes are fixed only in the x direction. The initial configuration of the pure MS model is plotted in Fig. 4.10(a), highlighting the initial crack and the ghost atoms. Deformed configurations after the 19th and 32nd load steps are plotted in Fig. 4.10(b) and Fig. 4.10(c), respectively. Note that because of the prescribed displacement boundary conditions the cracks travel in the opposite directions,

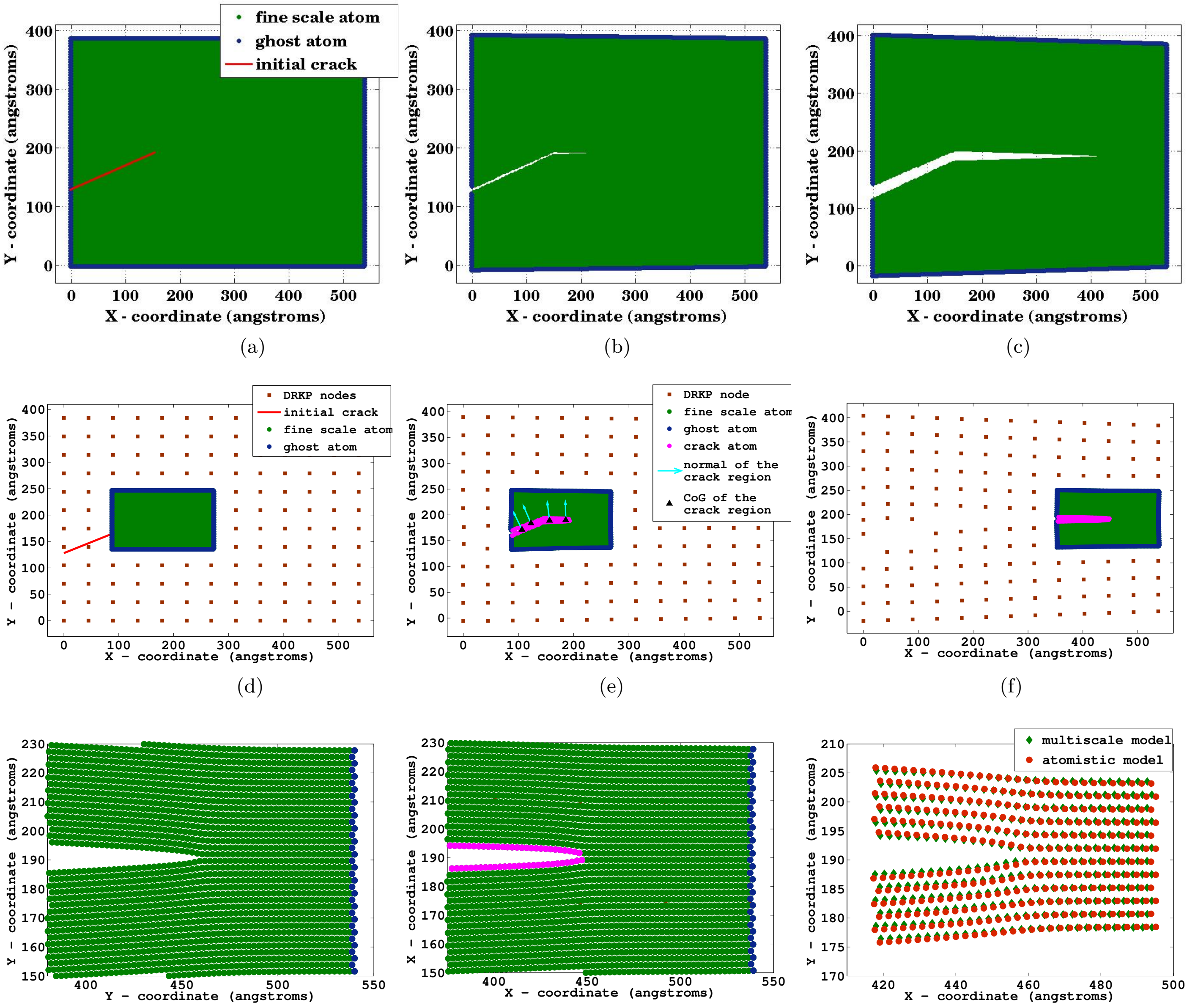

(a) (b) (c)

(d) (e) (f)

(g) (h) (i)

Figure 4.7: Development of the multiscale model, for the quasi-static propagation of an angled edge crack. Configuration of the atomistic model: (a) at the start of the simulation, (b) at the 16th load step, as the crack in the fine scale model starts to open and propagate and (c) at the 42nd load step, at the end of the simulation. Configuration of the multiscale model: (d) at the start of the simulation, (e) at the 16th load step, crack after changing the direction of propagation and (f) at the end of the simulation. A closeup around the crack tip; (g) of the atomistic model in figure (c) and (h) of the multiscale model in figure (f). (i) Comparison of the positions of atoms around the crack tip in (g) and (h).

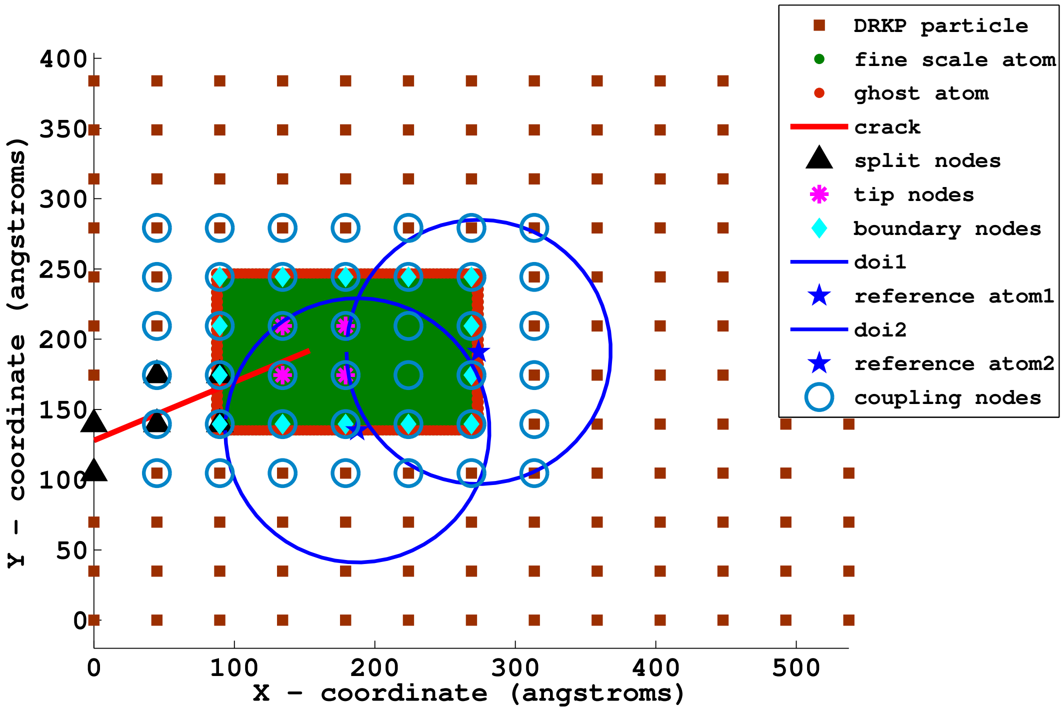

Figure 4.8: Initial nodes, atoms, crack orientation and the domain of influence of the multiscale model based on the DRKP method.

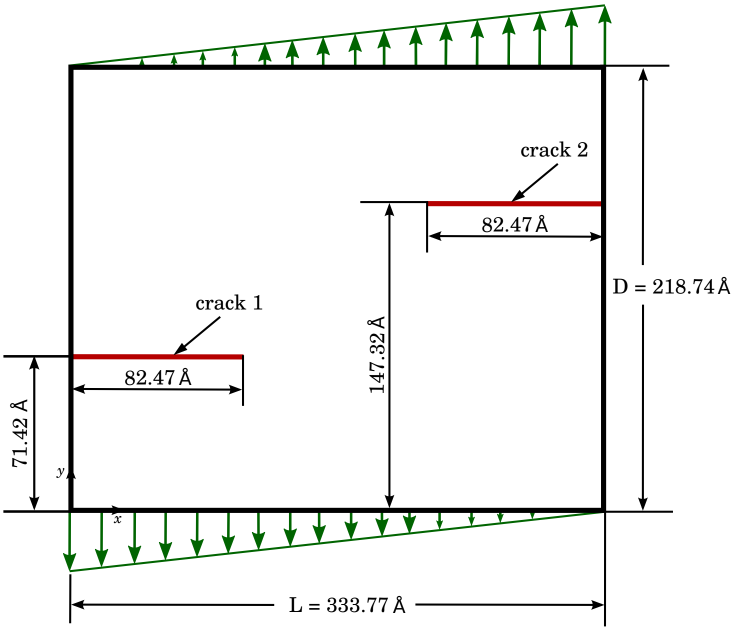
crack 2
82.47 Å
D = 218.74 Å
crack 1
82.47 Å
147.32 Å
71.42 Å
y
x
L = 333.77 Å

Figure 4.9: Geometry of the double-notched specimen with initial cracks and prescribed displacements studied in example 2.

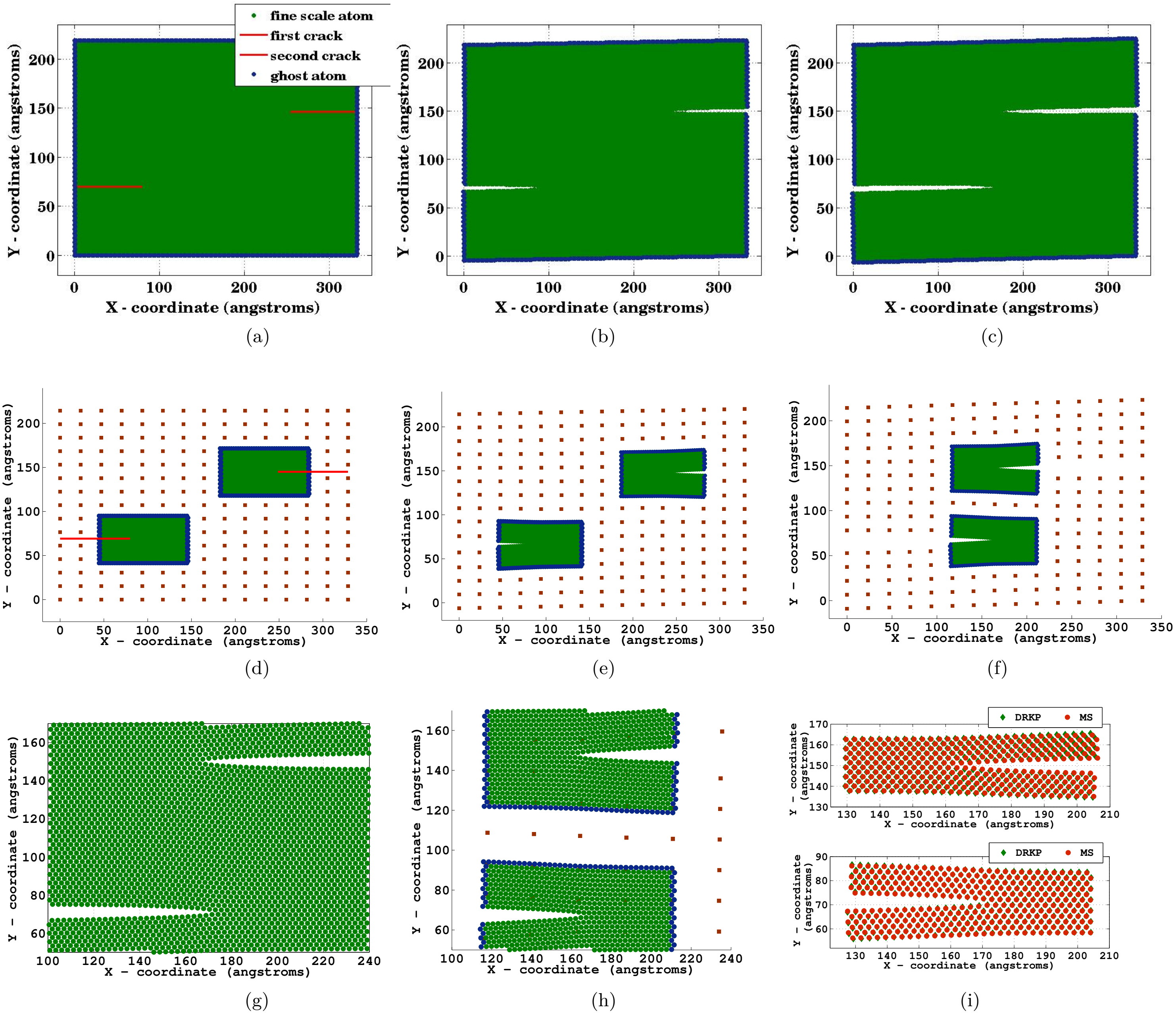

(a) (b) (c)

(d) (e) (f)

(g) (h) (i)

Figure 4.10: Development of the multiscale model for quasi-static propagation of a double edge notched specimen. Configurations at the start of the simulation, at the 19th load step and the end of the simulation; of the MS and the coupled models are plotted in (a)-(c) and (d)-(f), respectively. A closeup around the crack tip; (g) of the atomistic model in figure (c) and (h) of the multiscale model in figure (f). (i) Comparison of the positions of atoms around the crack tip in (g) and (h).

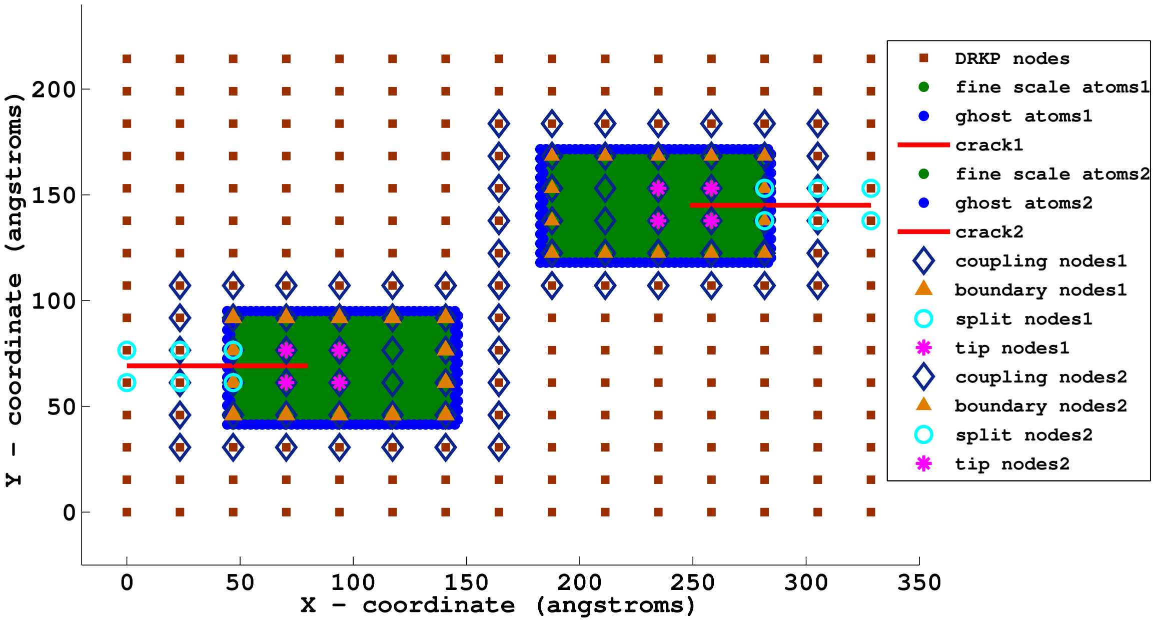

Figure 4.11: Initial nodes, atoms, crack orientation and the domain of influence of the multiscale model based on the DRKP method.

crossing each other at the center. Further load application leads to block the propagation of each other, as the tensile forces in one crack will act as the compressive forces in the other crack. Therefore, we stopped the simulation when both the cracks propagates until half the length of the domain.

Figure 4.10(d) shows the initial configuration of the multiscale model. Figure 4.11 shows more details of the initial configuration of the coupled model, highlighting the initial crack, DRKP particles, split, tip and boundary nodes, atoms in the fine scale region along with the ghost atoms. The deformed configurations after the 19^{th} and the 32^{nd} load steps of the multiscale model are plotted in Fig. 4.10(e) and Fig. 4.10(f), respectively. A closeup of the atomistic model in Fig. 4.10(c) around the crack tips is shown in Fig. 4.10(g). A similar picture for the multiscale model in Fig. 4.10(f) around the crack tips is shown in Fig. 4.10(h). The atom positions from the atomistic and the coupled models at the end of the simulation are compared in Fig. 4.10(i).

4.3.3 Example 3: Mixed mode edge crack propagation

In the final example, we study the mixed mode crack propagation in a edge cracked specimen as shown in Fig. 4.12. In the fine scale, the same lattice and the potential functions used in the first and second examples are adopted. The pure atomistic model consists of 4410 atoms in total along with 262 ghost atoms. A triangular displacement of 13.456Å is prescribed at an angle of 45^0 to the x axis, on the top and bottom edges in opposite directions (refer to

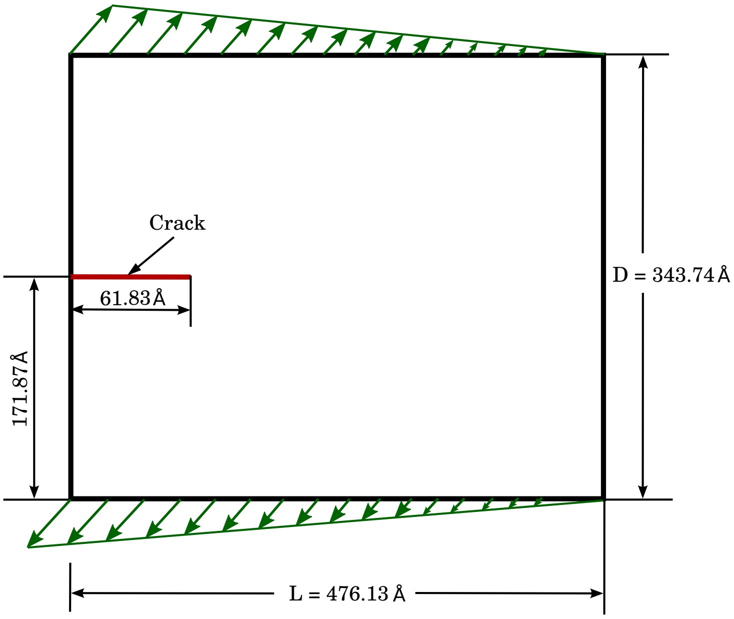

Figure 4.12: Schematic of the specimen with edge crack in mixed mode propagation studied in example 3.

Fig. 4.12), in 58 equal load steps. The top and bottom edge atoms are fixed in both the x and the y directions. The multiscale model in the initial configuration is shown in Fig. 4.13. Configurations at the start of the simulation, at the 27$^{\text{th}}$ load step and at the 42$^{\text{th}}$ load step of the MS are plotted in Fig. 4.13(a)-(c), and the corresponding deformed configurations of the multiscale model are plotted in Fig. 4.13(d), Fig. 4.13(e) and Fig. 4.13(f), respectively. Closeups around the crack tip are plotted in Fig. 4.13(g) and Fig. 4.13(h), respectively. A close agreement of the atom positions around the crack tip from the MS and the multiscale model are observed.

4.4 Discussion

First novel meshless adaptive multiscale method for fracture has been discussed. The developed multiscale method is employed to perform energy minimization of a triangular lattice which contains stably propagating fractures. Coupling of the continuum and atomistic models was realized through the use of a bridging scale method. The DRKP is enhanced so that arbitrary cracks are admissible at the coarse scale based on the enrichment leading to a Meshfree Adaptive Multiscale Method for Fracture. The crack was incorporated into the fine scale model by breaking atomic bonds. The crack in the coarse scale is modeled by node enrichment. The fine scale and coarse scale models are coupled by enforcing the displacement boundary conditions on the ghost atoms.

The MAMMF was used to study the crack propagation in three examples. In the first example, a triangular displacement was prescribed to a domain containing an angled edge

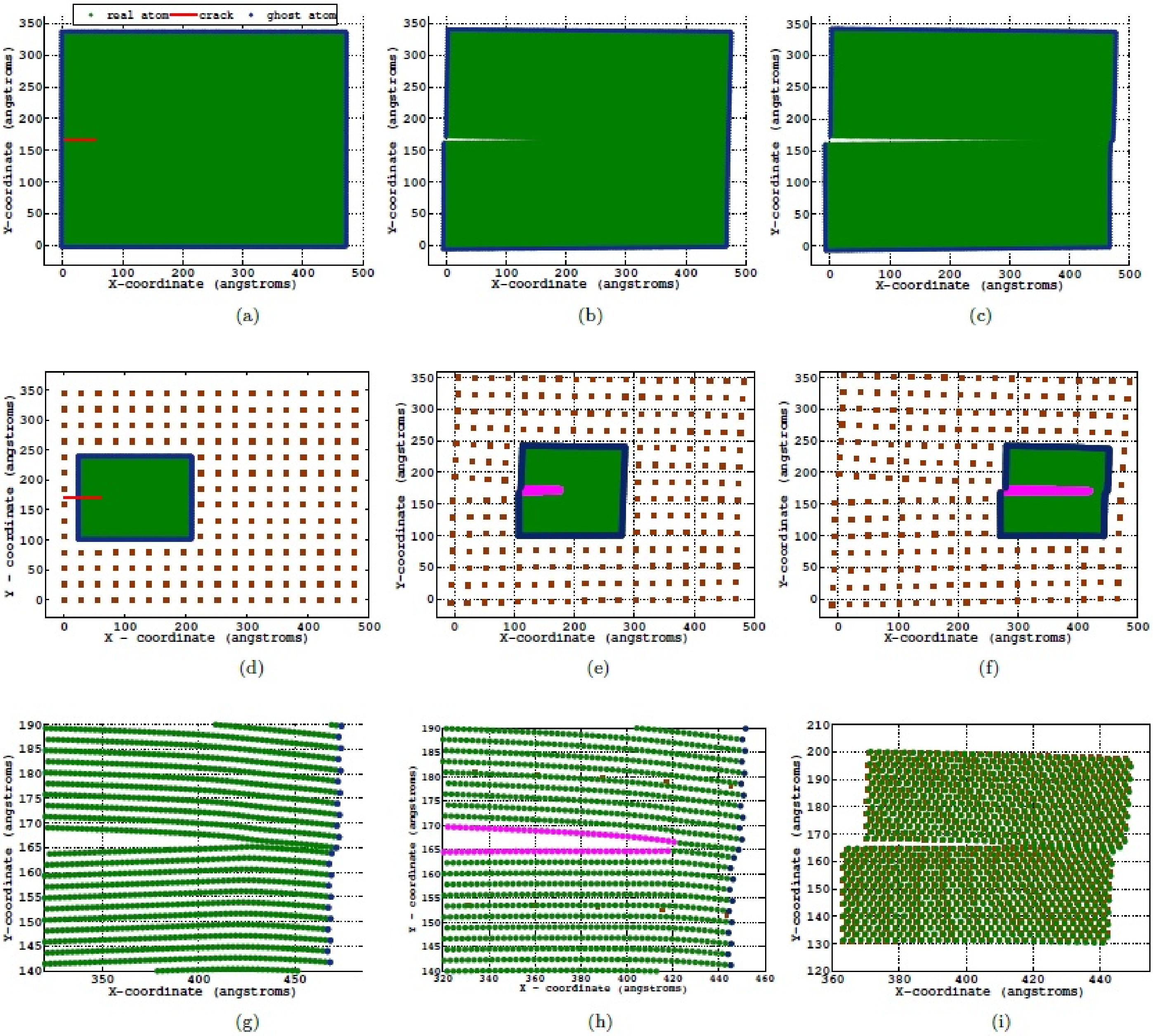

Figure 4.13: Development of the multiscale model for mixed mode propagation of a edge crack specimen. Configurations at the start of the simulation, at the 27th load step and at the 42nd load step of the MS model are plotted in (a)-(c), and the corresponding deformed configurations of the multiscale model are plotted in (d)-(f), respectively. A closeup (c) and (d) around the crack tip are plotted in (g) and (h), respectively. A comparison of the atom positions around the crack tip from the MS and the DRKP models are plotted in (i).

crack. The value of the prescribed displacement was chosen so that the crack propagates close to the right edge. The atom positions around the crack tip from the MS and MAMMF were compared. The error in displacement between the MS and MAMMF was found to be 0.2%. In the second example, crack propagation in a double-notched specimen propagating in the opposite directions was studied. In the final example, mixed mode propagation of a specimen edge crack was studied. The positions of atoms around the crack tip were compared between the MS and the MAMMF. Adaptive refinement and coarsening schemes were implemented in all the examples, during crack propagation. Very close agreement in the atom positions is observed between the MS and the MAMMF models. The MAMMF is 3 times more computationally efficient than the MS.

A meshless adaptive multiscale framework has been introduced here; it serves as a sound basis for future studies of three dimensional crack propagation and other material defects.

Chapter 5

Crack propagation in Graphene on Silicon surface

In this chapter [4,5], a multiscale method to model the fracture in Graphene on Silicon surface has been developed. To begin with, the crack initiation and growth mechanisms in the two dimensional (2D) Graphene lattice structure are studied based on the molecular dynamics simulations. Crack growth in an initial edge crack model in the arm-chair and the zig-zag lattice configurations of Graphene are considered. Influence of the time steps (1 fs and 0.1 fs) on the post yielding behaviour of Graphene is investigated. Variation of the potential energy and the stress along the loading direction are also studied. A systematic study of the bond stretching and bond reorientation phenomena is performed. It is observed that the crack propagates after significant bond elongation and rotation in Graphene. Variation of the crack speed with the change in crack length is estimated for arm-chair and zig-zag Graphene. Three dimensional coarse scale model to simulate the fracture in Silicon has been developed. The coarse scale domain containing Silicon need to be coupled with the atomistic domain consisting of Graphene, leading to a multiscale model for Graphene on Silicon surface.

5.1 Introduction

Graphene is the first two-dimensional (2D) atomic crystal consisting of carbon atoms arranged in a hexagonal lattice. The excellent material properties of Graphene have attracted researchers of different backgrounds. For example, Graphene (i) is a giant molecule which can be readily modified for chemical applications [134–137] (ii) can be used as a novel electronic system [138, 139] (iii) is promising for a wide range of applications ranging from medical applications to composite materials [140–143]. Some characteristics of Graphene measured in experiments have reached the theoretically predicted limits [144]. The properties of Graphen

---

[4] This work is done in collaboration with the Dept. of Aerospace Engg., IISc, Bangalore, India.

[5] This work is planned to submit to the Journal of Applied Physics.

include: (i) the ability to sustain extremely high densities of electric current, a million times higher than copper [145], (ii) complete impermeability to any gases [146] (iii) extremely high Young's modulus of 1 TPa and intrinsic strength of 130 GPa [147, 148], (iv) very high thermal conductivity [149] and optical absorption [150], (v) room-temperature electron mobility [151] and (vi) the ability to chemically functionalize [152]. However, some of the above characteristics have been achieved only for the samples of highest quality, which are prepared in extremely controlled environments. Such manufacturing techniques will be very expensive and not suitable for mass production. Defects occurring during the synthesis and fabrication of Graphene-based devices [153] are unavoidable. Therefore, the presence and propagation of the defects can affect the extraordinary mechanical properties [154].

Estimating the fracture properties of Graphene is difficult due to the practical difficulties in setting-up the experiments [155]. Numerical simulations are good alternative for predicting the fracture related properties of Graphene. Due to their extreme Young's modulus values carbon nanotubes (Graphene sheet folded into a cylinder) helps in stiffening the polymers in which they are distributed [156]. Zhang *et al.* [157] have investigated the influence of the polymer wrapped on two neighbouring single-walled carbon nanotubes on their load transfer by MD simulations. They [158] developed an analytical model for the interface debonding, for large diameter carbon nanotube-reinforced composite with functionally graded variation inter-phase. Due to the extremely small out-of-plane stiffness of Graphene, the differential thermal expansion causes the formation of wrinkles during the chemical vapor deposition [159]. The collapse of the standing wrinkles leads to folds in Graphene [160]. A quasi-analytical solution based on the minimum length has been proposed in [161], to estimate the system energy of the stable multi-layer folded Graphene wrinkles. Jiang *et al.* [162] have investigated the interlayer energy of the twisting bilayer Graphene by molecular mechanics simulations using both the registry-dependent potential and the Lennard-Jones potential. The high stiffness and large surface area of Graphene combined with low mass of carbon atoms, makes it an excellent mass sensor to detect individual atoms or molecules [163]. The enhancement of the mass sensitivity and resonant frequency of Graphene nano-mechanical resonators are investigated through MD simulation in [164] by driving the nano-resonators into the nonlinear oscillation regime. The mechanisms underpinning the unresolved, experimentally observed temperature-dependent scaling transition in the quality factors of Graphene nano-mechanical resonators is investigated in [165].

Zhao *et al.* [166] performed MD simulations to estimate the mechanical properties of three types of carbon allotropes: super-Graphene, cyclic-Graphene and graphyne. They studied the chirality dependence of the mechanical properties including Young's moduli, shear moduli, Poisson's ratio, ultimate strength/strains, based on the adaptive intermolecular reactive empirical bond order (AIREBO) potential. The cohesive energy between the carbon nanotubes and the Graphene and its substrates has been theoretically estimated in [167], by modeling the van der Waals interactions. Further, the stick-spiral and beam models are developed in [168] to model Graphene based on the principles of continuum mechanics. The analytical solutions help in arriving at quick estimates for understanding the interaction between the nanostructures and substrates, and designing composites and nano-electro-mechanical systems. The extreme reduction of the thermal conductivity due to the presence of defects and folds in carbon nanocoils is studied in [169], based on the non-equilibrium MD simulations. The presence of the vacancy defects significantly reduces the ultimate strength of Graphene in the zig-zag direction [170], while the effect is minimal on the Young's modulus. The effects of the vacancy defects on the fracture strength of Graphene sheets are studied in [171] with the AIREBO potential and was found that the temperature and loading directions will significantly affect the fracture strength.

Omeltchenko *et al.* [172] performed the MD simulations of notched graphite sheets under uni-axial tension. Multiple branching cracks were observed sprouting off the primary crack front. The retention of the cutoff function of early version potential made the quantitative aspects of results questionable [173]. However, the predicted values of the stress intensity factor (K_{IC}) in [172] are within the same range as those reported in [155, 174]. The fracture of Graphene nano-ribbons under uni-axial tension are studied in [175]. Terdalkar *et al.* [176] have performed MD simulations with an analytical bond-order potential (BOPS4) to investigate the kinetic processes of bond breaking and bond rotation near a crack tip in Graphene. They report that the fracture of Graphene bond is governed by the competition between bond breaking and bond rotation at the crack tip. An experimental and theoretical study on cracks in suspended mono-layer Graphene membranes is presented in [155]. It is suggested that the preferred tear direction depends on the Graphene edge energy and the edge orientation with respect to the lattice.

5.2 Three dimensional Adaptive Multiscale Method

In this section, the modeling aspects of the three dimensional adaptive multiscale method (TAMM) are discussed. Consider the TAMM model consisting of the coarse and fine scale regions along with the crack surface is shown in Fig. 5.1(a). The discretized coarse scale model along with the crack surface is shown in Fig. 5.1(b). Note that the completely cracked elements are shown in dotted lines in Fig. 5.1(b). The fine scale model is shown in Fig. 5.1(c). The material behaviour at the crack tip is expected to be highly non-linear and/or non-homogeneous, and away from the tip it is expected to be homogeneous.

5.2.1 Coarse scale model

The unit cell of the periodic diamond crystal structure of Silicon in an isometric view is shown in Fig. 5.2(a), Fig. 5.2(b) shows the front view of Fig. 5.2(a) and the space lattice of the Silicon is shown in Fig. 5.2(c). The geometric parameters of the diamond crystal lattice are expressed using the lattice constant a, as shown in Fig. 5.2(a). Because of the symmetry

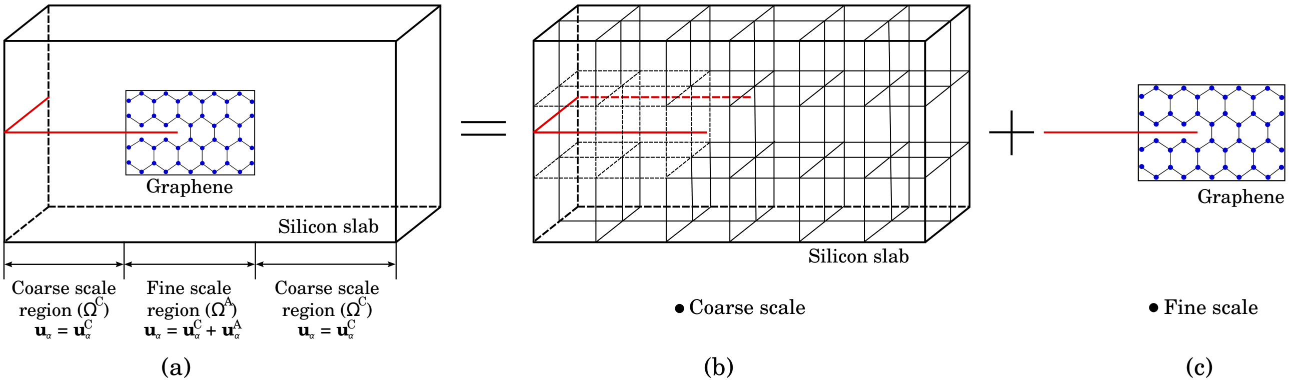
Graphene
Silicon slab
Coarse scale region (Ω^C)
$\mathbf{u}_\alpha = \mathbf{u}_\alpha^C$
Fine scale region (Ω^A)
$\mathbf{u}_\alpha = \mathbf{u}_\alpha^C + \mathbf{u}_\alpha^A$
Coarse scale region (Ω^C)
$\mathbf{u}_\alpha = \mathbf{u}_\alpha^C$
=
Silicon slab
● Coarse scale
+
Graphene
● Fine scale
(a)
(b)
(c)

Figure 5.1: (a) Multiscale partition of a cracked atomistic lattice. The solid circles represent the atoms from the cracked atomistic model. The coarse scale nodes are denoted by squares. (b) A zoom around the crack tip.

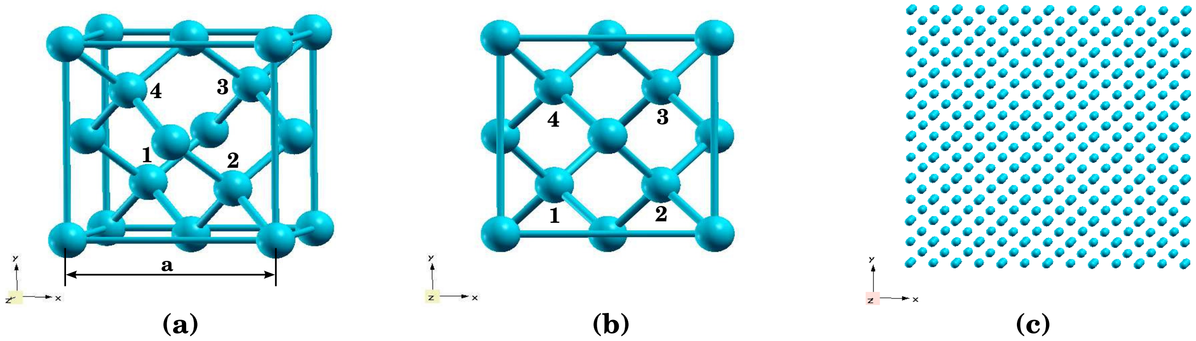
4
3
1
2
a
y
z
x
4
3
1
2
y
z
x
y
z
x
(a)
(b)
(c)

Figure 5.2: Silicon unit lattice in (a) an isometric view and (b) front view, highlighting the quarter atoms. (c) The front view of the space lattice.

of the crystal structure, the coarse scale can be modeled based on the VAC, as explained in the section 2.1.2. The coarse scale displacement $\mathbf{u}_\alpha^{\mathrm{C}}$ of an atom α in the VAC can be estimated using equation (2.2).

The total potential energy of a fine scale system is given by the sum of all bond potentials ϕ_α, estimated using equation (B.2). Consider an equivalent coarse scale model based on the VAC is illustrated in Fig. 5.3. Figure 5.3(a) shows an isometric view of the space lattice, Fig. 5.3(b) shows the equivalent VAC based continuum model and the VAC considered in the present work is shown in Fig. 5.3(c). Since we want the fine scale and coarse scale models to be equivalent, their potential energy must be equal. Hence, we define ϕ_ρ as the distributed energy density function from the VAC model. The discrete summation of the potential energy defined in the original molecular structure, can now be replaced with an integral based on the VAC model, i.e.

$$W^{\mathrm{int}} = \sum_{\alpha=1}^{n^{\mathrm{A}}} \phi_\alpha = \int_{\Omega_0} \phi_\rho d\Omega_0 \approx \sum_G w_{\mathrm{G}} \phi_\rho^{\mathrm{G}}. \tag{5.1}$$

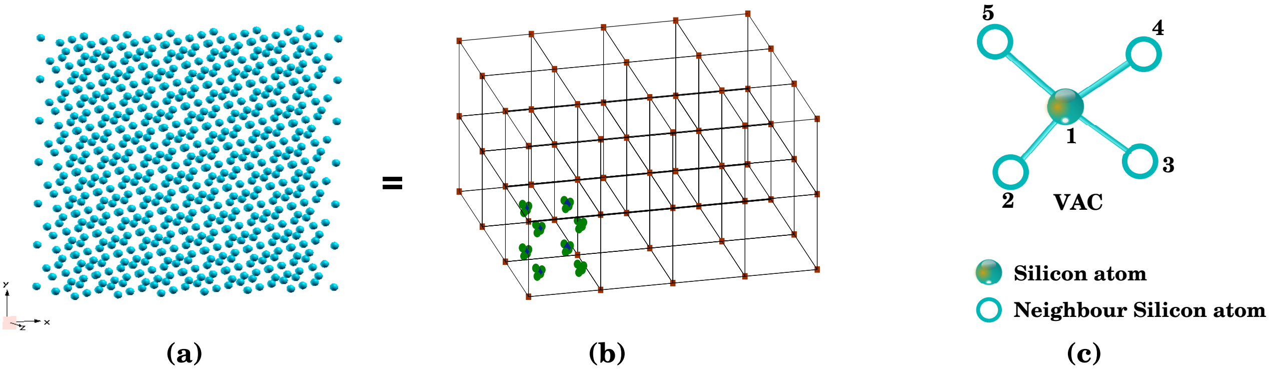

Figure 5.3: Silicon space lattice in (a) isometric view, (b) equivalent VAC based continuum model, showing the VAC placed at the Gauss points in the lowest left element. Due to the periodicity of the lattice structure (refer Fig. (5.2)), any single atom can be considered as VAC. (c) The considered single atom VAC (atom 1) along with its four nearest neighbors.

Due to the periodic nature of the lattice, we can define ϕ_ρ as the potential energy of a VAC divided by the volume of the VAC. For a homogeneous lattice, as considered in this article, each VAC consists of a single atom and its volume is that of the unit cell of the lattice. The volume of the VAC for a diamond lattice is $\mathrm{V}_0 = \frac{a^3}{8}$. When only nearest neighbour interactions are considered, each atom in the diamond lattice interacts with four neighbouring atoms, refer Fig. 5.3(c). The energy attributed to a central atom involves summing the contributions from each bond with neighbouring atoms. The energy of the central atom is the energy of the VAC. The number of neighbours that the central atom has does not influence the volume/area attributed to the atom and therefore does not effect the volume/area attributed to the VAC. In other words, the volume/area of the VAC do not increase if more neighbours are considered in the computation of the potential energy of the central atom. Using the numbering scheme shown in Fig. 5.3(c), the potential energy of the VAC is given by

$$\phi_{\mathrm{VAC}} = \frac{1}{2}\sum_{\beta=2}^{5} V(r_{1\beta}). \tag{5.2}$$

Therefore, the distributed energy density function ϕ_ρ can be defined as

$$\phi_\rho = \frac{\phi_{\mathrm{VAC}}}{\mathrm{V}_0} = \frac{1}{2}\sum_{\beta=2}^{5}\frac{V(r_{1\beta})}{a^3/8} = \frac{1}{2}\sum_{\beta=2}^{5}\phi_{1\beta} \tag{5.3}$$

where

$$\phi_{1\beta} = \frac{V(r_{1\beta})}{a^3/8}. \tag{5.4}$$

Hence, the energy density function ϕ_ρ becomes

$$\phi_\rho = \frac{1}{2}(\phi_{12} + \phi_{13} + \phi_{14} + \phi_{15}). \tag{5.5}$$

in which $\phi_{1\beta}$ are the bonding energy densities. w_{G} denote the quadrature weight and ϕ_ρ^{G} is the corresponding energy density function evaluated at a quadrature point. The internal forces on node 'I' in the coarse scale region, can be estimated by taking the derivative of equation (5.1) with respect to the nodal displacements $\mathbf{u}_I^{\mathrm{C}}$

$$\mathbf{F}_I^{\mathrm{int}} = -\frac{\partial W^{\mathrm{int}}}{\partial \mathbf{u}_I^{\mathrm{C}}} = \int_{\Omega_0} -\frac{\partial \phi_\rho}{\partial \mathbf{u}_I^{\mathrm{C}}} d\Omega_0 = \int_{\Omega_0} -\frac{\partial \phi_\rho}{\partial \mathbf{u}}\frac{\partial \mathbf{u}}{\partial \mathbf{u}_I^{\mathrm{C}}} d\Omega_0 \approx -\sum_{\mathrm{G}} w_{\mathrm{G}} \frac{\partial \phi_\rho^{\mathrm{G}}}{\partial \mathbf{u}}\frac{\partial \mathbf{u}}{\partial \mathbf{u}_I^{\mathrm{C}}}. \tag{5.6}$$

Therefore, the internal forces are calculated from the potential energy density of the VAC, which is placed at each Gauss point. As shown in Fig. 5.3(c), there are 5 atoms including the central VAC atom and its neighbours. Therefore, the energy density function $\phi_\rho^{\mathrm{G}} = \phi_\rho^{\mathrm{G}}(\mathbf{r}_1, \mathbf{r}_2, \mathbf{r}_3, \mathbf{r}_4, \mathbf{r}_5)$. Since the VAC model is used in the coarse scale equation which assumes $\mathbf{u}_\alpha = \mathbf{u}_\alpha^{\mathrm{C}}$, for α = 1–5. Therefore,

$$\mathbf{F}_I^{\mathrm{int}} \approx -\sum_{\mathrm{G}} w_{\mathrm{G}} \frac{\partial \phi_\rho^{\mathrm{G}}}{\partial \mathbf{u}}\frac{\partial \mathbf{u}}{\partial \mathbf{u}_I^{\mathrm{C}}} \approx -\sum_{\mathrm{G}} w_{\mathrm{G}} \sum_{\alpha=1}^{5} \frac{\partial \phi_\rho^{\mathrm{G}}}{\partial \mathbf{u}_\alpha^{\mathrm{C}}}\frac{\partial \mathbf{u}_\alpha^{\mathrm{C}}}{\partial \mathbf{u}_I^{\mathrm{C}}}. \tag{5.7}$$

Using the definition of $\mathbf{u}_\alpha^{\mathrm{C}}$ from equation (2.2), the second term on the right hand side of equation (5.7) can be reduced to

$$\frac{\partial \mathbf{u}_\alpha^{\mathrm{C}}}{\partial \mathbf{u}_I^{\mathrm{C}}} = N_I(\mathbf{X}_\alpha). \tag{5.8}$$

Therefore, after substituting equation (5.8) into equation (5.7), the nodal internal forces in the coarse scale domain are given by

$$\mathbf{F}_I^{\mathrm{int}} = -\sum_{\mathrm{G}=1}^{n^{\mathrm{G}}} w_{\mathrm{G}} \sum_{\alpha=1}^{5} \frac{\partial \phi_\rho^{\mathrm{G}}}{\partial \mathbf{u}_\alpha^{\mathrm{C}}} N_I(\mathbf{X}_\alpha). \tag{5.9}$$

The term $\frac{\partial \phi_\rho}{\partial \mathbf{u}_\alpha^{\mathrm{C}}}$ in equation (5.9) can be evaluated for each α as given below:
$\alpha = 1$

$$\frac{\partial \phi_\rho}{\partial u_{1i}^{\mathrm{C}}} = \frac{\partial \phi_{12}}{\partial r_{12}}\frac{r_{12i}}{r_{12}} + \frac{\partial \phi_{13}}{\partial r_{13}}\frac{r_{13i}}{r_{13}} + \frac{\partial \phi_{14}}{\partial r_{14}}\frac{r_{14i}}{r_{14}} + \frac{\partial \phi_{15}}{\partial r_{15}}\frac{r_{15i}}{r_{15}} \tag{5.10}$$

$\alpha = 2$

$$\frac{\partial \phi_\rho}{\partial u_{2i}^{\mathrm{C}}} = -\frac{\partial \phi_{12}}{\partial r_{12}}\frac{r_{12i}}{r_{12}} \tag{5.11}$$

$\alpha = 3$

$$\frac{\partial \phi_\rho}{\partial u^{\mathrm{C}}_{3i}} = -\frac{\partial \phi_{13}}{\partial r_{13}}\frac{r_{13i}}{r_{13}} \tag{5.12}$$

$\alpha = 4$

$$\frac{\partial \phi_\rho}{\partial u^{\mathrm{C}}_{4i}} = -\frac{\partial \phi_{14}}{\partial r_{14}}\frac{r_{14i}}{r_{14}} \tag{5.13}$$

$\alpha = 5$

$$\frac{\partial \phi_\rho}{\partial u^{\mathrm{C}}_{5i}} = -\frac{\partial \phi_{15}}{\partial r_{15}}\frac{r_{15i}}{r_{15}} \tag{5.14}$$

where i is the index of the coordinate axes. In equations (5.10) to (5.14), $r_{\alpha\beta i}$ is the component of $r_{\alpha\beta}$ in the i^{th} direction, which is defined as

$$r_{\alpha\beta i} = r_{\alpha i} - r_{\beta i}. \tag{5.15}$$

The detailed derivation of the term $\frac{\partial \phi_\rho}{\partial \mathbf{u}^{\mathrm{C}}_{\alpha}}$ for a single atom VAC in a face centered cubic (fcc) lattice structure is given in appendix section C. The same methodology can be extended to the single atom VAC of a diamond lattice structure considered in the present work. Equations (5.10) to (5.15) are substituted into equation (5.9) to calculate the internal nodal forces. The minimization problem can be solved for the coarse scale solution by minimizing the potential energy for the given boundary conditions.

5.3 Numerical examples

In this section, we study the crack propagation in Graphene through two numerical examples, with the lattice structure oriented along the arm-chair and the zig-zag directions, respectively. The arm-chair and the zig-zag arrangement of the Graphene lattice structure are shown in Fig. (5.4)(a) and Fig. (5.4)(b), respectively. In the first example, we consider the crack propagation of an initial edge crack in the armchair Graphene. The crack propagation of an initial edge crack in the zig-zag Graphene is considered in the second example.

5.3.1 Example 1: Crack propagation in the armchair Graphene with an initial edge crack

Consider the mode I propagation of an initial edge crack in Graphene, as shown in Fig. 5.5. The hexagonal lattice structure of the Graphene layer with a lattice constant 2.45Å and oriented along the arm-chair direction as shown in Fig. (5.4)(a), is adopted to develop the atomistic model. The Tersoff potential [177] is used to model the atom to atom interactions. The details of the Tersoff potential function are mentioned in appendix B.2 and the first

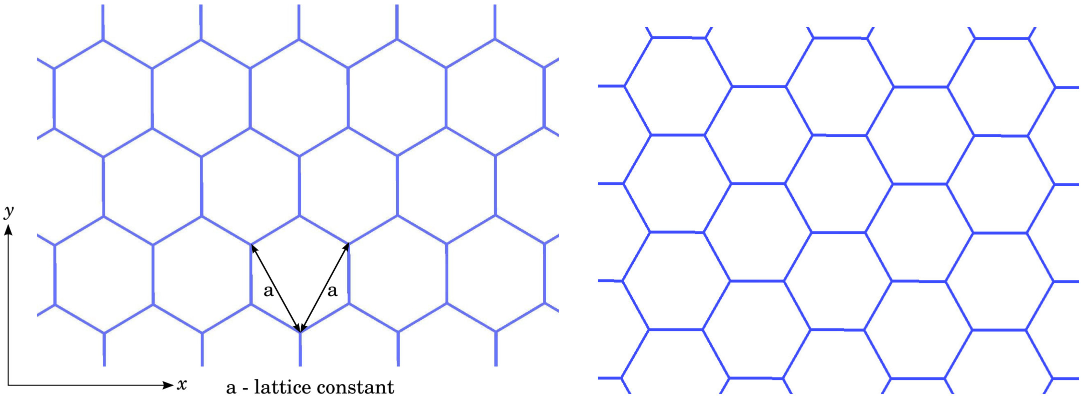

(a) arm-chair

(b) zig-zag

Figure 5.4: Lattice orientation of grahene in the (a) arm-chair and in the (b) zig-zag directions.

derivative is given in section B.3. The initial crack tip is located at (144Å, 216.15Å). The crack in the atomistic region is simulated by segregating the total domain into several regions, as shown in Fig. 5.5. Region 1 and 4 consists of the atoms on the top and bottom edges, respectively. The initial crack is modeled by restricting the neighbour interactions between the regions 2 and 3. Region 5 consists of the atoms contained in the shaded region. The forces in the y direction of the top and bottom edge atoms are set to zero, whereas forces on the left and right edge atoms in the x direction are set to zero. These boundary conditions will lead to arresting the degrees of freedom of the top and bottom edge atoms in the y direction and left and right edge atoms in the x direction, respectively. The full scale atomistic model consists of 75269 atoms with 1625 atoms on the top and bottom edges and 1043 atoms on the left and right edges.

To propagate the crack, a velocity of 0.1 angstroms/pico-seconds (Å/ps) is prescribed on the top and bottom edge atoms. A velocity ramp profile as shown in Fig. 5.5 is applied in the middle of lattice. A load cycle is defined as prescribing the velocity on the top and bottom edge atoms for a specified time period, followed by an equilibration for another specified time period. In each load cycle, the prescribed velocity on the top and bottom edge atoms is applied for a period of 1 ps, after which the system is equilibrated for a period of 40 ps, so that each load cycle yields a strain rate of the order of 4.4×10^7 per second. Fig. 5.6(a) shows the distribution of the strain over time. The stress computed in the present work is the averaged stress estimated based on the Virial theorem. In this example, crack growth is studied with two time steps, 0.1 fs and 1 fs. Therefore, each load cycle corresponds to 1000 steps for velocity loading and 40000 steps for equilibration with a time step of 1 fs. The corresponding number of steps with time step equal to 0.1 fs are 10 times to that of the number of steps with time step equal to 1 fs. The velocity-Verlet scheme is applied to estimate the current atom positions in the current time step. Several simulations are performed to study the effect of the time step on the crack initiation and further growth in Graphene.

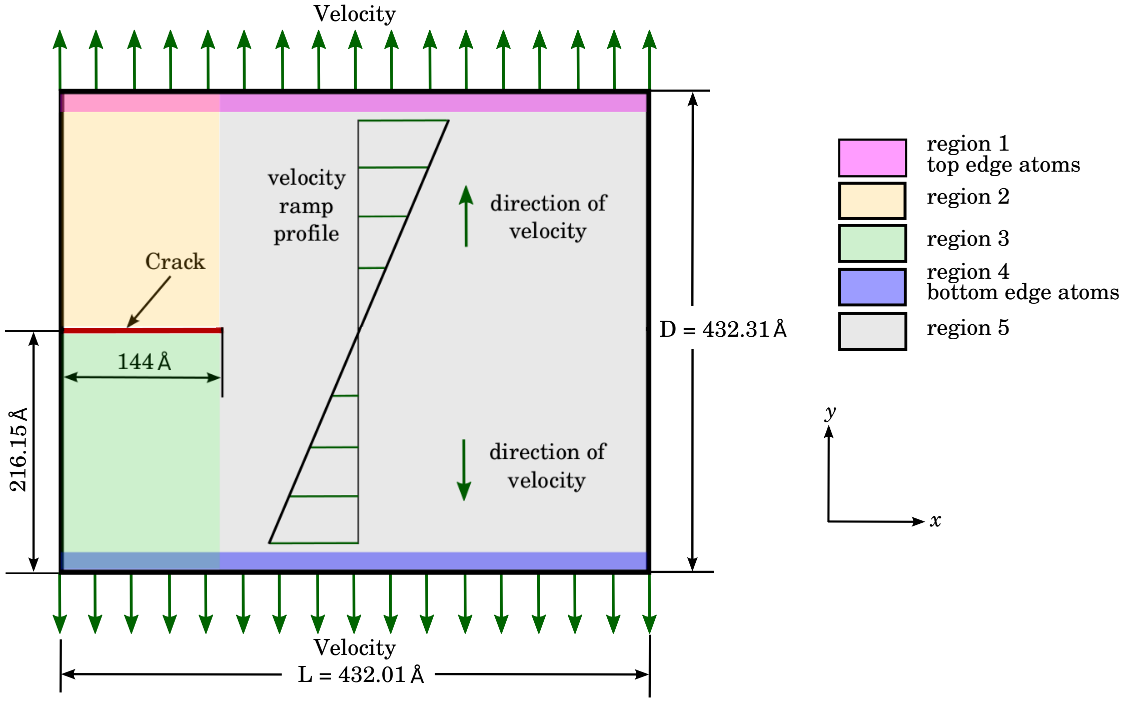

Figure 5.5: Schematic of the edge crack model used in examples 1 and 2.

Figure (5.7) shows the distribution of stress per atom along the y direction (σ_{yy}) in the deformed configuration of the atomistic model at various times. Each picture in Fig. 5.7 consists of two sub pictures. The sub picture on the top shows a closeup of the distribution of stress per atom around the crack tip and the sub picture on the bottom shows the location of the crack tip along with highlighting the atoms on the crack surface. The deformed configuration of the full scale atomistic model at 990.5 ps, just before the crack starts to propagate is plotted in Fig. 5.7(a). The deformed configuration at the 991.5 ps is plotted in Fig. 5.7(b). The breaking of first bonds close to the crack tip can be observed in Fig. 5.7(b). With the continuous application of load the crack starts to propagate after initiating at 991.5 ps. Deformed configurations at the 993.0 ps is plotted in Fig. 5.7(c). From figures 5.7(b) and (c), the time taken for the crack tip to travel along the x direction, from around 140Å to around 190Å is observed to be 1.5 ps. During the period between 991.5 ps to 993.0 ps, a drop in the system potential energy is shown in Fig. 5.6(b), which corresponds to a drop from the point R1 to the point R2 in Fig. 5.6(c). Similar drop in the stress per atom along the y direction with strain, can be observed in Fig. 5.6(d) and Fig. 5.6(e), respectively.

With the continuous application of the velocity on the top and bottom edge atoms, crack continues to grow. The deformed configurations at 994.5 ps, 995.5 ps and 996.0 ps are plotted in Fig. 5.7(d), (e) and (f), where the crack tip is observed to be located around 240Å, 280Å and 290Å, respectively. The potential energy drops between the points R3 to R4 in Fig. 5.6(c), corresponds to the time slot between 994.5 ps to 996.0 ps. From Fig. 5.7(f), it can be observed that the crack front took a small kink and the crack tip is oriented along the y

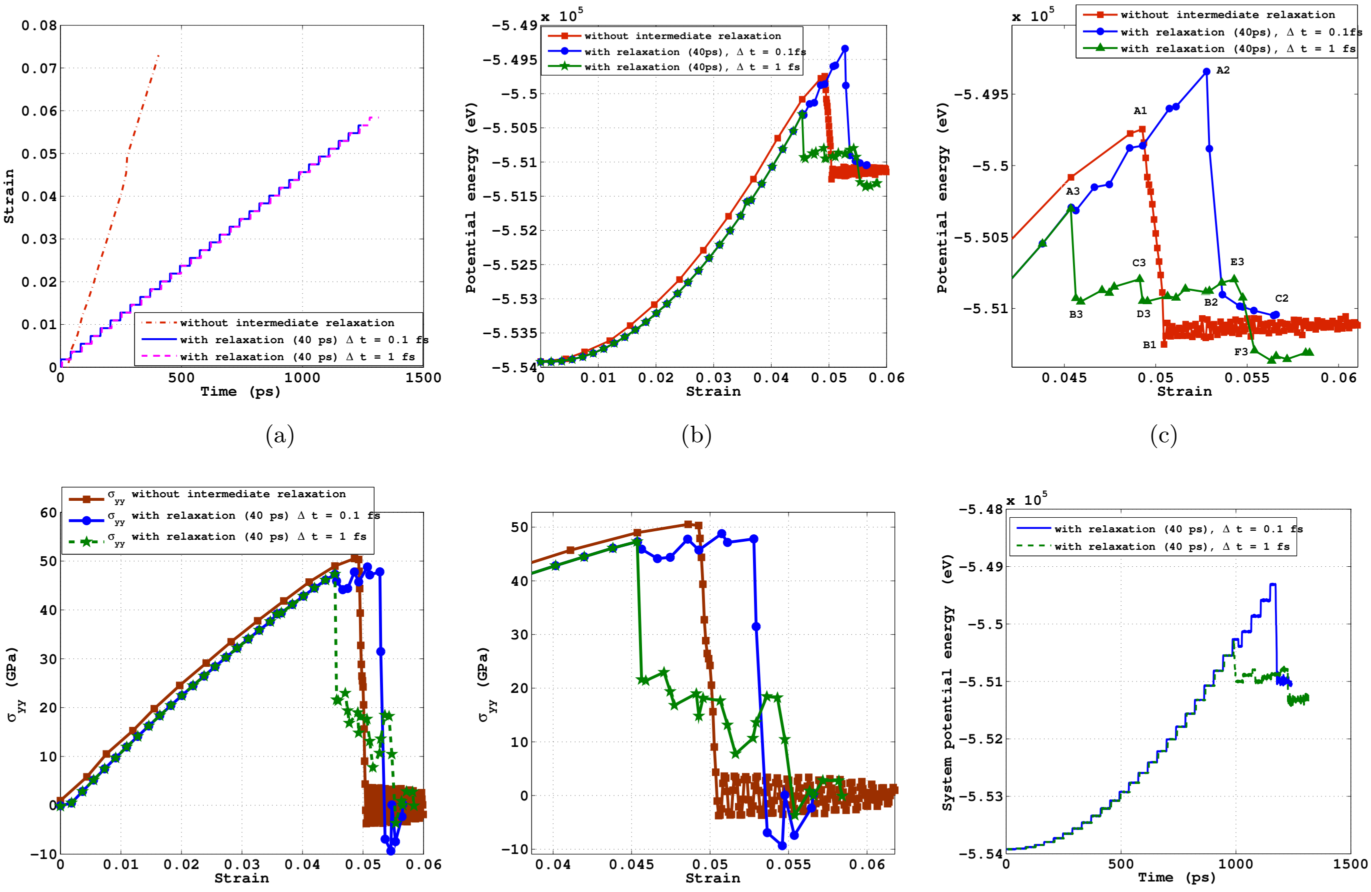

(a) (b) (c)

(d) (e) (f)

Figure 5.6: Distribution of the (a) strain with time, (b) system potential energy with strain and (c) a closeup of (b) around the crack propagation zone. Variation of the (d) stress along the y direction with strain, (e) a closeup of (d) around the crack propagation zone and (f) distribution of the potential energy with time for the crack growth in the arm-chair Graphene.

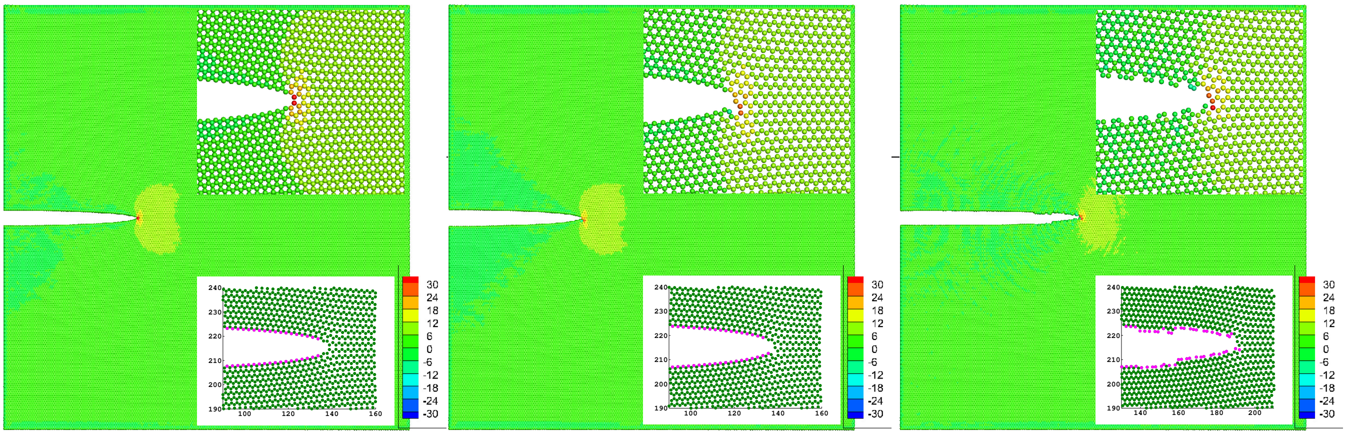

(a) at 990.5 ps, Δt = 1 fs (b) at 991.5 ps, Δt = 1 fs (c) at 993.0 ps, Δt = 1 fs

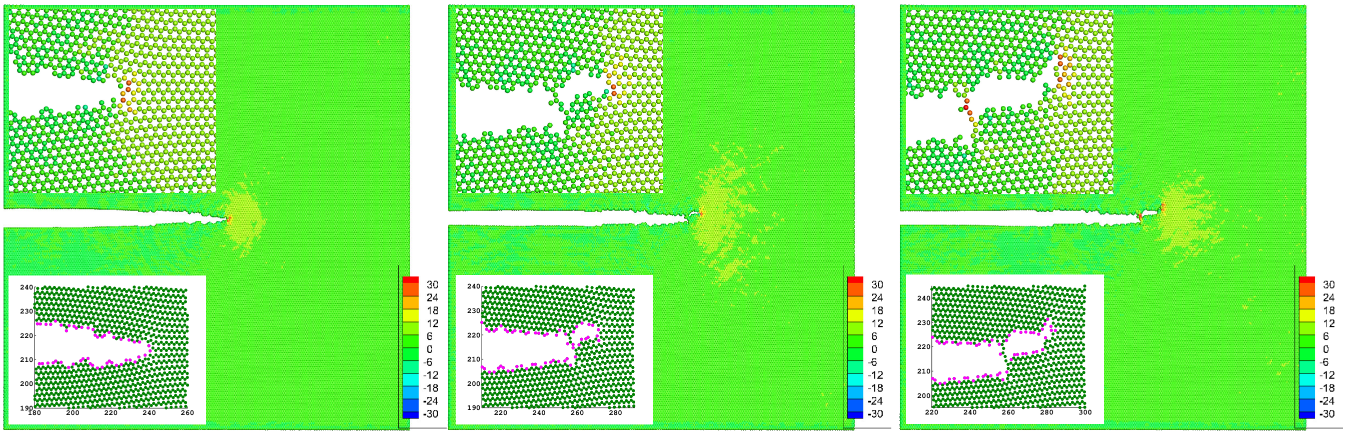

(d) at 994.5 ps, Δt = 1 fs (e) at 995.5 ps, Δt = 1 fs (f) at 996.0 ps, Δt = 1 fs

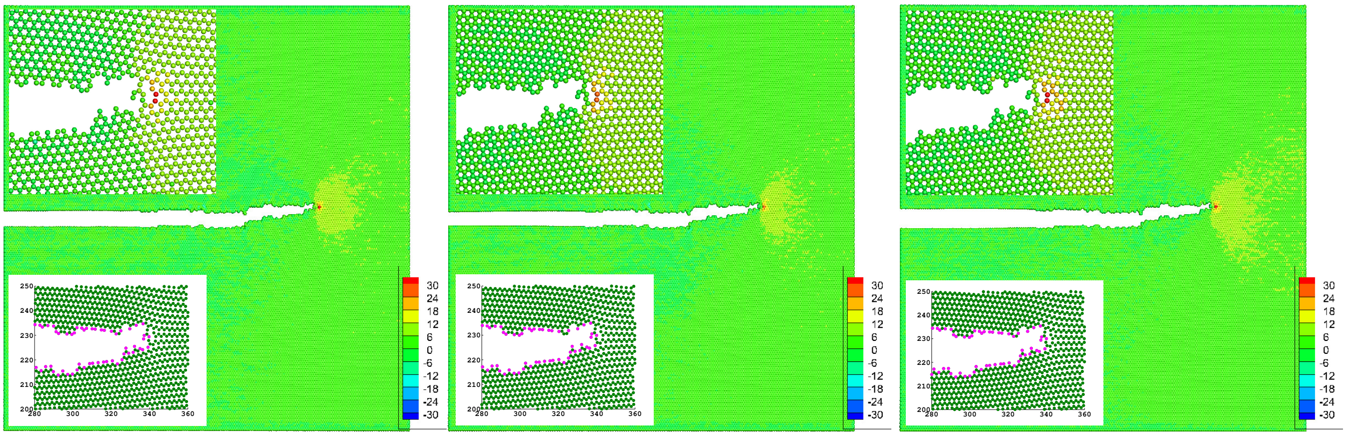

(g) at 1009.5 ps, Δt = 1 fs (h) at 1031.0 ps, Δt = 1 fs (i) at 1072.0 ps, Δt = 1 fs

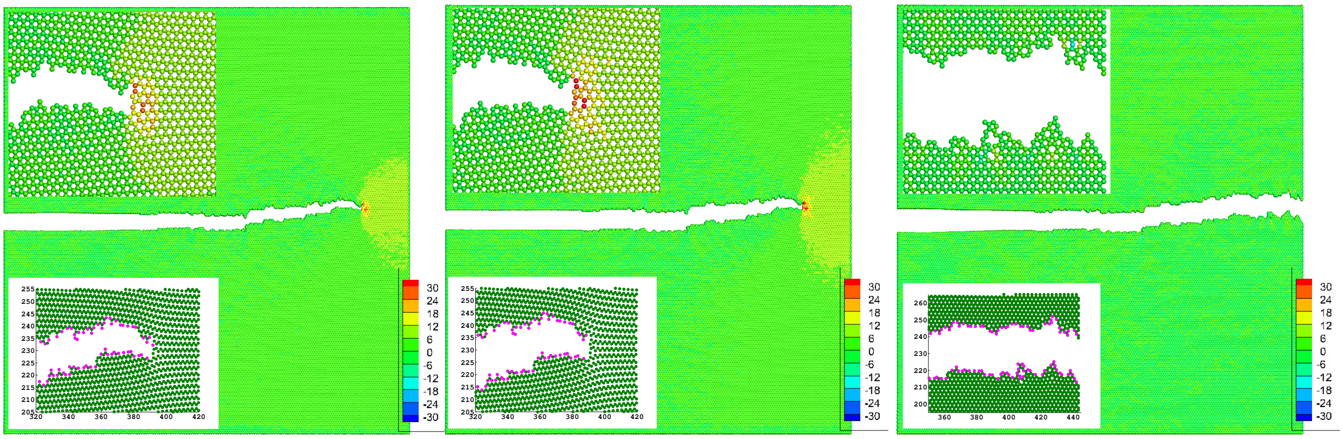

(j) at 1113.0 ps, Δt = 1 fs (k) at 1196.0 ps, Δt = 1 fs (l) at 1236.0 ps, Δt = 1 fs

Figure 5.7: Distribution of the stress per atom along the y direction in Graphene, with the lattice oriented in the arm-chair direction, at various times with $\Delta t = 1$ fs. The sub picture on the top shows a closeup around the crack tip and the sub picture on the bottom shows the location of the crack tip along with highlighting the atoms on the crack surface.

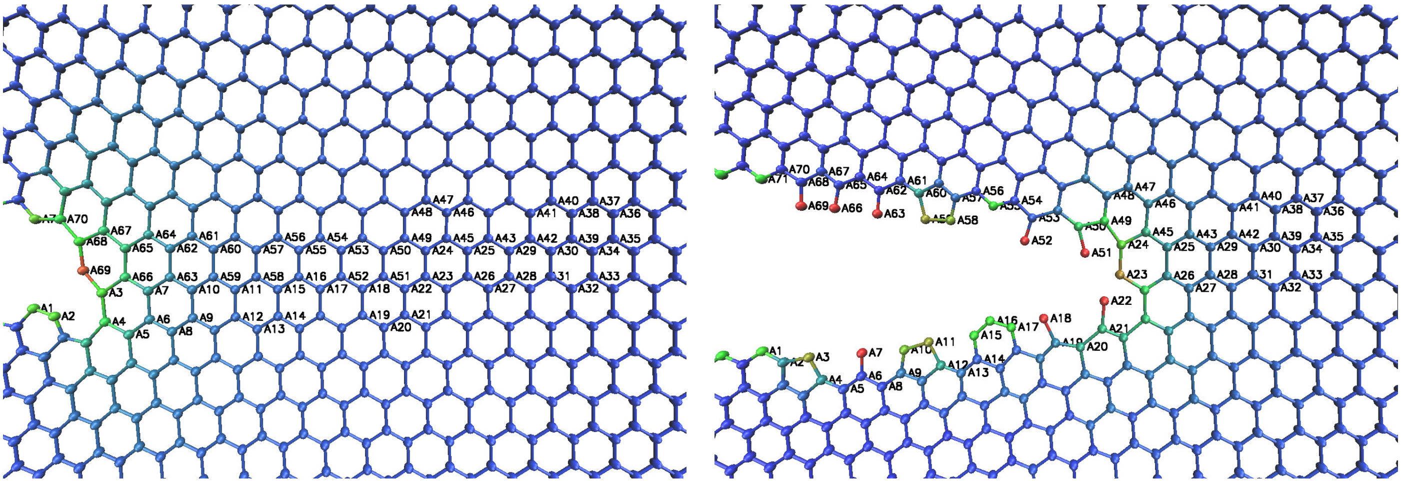

(a) at 991.5 ps, Δt = 1 fs (b) at 992.0 ps, Δt = 1 fs

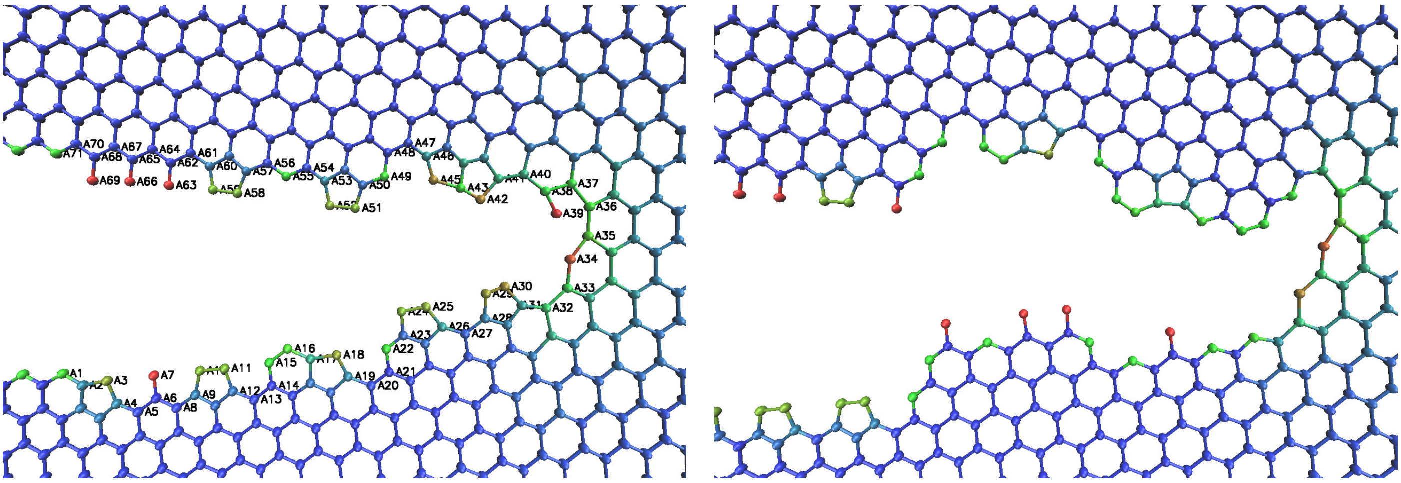

(c) at 992.5 ps, Δt = 1 fs (d) at 997.5 ps, Δt = 1 fs

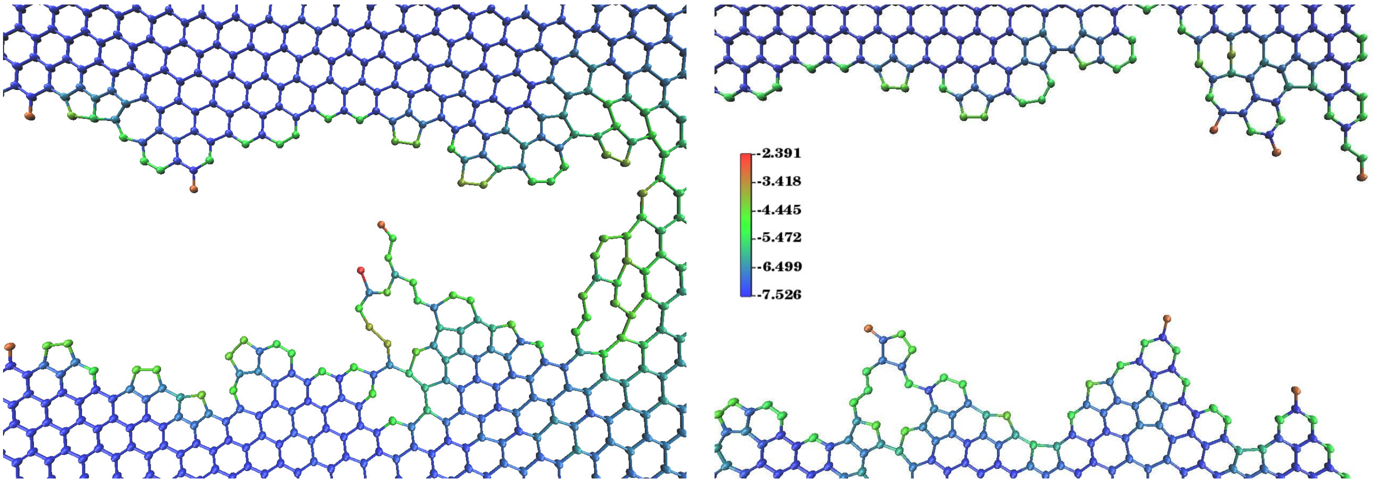

(e) at 1185.5 ps, Δt = 1 fs (f) at 1188.5 ps, Δt = 1 fs

Figure 5.8: Distribution of the potential energy per atom on the atoms around the crack tip at various times, with the lattice oriented in the arm-chair direction and time step equal to 1 fs.

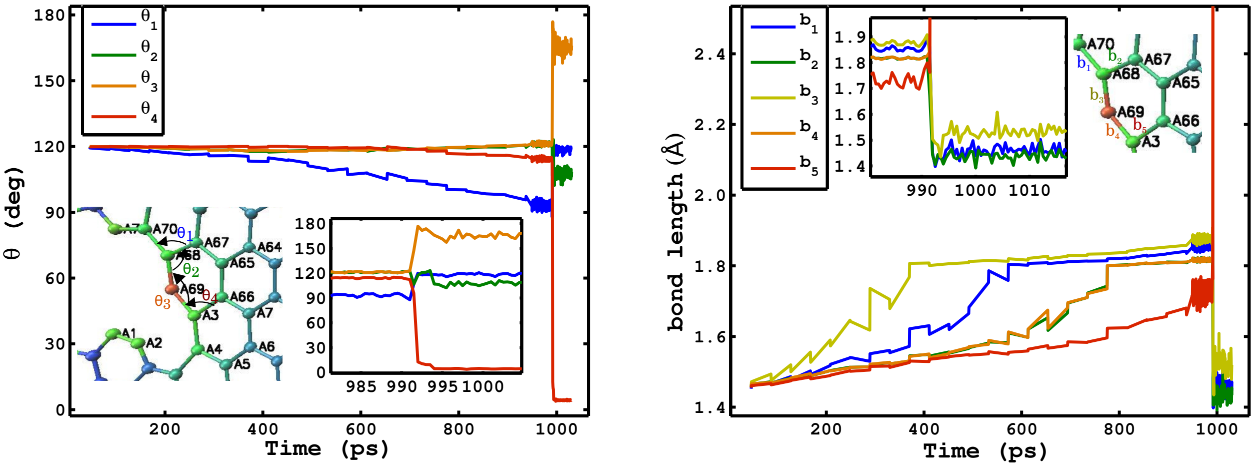

(a) arm-chair, Δt=1 fs

(b) arm-chair, Δt=1 fs

Figure 5.9: Variation of (a) the bond angle and (b) the bond length when the time step is equal to 1 fs and the lattice is oriented along the arm-chair direction. The corresponding atoms and the bonds around the crack tip actively involved in the bond stretching and the reorientation are shown in the sub-picture, highlighting the atom numbers shown in Fig. 5.8(a). Another sub-picture shows a closeup of the variation at the initiation of the crack propagation. Legends indicate the defined bond angles and the bond lengths in the atomic model.

direction. However, later on the crack tip changed its orientation and continues to propagate along the x direction.

The bond breaking and the crack growth process can be understood from the bond stretching and bond rotation phenomena as explained below. With the application of the load, the bonds continue to stretch and change the orientation, as shown in Fig. 5.8(a), until point R1 in Fig. 5.6(c). Which in turn leads to continuous increase of σ_{yy} and hence the potential energy. The variation of the bond angle and the bond length with time where $\Delta t = 1fs$, at a particular point around the crack tip, immediately after the initiation of the crack propagation, are plotted in Fig. 5.9(a) and Fig. 5.9(b), respectively. From Fig. 5.9, the increase in the bond length and the change in the bond orientation with time can be noticed, leading to the accumulation of the system potential energy and hence the increase in σ_{yy}. The energy of the atoms around the crack tip will be the highest in the entire lattice. Therefore, the process of bond stretching and reorientation will be more intense in the regions around the crack tip. From Fig. 5.9(a) and (b), it can be observed that the initial loading leads to change in bond angle θ_1, which leads to increase in the length of the bond b_1. The bond b_1 starts to stretch after reaching the maximum bond length of 1.8 Å. Similarly, bonds b_2 and b_4 starts stretching, after bond b_1 reaches the critical bond length. Finally, the last bond b_5 starts taking the load, and once the bond b_5 reaches the critical bond length, a sudden rise in the bond angle θ_3 is observed, which leads to the bond breaking and hence the crack growth in Graphene. Results indicate that all the bonds reach their critical bond length before breaking, which is independent of the bond angle. However, the bonds break only after the stretching of the last bond (b_5) and the subsequent change in the bond angle θ_3 until the sudden failure, as discussed above. The similar behavior of bond stretching and bond rotation is also observed for other cases considered in the present study as shown in Fig. 5.12, Fig. 5.15 and Fig. 5.17 for the arm-chair Graphene with Δ t = 0.1 fs and zig-zag Graphene with Δ t = 1 fs and Δ t = 0.1 fs, respectively. Further details on Fig. 5.12, Fig. 5.15 and Fig. 5.17 are provided in the subsequent sections. The study of bond stretching and bond rotation is repeated at several locations of the Graphene sheet and the results (not shown here) are found to be consistent with the phenomena reported above. At point R1, the stresses exceeds the failure stresses leading to sudden failure of the Graphene bond. As a result, the stress reduces drastically to point R2, which leads to relaxation in the bond energy and hence a drop in the potential energy can be observed from point R1 to point R2 in Fig. 5.6(c). The bond breaking at 991.5 ps can be observed in Fig. 5.9, where the bond angle and the bond lengths are drastically changing. Since some of the bonds are broken in the process as shown in Fig. 5.8(b), the crack tip moves to a new location, exposing the broken bonds. Further loading leads to stretching of the bond and therefore increase of the potential energy from point R2 to R3 in Fig. 5.6(c). At point R3 where the stresses are more than the fracture strength, further breaking of the bonds occurs and the process continues as shown in Fig. 5.8(c)-(f).

The deformed configurations at 1009.5 ps, 1031.0 ps and 1072.0 ps are plotted in Fig. 5.7(g), (h) and (i), respectively, and the crack tip is observed to be located around

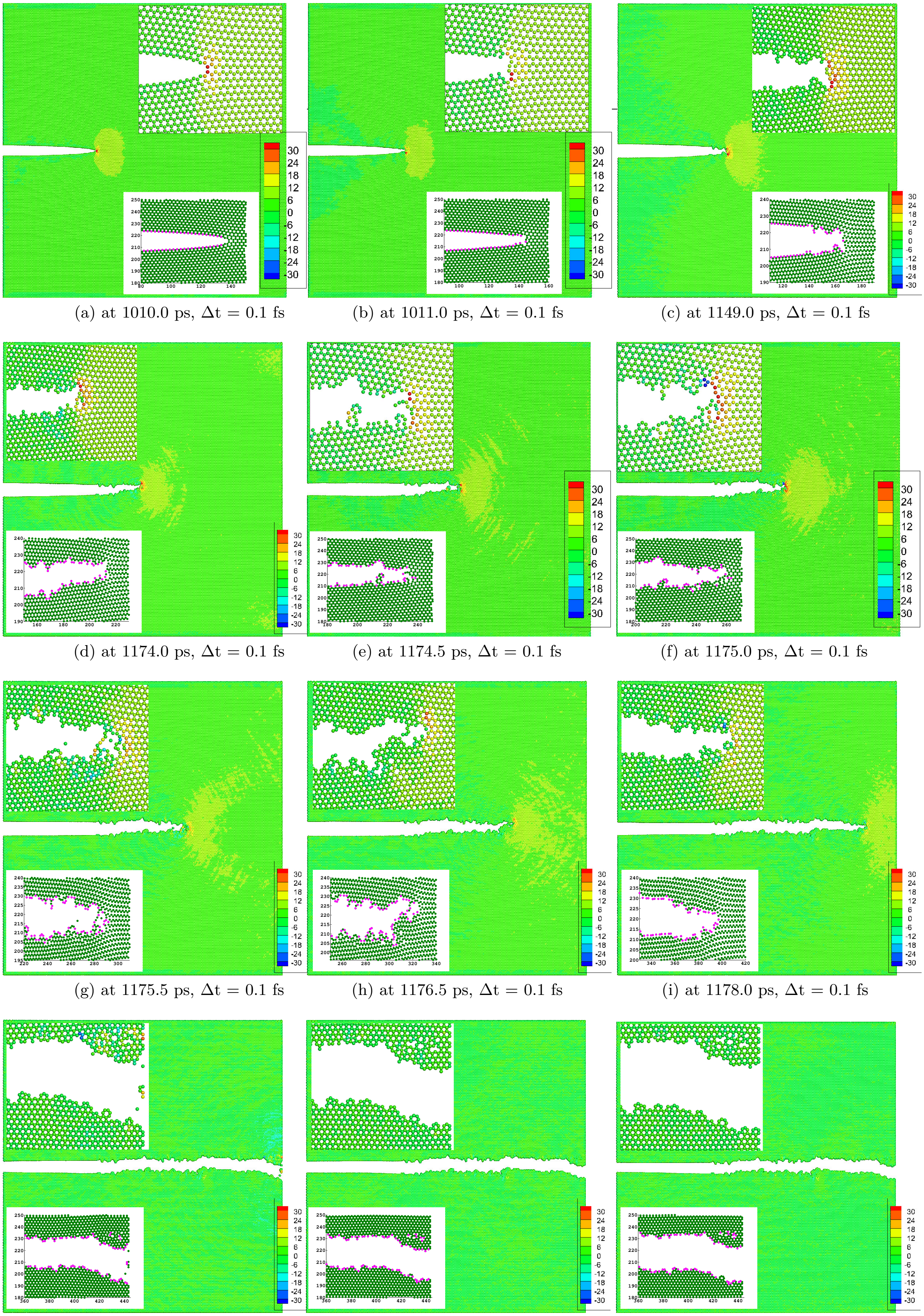

(a) at 1010.0 ps, Δt = 0.1 fs (b) at 1011.0 ps, Δt = 0.1 fs (c) at 1149.0 ps, Δt = 0.1 fs

(d) at 1174.0 ps, Δt = 0.1 fs (e) at 1174.5 ps, Δt = 0.1 fs (f) at 1175.0 ps, Δt = 0.1 fs

(g) at 1175.5 ps, Δt = 0.1 fs (h) at 1176.5 ps, Δt = 0.1 fs (i) at 1178.0 ps, Δt = 0.1 fs

(j) at 1179.0 ps, Δt = 0.1 fs (k) at 1191.5 ps, Δt = 0.1 fs (l) at 1231.0 ps, Δt = 0.1 fs

Figure 5.10: Distribution of stress per atom along the y direction in Graphene, with the lattice oriented in the arm-chair direction, at various times with Δt = 0.1 fs. The sub picture on the top shows a closeup around the crack tip and the sub picture on the bottom shows the location of the crack tip along with highlighting the atoms on the crack surface.

340Å at all the above times. Therefore, the crack has not propagated between 996.0 ps to 1072.0 ps. This is because of the bond stretching and reorientation during this time slot, as explained in the above paragraph. The system potential energy is observed to increase corresponding to the region between the points R4 to R5 in Fig. 5.6(c). The deformed configurations at 1113.0 ps, 1196.0 ps and 1236.0 ps are plotted in Fig. 5.7(j), (k) and (l), where the crack tip is observed to be at around 385Å, 390Å and 440Å, respectively. From Fig. 5.7(l), the crack tip has reached the right edge at 1236.0 ps and therefore, the specimen is separated into two. The drop in the system potential energy corresponding to the time slot between 1113.0 ps to 1236.0 ps, can be observed between the points R5 to R6 in Fig. 5.6(c).

To study the effect of the time step on the crack growth, the above analysis is repeated with time step equal to 0.1 ps. The deformed configuration including the crack propagation with time step equal to 0.1 ps, is plotted in Fig. 5.10. The deformed configuration of the full scale atomistic model at 1010.0 ps, just before the initiation of the crack propagation is plotted in Fig. 5.10(a). The atoms around the crack tip in Fig. 5.10(a) possess the highest values of σ_y and hence the bonds are ready to be broken. The deformed configuration at the 1011.0 ps is plotted in Fig. 5.10(b). The breaking of first bonds close to the crack tip can be observed in Fig. 5.10(b). With the continuous application of load the crack starts to propagate after initiating at 1011.0 ps. Deformed configurations at the 1149.0 ps is plotted in Fig. 5.10(c). A closeup of the atoms around the crack tip along with their potential energy at various times are plotted in Fig. 5.11. The variation of the bond angle and the bond length with time where $\Delta t = 0.1fs$, at a particular point around the crack tip, immediately after the initiation of the crack propagation, are plotted in Fig. 5.12(a) and Fig. 5.12(b), respectively. From Fig. 5.12, the increase in the bond length and the change in the bond orientation with time can be noticed, leading to the accumulation of the system potential energy and hence the σ_{yy}. From Fig. 5.10(b), the onset of the crack propagation is observed at 1010.5 ps, which is confirmed by the significant change in the bond angle and the bond orientation around 1010 ps in Fig. 5.12.

The crack propagate smoothly along the x direction without any kink, as opposed to a kink at 996.0 ps in Fig. 5.7(f) when the time step is equal to 1 fs. The crack tip reached the right edge at 1179.0 ps as shown in Fig. 5.7(j) and the two sections continue to separate each other there after as shown in the deformed configurations at 1191.5 ps and 1231.0 ps in Fig. 5.7(j) and (l), respectively. We estimated that in total 1.236 million time steps are required to completely propagate the crack through the length, with 1 fs time step. Whereas, 12.31 million steps are required with the 0.1 fs time step.

From Fig. 5.6(e), it is observed that the crack initiation in both the cases occurred at the same time, which is of the similar order at strain equal to 0.046. Afterwards, a drop in the σ_y is noticed in both the cases, i.e., Δt = 1 fs and 0.1 fs. However, the case with Δt = 1 fs shows a large drop compared to the case with Δt = 0.1 fs. Results indicate that lower relaxation times and higher time steps can lead to inaccurate post yielding material behaviour. This is confirmed with a further lower relaxation rate, as discussed as discussed

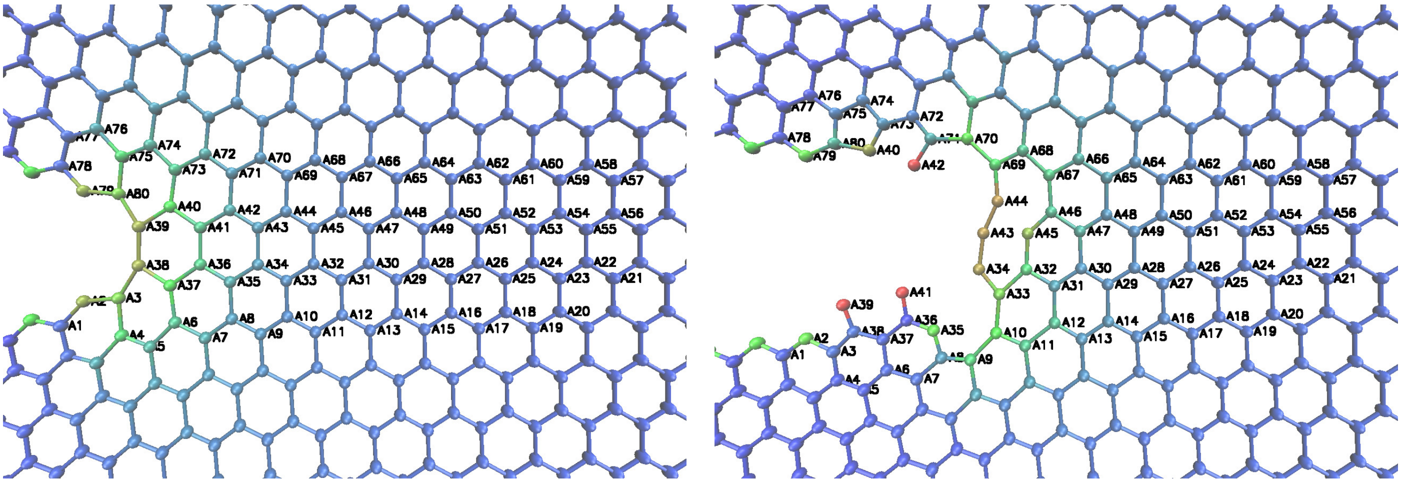
A1
A2
A3
A4
A5
A6
A7
A8
A9
A10
A11
A12
A13
A14
A15
A16
A17
A18
A19
A20
A21
A22
A23
A24
A25
A26
A27
A28
A29
A30
A31
A32
A33
A34
A35
A36
A37
A38
A39
A40
A41
A42
A43
A44
A45
A46
A47
A48
A49
A50
A51
A52
A53
A54
A55
A56
A57
A58
A59
A60
A61
A62
A63
A64
A65
A66
A67
A68
A69
A70
A71
A72
A73
A74
A75
A76
A77
A78
A79
A80

(a) at 1010.0 ps, Δt = 0.1 fs (b) at 1010.5 ps, Δt = 0.1 fs

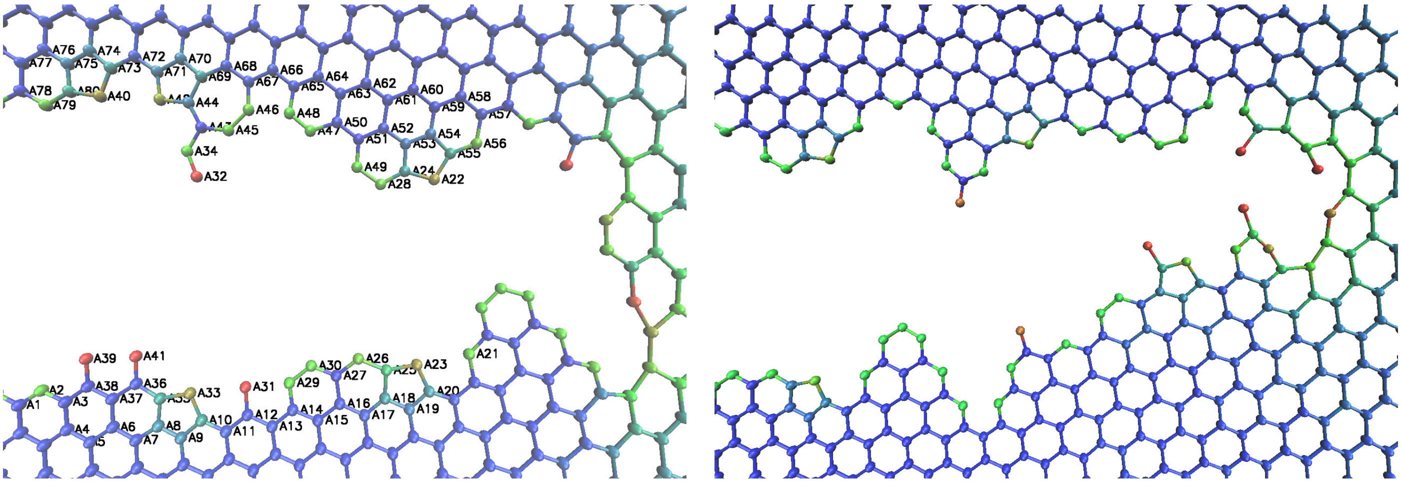
A1
A2
A3
A4
A6
A7
A8
A9
A10
A11
A12
A13
A14
A15
A16
A17
A18
A19
A20
A21
A22
A23
A24
A25
A26
A27
A28
A29
A30
A31
A32
A33
A34
A36
A37
A38
A39
A40
A41
A44
A45
A46
A47
A48
A49
A50
A51
A52
A53
A54
A55
A56
A57
A58
A59
A60
A61
A62
A63
A64
A65
A66
A67
A68
A69
A70
A71
A72
A73
A74
A75
A76
A77
A78
A79
A80

(c) at 1011.5 ps, Δt = 0.1 fs (d) at 1173.5 ps, Δt = 0.1 fs

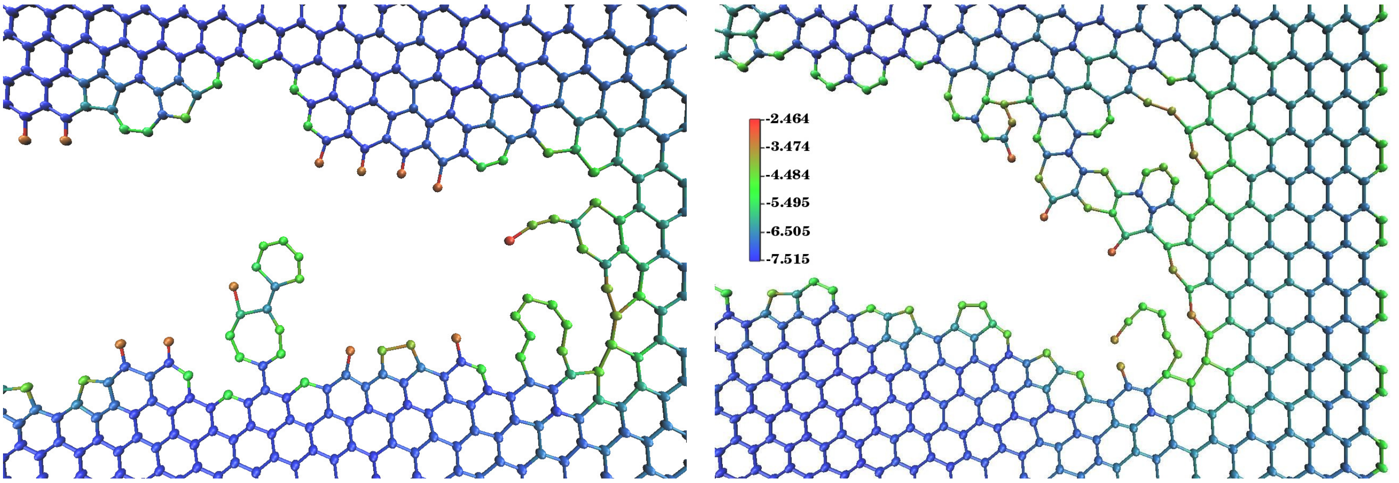
-2.464
-3.474
-4.484
-5.495
-6.505
-7.515

(e) at 1174.5 ps, Δt = 0.1 fs (f) at 1178.5 ps, Δt = 0.1 fs

Figure 5.11: Distribution of the potential energy per atom on the atoms around the crack tip at various times, with the lattice oriented in the arm-chair direction and time step equal to 0.1 fs.

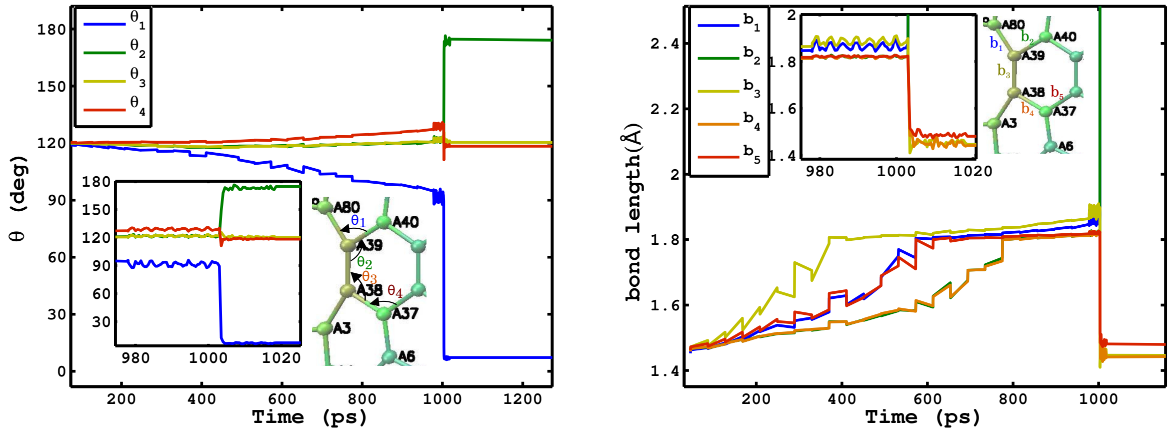

(a) arm-chair, Δt=0.1 fs

(b) arm-chair, Δt=0.1 fs

Figure 5.12: Variation of (a) the bond angle and (b) the bond length when the time step is equal to 0.1 fs and the lattice is oriented along the arm-chair direction. The corresponding atoms and the bonds around the crack tip actively involved in the bond stretching and the reorientation are shown in the sub-picture, highlighting the atom numbers shown in Fig. 5.11(a). Another sub-picture shows a closeup of the variation at the initiation of the crack propagation. Legends indicate the defined bond angles and the bond lengths in the atomic model.

in the next paragraph. The post yielding behavior of Graphene with time step equal 0.1 fs is compared with another higher time step Δt = 0.2 fs. The results (not shown here) with Δt = 0.1 fs and Δt = 0.2 fs shows the similar post yielding behavior. Based on the results, we conclude that 0.1 fs time step is accurate enough to predict the post yielding behavior of Graphene. A large drop in potential energy as well as σ_{yy} can be seen (from point R1 to R2) in Fig. 5.6(c), for the case with Δt = 1 fs. However, the case with Δt = 0.1 fs shows a small drop in potential energy as well as σ_{yy}, from point Q1 to Q2 in Fig. 5.6(c). Further loading shows hardening in both the cases, from points R2 to R3 and Q2 to Q3, respectively Fig. 5.6(c).

Finally, to study the effect of the lower relaxation on the crack growth we performed a simulation of the problem shown in Fig. 5.5 with time step equal to 1 fs and without any intermediate relaxation. The strain loading on the top and bottom edge atoms with time is plotted in Fig. 5.6(a). From Fig. 5.6(b) and (d), the onset of crack initiation (corresponding to point P1 in Fig. 5.6(c)) lies on the higher side as compared to the cases with intermediate relaxation with time step equal to 1 fs and 0.1 fs. However, after the crack initiation the crack propagation is not smooth and stable. This can be observed through the zig-zag pattern of the potential energy after point P2 in Fig. 5.6(c) and in Fig. 5.6(e). Results indicate that the intermediate relaxations are indeed essential for obtaining accurate post yielding behaviour. Therefore, in the present work, we are not considering the case without intermediate

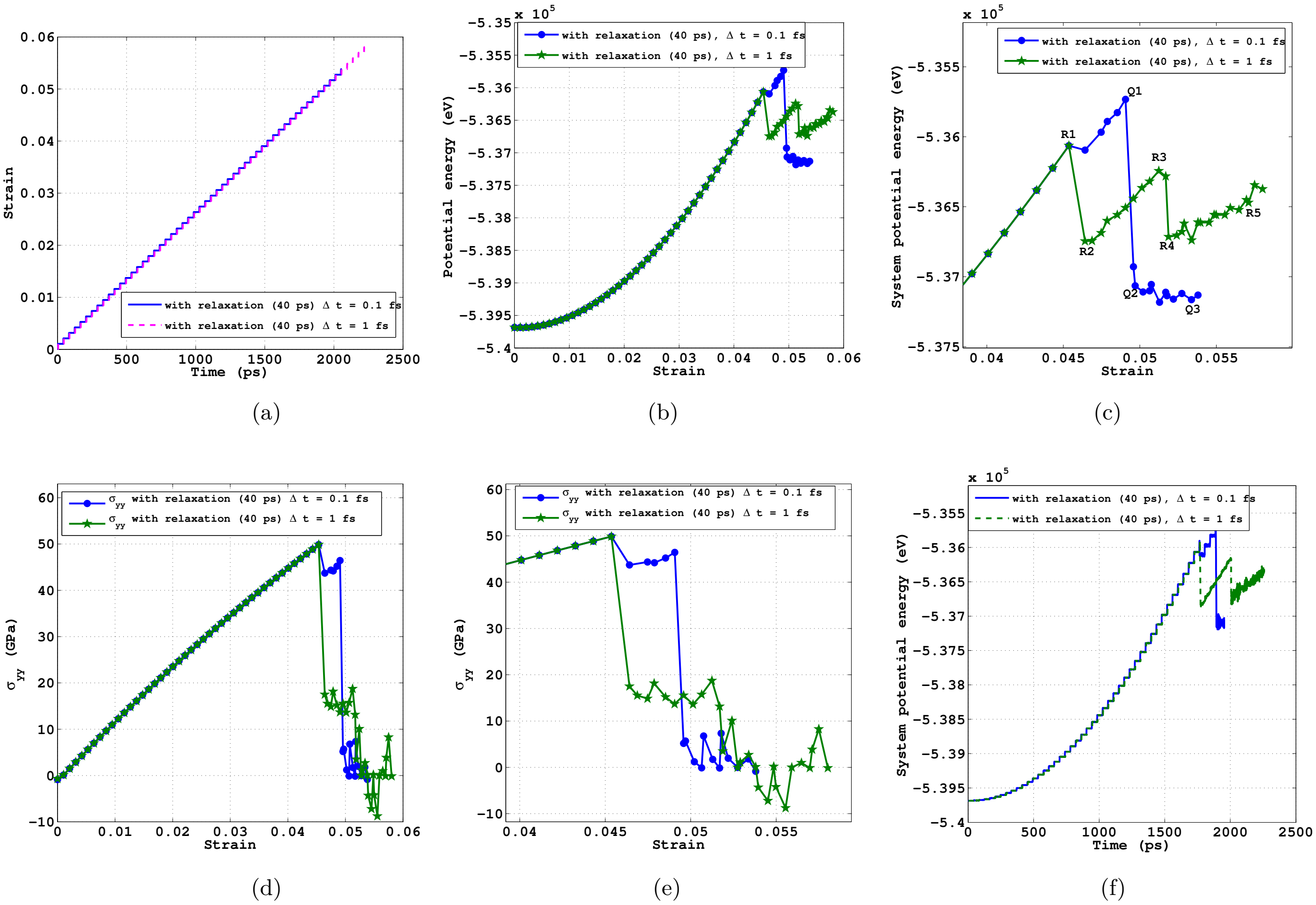

(a) (b) (c)

(d) (e) (f)

Figure 5.13: Distribution of the (a) strain with time, (b) potential energy with strain and (c) a closeup of (b) around the crack propagation zone. Variation of the (d) stress along the y direction with strain, (e) a closeup of (d) around the crack propagation zone and (f) distribution of the potential energy with time for the crack growth in zig-zag Graphene.

relaxation.

5.3.2 Example 2: Crack propagation in zigzag Graphene with an initial edge crack

In this example, the crack propagation in the Graphene sheet as shown in schematic Fig. (5.5), with lattice oriented along the zig-zag direction (Fig. (5.4)(b)) is studied. The same domain dimensions, boundary conditions, loading cycle and the time steps, as discussed in example 1 are adopted in this example as well.

To propagate the crack, a velocity of 0.1 angstroms (Å) per pico-seconds (ps) is prescribed on the top and bottom edge atoms, refer to Fig. 5.5. A velocity ramp profile as shown in Fig. 5.5, is applied in the middle of lattice. Distribution of the strain, system potential energy

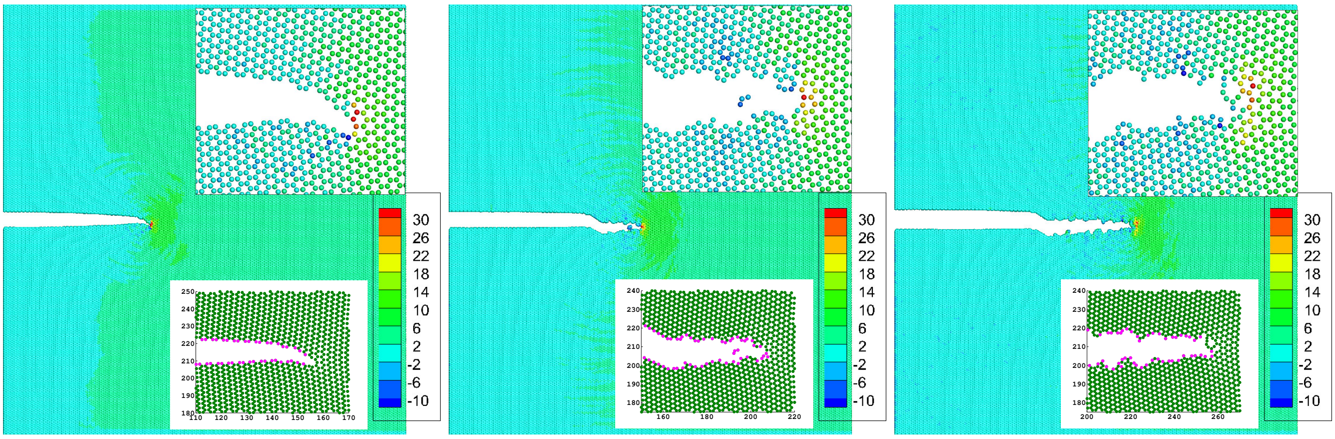

(a) at 1769.0 ps, $\Delta t = 1$ fs (b) at 1770.0 ps, $\Delta t = 1$ fs (c) at 1771.0 ps, $\Delta t = 1$ fs

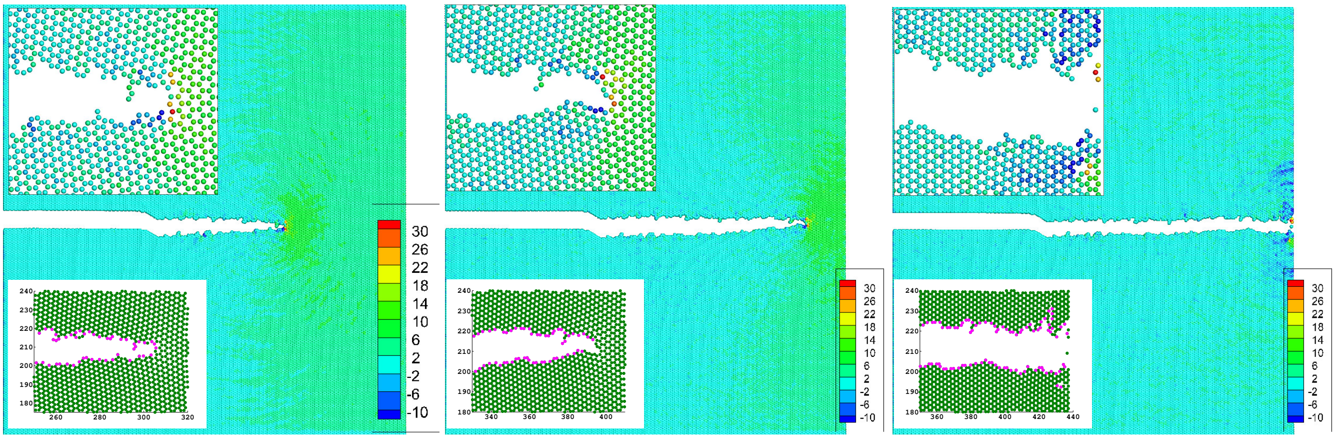

(d) at 1772.0 ps, $\Delta t = 1$ fs (e) at 2006.5 ps, $\Delta t = 1$ fs (f) at 2007.5 ps, $\Delta t = 1$ fs

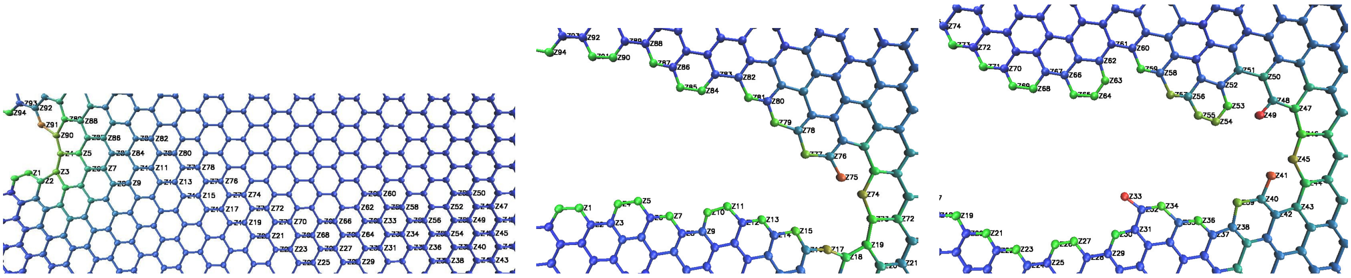

(g) at 1767.0 ps, $\Delta t = 1$ fs (h) at 1769.0 ps, $\Delta t = 1$ fs (i) at 1769.5 ps, $\Delta t = 1$ fs

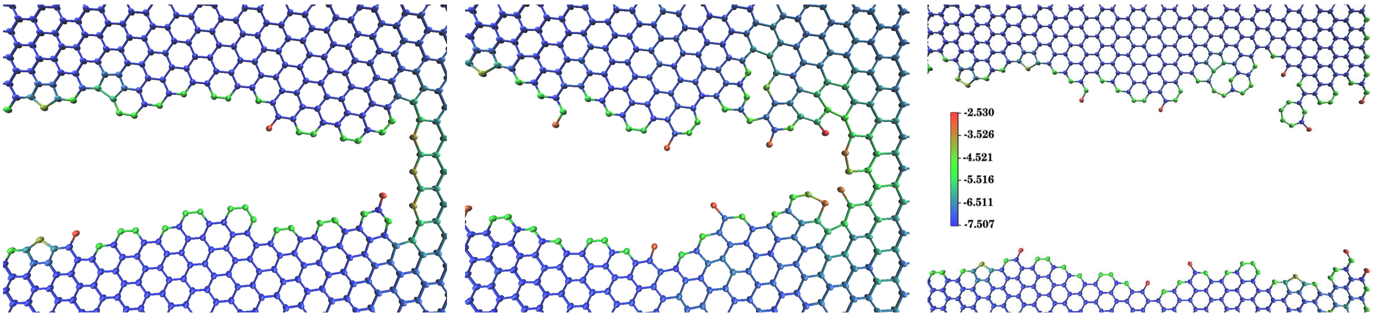

(j) at 1807.5 ps, $\Delta t = 1$ fs (k) at 2007.0 ps, $\Delta t = 1$ fs (l) at 2012.5 ps, $\Delta t = 1$ fs

Figure 5.14: Figures (a)-(f): Distribution of stress per atom along the y direction in Graphene, with the lattice oriented along the zig-zag direction, with $\Delta t = 1$ fs. The sub picture on the top shows a closeup around the crack tip and the sub picture on the bottom shows the location of the crack tip along with highlighting the atoms on the crack surface. Figures (g)-(l): Distribution of the potential energy per atom on the atoms around the crack tip at various times, with the lattice oriented in the arm-chair direction and $\Delta t = 1$ fs.

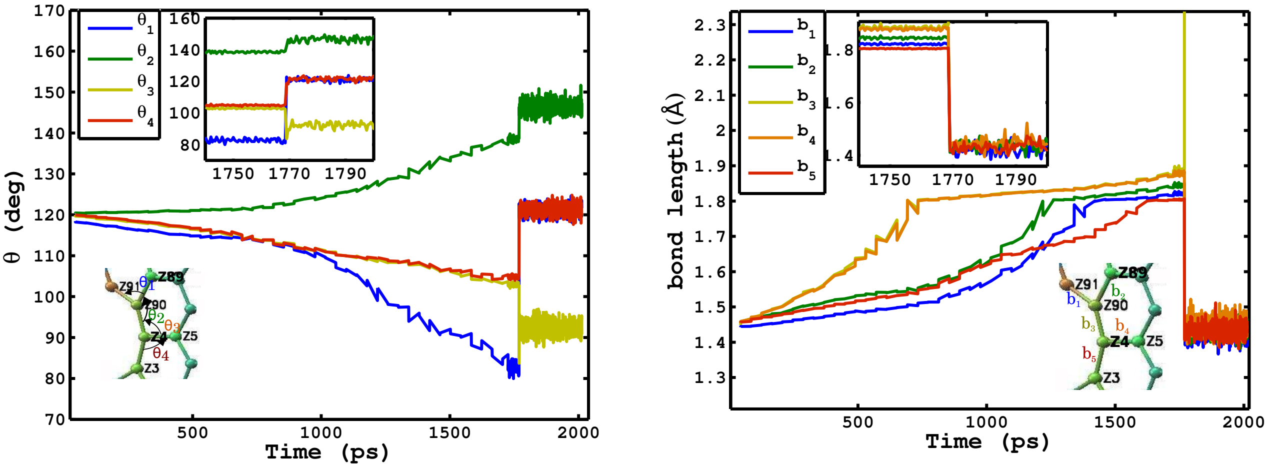

(a) zig-zag, Δt=1 fs

(b) zig-zag, Δt=1 fs

Figure 5.15: Variation of (a) the bond angle and (b) the bond length when the time step is equal to 1 fs and the lattice is oriented along the zig-zag direction. The corresponding atoms and the bonds around the crack tip actively involved in the bond stretching and the reorientation are shown in the sub-picture, highlighting the atom numbers shown in Fig. 5.14(g). Another sub-picture shows a closeup of the variation at the initiation of the crack propagation. Legends indicate the defined bond angles and the bond lengths in the atomic model.

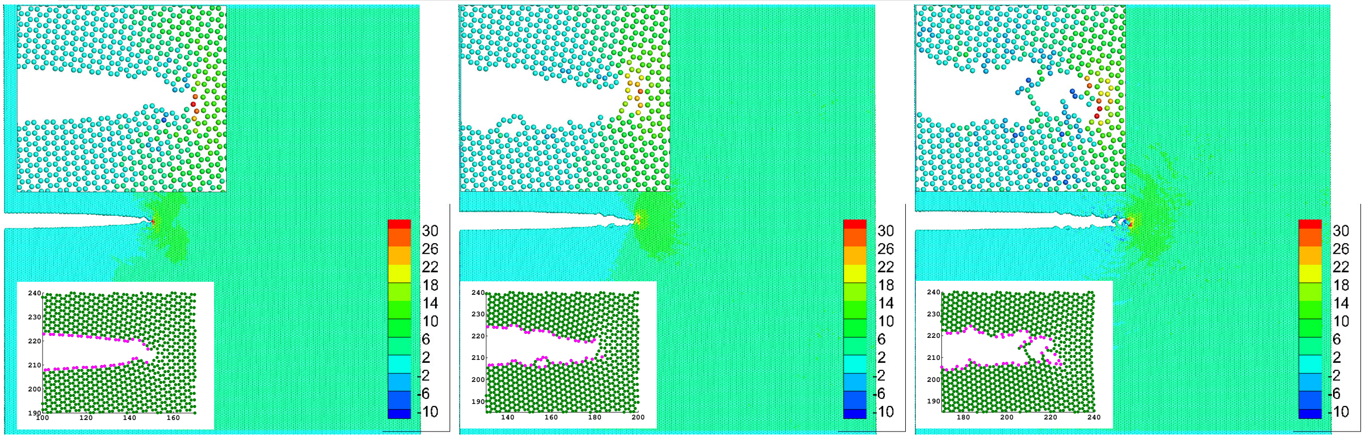

(a) at 1765.5 ps, Δt = 0.1 fs (b) at 1888.5 ps, Δt = 0.1 fs (c) at 1890.0 ps, Δt = 0.1 fs

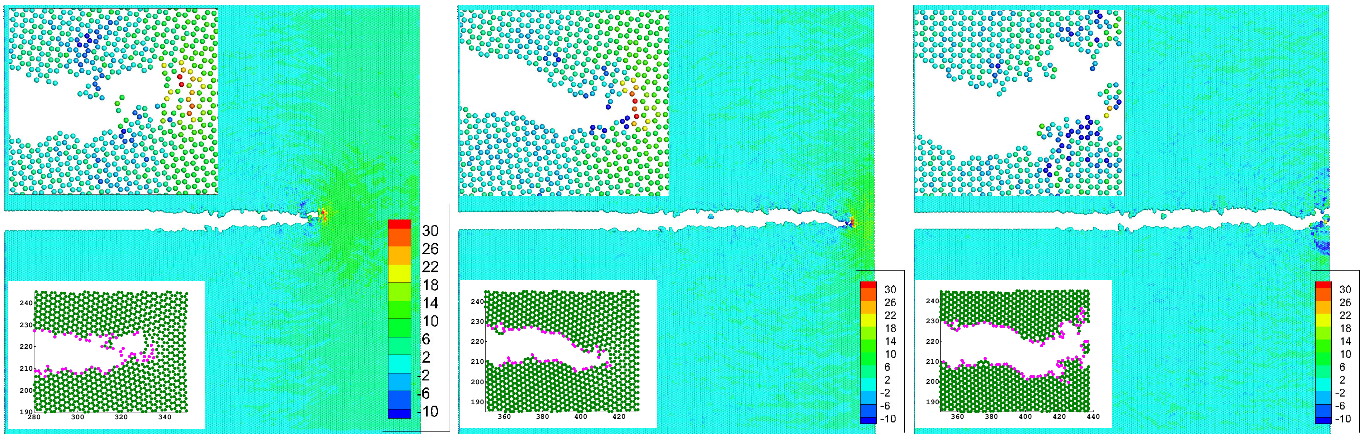

(d) at 1892.0 ps, Δt = 0.1 fs (e) at 1893.5 ps, Δt = 0.1 fs (f) at 1894.0 ps, Δt = 0.1 fs

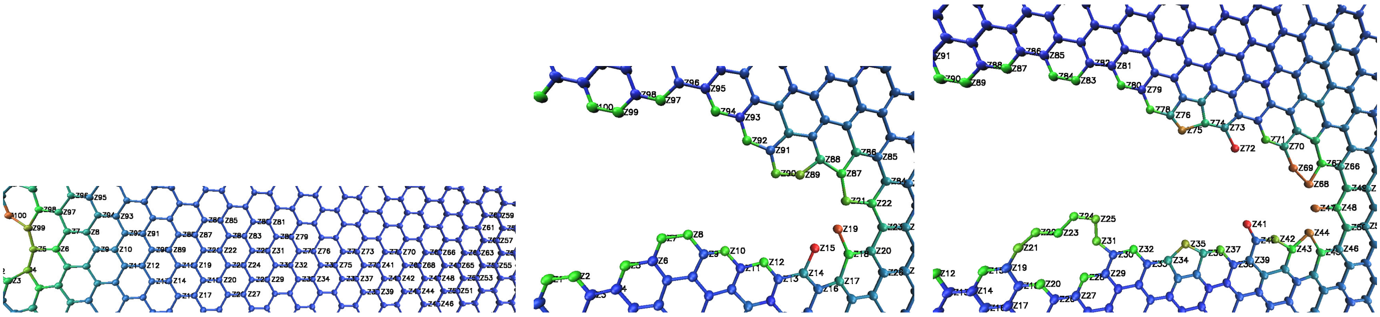

(g) at 1765.0 ps, Δt = 0.1 fs (h) at 1765.5 ps, Δt = 0.1 fs (i) at 1766.0 ps, Δt = 0.1 fs

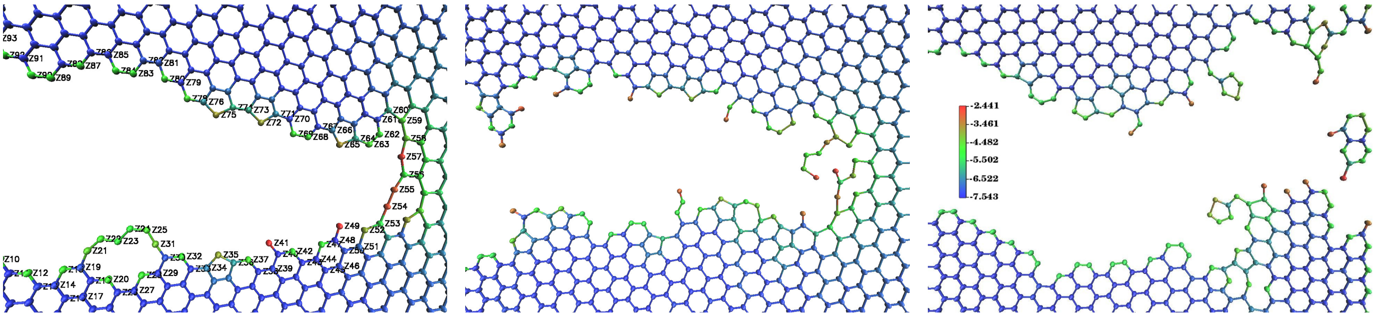

(j) at 1766.5 ps, Δt = 0.1 fs (k) at 1892.5 ps, Δt = 0.1 fs (l) at 1894.0 ps, Δt = 0.1 fs

Figure 5.16: Figures (a)-(f): Distribution of stress per atom along the y direction in Graphene, with the lattice oriented along the zig-zag direction, with Δt = 0.1 fs. The sub picture on the top shows a closeup around the crack tip and the sub picture on the bottom shows the location of the crack tip along with highlighting the atoms on the crack surface. Figures (g)-(l): Distribution of the potential energy per atom on the atoms around the crack tip at various times, with the lattice oriented in the arm-chair direction and Δt = 0.1 fs.

and the stress along the y direction with time and strain are plotted in Fig. 5.13. Fig. 5.13(f) shows the distribution of the system potential energy with time, for the simulations with intermediate relaxation for 40 ps, with time step equal to 1 fs and 0.1 fs. The intermediate steps in Fig. 5.13(f) corresponds to the equilibration period. Figure 5.14(a-f) shows the distribution of stress per atom along the y direction (σ_y) in the deformed configuration of the atomistic model, at various times for $\Delta \mathrm{t} = 1$ fs. A closeup of the atoms around the crack tip along with their potential energy at various times with time step equal to 1 fs is plotted in Fig. 5.14(g-l).

The deformed configuration of the full scale atomistic model at 1769.0 ps, soon after the crack starts to propagate is plotted in Fig. 5.14(a). The deformed configurations at the 1770.0 ps, 1771.0 ps and 1772.0 ps are plotted in Fig. 5.14(b), (c) and (d) where the crack tip is located around 210Å, 260Å and 310Å along the x direction, respectively. The crack progression is continuous until 1772.0 ps, after initiating at 1769.0 ps. However, because of the bond rotation and stretching at 1772.0 ps, the crack does not progress and only opens up, until 2006.5 ps. The variation of the bond angle and the bond length with time where $\Delta t = 1fs$, at a particular point around the crack tip, immediately after the initiation of the crack propagation, are plotted in Fig. 5.15(a) and Fig. 5.15(b), respectively. From Fig. 5.15, the increase in the bond length and the change in the bond orientation with time can be noticed, leading to the accumulation of the system potential energy and hence the σ_{yy}.

In order to investigate the effect of the time step on the crack propagation with the lattice oriented along the zig-zag direction, another simulation with time step equal to 0.1 fs is performed. The deformed configurations at 1765.5 ps, 1888.5 ps, 1890.0 ps, 1892.0 ps, 1893.5 ps and 1894.0 ps are plotted in Fig. 5.16(a) to (f), respectively. A closeup of the atoms around the crack tip along with their potential energy at various times with time step equal to 0.1 fs are plotted in Fig. 5.16(g-l). The variation of the bond angle and the bond length with time where $\Delta t = 0.1fs$, at a particular point around the crack tip, immediately after the initiation of the crack propagation, are plotted in Fig. 5.17(a) and Fig. 5.17(b), respectively.

Based on the first and second examples, for smooth crack growth time step of 0.1 fs is recommended. The crack speed is estimated by dividing the distance traveled by the crack front with the time taken. The distance traveled is calculated from the positions of the crack tip in the current and previous times. Variation of the crack speed for different scenarios is plotted in Fig. (5.18). From Fig. (5.18), the crack speed is observed to increase with the crack length.

5.3.3 Example 3: Crack growth in Graphene on Silicon surface

In this example, we study the crack growth in Graphene on Silicon surface. Consider a three dimensional atomistic model with dimensions 543.09Å× 543.09Å× 5.4309. The initial crack of length 180.23Å in the x direction located at 271.5Å in the y direction, is created in the fine scale model by restricting the interaction between the atoms. The atom to atom interactions

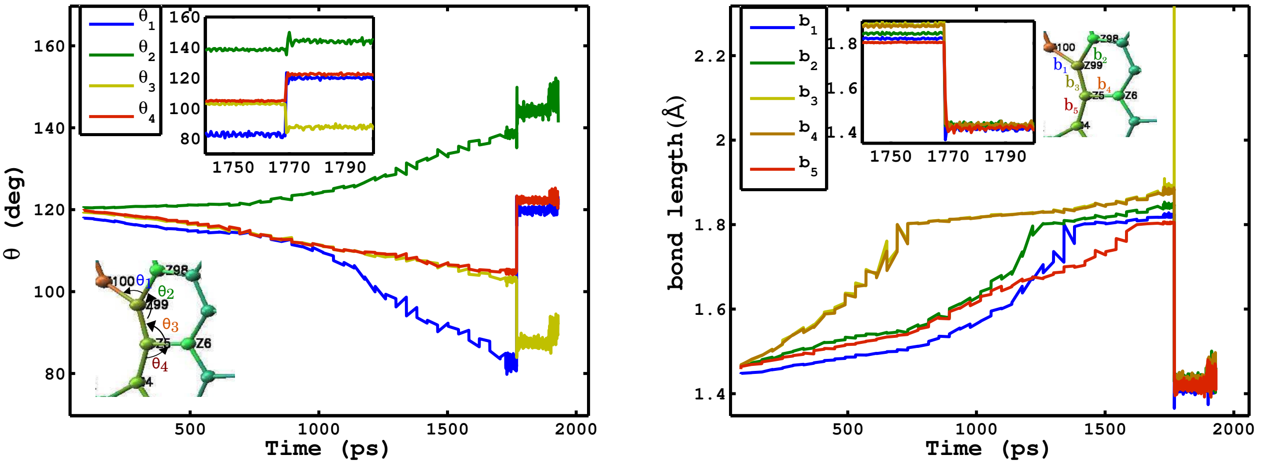

(a) zig-zag, Δt=0.1 fs

(b) zig-zag, Δt=0.1 fs

Figure 5.17: Variation of (a) the bond angle and (b) the bond length when the time step is equal to 0.1 fs and the lattice is oriented along the zig-zag direction. The corresponding atoms and the bonds around the crack tip actively involved in the bond stretching and the reorientation are shown in the sub-picture, highlighting the atom numbers shown in Fig. 5.14(g). Another sub-picture shows a closeup of the variation at the initiation of the crack propagation. Legends indicate the defined bond angles and the bond lengths in the atomic model.

are modeled based on the Tersoff potential. To simulate the mode I crack propagation of an edge crack, the triangular displacement loads are applied in small increments, in the *y* direction, on the top and bottom rows of atoms. The neighbours are updated after each load step. The atom positions are estimated after each load step by minimizing the system potential energy.

Atom positions in the deformed configuration after the final load step from the atomistic model are plotted in Fig. 5.19. Fig. 5.19(a) and Fig. 5.19(b) shows the crack opening and growth in Graphene and Silicon at the end of the simulation. Fig. 5.19(c) shows the Graphene atoms atoms are bonded to the Silicon atoms on the surface. The crack propagation in the coupled Graphene on Silicon surface is shown in Fig. 5.19(d).

The deformed configuration of the coarse scale model developed based on the VAC in the *xy* plane is shown in Fig. 5.20(a). Rotated view of Fig. 5.20(a) in the *yz* plane is shown in Fig. 5.20(b).

5.4 Discussion

Fracture in two dimensional Graphene structure is studied. The bond stretching and the bond reorientation are the net mechanisms of the crack growth. The crack propagation in Graphene is studied through two numerical examples. In both the examples, a model with initial edge crack model is considered. In the first example, the Graphene lattice oriented along the arm-chair direction is considered and in the second example it is oriented along the zig-zag direction. We also studied the influence of the time step on fracture. Therefore,

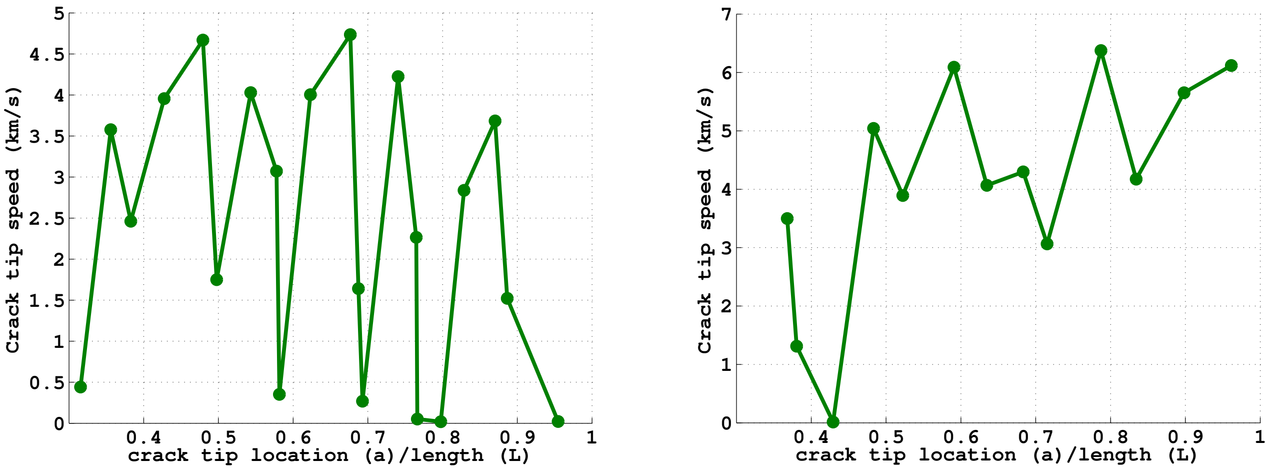

(a) arm-chair, Δt=1 fs (b) arm-chair, Δt=0.1 fs

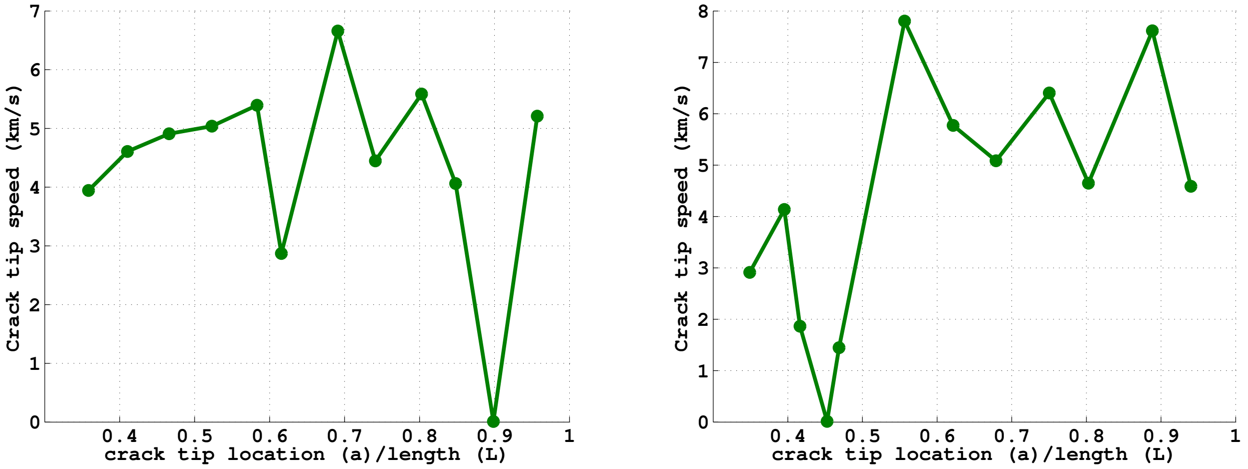

(c) zig-zag, Δt=1 fs (d) zig-zag, Δt=0.1 fs

Figure 5.18: Variation of the crack speed with the location of the crack tip, when lattice is oriented along the (a) arm-chair direction, with time step equal to 1 fs, (b) arm-chair direction, with time step equal to 0.1 fs, (c) zig-zag direction, with time step equal to 1 fs and (d) zig-zag direction, with time step equal to 0.1 fs.

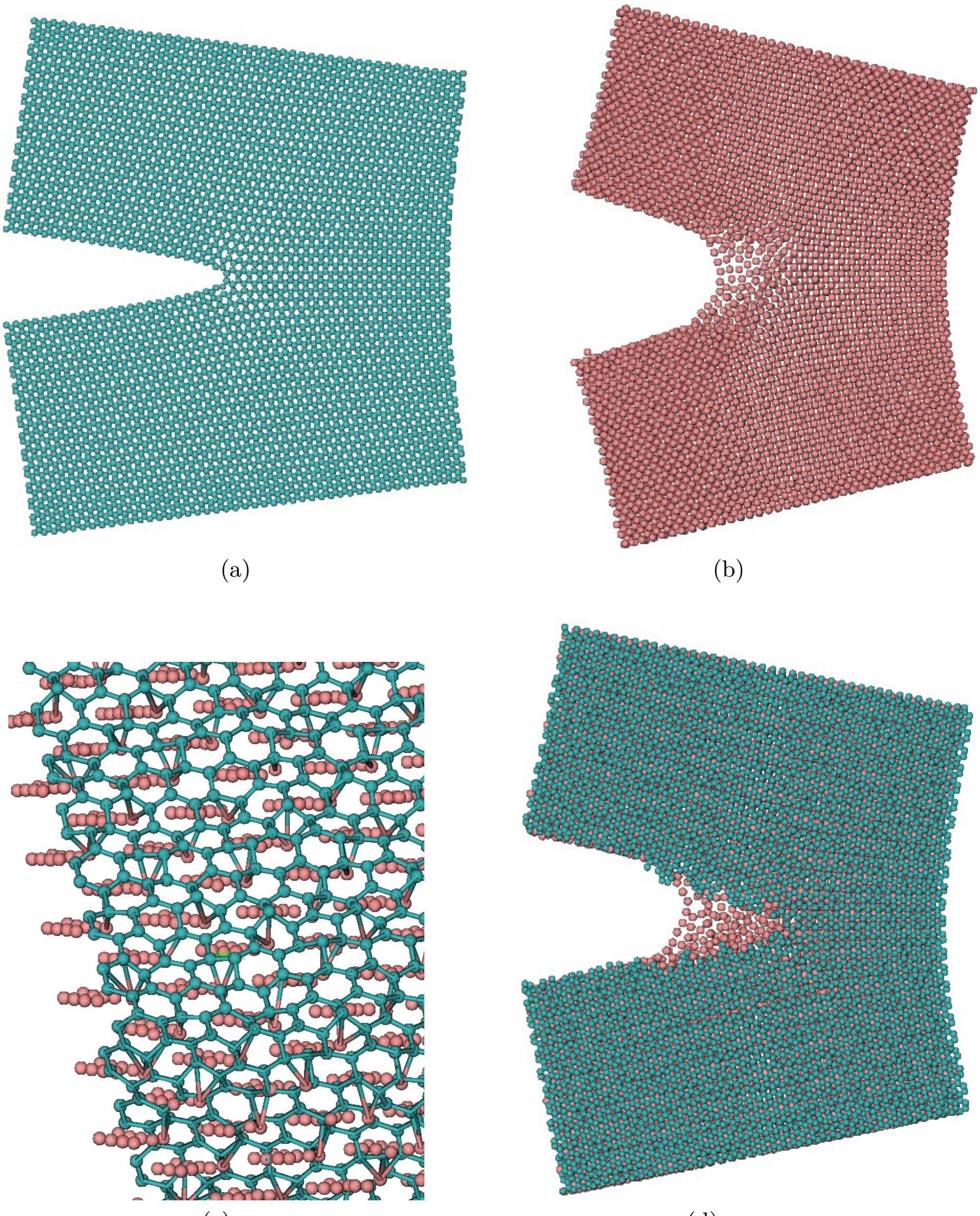

(a) (b)

(c) (d)

Figure 5.19: Crack propagation in (a) Graphene sheet, (b) Silicon. (c) Graphene on Silicon surface highlighting the bonds of the Silicon atoms connected to the Graphene atoms and (d) Crack propagation in the combined Graphene on Silicon surface.

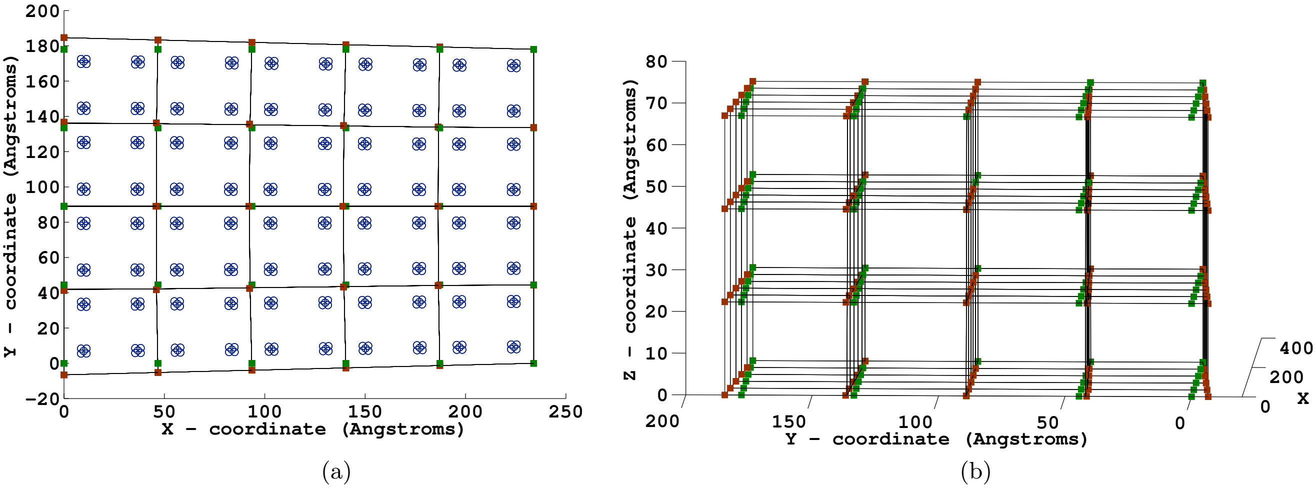

(a) (b)

Figure 5.20: Deformed configuration of the coarse model highlighting the initial and final positions of the nodes (a) in the front view and in an (b) an isometric view.

two different time steps, 1 fs and 0.1 fs, with an intermediate relaxation period of 40 ps are considered.

A sudden drop in the system potential energy is noticed just before the crack propagation. Breaking of the severely stressed bonds increases the crack length, exposing the new set of atoms to resist the applied load. The phenomena continues until the crack front reaches the other boundary, where the specimen is separated into two. The crack propagates at a later stage in the zig-zag Graphene than the arm-chair Graphene as the lattice structure of the zig-zag Graphene resists higher tensile loads compared to the arm-chair Graphene. Similar crack initiations are observed for $\Delta t = 1$ fs and 0.1 fs. However, when $\Delta t = 0.1$ fs the post yielding behaviour of Graphane is more accurate.

The crack speed is estimated by dividing the distance travelled by the crack front with the time taken. The distance travelled is calculated from the positions of the crack tip in the current and previous times. Variation of the crack speed for different scenarios is plotted and the crack speed is observed to increase with the crack length. Pure atomistic simulations of fracture in Graphene on Silicon surface are presented. Details of the mathematical modeling of the three dimensional multiscale method are discussed.

Chapter 6

Concluding remarks and future scope

6.1 Conclusions

A novel adaptive multiscale method for fracture has been developed by enhancing the BSM using the phantom node method so that cracks can be modeled at the coarse scale. To ensure self-consistency in the bulk, a virtual atom cluster is devised providing the response of the intact material at the coarse scale. A molecular statics model is employed in the fine scale where crack propagation is modeled by naturally breaking the bonds. The fine scale and coarse scale models are coupled by enforcing the displacement boundary conditions on the ghost atoms. Adaptive refinement and coarsening schemes are developed and implemented during the crack propagation. The simulated fracture pattern based on the AMM, accurately matches with the pure atomistic simulations. Atom positions around the crack tip from the pure atomistic model and the AMM were compared. The error in the displacement and the potential energy between the pure atomistic and the AMM simulations is found to be 0.208% and 0.824%, respectively. The AMM is observed to be 9 times more computationally efficient compared to the pure atomistic simulations. However, the computational efficiency will be multiplied for problems of large domain dimensions.

A three dimensional (3D) coarse graining technique to convert a given atomistic region into an equivalent coarse region, in the context of multiscale fracture has been developed. The present method is the first of its kind. The developed CG technique can be applied to identify and upscale the defects like: cracks, dislocations and shear bands. Atoms lying on the crack surface in the fine scale model are separated from the atoms not on the crack surface through the centro symmetry parameter. A rectangular discretization is superimposed on the fine scale model to capture the atoms into rectangular cells. The crack path in each cell is approximated using the atoms on the crack surface and their neighbours. An equivalent crack surface in the coarse scale model is obtained by joining the cellular crack paths. The current method has been applied to estimate the equivalent coarse scale models of several complex fracture patterns arrived from the pure atomistic simulations. The upscaled fracture pattern agree well with the actual fracture pattern. The error in the potential energy of the pure atomistic and the CG model was found to be well within the acceptable limits.

First novel meshless adaptive multiscale method for fracture has been developed. The phantom node method is replaced by a meshless differential reproducing kernel particle method. The DRKP method is comparatively more expensive but allows for a more “natural” coupling between the two scales due to the meshless interpolation functions. The higher order continuity is also beneficial. The developed multiscale method is employed to study the complex crack propagation. Results based on the MAMMF were observed to be in excellent agreement with the pure atomistic simulations. Atom positions around the crack tip from the pure atomistic and the MAMMF simulations are compared. The error in displacement between the MS and MAMMF was found to be 0.2%. The MAMMF is observed to be 6 times more computationally efficient than the pure atomistic simulations.

The developed multiscale methods are applied to study the fracture in practical materials like Graphene and Graphene on Silicon surface. The bond stretching and the bond reorientation were observed to be the net mechanisms of the crack growth in Graphene. Crack growth in both the arm-chair an dteh zig-zag Graphene are studied. The influence of time step on the crack propagation was studied using two different time steps, 1 fs and 0.1 fs with an intermediate relaxation period of 40 ps. The post yielding behaviour of Graphane was found to be more accurate when $\Delta t = 0.1$ fs. Pure atomistic simulations of fracture in Graphene on Silicon surface are presented. Details of the mathematical modeling of the three dimensional multiscale method are discussed.

6.2 Future scope

The CG technique can be employed in the context of a concurrent multiscale models [74, 76, 84]. An error estimator can be developed to determine the size of the fine scale domain (inside the coarse scale domain) and to drive an adaptive refinement in the context of concurrent multiscale methods for fracture.

The developed multiscale methods can be applied to practical problems like fracture in Silicon, which is used in applications like photo-voltaic cells. Silicon being a very brittle material, several micro-cracks are developed [178] during the transportation, installation and due to the external loads like snow, rain and wind loads on the installed panels. The micro-cracks significantly reduce the over all yield [179] of the solar panels. To improve the fracture strength and to improve the electrical properties of Silicon, the latest technique is to add a layer of Graphene on the surface of Silicon. Developing multiscale techniques incorporating the surface effects like Graphene on the Silicon surface is challenging. The author would like to pursue the above goals during his post-doctoral studies.

Appendix A

Derivation of the internal forces: fine scale

The internal forces in equation (2.6) can be further simplified using the chain rule to split the partial derivative with respect to $r_{\alpha\beta}$, as explained below

$$\frac{\partial W^{\text{int}}}{\partial \mathbf{r}_{\lambda}} = \frac{1}{2}\sum_{\alpha=1}^{n^{\text{A}}}\sum_{\beta\neq\alpha}^{n^{\text{A}}}\frac{\partial V(r_{\alpha\beta})}{\partial r_{\alpha\beta}}\frac{\partial r_{\alpha\beta}}{\partial \mathbf{r}_{\lambda}}. \tag{A.1}$$

Substituting equation (2.9) into the second term on the right hand side of equation (A.1)

$$\frac{\partial r_{\alpha\beta j}}{\partial r_{\lambda k}} = \frac{\partial\sqrt{\sum_{j=1}^{3}(r_{\alpha j}-r_{\beta j})^2}}{\partial r_{\lambda k}} = \frac{\sum_{j=1}^{3}(r_{\alpha j}-r_{\beta j})}{\sqrt{\sum_{j=1}^{3}(r_{\alpha j}-r_{\beta j})^2}}(\delta_{\alpha\lambda}-\delta_{\beta\lambda}) = \frac{\mathbf{r}_{\alpha\beta}}{r_{\alpha\beta}}(\delta_{\alpha\lambda}-\delta_{\beta\lambda}) \tag{A.2}$$

Further, we will drop the summation symbol in equation (A.2). Lets consider two possible cases for λ. First, when $\lambda=\alpha$ and $\lambda\neq\beta$

$$\frac{\partial r_{\alpha\beta j}}{\partial r_{\alpha k}} = \frac{(r_{\alpha j}-r_{\beta j})}{r_{\alpha\beta}}(1) \tag{A.3}$$

and secondly, when $\lambda=\beta$ and $\lambda\neq\alpha$

$$\frac{\partial r_{\alpha\beta j}}{\partial r_{\beta k}} = \frac{(r_{\alpha j}-r_{\beta j})}{r_{\alpha\beta}}(-1). \tag{A.4}$$

Since α and β are interchangeable, after exchanging β with α and vice-versa, equation (A.4) becomes,

$$\frac{\partial r_{\beta\alpha j}}{\partial r_{\alpha k}} = \frac{(r_{\beta j}-r_{\alpha j})}{r_{\beta\alpha}}(-1) = \frac{(r_{\alpha j}-r_{\beta j})}{r_{\alpha\beta}}. \tag{A.5}$$

Combining both cases in equations (A.3) and (A.5) for any arbitrary atom λ, yields

$$\frac{\partial r_{\alpha\beta}}{\partial \mathbf{r}_{\lambda}} = 2\frac{(\mathbf{r}_{\alpha} - \mathbf{r}_{\beta})}{r_{\alpha\beta}}. \tag{A.6}$$

Therefore, substituting equation (A.6) into equation (A.1) using equation (2.6), the internal forces on an atom α are defined as

$$\mathbf{F}_{\alpha}^{\text{int}} = -\sum_{\beta\neq\alpha}^{n^{\text{A}}} \frac{\partial V(r_{\alpha\beta})}{\partial r_{\alpha\beta}} \left(\frac{\mathbf{r}_{\alpha} - \mathbf{r}_{\beta}}{r_{\alpha\beta}}\right). \tag{A.7}$$

Appendix B

Bond potentials

The bond potentials used to model the atom to atom interactions in the present thesis are explained below

B.1 Lennard-Jones potential

The mathematical expression of the Lennard-Jones potential is given by

$$V(r_{\alpha\beta}) = 4\epsilon \left[\left(\frac{\sigma}{r_{\alpha\beta}} \right)^{12} - \left(\frac{\sigma}{r_{\alpha\beta}} \right)^{6} \right] \tag{B.1}$$

where σ and ϵ are the specific Lennard-Jones parameters and $r_{\alpha\beta}$ is the distance between the atoms α and β defined in equation (2.9).

B.2 Tersoff potential

The mathematical expression of the bond energy based on the Tersoff potential is given by [177]

$$V(r_{\alpha\beta}) = f_c(r_{\alpha\beta})[f_R(r_{\alpha\beta}) + b_{\alpha\beta} f_A(r_{\alpha\beta})]. \tag{B.2}$$

The bond energy in the Tersoff framework is a combination of repulsive (f_R) energy function which is exponentially decaying and attractive (f_A) energy function that exponentially increases; with the increase of distance between the atoms. f_c is a smooth spherical cutoff function around atom α based upon the distance to the first nearest-neighbor shell. The function f_c in equation (B.2) is defined as [177]

$$f_c(r_{\alpha\beta}) = \begin{cases} 1 & \text{when } r_{\alpha\beta} < \mathcal{R}_{\alpha\beta} \\ \frac{1}{2} + \frac{1}{2}\cos\left(\frac{\pi(r_{\alpha\beta} - \mathcal{R}_{\alpha\beta})}{(\mathcal{S}_{\alpha\beta} - \mathcal{R}_{\alpha\beta})}\right) & \text{when } \mathcal{R}_{\alpha\beta} < r_{\alpha\beta} < \mathcal{S}_{\alpha\beta} \\ 0 & \text{when } r_{\alpha\beta} > \mathcal{S}_{\alpha\beta} \end{cases} \tag{B.3}$$

Variable	Silicon (Si)	Carbon (C)
$\mathcal{R}$ (Å)	2.7	1.8
$\mathcal{S}$ (Å)	3.0	2.1
$\mathcal{A}$ (eV)	1.8308×10^{3}	1.3936×10^{3}
$\mathcal{B}$ (eV)	4.7118×10^{2}	3.4670×10^{2}
$\mathcal{D}$ (Å^{-1})	2.4799	3.4879
$\mathcal{E}$ (Å^{-1})	1.7322	2.2119
$\mathcal{P}$	1.1000×10^{-6}	1.5724×10^{-7}
q	7.8734×10^{-1}	7.2751×10^{-1}
c	1.0039×10^{5}	3.8049×10^{4}
d	1.6217×10^{1}	4.3840×10^{0}
h	-5.9825×10^{-1}	-5.7058×10^{-1}

Table B.1: Parameters for Silicon and Carbon to be used in equation (B.2), adopted from [177]. $\mathcal{R}$ and $\mathcal{S}$ were not systematically optimized.

from equation(B.3), f_c returns a value of 1 if $r_{\alpha\beta}$ is less than $\mathcal{R}_{\alpha\beta}$ and 0 when $r_{\alpha\beta}$ greater than $\mathcal{S}_{\alpha\beta}$. The values of the constants $\mathcal{R}_{\alpha\beta} = \sqrt{\mathcal{R}_\alpha \mathcal{R}_\beta}$ and $\mathcal{S}_{\alpha\beta} = \sqrt{\mathcal{S}_\alpha \mathcal{S}_\beta}$, (where α and β can be two different atom types, like Silicon and Carbon) are listed for Silicon and Carbon atoms in table (B.1). The repulsive and attractive potential energies are tuned with the parameters $\mathcal{A}_{\alpha\beta}$ and $\mathcal{B}_{\alpha\beta}$, respectively. The repulsive potential energy is defined as [177]

$$f_R(r_{\alpha\beta}) = \mathcal{A}_{\alpha\beta} e^{-\mathcal{D}_{\alpha\beta} r_{\alpha\beta}} \tag{B.4}$$

and the attractive potential energy is estimated from [177]

$$f_A(r_{\alpha\beta}) = -\mathcal{B}_{\alpha\beta} e^{-\mathcal{E}_{\alpha\beta} r_{\alpha\beta}} \tag{B.5}$$

where $\mathcal{A} = \sqrt{\mathcal{A}_\alpha \mathcal{A}_\beta}$, $\mathcal{B} = \sqrt{\mathcal{B}_\alpha \mathcal{B}_\beta}$, $\mathcal{D}_{\alpha\beta} = (\mathcal{D}_\alpha + \mathcal{D}_\beta)/2$ and $\mathcal{E}_{\alpha\beta} = (\mathcal{E}_\alpha + \mathcal{E}_\beta)/2$, in equations (B.4) and (B.5), are the constants listed in table (B.1). The variable $b_{\alpha\beta}$ in equation (B.2) is designed to represent the bond strength of the potential. $b_{\alpha\beta}$ is inversely proportional to the coordination number and is defined as [177]

$$b_{\alpha\beta} = \xi_{\alpha\beta} \left(1 + \mathcal{P}_\alpha^{q_\alpha} \zeta_{\alpha\beta}^{q_\alpha}\right)^{-1/2q_\alpha} \tag{B.6}$$

where $\mathcal{P}$ and q are the constants listed in table (B.1). $\zeta_{\alpha\beta}$ provides a weighted measure of the number of other bonds (γ) competing with the bond α-β, which is defined as [177]

$$\zeta_{\alpha\beta} = \sum_{\gamma \neq \alpha,\beta} f_c\left(r_{\alpha\gamma}\right) g\left(\theta_{\alpha\beta\gamma}\right) \tag{B.7}$$

where $\xi_{\alpha\beta}$ is the strengthening or weakening factor of the hetero-polar bonds and $g\left(\theta_{\alpha\beta\gamma}\right)$ provides a measure of dependence on the bonding angle $\theta_{\alpha\beta\gamma}$, subtended at atom α by atoms β and γ. The variable $g\left(\theta_{\alpha\beta\gamma}\right)$ is included to stabilize the atomic geometry under shear operations and to provide an effective coordination contribution based on the elastic energy of the current configuration, which is defined as [177]

$$g\left(\theta_{\alpha\beta\gamma}\right) = 1 + \frac{c_\alpha^2}{d_\alpha^2} - \frac{c_\alpha^2}{d_\alpha^2 + \left(h_\alpha - \cos\left(\theta_{\alpha\beta\gamma}\right)\right)^2} \tag{B.8}$$

where c_α, d_α and h_α are the constants listed in table(B.1). Refer appendix for the derivation of the first derivative of the potential function in equation (B.2).

B.3 First derivative of the Tersoff potential

The internal forces in equation (2.6) estimated based on the Tersoff potential function in equation (B.2) are derived below. Considering the first derivative of the bond potential function (V($r_{\alpha\beta}$)) in equation (B.2), with respect to the position of a particular atom λ in a particular direction k, i.e.,

$$\begin{aligned}\frac{\partial V(r_{\alpha\beta})}{\partial r_{\lambda k}} &= \frac{\partial(f_c(r_{\alpha\beta})[f_R(r_{\alpha\beta}) + b_{\alpha\beta} f_A(r_{\alpha\beta})])}{\partial r_{\lambda k}} \\ &= f_c\left(r_{\alpha\beta}\right)\left[\frac{\partial f_R(r_{\alpha\beta})}{\partial r_{\lambda k}} + b_{\alpha\beta}\frac{\partial f_A(r_{\alpha\beta})}{\partial r_{\lambda k}} + \frac{\partial b_{\alpha\beta}}{\partial r_{\lambda k}} f_A(r_{\alpha\beta})\right] + \frac{\partial f_c(r_{\alpha\beta})}{\partial r_{\lambda k}}[f_R(r_{\alpha\beta}) + b_{\alpha\beta} f_A(r_{\alpha\beta})].\end{aligned} \tag{B.9}$$

The terms, $\frac{\partial f_R(r_{\alpha\beta})}{\partial r_{\lambda k}}$, $\frac{\partial f_A(r_{\alpha\beta})}{\partial r_{\lambda k}}$ and $\frac{\partial f_c(r_{\alpha\beta})}{\partial r_{\lambda k}}$ in equation (B.9) are further split, based on the chain rule of the derivatives as shown below

$$\frac{\partial f(r_{\alpha\beta})}{\partial r_{\lambda k}} = \frac{\partial f(r_{\alpha\beta})}{\partial r_{\alpha\beta}} \frac{\partial r_{\alpha\beta}}{\partial r_{\lambda k}} \tag{B.10}$$

where $r_{\alpha\beta}$ is defined in equation (2.9). Therefore, the derivative $\frac{\partial r_{\alpha\beta}}{\partial r_{\lambda k}}$ in equation (B.10) can be evaluated by substituting definition of $r_{\alpha\beta}$ from equation (2.9)

$$\frac{\partial r_{\alpha\beta}}{\partial r_{\lambda k}} = \frac{\partial\sqrt{\sum_{j=1}^{3}(r_{\alpha j} - r_{\beta j})^2}}{\partial r_{\lambda k}} = \frac{(r_{\alpha j} - r_{\beta j})}{\sqrt{\sum_{j=1}^{3}(r_{\alpha j} - r_{\beta j})^2}}(\delta_{\alpha\lambda} - \delta_{\beta\lambda}) = \frac{r_{\alpha\beta j}}{r_{\alpha\beta}}(\delta_{\alpha\lambda} - \delta_{\beta\lambda}) \tag{B.11}$$

Lets consider two possible cases for λ. First, when $\lambda = \alpha$ and $\lambda \neq \beta$

$$\frac{\partial r_{\alpha\beta j}}{\partial r_{\alpha k}} = \frac{(r_{\alpha j} - r_{\beta j})}{r_{\alpha\beta}}(1) \tag{B.12}$$

and secondly, when $\lambda = \beta$ and $\lambda \neq \alpha$

$$\frac{\partial r_{\alpha\beta j}}{\partial r_{\beta k}} = \frac{(r_{\alpha j} - r_{\beta j})}{r_{\alpha\beta}}(-1). \tag{B.13}$$

Since α and β are interchangeable, after exchanging β with α and vice-versa, equation (B.13) becomes,

$$\frac{\partial r_{\beta\alpha j}}{\partial r_{\alpha k}} = \frac{(r_{\beta j} - r_{\alpha j})}{r_{\beta\alpha}}(-1) = \frac{(r_{\alpha j} - r_{\beta j})}{r_{\alpha\beta}} = \frac{r_{\alpha\beta j}}{r_{\alpha\beta}}. \tag{B.14}$$

Combining both cases in equations (B.12) and (B.14) for any arbitrary atom λ, yields

$$\frac{\partial r_{\alpha\beta}}{\partial \mathbf{r}_\lambda} = 2\frac{(\mathbf{r}_\alpha - \mathbf{r}_\beta)}{r_{\alpha\beta}}. \tag{B.15}$$

The first derivative of the function f with respect to $r_{\alpha\beta}$ in equation (B.10) can now be estimated as

$$\frac{\partial f_R(r_{\alpha\beta})}{\partial r_{\alpha\beta}} = -\mathcal{D}_{\alpha\beta}\mathcal{A}_{\alpha\beta}e^{-\mathcal{D}_{\alpha\beta}r_{\alpha\beta}} \tag{B.16}$$

and

$$\frac{\partial f_A(r_{\alpha\beta})}{\partial r_{\alpha\beta}} = \mathcal{E}_{\alpha\beta}\mathcal{B}_{\alpha\beta}e^{-\mathcal{E}_{\alpha\beta}r_{\alpha\beta}}. \tag{B.17}$$

The cutoff function (f_c) is differentiable only in the range of $\mathcal{R}_{\alpha\beta} < r_{\alpha\beta} < \mathcal{S}_{\alpha\beta}$. Therefore,

$$\frac{\partial f_c(r_{\alpha\beta})}{\partial r_{\alpha\beta}} = -\frac{1}{2}\sin\left(\frac{\pi(r_{\alpha\beta} - \mathcal{R}_{\alpha\beta})}{\mathcal{S}_{\alpha\beta} - \mathcal{R}_{\alpha\beta}}\right)\frac{\pi}{\mathcal{S}_{\alpha\beta} - \mathcal{R}_{\alpha\beta}}. \tag{B.18}$$

Now, the derivative of $b_{\alpha\beta}$ in equation (B.9) is given by

$$\begin{aligned}\frac{\partial b_{\alpha\beta}}{\partial r_{\lambda k}} &= -\frac{1}{2q_\alpha}\xi_{\alpha\beta}\left(1 + \mathcal{P}_\alpha^{q_\alpha}\zeta_{\alpha\beta}^{q_\alpha}\right)^{(-1/2q_\alpha - 1)} q_\alpha\mathcal{P}_\alpha^{q_\alpha}\zeta_{\alpha\beta}^{q_\alpha - 1}\frac{\partial\zeta_{\alpha\beta}}{\partial r_{\lambda k}} \\ &= -\frac{1}{2}\frac{b_{\alpha\beta}\mathcal{P}_\alpha^{q_\alpha}}{\left(\zeta_{\alpha\beta}^{(1-q_\alpha)} + \mathcal{P}_\alpha^{q_\alpha}\zeta_{\alpha\beta}\right)}\frac{\partial\zeta_{\alpha\beta}}{\partial r_{\lambda k}}\end{aligned} \tag{B.19}$$

where

$$\frac{\partial\zeta_{\alpha\beta}}{\partial r_{\lambda k}} = \sum_{\gamma\neq\alpha,\beta}\left(\frac{\partial f_c(r_{\alpha\gamma})}{\partial r_{\alpha\gamma}}\frac{\partial r_{\alpha\gamma}}{\partial r_{\lambda k}}g(\theta_{\alpha\beta\gamma}) + f_c(r_{\alpha\gamma})\frac{\partial g(\theta_{\alpha\beta\gamma})}{\partial\cos(\theta_{\alpha\beta\gamma})}\frac{\partial\cos(\theta_{\alpha\beta\gamma})}{\partial r_{\lambda k}}\right) \tag{B.20}$$

and

$$\frac{\partial g(\theta_{\alpha\beta\gamma})}{\partial\cos(\theta_{\alpha\beta\gamma})} = -\frac{2c_\alpha^2(h_\alpha - \cos(\theta_{\alpha\beta\gamma}))}{(d_\alpha^2 + (h_\alpha - \cos^2(\theta_{\alpha\beta\gamma}))^2}. \tag{B.21}$$

The subtended angle $\cos(\theta_{\alpha\beta\gamma})$ can be evaluated from

$$\cos(\theta_{\alpha\beta\gamma}) = \frac{\mathbf{r}_{\alpha\beta}\cdot\mathbf{r}_{\alpha\gamma}}{r_{\alpha\beta}r_{\alpha\gamma}} = \frac{r_{\alpha\beta i}r_{\alpha\gamma i} + r_{\alpha\beta j}r_{\alpha\gamma j} + r_{\alpha\beta k}r_{\alpha\gamma k}}{r_{\alpha\beta}r_{\alpha\gamma}}. \tag{B.22}$$

Therefore, the derivative of $\cos(\theta_{\alpha\beta\gamma})$ with respect to $r_{\lambda k}$ can be evaluated as

$$\frac{\partial\cos(\theta_{\alpha\beta\gamma})}{\partial r_{\lambda k}} = \frac{r_{\alpha\beta}r_{\alpha\gamma}\frac{\partial(\mathbf{r}_{\alpha\beta}\cdot\mathbf{r}_{\alpha\gamma})}{\partial r_{\lambda k}} - \frac{\partial(r_{\alpha\beta}r_{\alpha\gamma})}{\partial r_{\lambda k}}(\mathbf{r}_{\alpha\beta}\cdot\mathbf{r}_{\alpha\gamma})}{(r_{\alpha\beta}r_{\alpha\gamma})^2} \tag{B.23}$$

where the term $\frac{\mathbf{r}_{\alpha\beta}\cdot\mathbf{r}_{\alpha\gamma}}{\partial r_{\lambda k}}$ in equation (B.23) can be calculated as

$$\frac{\partial(\mathbf{r}_{\alpha\beta}\cdot\mathbf{r}_{\alpha\gamma})}{\partial r_{\lambda k}} = \frac{\partial(r_{\alpha\beta i}r_{\alpha\gamma i} + r_{\alpha\beta j}r_{\alpha\gamma j} + r_{\alpha\beta k}r_{\alpha\gamma k})}{\partial r_{\lambda k}} = \frac{\partial(\sum_{l=1}^{3} r_{\alpha\beta l}r_{\alpha\gamma l})}{\partial r_{\lambda k}} = \frac{\partial[\sum_{l=1}^{3}(r_{\beta l}-r_{\alpha l})(r_{\gamma l}-r_{\alpha l})]}{\partial r_{\lambda k}}$$
$$= r_{\alpha\beta l}(\delta_{\alpha\lambda}-\delta_{\gamma\lambda}) + (\delta_{\alpha\lambda}-\delta_{\beta\lambda})r_{\alpha\gamma l}. \tag{B.24}$$

The term $\frac{\partial(r_{\alpha\beta}r_{\alpha\gamma})}{\partial r_{\lambda k}}$ in equation (B.23) becomes

$$\frac{\partial(r_{\alpha\beta}r_{\alpha\gamma})}{\partial r_{\lambda k}} = \frac{\partial\left(\sqrt{\sum_{l=1}^{3}(r_{\alpha l}-r_{\beta l})^2}\sqrt{\sum_{l=1}^{3}(r_{\alpha l}-r_{\gamma l})^2}\right)}{\partial r_{\lambda k}} = r_{\alpha\beta}\frac{r_{\alpha\gamma l}(\delta_{\alpha\lambda}-\delta_{\gamma\lambda})}{r_{\alpha\gamma}} + \frac{r_{\alpha\beta l}(\delta_{\alpha\lambda}-\delta_{\beta\lambda})}{r_{\alpha\beta}}r_{\alpha\gamma} \tag{B.25}$$

Therefore, substituting equations (B.24) and (B.25) in equation (B.23), yields

$$\frac{\partial\cos(\theta_{\alpha\beta\gamma})}{\partial r_{\lambda k}} = \frac{r_{\alpha\beta l}(\delta_{\alpha\lambda}-\delta_{\gamma\lambda}) + (\delta_{\alpha\lambda}-\delta_{\beta\lambda})r_{\alpha\gamma l}}{r_{\alpha\beta}r_{\alpha\gamma}} - \cos(\theta_{\alpha\beta\gamma})\left(\frac{r_{\alpha\gamma l}(\delta_{\alpha\lambda}-\delta_{\gamma\lambda})}{r_{\alpha\gamma}^2} + \frac{r_{\alpha\beta l}(\delta_{\alpha\lambda}-\delta_{\beta\lambda})}{r_{\alpha\beta}^2}\right). \tag{B.26}$$

Considering the case when (i) $\lambda = \alpha$, $\lambda \neq \beta$ and $\lambda \neq \gamma$

$$\frac{\partial\cos(\theta_{\alpha\beta\gamma})}{\partial r_{\alpha k}} = \frac{r_{\alpha\beta l} + r_{\alpha\gamma l}}{r_{\alpha\beta}r_{\alpha\gamma}} - \cos(\theta_{\alpha\beta\gamma})\left(\frac{r_{\alpha\gamma l}}{r_{\alpha\gamma}^2} + \frac{r_{\alpha\beta l}}{r_{\alpha\beta}^2}\right), \tag{B.27}$$

when (ii) $\lambda = \beta$, $\lambda \neq \alpha$ and $\lambda \neq \gamma$

$$\frac{\partial\cos(\theta_{\alpha\beta\gamma})}{\partial r_{\beta k}} = -\frac{r_{\alpha\gamma l}}{r_{\alpha\beta}r_{\alpha\gamma}} + \cos(\theta_{\alpha\beta\gamma})\frac{r_{\alpha\beta l}}{r_{\alpha\beta}^2} \tag{B.28}$$

and when (iii) $\lambda = \gamma$, $\lambda \neq \alpha$ and $\lambda \neq \beta$

$$\frac{\partial\cos(\theta_{\alpha\beta\gamma})}{\partial r_{\gamma k}} = -\frac{r_{\alpha\beta l}}{r_{\alpha\beta}r_{\alpha\gamma}} + \cos(\theta_{\alpha\beta\gamma})\frac{r_{\alpha\gamma l}}{r_{\alpha\gamma}^2} \tag{B.29}$$

Appendix C

Derivation of the internal forces: coarse scale

The term $\frac{\partial \phi_\rho}{\partial \mathbf{u}_\alpha^{\mathrm{C}}}$ in equation (2.20) can be evaluated for any arbitrary atom λ as given below:

$$\frac{\partial \phi_\rho}{\partial \mathbf{u}_\lambda^{\mathrm{C}}} = \frac{\partial \phi_\rho}{\partial r_{\alpha\beta}} \frac{\partial r_{\alpha\beta}}{\partial \mathbf{u}_\lambda^{\mathrm{C}}}. \tag{C.1}$$

Substituting the the expression for $r_{\alpha\beta}$ from equation (2.9) into equation (C.1) yields

$$\frac{\partial r_{\alpha\beta j}}{\partial \mathbf{u}_{\lambda k}^{\mathrm{C}}} = \frac{\partial \left(\sqrt{\sum_{j=1}^{3} (r_{\alpha j} - r_{\beta j})^2} \right)}{\partial \mathbf{u}_{\lambda k}^{\mathrm{C}}} = \frac{\sum_{j=1}^{3} (r_{\alpha j} - r_{\beta j})}{r_{\alpha\beta}} \left(\frac{\partial \mathbf{r}_{\alpha j}}{\partial \mathbf{u}_{\lambda k}^{\mathrm{C}}} - \frac{\partial \mathbf{r}_{\beta j}}{\partial \mathbf{u}_{\lambda k}^{\mathrm{C}}} \right). \tag{C.2}$$

The position of atom α in the current configuration $\mathbf{r}_\alpha$ is given by

$$\mathbf{r}_{\alpha j} = \mathbf{R}_{\alpha j} + \mathbf{u}_{\alpha j}^{\mathrm{C}}. \tag{C.3}$$

where $\mathbf{R}_\alpha$ denote the initial atom positions. Similarly for the atom β

$$\mathbf{r}_{\beta j} = \mathbf{R}_{\beta j} + \mathbf{u}_{\beta j}^{\mathrm{C}}. \tag{C.4}$$

Using equations equations (C.3) and (C.4) in equation (C.2)

$$\left(\frac{\partial \mathbf{r}_{\alpha j}}{\partial \mathbf{u}_{\lambda k}^{\mathrm{C}}} - \frac{\partial \mathbf{r}_{\beta j}}{\partial \mathbf{u}_{\lambda k}^{\mathrm{C}}} \right) = \delta_{\alpha\lambda}\delta_{jk} - \delta_{\beta\lambda}\delta_{jk} = (\delta_{\alpha\lambda} - \delta_{\beta\lambda})\delta_{jk}. \tag{C.5}$$

Hence, after dropping the summation symbol over the free index j, equation (C.2) becomes

$$\frac{\partial r_{\alpha\beta j}}{\partial \mathbf{u}_{\lambda k}^{\mathrm{C}}} = \frac{(r_{\alpha j} - r_{\beta j})}{r_{\alpha\beta}} (\delta_{\alpha\lambda} - \delta_{\beta\lambda})\delta_{jk}. \tag{C.6}$$

Lets consider two possible cases for λ. The first case, when $\lambda = \alpha$ and $\lambda \neq \beta$

$$\frac{\partial r_{\alpha\beta j}}{\partial \mathbf{u}^{\mathrm{C}}_{\alpha k}} = \frac{(r_{\alpha j} - r_{\beta j})}{r_{\alpha\beta}}(1) \tag{C.7}$$

and the second case, when $\lambda = \beta$ and $\lambda \neq \alpha$

$$\frac{\partial r_{\alpha\beta j}}{\partial \mathbf{u}^{\mathrm{C}}_{\beta k}} = \frac{(r_{\alpha j} - r_{\beta j})}{r_{\alpha\beta}}(-1). \tag{C.8}$$

Since α and β are interchangeable, after exchanging β with α and vice-versa, equation (C.8) becomes,

$$\frac{\partial r_{\beta\alpha j}}{\partial \mathbf{u}^{\mathrm{C}}_{\alpha k}} = \frac{(r_{\beta j} - r_{\alpha j})}{r_{\beta\alpha}}(-1) = \frac{(r_{\alpha j} - r_{\beta j})}{r_{\beta\alpha}}. \tag{C.9}$$

Combining both the cases in equations (C.7) and (C.9) for any arbitrary atom λ, yields

$$\frac{\partial r_{\alpha\beta j}}{\partial \mathbf{u}^{\mathrm{C}}_{\lambda k}} = 2\frac{(r_{\alpha j} - r_{\beta j})}{r_{\alpha\beta}} \tag{C.10}$$

Substituting equation (C.10) into equation (C.1)

$$\frac{\partial \phi_\rho}{\partial \mathbf{u}^{\mathrm{C}}_{\lambda i}} = \frac{\partial \phi_\rho}{\partial r_{\alpha\beta}}\frac{\partial r_{\alpha\beta}}{\partial \mathbf{u}^{\mathrm{C}}_{\lambda i}} = 2\frac{\partial \phi_\rho}{\partial r_{\alpha\beta}}\frac{(r_{\alpha i} - r_{\beta i})}{r_{\alpha\beta}} = 2\frac{\partial \phi_\rho}{\partial r_{\alpha\beta}}\frac{r_{\alpha\beta i}}{r_{\alpha\beta}} \tag{C.11}$$

where $r_{\alpha\beta i}$ is defined in equation (2.28). For the VAC configuration shown in the fourth column of Fig. 2.4(2b), α is always set to 1 and β varies from 2 to 7. Therefore, using the definition of ϕ_ρ from equation (2.16) in equation (C.11) and considering the case where $\lambda = \alpha$ and $\lambda \neq \beta$, equation (C.11) becomes

$$\frac{\partial \phi_\rho}{\partial \mathbf{u}^{\mathrm{C}}_{\alpha i}} = \sum_{\beta=2}^{7}\frac{\partial \phi_{\alpha\beta}}{\partial r_{\alpha\beta}}\frac{r_{\alpha\beta i}}{r_{\alpha\beta}} \overset{\alpha=1}{\Longrightarrow} \frac{\partial \phi_\rho}{\partial \mathbf{u}^{\mathrm{C}}_{1i}} = \sum_{\beta=2}^{7}\frac{\partial \phi_{1\beta}}{\partial r_{1\beta}}\frac{r_{1\beta i}}{r_{1\beta}}. \tag{C.12}$$

Second part of equation (C.12) is nothing but equation (2.21). Equations (2.22) to (2.27) can be obtained by interchanging α and β and considering the case $\lambda = \beta$ and $\lambda \neq \alpha$ in the first part of equation (C.12). Since α is always set to 1 and β varies from 2 to 7, the summation in equation (C.12) can be removed. Therefore,

$$\frac{\partial \phi_\rho}{\partial \mathbf{u}^{\mathrm{C}}_{\beta i}} = \frac{\partial \phi_{\beta 1}}{\partial r_{\beta 1}}\frac{r_{\beta 1 i}}{r_{\beta 1}}. \tag{C.13}$$

Now equations (2.22) to (2.27) can be obtained by varying β from 2 to 7 and accepting the following equalities: $\phi_{\beta 1} = \phi_{1\beta}$, $r_{\beta 1} = r_{1\beta}$ and $r_{\beta 1 i} = -r_{1\beta i}$.

Appendix D

Algorithms

D.1 Energy based refinement algorithm

The energy based refinement algorithm is explained in algorithm 1.

D.2 Energy based coarsening algorithm

The energy based coarsening algorithm is explained in algorithm 2.

D.3 CSP based refinement algorithm

The refining algorithm 3 explains the adaptive refinement process adopted in the MAMM.

D.4 CSP based coarsening algorithm

The coarsening algorithm 4 explains the adaptive coarsening process adopted in MAMM.

```
input  : $\mathcal{E}_n^{\mathrm{A}}$, $\mathcal{E}_n^{\mathrm{C}}$, $\mathcal{E}_n^{\mathrm{split}}$, $\mathcal{E}_n^{\mathrm{tip}}$, $nlist_n, nconn_n$
output: $\mathcal{E}_{n+1}^{\mathrm{A}}$, $\mathcal{E}_{n+1}^{\mathrm{C}}$, $\mathcal{E}_{n+1}^{\mathrm{split}}$, $\mathcal{E}_{n+1}^{\mathrm{tip}}$, $\mathbf{r}_{n+1}^{\mathrm{refA}}, nlist_{n+1}, nconn_{n+1}$
$\mathcal{E}_n^{\mathrm{HE}} = \emptyset$
for each atom $\alpha$ do
    if energy $> tol^E$ then
        e = element containing $\alpha$ in $\Omega_0^{\mathrm{A}}$
        add e to $\mathcal{E}_n^{\mathrm{HE}}$
    end
end
$\mathcal{E}_{n+1}^{\mathrm{minA}} = \mathcal{E}_n^{\mathrm{HE}}$
for each element e in $\mathcal{E}_n^{HE}$ do
    add neighbours of e to set $\mathcal{E}_{n+1}^{\mathrm{minA}}$
end
$\mathcal{E}_n^{\mathrm{refine}} = \mathcal{E}_n^{\mathrm{A}} / \mathcal{E}_{n+1}^{\mathrm{minA}}$
Create the atoms in the element set $\mathcal{E}_n^{\mathrm{refine}}$.
for each element e in $\mathcal{E}_n^{refine}$ do
    for each atom $\alpha$ in element e do
        Initialize the positions ($\mathbf{r}_{n+1}^{\mathrm{refA}}$) using equation (2.2).
    end
end
$\mathcal{E}_{n+1}^{\mathrm{refA}} = \mathcal{E}_n^{\mathrm{A}} \cup \mathcal{E}_n^{\mathrm{refine}}$
$\mathcal{E}_{n+1}^{\mathrm{refC}} = \mathcal{E}_{n+1}^{\mathrm{refA}} / \mathcal{E}$
for each element e in $\mathcal{E}_{n+1}^{refA}$ do
    for each atom $\alpha$ in element e do
        Update the neighbour list ($nlist_{n+1}$)
    end
end
$\mathcal{E}_{n+1}^{\mathrm{nsplit}} = (\mathcal{E}_n^{\mathrm{split}} \cup \mathcal{E}_n^{\mathrm{tip}}) / \mathcal{E}_n^{\mathrm{HE}}$
for each element e in $\mathcal{E}_{n+1}^{nsplit}$ do
    Create the phantom nodes
end
$\mathcal{E}_{n+1}^{\mathrm{split}} = \mathcal{E}_n^{\mathrm{split}} \cup \mathcal{E}_{n+1}^{\mathrm{nsplit}}$
Update the crack tip element $\mathcal{E}_{n+1}^{\mathrm{tip}}$.
Initialize the positions of the new phantom nodes by interpolation.
Update the nodal connectivity ($nconn_{n+1}$) table.
if coarsening then
    $\mathcal{E}_n^{\mathrm{A}} = \mathcal{E}_{n+1}^{\mathrm{refA}}$
    $\mathcal{E}_n^{\mathrm{C}} = \mathcal{E}_{n+1}^{\mathrm{refC}}$
    $\mathcal{E}_n^{\mathrm{split}} = \mathcal{E}_{n+1}^{\mathrm{split}}$
    else
    ;
    $\mathcal{E}_{n+1}^{\mathrm{A}} = \mathcal{E}_{n+1}^{\mathrm{refA}}$
    $\mathcal{E}_{n+1}^{\mathrm{C}} = \mathcal{E}_{n+1}^{\mathrm{refC}}$
end
```

Algorithm 1: Steps to model refinement, n is the load step indicator.

```
input  : $\mathcal{E}_n^{\mathrm{A}}, \mathcal{E}_n^{\mathrm{C}}, \mathcal{E}_n^{\mathrm{BA}}, \mathcal{E}_n^{\mathrm{split}}$
output: $\mathcal{E}_{n+1}^{\mathrm{A}}, \mathcal{E}_{n+1}^{\mathrm{C}}, \mathcal{E}_{n+1}^{\mathrm{split}}, nlist_{n+1}$
$\mathcal{E}_n^{\mathrm{HE}} = \emptyset$
for each atom $\alpha$ do
    if $energy > tol^E$ then
        e = element containing $\alpha$ in $\Omega_0$
        add e to $\mathcal{E}_n^{\mathrm{HE}}$
    end
end
$\mathcal{E}_n^{\mathrm{LE}} = \mathcal{E}_n^{\mathrm{HE}} \diagup \mathcal{E}_n^{\mathrm{A}}$
$\mathcal{E}_n^{\mathrm{coarsen}} = \mathcal{E}_n^{\mathrm{LE}} \cap \mathcal{E}_n^{\mathrm{BA}}$
for each element e in $\mathcal{E}_n^{coarsen}$ do
    Delete the fine scale atoms.
end
$\mathcal{E}_{n+1}^{\mathrm{coaA}} = \mathcal{E}_n^{\mathrm{coarsen}} \diagup \mathcal{E}_n^{\mathrm{A}}$
$\mathcal{E}_{n+1}^{\mathrm{coaC}} = \mathcal{E}_{n+1}^{\mathrm{coaA}} \diagup \mathcal{E}$
$\mathcal{E}_n^{\mathrm{split'}} = \mathcal{E}_n^{\mathrm{split}} \cap \mathcal{E}_n^{\mathrm{coarsen}}$
$\mathcal{E}_{n+1}^{\mathrm{split}} = \mathcal{E}_n^{\mathrm{split'}} \diagup \mathcal{E}_n^{\mathrm{split}}$
for each element e in $\mathcal{E}_{n+1}^{coaA}$ do
    for each atom $\alpha$ in element e do
        Update the neighbour list ($nlist_{n+1}$)
    end
end
$\mathcal{E}_{n+1}^{\mathrm{A}} = \mathcal{E}_{n+1}^{\mathrm{coaA}}$
$\mathcal{E}_{n+1}^{\mathrm{C}} = \mathcal{E}_{n+1}^{\mathrm{coaC}}$
```

Algorithm 2: Steps to model coarsening, n is the load step indicator.

```
input  : $\mathcal{P}_{\rm n}^{\rm A}$, $\mathcal{P}_{\rm n}^{\rm C}$, $\mathcal{P}_{\rm n}^{\rm split}$, $\mathcal{P}_{\rm n}^{\rm tip}$, $nlist_{\rm n}, nconn_{\rm n}$
output: $\mathcal{P}_{\rm n+1}^{\rm A}$, $\mathcal{P}_{\rm n+1}^{\rm C}$, $\mathcal{P}_{\rm n+1}^{\rm split}$, $\mathcal{P}_{\rm n+1}^{\rm tip}$, $\mathbf{r}_{\rm n+1}^{\rm refA}, nlist_{\rm n+1}, nconn_{\rm n+1}$
$\mathcal{P}_{\rm n}^{\rm csp} = \emptyset$
for each atom $\alpha$ do
    if $csp > tol^{csp}$ then
        p = particle containing $\alpha$ in $\Omega_0^{\rm A}$
        add p to $\mathcal{P}_{\rm n}^{\rm csp}$
    end
end
$\mathcal{P}_{\rm n+1}^{\rm minA} = \mathcal{P}_{\rm n}^{\rm csp}$
for each particle p in $\mathcal{P}_n^{csp}$ do
    add neighbours of p to set $\mathcal{P}_{\rm n+1}^{\rm minA}$
end
$\mathcal{P}_{\rm n}^{\rm refine} = \mathcal{P}_{\rm n}^{\rm A} \diagup \mathcal{P}_{\rm n+1}^{\rm minA}$
Create the atoms in the particle set $\mathcal{P}_{\rm n}^{\rm refine}$.
for each particle p in $\mathcal{P}_n^{refine}$ do
    for each atom $\alpha$ in particle p do
        Initialize the positions ($\mathbf{r}_{\rm n+1}^{\rm refA}$) using equation (4.32).
    end
end
$\mathcal{P}_{\rm n+1}^{\rm refA} = \mathcal{P}_{\rm n}^{A} \cup \mathcal{P}_{\rm n}^{\rm refine}$
$\mathcal{P}_{\rm n+1}^{\rm refC} = \mathcal{P}_{\rm n+1}^{\rm refA} \diagup \mathcal{P}$
for each particle p in $\mathcal{P}_{n+1}^{refA}$ do
    for each atom $\alpha$ in particle p do
        Update the neighbour list ($nlist_{\rm n+1}$)
    end
end
$\mathcal{P}_{\rm n+1}^{\rm nsplit} = (\mathcal{P}_{\rm n}^{\rm split} \cup \mathcal{P}_{\rm n}^{\rm tip}) \diagup \mathcal{P}_{\rm n}^{\rm csp}$
for each particle p in $\mathcal{P}_{n+1}^{nsplit}$ do
    Create the phantom nodes
end
$\mathcal{P}_{\rm n+1}^{\rm split} = \mathcal{P}_{\rm n}^{\rm split} \cup \mathcal{P}_{\rm n+1}^{\rm nsplit}$
Update the crack tip particle $\mathcal{P}_{\rm n+1}^{\rm tip}$.
Initialize the positions of the newly cracked particles by interpolation.
Update the nodal connectivity ($nconn_{\rm n+1}$) table.
if coarsening then
    $\mathcal{P}_{\rm n}^{A} = \mathcal{P}_{\rm n+1}^{\rm refA}$
    $\mathcal{P}_{\rm n}^{C} = \mathcal{P}_{\rm n+1}^{\rm refC}$
    $\mathcal{P}_{\rm n}^{\rm split} = \mathcal{P}_{\rm n+1}^{\rm split}$
    else
    ;
    $\mathcal{P}_{\rm n+1}^{A} = \mathcal{P}_{\rm n+1}^{\rm refA}$
    $\mathcal{P}_{\rm n+1}^{C} = \mathcal{P}_{\rm n+1}^{\rm refC}$
end
```

Algorithm 3: Steps to model refinement, n is the load step indicator.

```
input  : $\mathcal{P}_{\mathrm{n}}^{\mathrm{A}}, \mathcal{P}_{\mathrm{n}}^{\mathrm{C}}, \mathcal{P}_{\mathrm{n}}^{\mathrm{BA}}, \mathcal{P}_{\mathrm{n}}^{\mathrm{split}}$
output: $\mathcal{P}_{\mathrm{n+1}}^{\mathrm{A}}, \mathcal{P}_{\mathrm{n+1}}^{\mathrm{C}}, \mathcal{P}_{\mathrm{n+1}}^{\mathrm{split}}, nlist_{\mathrm{n+1}}$
$\mathcal{P}_{\mathrm{n}}^{\mathrm{csp}} = \emptyset$
for each atom $\alpha$ do
    if $csp > tol^{csp}$ then
        p = particle containing $\alpha$ in $\Omega_0$
        add p to $\mathcal{P}_{\mathrm{n}}^{\mathrm{csp}}$
    end
end
$\mathcal{P}_{\mathrm{n}}^{\mathrm{LE}} = \mathcal{P}_{\mathrm{n}}^{\mathrm{csp}} / \mathcal{P}_{\mathrm{n}}^{A}$
$\mathcal{P}_{\mathrm{n}}^{\mathrm{coarsen}} = \mathcal{P}_{\mathrm{n}}^{\mathrm{LE}} \cap \mathcal{P}_{\mathrm{n}}^{\mathrm{BA}}$
Employ the coarse graining scheme discussed in section 4.2.2
for each particle p in $\mathcal{P}_{n}^{coarsen}$ do
    Delete the fine scale atoms.
end
$\mathcal{P}_{\mathrm{n+1}}^{\mathrm{coaA}} = \mathcal{P}_{\mathrm{n}}^{\mathrm{coarsen}} / \mathcal{P}_{\mathrm{n}}^{A}$
$\mathcal{P}_{\mathrm{n+1}}^{\mathrm{coaC}} = \mathcal{P}_{\mathrm{n+1}}^{\mathrm{coaA}} / \mathcal{P}$
$\mathcal{P}_{\mathrm{n}}^{split'} = \mathcal{P}_{\mathrm{n}}^{\mathrm{split}} \cap \mathcal{P}_{\mathrm{n}}^{\mathrm{coarsen}}$
$\mathcal{P}_{\mathrm{n+1}}^{\mathrm{split}} = \mathcal{P}_{\mathrm{n}}^{split'} / \mathcal{P}_{\mathrm{n}}^{\mathrm{split}}$
for each particle p in $\mathcal{P}_{n+1}^{coaA}$ do
    for each atom $\alpha$ in particle p do
        Update the neighbour list ($nlist_{\mathrm{n+1}}$)
    end
end
$\mathcal{P}_{\mathrm{n+1}}^{A} = \mathcal{P}_{\mathrm{n+1}}^{\mathrm{coaA}}$
$\mathcal{P}_{\mathrm{n+1}}^{C} = \mathcal{P}_{\mathrm{n+1}}^{\mathrm{coaC}}$
```

Algorithm 4: Steps to model coarsening, n is the load step indicator.

References

[1] Abraham FF, Walkup Robert, Gao Huajian, Duchaineau Mark, DeLaRubia Tomas-Diaz, and Seager. Mark. Simulating materials failure by using up to one billion atoms and the world's fastest computer: Work-hardening. *Proceedings of the National Academy of Sciences*, 99(9):5777–5782, 2002.

[2] Buehler MJ, Hartmaier Alexander, Gao Huajian, Duchaineau Mark, and Abraham. FF. Atomic plasticity: description and analysis of a one-billion atom simulation of ductile materials failure. *Computer Methods in Applied Mechanics and Engineering*, 193, 2004.

[3] VP Nguyen, T Rabczuk, SP Bordas, and Duflot M. Meshless methods: A review and computer implementation aspects. *Mathematics and Computers in Simulation*, 79(3):763–813, 2008.

[4] T Rabczuk, Belytschko T, and SP Xiao. Stable particle methods based on lagrangian kernels. *Computational Methods in Applied Mechanics and Engineering*, 193(12-14):1035–1063, 2004.

[5] GR Liu and Gu YT. A local radial point interpolation method (lrpim) for free vibration analyses of 2-d solids. *Journal of Sound and Vibration*, 246(1):29–46, 2001.

[6] Belytschko T, Lu YY, and L Gu. Element-free galerkin methods. *International Journal for Numerical Methods in Engineering*, 37:229–256, 1994.

[7] Belytschko T and SP Xiao. Coupling methods for continuum model with molecular model. *International Journal for Multiscale Computational Engineering*, 1(1):115–126, 2003.

[8] Liu WK, S Jun, and Zhang YF. Reproducing kernel particle methods. *International Journal for Numerical Methods in Fluids*, 20:1081–1106, 1995.

[9] Liu WK, S Jun, S Li, J Adee, and Belytschko T. Reproducing kernel particle methods for structural dynamics. *International Journal for Numerical Methods in Engineering*, 38:1655–1679, 1995.

[10] JJ Monaghan. Smoothed particle hydrodynamics. *Reports on Progress in Physics*, 68(8):1703–1759, 2005.

[11] Zhuang X and YC Cai. A meshless local petrov-galerkin shepard and least-squares method based on duo nodal supports. *Mathematical Problems in Engineering*, 2013.

[12] Zhuang X, Zhu H, and C Augarde. An improved meshless shepard and least square method possessing the delta property and requiring no singular weight function. *Computational Mechanics*, DOI:10.1007/s00466–013–0912–1, 2013.

[13] X Zhuang, CE Augarde, and Bordas SPA. Accurate fracture modelling using meshless methods and level sets: formulation and 2D modelling. *International Journal for Numerical Methods in Engineering*, 86:249–268, 2011.

[14] SP Bordas, T Rabczuk, H Nguyen-Xuan, S Natarajan, T Bog, VP Nguyen, Q Do, Minh, and Nguyen Vinh H. Strain smoothing in fem and xfem. *Computers and Structures*, 88(23-24):1419–1443, 2010.

[15] SP Bordas, S Natarajan, S Dal, Pont, T Rabczuk, P Kerfriden, DR Mahapatra, D Noel, and Gao Z. On the performance of strain smoothing for enriched finite element approximations (xfem/gfem/pufem). *International Journal for Numerical Methods in Engineering*, 86(4-5):637–666, 2011.

[16] Daux C, Moes N, Dolbow J, Sukumar N, and T Belytschko. Arbitrary branched and intersecting cracks with the extended finite element method. *International Journal for Numerical Methods in Engineering*, 48:1741–1760, 2000.

[17] Sukumar N, Moes N, Moran B, and T Belytschko. Extended finite element method for three-dimensional crack modelling. *International Journal for Numerical Methods in Engineering*, 48(11):1549–1570, 2000.

[18] G Zi, H Chen, JX Xu, and Belytschko T. The extended finite element method for dynamic fractures. *Shock and Vibration*, 12(1):9–23, 2005.

[19] Areias P and T Belytschko. Analysis of three-dimensional crack initiation and propagation using the extended finite element method. *International Journal for Numerical Methods in Engineering*, 63:760–788, 2005.

[20] Nguyen-Thanh Nhon, Kiendl J, Nguyen-Xuan H, Wuchner R, Bletzinger KU, Bazilevs Y, and Rabczuk. T. Rotation free isogeometric thin shell analysis using pht-splines. *Computer Methods in Applied Mechanics and Engineering*, 200(47-48):3410–3424, 2011.

[21] Nguyen-Xuan H, Liu GR, Bordas SPA, Natarajan S, and Rabczuk. T. An adaptive singular es-fem for mechanics problems with singular field of arbitrary order. *Computer Methods in Applied Mechanics and Engineering*, 253:252–273, 2013.

[22] Vu-Bac N, Nguyen-Xuan H, Chen L, Bordas SPA, Kerfriden P, Simpson RN, Liu GR, and Rabczuk. T. A noded-based smoothed xfem for fracture mechanics. *Computer Modeling in Engineering and Sciences*, 73:331–356, 2011.

[23] Strouboulis T, Copps K, and I Babŭska. The generalized finite element method: an example of its implementation and illustration of its performance. *International Journal for Numerical Methods in Engineering*, 47:1401–1417, 2000.

[24] Strouboulis T, Copps K, and I Babŭska. The generalized finite element method. *Computer Methods in Applied Mechanics and Engineering*, 190(32-33):4081–4193, 2001.

[25] Strouboulis T, Zhang L, and I Babŭska. Generalized finite element method using mesh-based handbooks: application to problems in domains with many voids. *Computer Methods in Applied Mechanics and Engineering*, 192(28):3109–3161, 2003.

[26] Strouboulis T, Babŭska I, and R Hidajat. The generalized finite element method for helmholtz equation: theory, computation, and open problems. *Computer Methods in Applied Mechanics and Engineering*, 195:4711–4731, 2006.

[27] Strouboulis T, Hidajat R, and I Babŭska. The generalized finite element method for helmholtz equation, part ii: effect of choice of handbook functions, error due to absorbing boundary conditions and its assessment. *Computer Methods in Applied Mechanics and Engineering*, 197:364–380, 2008.

[28] Ivo Babŭska, Banerjee Uday, and E Osborn. John. Generalized finite element methods:

Main ideas, results, and perspective. *International Journal of Computational Methods*, 1(1):67–103, 2004.

[29] Belytschko Ted, Gracie Robert, and Giulio Ventura. A review of extended/generalized finite element methods for material modeling. *Modelling and Simulation in Materials Science and Engineering*, 17:043001(24pp), 2009.

[30] Melenk JM and I Babŭska. The partition of unity finite element method: Basic theory and applications. *Computer Methods in Applied Mechanics and Engineering*, 139(1-4):289–314, 1996.

[31] Cai Y, Zhuang X, and C Augarde. A new partition of unity finite element free from linear dependence problem and processing delta property. *Computer Methods in Applied Mechanics & Engineering*, 199:1036–1043, 2010.

[32] T Rabczuk, SP Bordas, and Zi G. A three-dimensional meshfree method for continuous multiple-crack initiation, propagation and junction in statics and dynamics. *Computational Mechanics*, 40(3):473–495, 2007.

[33] Rabczuk Timon and Goangseup Zi. A meshfree method based on the local partition of unity for cohesive cracks. *Computational Mechanics*, 39:743–760, 2007.

[34] G Zi, Rabczuk Timon, and Wolfgang Wall. Extended meshfree methods without branch enrichment for cohesive cracks. *Computational Mechanics*, 40(2):367–382, 2007.

[35] SP Bordas, T Rabczuk, and Zi G. Three-dimensional crack initiation, propagation, branching and junction in non-linear materials by an extended meshfree method without asymptotic enrichment. *Engineering Fracture Mechanics*, 75(5):943–960, 2008.

[36] T Rabczuk, G Zi, S Bordas, and Nguyen-Xuan H. A geometrically non-linear three dimensional cohesive crack method for reinforced concrete structures. *Engineering Fracture Mechanics*, 75(16):4740–4758, 2008.

[37] T Rabczuk and Samaniego E. Discontinuous modelling of shear bands using adaptive meshfree methods. *Computer Methods in Applied Mechanics and Engineering*, 197(6-8):641–658, 2008.

[38] T Rabczuk, R Gracie, JH Song, and Belytschko T. Immersed particle method for fluid-structure interaction. *International Journal for Numerical Methods in Engineering*, 81(1):48–71, 2010.

[39] G Ventura, XJ Xu, and Belytschko T. A vector level set method and new discontinuity approximations for crack growth by efg. *International Journal for Numerical Methods in Engineering*, 54:923–944, 2002.

[40] T Rabczuk and T Belytschko. Cracking particles: a simplified meshfree method for arbitrary evolving cracks. *International Journal for Numerical Methods in Engineering*, 61:2316–2343, 2004.

[41] T Rabczuk and Areias PMA. A new approach for modelling slip lines in geological materials with cohesive models. *International Journal for Numerical and Analytical Methods in Engineering*, 30(11):1159–1172, 2006.

[42] T Rabczuk and Belytschko T. Application of particle methods to static fracture of

reinforced concrete structures. *International Journal of Fracture*, 137(1-4):19–49, 2006.

[43] Rabczuk T and T Belytschko. A three dimensional large deformation meshfree method for arbitrary evolving cracks. *Computer Methods in Applied Mechanics and Engineering*, 1960(29-30):2777–2799, 2007.

[44] Rabczuk T, Areias PMA, and T Belytschko. A simplified meshfree method for shear bands with cohesive surfaces. *International Journal for Numerical Methods in Engineering.*

[45] T Rabczuk, JH Song, and Belytschko T. Simulations of instability in dynamic fracture by the cracking particles method. *Engineering Fracture Mechanics*, 76(6):730–741, 2009.

[46] T Rabczuk, G Zi, SP Bordas, and Nguyen-Xuan H. A simple and robust three-dimensional cracking-particle method without enrichment. *Computer Methods in Applied Mechanics and Engineering*, 199(37-40):2437–2455, 2010.

[47] Vu-Bac N, Nguyen-Xuan H, Chen L, Bordas S, Zhuang X, Liu GR, and T Rabczuk. A phantom-node method with edge-based strain smoothing for linear elastic fracture mechanics. *Journal of Applied Mathematics*, doi:10.1155/2013/978026, 2013.

[48] T Chau-Dinh, G Zi, PS Lee, JH Song, and Rabczuk T. Phantom-node method for shell models with arbitrary cracks. *Computers and Structures*, 92-93:242–256, 2010.

[49] T Rabczuk, G Zi, A Gerstenberger, and WA Wall. A new crack tip element for the phantom node method with arbitrary cohesive cracks. *International Journal for Numerical Methods in Engineering*, 75(5):577–599, 2008.

[50] Song JH, Areias P, and T Belytschko. A method for dynamic crack and shear band propagation with phantom nodes. *International Journal for Numerical Methods in Engineering.*

[51] Hansbo A and P Hansbo. A finite element method for the simulation of strong and weak discontinuities in solid mechanics. *Computer Methods in Applied Mechanics and Engineering*, 193:3523–3540, 2004.

[52] Mergheim J, Kuhl E, and P Steinmann. A finite element method for the computational modelling of cohesive cracks. *International Journal for Numerical Methods in Engineering*, 63:276–289, 2005.

[53] Mergheim J, Kuhl E, and P Steinmann. Towards the algorithmic treatment of 3d strong discontinuities. *Communications in Numerical Methods in Engineering*, 23:97–108, 2007.

[54] Cai Y, Zhuang X, and H Zhu. A generalized and efficient method for finite cover generation in the numerical manifold method. *International Journal of Computational Methods*, 10(5):1350028, 2013.

[55] Ma Guowei, An Xinmei, and Lei He. The numerical manifold method: a review. *International Journal of Computational Methods*, 7:1–32, 2010.

[56] Hughes T, Cottrell J, and Bazilevs. Y. Isogeometric analysis: Cad, finite elements, nurbs, exact geometry and mesh refinement. *Computer Methods in Applied Mechanics and Engineering*, 194:4135–4195, 2005.

[57] Bazilevs Y, Calo VM, Cottrell JA, Evans JA, Hughes TJR, Lipton S, Scott MA, and Sederberg. TW. Isogeometric analysis using t-splines. *Computer Methods in Applied Mechanics and Engineering*, 199(5-8), 2010.

[58] VP Nguyen and Nguyen-Xuan. H. High-order b-splines based finite elements for the delamination analysis of laminated composites. *Composite Structures*, 102:261–275, 2013.

[59] HT Chien, Ferreira AJ, Carrera E, and Nguyen-Xuan. H. Isogeometric analysis of laminated composite and sandwich plates using a layerwise deformation theory. *Composite Structures*, 104:196–214, 2013.

[60] HT Chien, Ferreira AJM, Rabczuk T, Bordas SPA, and Nguyen-Xuan. H. Isogeometric analysis of laminated composite and sandwich plates using a new inverse trigonometric shear deformation theory. *European Journal of Mechanics - A/Solids*, 43:89–108, 2014.

[61] Nguyen-Xuan H, Thai CH, and Nguyen-Thoi. T. Isogeometric finite element analysis of composite sandwich plates using a new higher order shear deformation theory. *Composite Part B*, 55:558–574, 2013.

[62] Nguyen-Xuan H, Hoang T, and Nguyen. VP. An isogeometric analysis for elliptic homogenization problems. *Computer Methods in Applied Mechanics and Engineering*, http://dx.doi.org/10.1016/j.camwa.2014.01.001, 2014.

[63] Feyel F. Multiscale fe^2 elastoviscoplastic analysis of composite structures. *Computational Materials Science*, 16(1-4):344–354, 1999.

[64] F Feyel and Chaboche JL. fe^2 multiscale approach for modeling the elastoviscoplastic behavior of long fiber sic/ti composite materials. *Computer Methods in Applied Mechanics and Engineering*, 183:309–330, 2000.

[65] F Feyel and Chaboche JL. Multi-scale non linear fe^2 analysis of composite structures: damage and fiber size effects. in: Saanouni, k.(ed.). *Numerical Modelling in Damage Mechanics - NUMEDAMÓ0, Revue Europeenne des Elements Finis*, 10:449–472, 2001.

[66] F Feyel and Chaboche JL. A multilevel finite element method (fe^2) to describe the response of highly non-linear structures using generalized continua. *Computer Methods in Applied Mechanics and Engineering*, 192:3233–3244, 2003.

[67] SP Xiao and T. Belytschko. A bridging domain method for coupling continua with molecular dynamics. *Computer Methods in Applied Mechanics and Engineering*, 193(17-20):1645–1669, 2004.

[68] Guidault PA and Belytschko. T. Bridging domain methods for coupled atomistic–continuum models with l^2 or h^1 couplings. *International Journal for Numerical Methods in Engineering*, 77:1566–1592, 2009.

[69] Liu WK, Hao Su, Belytschko Ted, Li Shaofan, and CT Chang. Multi-scale methods. *International Journal for Numerical Methods in Engineering*, 47:1343–1361, 2000.

[70] Park HS, Karpov EG, Liu WK, and PA Klein. The bridging scale for two-dimensional atomistic/continuum coupling. *Philosophical Magazine*, 85(1):79–113, 2005.

[71] WK Liu, HS Park, D Qian, EG Karpov, H Kadowaki, and Wagner GJ. Bridging scale

methods for nanomechanics and materials. *Computer Methods in Applied Mechanics and Engineering*, 195:1407–1421, 2006.

[72] Farrell DE, Park HS, and WK Liu. Implementation aspects of the bridging scale method and application to intersonic crack propagation. *International Journal for Numerical Methods in Engineering*, 71:583–605, 2007.

[73] Wagner GJ and WK Liu. Coupling of atomistic and continuum simulations using a bridging scale decomposition. *Journal of Computational Physics*, 190(1):249–279, 2003.

[74] Budarapu Pattabhi, Robert Gracie, Bordas Stéphane, and Timon Rabczuk. An adaptive multiscale method for quasi-static crack growth. *Computational Mechanics*, 53(6):1129–1148, 2014.

[75] Talebi H, Silani M, Bordas S, Kerfriden P, and T Rabczuk. A computational library for multiscale modelling of material failure. *Computational Mechanics*, 53(5):1047–1071, 2014.

[76] Talebi H, Silani M, Bordas S, Kerfriden P, and Timon Rabczuk. Molecular dynamics/xfem coupling by a three dimensional extended bridging domain with applications to dynamic brittle fracture. *International Journal for Multiscale Computational Engineering*, 11(6):527–541, 2013.

[77] Yang [Shih-Wei, Budarapu]$^{\mathrm{equal}}$ Pattabhi, DR Mahapatra, Bordas Stéphane, Zi Goanseup, and Rabczuk. Timon. A meshless adaptive multiscale method for fracture. *Computational Materials Science*, accepted for publication, 2014.

[78] EB Tadmor, M Ortiz, and Phillips R. Quasicontinuum analysis of defects in solids. *Philosophical Magazine A*, 73(6):1529–1563, 1996.

[79] RE Miller and Tadmor EB. The quasicontinuum method: Overview, applications and current directions. *Journal of Computer-Aided Materials Design*, 9(3):203–239, 2002.

[80] Dhia HB and G. Rateau. The arlequin method as a flexible engineering design tool. *International Journal for Numerical Methods in Engineering*, 62:1442–1462, 2006.

[81] Dhia HB. The arlequin method: a partition of models for concurrent multiscale analyses. *Challenges in Computational Mechanics Workshop*, Cachan, France:10–12 May, 2006, 2006.

[82] FF Abraham, Broughton JQ, Bernstein N, and E Kaxiras. Spanning the length scales in dynamic simulation. *Computational Physics*, 12:538–546, 1998.

[83] Gracie Robert and Ted Belytschko. Concurrently coupled atomistic and xfem models for dislocations and cracks. *International Journal for Numerical Methods in Engineering*, 78:354–378, 2008.

[84] R Gracie and Belytschko T. Adaptive continuum-atomistic simulations of dislocation dynamics. *International Journal for Numerical Methods in Engineering*, 86(4-5):575–597, 2011.

[85] S Loehnert and Belytschko T. A multiscale projection method for macro/microcrack simulations. *International Journal for Numerical Methods in Engineering*, 71(12):1466–1482, 2007.

[86] WA Curtin and RE. Miller. Atomistic/continuum coupling in computational materials science. *Modelling and Simulation in Materials Science*, 11:R33–R68, 2003.

[87] LE Shilkrot, WA Curtin, and RE. Miller. A coupled atomistic/continuum model of defects in solids. *Journal of the Mechanics and Physics of Solids*, 50:2085–2106, 2002.

[88] LE Shilkrot, RE Miller, and WA. Curtin. Coupled atomistic and discrete dislocation plasticity. *Physical Review Letters*, 89:025501–1, 2002.

[89] LE Shilkrot, RE Miller, and WA. Curtin. Multiscale plasticity modeling: Coupled atomistics and discrete dislocation mechanics. *Journal of the Mechanics and Physics of Solids*, 52:755–787, 2003.

[90] RE Rudd and JQ. Broughton. Coarse-grained molecular dynamics and the atomic limit of finite elements. *Physical Review B*, 58:R5893, 1998.

[91] RE Rudd and JQ. Broughton. Coarse-grained molecular dynamics: Nonlinear finite elements and finite temperature. *Physical Review B*, 72:144104, 2005.

[92] J Broughton, FF Abraham, N Bernstein, and E. Kaxiras. Concurrent coupling of length scales: methodology and application. *Physical Review B*, 60(4):2391–2403, 1999.

[93] FF Abraham, D Brodbeck, RA Rafey, and WE. Rudge. Instability dynamics of fracture: A computer simulation investigation. *Physical Review Letters*, 73:272–275, 1994.

[94] FF Abraham, N Bernstein, JQ Broughton, and D. Hess. Dynamic fracture of silicon: Concurrent simulation of quantum electrons, classical atoms, and the continuum solid. *Materials Research Society Bulletin*, 25:27–32, 2000.

[95] FF. Abraham. The atomic dynamics of fracture. *Journal of the Mechanics and Physics of Solids*, 49:2095–2111, 2001.

[96] V Kouznetsova, Geers MGD, and WAM Brekelsmans. Multi-scale constitutive modeling of heterogeneous materials with a gradient-enhanced computational homogenization scheme. *International Journal for Numerical Methods in Engineering*, 54:1235–1260, 2002.

[97] S Nemat-Nasser and Hori M. *Micromechanics: Overall properties of heterogeneous materials*, volume Amsterdam. 1993.

[98] Belytschko Ted and Jeong-Hoon Song. Coarse-graining of multiscale crack propagation. *International Journal for Numerical Methods in Engineering*, 81(5):537–563, 2010.

[99] PA Guidault and T. Belytschko. On the l^2 and the h^1 couplings for an overlapping domain decomposition method using lagrange multipliers. *International Journal for Numerical Methods in Engineering*, 70:322–350, 2007.

[100] PA Guidault, O Allix, L Champaney, and Cornuault C. A multiscale extended finite element method for crack propagation. *Computer Methods in Applied Mechanics and Engineering*, 197:381–399, 2008.

[101] J Fish and W. Chen. Discrete-to-continuum bridging based on multigrid principles. *Computer Methods in Applied Mechanics and Engineering*, 193:1693–1711, 2004.

[102] LAA Beex, RHJ Peerlings, and MGD. Geers. A quasicontinuum methodology for multiscale analysis of discrete microstructural models. *International Journal for Numerical*

Methods in Engineering, 87:701–718, 2011.

[103] Sun Yi, Peng Qing, and Lu. Gang. Quantum mechanical modeling of hydrogen assisted cracking in aluminum. *Physical Review B*, 88(10):104109 (6pp), 2013.

[104] V Kouznetsova, Geers MGD, and WAM Brekelsmans. Computational homogenization for the multi-scale analysis of multi-phase materials. *Netherlands Institute for Metals Research, The Netherlands*, PhD Thesis, 2002.

[105] VP Nguyen, O Lloberas-Valls, and Sluys LJ. Stroeven, M. Homogenization-based multiscale crack modelling: From micro-diffusive damage to macro-cracks. *Computer Methods in Applied Mechanics and Engineering*, 200(9-12):1220–1236, 2011.

[106] CV Verhoosel, JJC Remmers, MA Gutiérrez, and Borst R. de. Computational homogenization for adhesive and cohesive failure in quasi-brittle solids. *International Journal for Numerical Methods in Engineering*, 83(8-9):1155–1179, 2010.

[107] T Belytschko, Loehnert S, and JH Song. Multiscale aggregating discontinuities: A method for circumventing loss of material stability. *International Journal for Numerical Methods in Engineering*, 73(6):869–894, 2008.

[108] P Aubertin, J Réthoré, and De Borst R. A coupled molecular dynamics and extended finite element method for dynamic crack propagation. *International Journal for Numerical Methods in Engineering*, 81:72–88, 2010.

[109] P Cresta, O Allix, C Rey, and Guinard S. Nonlinear localization strategies for domain decomposition methods: application to post-buckling analyses. *Computer Methods in Applied Mechanics and Engineering*, 196(80):1436–1446, 2007.

[110] IM Gitman, H Askes, and Sluys LJ. Coupled-volume multi-scale modelling of quasi-brittle material. *European Journal of Mechanics-A/Solids*, 27(3):302–327, 2008.

[111] P Bauman, H Dhia, N Elkhodja, J Oden, and S. Prudhomme. On the application of the arlequin method to the coupling of particle and continuum models. *Computational Mechanics*, 42(4):511–530, 2008.

[112] Xu Mei and Belytschko. Ted. Conservation properties of the bridging domain method for coupled molecular/continuum dynamics. *International Journal for Numerical Methods in Engineering*, 76:278–294, 2008.

[113] M Xu, R Gracie, and Belytschko T. *Bridging the Scales in Science and Engineering. Ed. J. Fish.*, chapter Multiscale Modeling with Extended Bridging Domain Method. Oxford University Press, United Kingdom, 2009.

[114] Xu Mei, Robert Gracie, and Belytschko. Ted. *A continuum-to-atomistic bridging domain method for composite lattices*, volume 81, pages 1635–1658. 2010.

[115] P Aubertin, J Réthoré, and De Borst R. Energy conservation of atomistic/continuum coupling. *International Journal for Numerical Methods in Engineering*, 78(11):1365–1386, 2009.

[116] VB Shenoy, RE Miller, EB Tadmor, D Rodney, R Phillips, and M. Ortiz. An adaptive finite element approach to atomic-scale mechanics-the quasicontinuum method. *ournal of the Mechanics and Physics of Solids*, 47(3):611–642, 1999.

[117] W Shan and U. Nackenhorst. An adaptive fe-md model coupling approach. *Computational Mechanics*, 46:577–596, 2010.

[118] Moseley Philip, Oswald Jay, and Ted Belytschko. Adaptive atomistic-to-continuum modeling of propagating defects. *International Journal for Numerical Methods in Engineering*, 92:835–856, 2012.

[119] Budarapu PR, Gracie R, Yang S-W, Zhuang X, and T Rabczuk. Efficient coarse graining in multiscale modeling of fracture. *Theoretical and Applied Fracture Mechanics*, 69:126–143, 2014.

[120] Qian D, Wagner GJ, and WK Liu. A multiscale projection method for the analysis of carbon nanotubes. *Computer Methods in Applied Mechanics and Engineering*, 193:1603–1632, 2003.

[121] D Qian and RH. Gondhalekar. A virtual atom cluster approach to the mechanics of nanostructures. *International Journal for multiscale computational engineering*, 2:277–289, 2004.

[122] Yang Ye, Chirputkar Shardool, Alpert David, Eason Thomas, Spottswood Stephen, and Qian. Dong. Enriched space–time finite element method: a new paradigm for multiscaling from elastodynamics to molecular dynamics. *International Journal for Numerical Methods in Engineering*, 92:115–140, 2011.

[123] Kelchner CL, Plimpton SJ, and JC Hamilton. Dislocation nucleation and defect structure during surface indentation. *Physical Review B*, 58:11085, 1998.

[124] Belytschko T, Krongauz Y, Organ D, Fleming M, and Krysl. I. Meshless methods: An overview and recent developments. *Computer Methods in Applied Mechanics and Engineering*, 139:3–47, 1996.

[125] GR Liu, GY Zhang, YT Gu, and YY. Wang. A meshfree radial point interpolation method (rpim) for three-dimensional solids. *Computational Mechanics*, 36(6):421–430, 2005.

[126] SN Atluri and S. Shengping. The meshless local petrov-galerkin (mlpg) method: A simple & less-costly alternative to the finite element and boundary element methods. *Computer Modeling in Engineering & Sciences*, 3(1):11–51, 2002.

[127] Kaiyuana Liu, Shuyaoa Long, and Guangyaob. Li. A simple and less-costly meshless local petrov-galerkin (mlpg) method for the dynamic fracture problem. *Engineering Analysis with Boundary Elements*, 30(1):72–76, 2006.

[128] Yang Shih-Wei, Wang Yung-Ming, Wu Chih-Ping, and Hsuan-Teh Hu. A meshless collocation method based on the differential reproducing kernel approximation. *Computer Modeling in Engineering and Sciences*, 60:1–39, 2010.

[129] Zhuang X, Heaney C, and C Augarde. On error control in the element-free galerkin method. *Engineering Analysis with Boundary Elements*, 36:351–360, 2012.

[130] Wu Chih-Ping, Chiu Kuan-Hao, and Yung Ming-Wang. A meshfree drk-based collocation method for the coupled analysis of functionally graded magneto-electro-elastic shells and plates. *Computer Modeling in Engineering and Sciences*, 35:181–214, 2008.

[131] Wu Chih-Ping, Wang Jian-Sin, and Yung Ming-Wang. A drk interpolation-based collocation method for the analysis of functionally graded piezoelectric hollow cylinders under electro-mechanical loads. *Computer Modeling in Engineering and Sciences*, 52:1–37, 2009.

[132] Wu Chih-Ping, Yang Shih-Wei, Ming Wang Yung, and Hsuan-Teh Hu. A meshless collocation method for the plane problems of functionally graded material beams and plates using the drk interpolation. *Mechanics Research Communications*, 38:471–476, 2011.

[133] Wang Yung-Ming, Chen Syuan-Mu, and Chih-Ping Wu. A meshless collocation method based on the differential reproducing kernel interpolation. *Computational Mechanics*, 45:585–606, 2010.

[134] R. Ruoff. Calling all chemists. *Nature Nanotechnology*, 3:10–11, 2008.

[135] Loh KP, Bao Q, Ang PK, and Yang. J. The chemistry of graphene. *Journal of Materials Chemistry*, 20:2277–2289, 2010.

[136] DK James Z, Sun and Tour. JM. Graphene chemistry: Synthesis and manipulation. *The journal of physical chemistry letters*, 2:2425–2432, 2011.

[137] Sarkar Santanu, Bekyarova Elena, and Haddon. RC. Covalent chemistry in graphene electronics. *Materials today*, 15(6):276–285, 2012.

[138] Neto AHC, Guinea F, Peres NMR, Novoselov KS, and Geim. AK. The electronic properties of graphene. *Reviews of Modern Physics*, 81:109–162, 2009.

[139] Castro1 EV, Novoselov KS, Morozov SV, Peres NMR, Santos JMBLd, Nilsson J, Guinea F, AK Geim, and Neto. AHC. Electronic properties of a biased graphene bilayer. *Journal of Physics: Condensed Matter*, 22:175503, 2010.

[140] Stankovich S, Dikin DA, Dommett GHB, Kohlhaas KM, Zimney EJ, Stach EA, Piner RD, Nguyen ST, and Ruoff. RS. Graphene-based composite materials. *Nature*, 442:282–286, 2006.

[141] Potts JR, Dreyer DR, Bielawski CW, and Ruoff. RS. Graphene-based polymer nanocomposites. *Polymer*, 52:5–25, 2011.

[142] Shen Wen, Yu Yuqi, Shu Jiangnan, and Cui. Hua. A graphene-based composite material noncovalently functionalized with a chemiluminescence reagent: synthesis and intrinsic chemiluminescence activity. *Chemical Communications*, 48:2894–2896, 2012.

[143] Pattabhi RB, Rammohan B, Vijay KS, Satish BD, and Raghunathan. R. Aero-elastic analysis of stiffened composite wing structure. *Advances in Vibration Engineering*, 8(3):255–264, 2009.

[144] Novoselov KS, Falko VI, Colombo L, Gellert PR, Schwab MG, and Kim. K. A roadmap for graphene. *Nature*, 490:192–400, 2012.

[145] J Moser, A Barreiro, and A Bachtold. Current-induced cleaning of graphene. *Applied Physics Letters*, 91:163513, 2007.

[146] Bunch JS, Verbridge SS, Alden JS, van der Zande AM, Parpia JM, Craighead HG, and McEuen. PL. Impermeable atomic membranes from graphene sheets. *Nano letters*,

8:2458–2462, 2008.

[147] F Liu, PM Ming, and J. Li. Ab initio calculation of ideal strength and phonon instability of graphene under tension. *Physical Review B*, 76:064120, 2007.

[148] C Lee, XD Wei, JW Kysar, and J. Hone. Measurement of the elastic properties and intrinsic strength of monolayer graphene. *Science*, 321:385–388, 2008.

[149] AA. Balandin. Thermal properties of graphene and nanostructured carbon materials. *Nature Materials*, 10:569–581, 2011.

[150] Nair RR, Blake P, Grigorenko1 AN, Novoselov KS, Booth TJ, Stauber T, Peres NMR, and Geim AK. Fine structure constant defines visual transparency of graphene. *Science*, 320(5881):1308, 2008.

[151] Mayorov AS, Gorbachev RV, Morozov SV, Britnell L, Jalil R, Ponomarenko LA, Blake P, Novoselov KS, Watanabe K, Taniguchi T, and Geim AK. Micrometer-scale ballistic transport in encapsulated graphene at room temperature. *Nano letters*, 11(6):2396–2399, 2011.

[152] Pérez LR, Herranz MA, and N Martín. The chemistry of pristine graphene. *Chemical Communications*, 49:3721, 2013.

[153] A Hashimoto, K Suenaga, A Gloter, K Urita, and S. Iijima. Direct evidence for atomic defects in graphene layers. *Nature*, 430:870–873, 2004.

[154] Griffith. AA. The phenomena of rapture and flow in solids. *Philosophical transactions of the royal society of London A*, 221:163–198, 1921.

[155] K Kim, VI Artyukhov, W Regan, Y Liu, MF Crommie, BI Yakobson, and A. Zettl. Ripping graphene: preferred directions. *Nano Letters*, 12:293–297, 2012.

[156] Budarapu PR, Sudhir SYB, Brahmanandam J, and Mahapatra. DR. Vibration analysis of multi-walled carbon nanotubes embedded in elastic medium. *Frontiers of Structural and Civil Engineering*, 8(2):151–159, 2014.

[157] Y Zhang, J Zhao, N Wie, JW Jiang, and T. Rabczuk. Effects of the dispersion of polymer wrapped two neighbouring single walled carbon nanotubes (swnts) on nano-engineering load transfer. *Composites Part B: Engineering*, 45(1):1714–1721, 2013.

[158] Y Zhang, J Zhao, Y Jia, T Mabrouki, Y Gong, N Wei, and T. Rabczuk. An analytical solution for large diameter carbon nanotube-reinforced composite with functionally graded variation interphase. *Composite Structures*, 104:261–269, 2013.

[159] Zhang Y, Gao T, Gao Y, Xie S, Ji Q, Yan K, Peng H, and Liu. Z. Defect-like structures of graphene on copper foils for strain relief investigated by high-resolution scanning tunneling microscopy. *ACS Nano*, 5(5):4014–4022, 2011.

[160] Zhu W, Low T, Perebeinos V, Bol AA, Zhu Y, Yan H, Tersoff J, and Avouris. P. Structure and electronic transport in graphene wrinkles. *Nano Letters*, 12:3431–3436, 2012.

[161] Y Zhang, N Wei, J Zhao, Y Gong, and T. Rabczuk. Quasi-analytical solution for the stable system of the multi-layer folded graphene wrinkles. *Journal of Applied Physics*, 114(6):DOI:10.1063/1.4817768, 2013.

[162] JW Jiang, BS wang, and T. Rabczuk. Why twisting angles are diverse in graphene moiré patterns? *Journal of Applied Physics*, 113:194304, 2013.

[163] Jensen K, Kim K, and Zettl. A. An atomic-resolution nanomechanical mass sensor. *Nature Nanotechnology*, 3:533–537, 2008.

[164] JW Jiang, HS Park, and T. Rabczuk. Enhancing the mass sensitivity of graphene nanoresonators via nonlinear oscillations: The effective strain mechanism. *Nanotechnology*, 23:475501, 2012.

[165] JW Jiang, BS Wang, H Park, and T. Rabczuk. Adsorbate migration effects on continuous and discontinuous temperature-dependent transitions in the quality factors of graphene nanoresonators. *Nanotechnology*, 25:025501, 2014.

[166] J Zhao, Z Fan, JW Jiang, and T. Rabczuk. Mechanical properties of three types of carbon allotropes. *Nanotechnology*, 24:09570, 2013.

[167] J Zhao, JW Jiang, Y Jia, W Guo, and T. Rabczuk. A theoretical analysis of cohesive energy between carbon nanotubes, graphene and substrates. *Carbon*, 57:108–119, 2013.

[168] J Zhao, L Wang, JW Jiang, Z Wang, W Guo, and T. Rabczuk. A comparative study of two molecular mechanics models based on harmonic potentials. *Journal Applied Physics*, 113:063509, 2013.

[169] J Zhao, J Wu, JW Jiang, Zhang Z, and T. Rabczuk. Thermal conductivity of carbon nanocoils. *Applied Physics Letters*, 103(23):233511, 2013.

[170] R Ansari, S Ajori, and Motevalli B. Mechanical properties of defective single-layered graphene sheets via molecular dynamics simulation. *Superlattices Microstructures*, 51:274–289, 2012.

[171] M Wang, C Yan, L Ma, N Hu, and M. Chen. Effect of defects on fracture strength of graphene sheets. *Computational Material Science*, 54:236–239, 2012.

[172] Omeltchenko A, Yu J, Kalia RK, and Vashishta. P. Crack front propagation and fracture in a graphite sheet: A molecular-dynamics study on parallel computers. *Physical Review Letters*, 78(11):2148–2151, 1997.

[173] R Khare, SL Mielke, JT Paci, S Zhang, R Ballarini, GC Schatz, and T. Belytschko. Coupled quantum mechanical/molecular mechanical modeling of the fracture of defective carbon nanotubes and graphene sheets. *Physical Review B*, 75:075412, 2007.

[174] M Xu, A Tabarraei, J Paci, J Oswald, and T. Belytschko. A coupled quantum/continuum mechanics study of graphene fracture. *International journal of fracture*, 173:163–173, 2012.

[175] Lu Q, Gao W, and Huang. R. Atomistic simulation and continuum modeling of graphene nanoribbons under uniaxial tension. *Modelling and Simulation in Materials Science and Engineering*, 19:54006, 2011.

[176] Terdalkar SS, Huang S, Yuan H, Rencis JJ, Zhu T, and Zhang. S. Nanoscale fracture in graphene. *Chemical Physics Letters*, 494:218–222, 2010.

[177] J. Tersoff. Modeling solid-state chemistry: Interatomic potentials for multicomponent systems. *Physical Review B*, 39(8):5566–5568, 1989.

[178] M Paggi, M Corrado, and MA. Rodriguez. A multi-physics and multi-scale numerical approach to microcracking and power-loss in photovoltaic modules. *Composite Structures*, 95:630–638, 2013.

[179] Infuso Andrea, Mauro Corrado, and Paggi. Marco. Image analysis of polycrystalline solar cells and modelling of intergranular and transgranular cracking. *Journal of the European Ceramic Society*, http://dx.doi.org/10.1016/j.jeurceramsoc.2013.12.051, 2014.